Gwangju Institute of
Science and Technology

School of Information and Communications

INFONET Journal Club 2013

Application Group

2014. 2. 3

Advisor: Prof. Heung-No Lee

Editor: Seungchan Lee, Haeung Choi

Gwangju Institute of
Science and Technology

BCI CS INFONET²

- Table of Contents -

5	2012-12-04	Gaming control using a wearable and wireless EEG-based brain-computer interface device with novel dry foam-based sensors
	SeungChan Lee	In this paper, they introduced a wearable, wireless and portable EEG-based BCI device with dry foam-based EEG sensors. Using this device, they demonstrated the game control application. This game application was controlled by real-time cognitive stage detection algorithm. The result of this study indicate that a portable wireless BCI device is conveniently and effectively control the application and the developed dry sensor also provided a good quality of EEG signals.
6	2012-12-11	Brain-Computer Interface Using a Simplified Functional Near-Infrared Spectroscopy System
	Evgenii Kim	In this paper, principles, experiments and progress in harnessing simplified function near-infrared spectroscopic systems (fNIRS) as non-invasive instrumentation for brain-computer interfaces were described. The system based on detecting haemodynamic responses. Results show that fNIRS can support simple BCI functionality and shows much potential.
7	2013-01-08	Two-dimensional ultrasound detection with unfocused frequency-randomized signals
	Pavel Ni	This paper was published in the Journal of Acoustical Society of America 2007. Until now in best of my knowledge the only one paper about unfocused ultrasound imaging method. Author proposed to use random frequency for each element of transducer to make randomized frequency pattern. In simulation study this approach was effective in detecting small objects when using frequencies in the 0.25-1.25 Mhz range.
8	2013-01-15	Probabilistic Reconstruction in Compressed Sensing : Algorithms, Phase Diagrams, and Threshold Achieving Matrices
	Hyeongho Baek	In this paper, they present the probabilistic approach to reconstruction and discuss its optimality and robustness. And they detail the derivation of the message passing algorithm for reconstruction. Moreover, they further develop the asymptotic analysis of the corresponding phase diagrams with and without measurement noise, for different distribution of signals.

9	2013-01-22	DASHER-An Efficient Writing System for Brain-Computer Interfaces?
	Soogil Woo	In this paper, they introduced DASHER and DASHER as a BCI user interface. DASHER is a user interface for entering text using discrete or continuous gestures, e.g. a mouse, touchscreen, or eye-tracker. DASHER have advantages. The operation of DASHER is simple, and immediately evident to new users. Also, DASHER has a rapid learning rate that is comparable to alternative text entry methods. So, they propose that DASHER would be well-matched to the low bit-rate, noisy output obtained from brain-computer interfaces(BCI), and discuss the issues surrounding the use of DASHER with BCI systems. In conclusion, they think that DASHER will be equally useful to users who retain functioning vision but are limited to communication through a BCI.
10	2013-01-29	Speckle-field digital holographic microscopy
	Nitin Rawat	This paper was published in the Optics express Journal in 2009. In this paper, they introduced the recording of the electric field of speckle which overcomes the drawbacks: poor spatial resolution, weak depth sectioning, and fixed pattern noise due to unwanted diffraction. This technique has great potential in studying biological samples with improved sensitivity, resolution and optical sectioning capability.
11	2013-02-05	Compressive multiple view projection incoherent holography
	Sangjun Park	In this seminar, the principles of the muliple view projection (MVP) holography technique are described. After understanding the principles, the intuition of the paper is shortly given. Finally, the new technique so called compressive multiple view projection (CMVP) holography is presented and the numberical simulations are also demonstrated.
12	2013-02-12	Compressed Sensing of EEG for Wireless Telemonitoring with Low Energy Consumption and Inexpensive Hardware
	Younghak Shin	Compressing EEG for telemonitoring is extremely difficult for current CS algorithms, because EEG is not sparse in the time domain nor sparse in transformed domains. In this study, they proposed to use the framework of block sparse Bayesian learning, which has superior performance to other existing CS algorithms in recovering non-sparse signals. Experimental results showed that it recovered EEG signals with good quality. Thus, it is very promising for wireless telemonitoring based cognitive neuroscience studies and engineering applications.

13	2013-02-19	Compressive sensing in medical ultrasound
	Jin-Taek Seong	In this paper, they review the basic theory of compressive sensing. Then, a review of the existing CS studies in the field of medical ultrasound is given: reconstruction of sparse scattering maps, pre-beamforming channel data, post-beamforming signals and slow time Doppler data.
14	2013-02-26	Enhanced performance by a hybrid NIRS-EEG brain computer interface
	Seungchan Lee	In this paper, they investigate whether near-infrared spectroscopy (NIRS) can be used to enhance the EEG approach. In the experiment, they applied both methods simultaneously in a real-time Sensory Motor Rhythm (SMR)-based BCI paradigm, involving executed movements as well as motor imagery. They tested how the classification of NIRS data can complement ongoing real-time EEG classification. From the results, simultaneous measurements of NIRS and EEG can significantly improve the classification accuracy of motor imagery in over 90% of considered subjects and increases performance by 5% on average (pb0:01).
15	2013-03-19	Frequency Domain Compressive Sampling for Ultrasound Imaging
	Pavel Ni	Conventional Ultrasound imaging systems rely on Shannon-Nyquist theorem. Often US devices use a sampling rate that is at least four times the central frequency. Consequently large amount of data should be processed in real time. Compressive sensing allows to reduce volume of data directly acquiring compressed signal. The purpose of this paper is to show mechanism involved in a successful CS reconstruction.
16	2013-03-26	Brain Computer Interface-Based Smart Living Environmental Auto-Adjustment Control System in UPnP Home Networking.
	Soogil Woo	A brain computer interface-based smart living environmental auto-adjustment control system (BSLEACS) is proposed in this paper. They integrated the BCI technique with universal plug and play (UPnP) home networking for smart house applications. This system has advantages. The advantages of low power consumption and small volume of the above modules are suitable for smart house applications in daily life. BSLEACS provides a novel system prototype for environmental control.

17	2013-04-02	Optical brain monitoring for operator training and mental workload assessment
	Evgenii Kim	In this paper, we provide evidence from two studies that fNIR can be used in ecologically valid environments to assess the: 1)mental workload of operators performing standardized and complex cognitive tasks, and 2) development of expertise during practice of complex cognitive and visuomotor tasks (piloting unmanned air vehicles — UAV). Results indicate that fNIR measures are sensitive to mental task load and practice level, and provide evidence of the fNIR deployment in the field for its ability to monitor hemodynamic changes that are associated with relative cognitive workload changes of operators.
18	2013-04-09	Direct recording of holograms by a CCD target and numerical reconstruction
	Nitin Rawat	In this paper, the principle of recording holograms directly on a CCD target is described. A real image of the object is reconstructed from the digitally sampled hologram by means of numerical methods.
19	2013-04-23	Localisation of cognitive tasks used in EEG-based BCIs
	Younghak Shin	In this paper, to provide candidate electrode sites and neurophysiological reference information for cognitive tasks, six cognitive tasks were tested against the idle state. Cross subject candidate electrode sites were obtained via a wrapper method based upon a sequential forward floating search algorithm. Source localisation results were obtained using sLORETA software
20	2013-04-30	Scanner-Free and Wide-Field Endoscopic Imaging by Using a Signle Multimode Optical Fiber
	Hwanchol Jang	In this letter, a method for eliminating the effect of mode dispersion and therefore realize wide-field endoscopic imaging by using only a single multimode fiber with no scanner attached to the fiber.
21	2013-05-14	A Compressive Sensing and Unmixing Scheme for Hyperspectral Data Processing
	Woongbi Lee	In this paper, a low complexity scheme is proposed for hyperspectral data compression and reconstruction. The data reconstruction minimizes the total variation of the abundance fractions subject to a preprocessed fidelity equation with a significantly reduced size, and other side constraints.

22	2013-05-21	Dry and NOncontact EEG sensors for Mobile Brain-Computer Interfaces
	Seungchan Lee	Dry and noncontact electroencephalographic (EEG) electrodes, which do not require gel or even direct scalp coupling, have been considered as an enabler of practical, real-world, brain–computer interface (BCI) platforms. This study compares wet electrodes to dry and through hair, noncontact electrodes within a steady state visual evoked potential (SSVEP) BCI paradigm. The construction of a dry contact electrode, featuring fingered contact posts and active buffering circuitry is presented. Additionally, the development of a new, noncontact, capacitive electrode that utilizes a custom integrated, high-impedance analog front-end is introduced.
23	2013-05-28	Exemplar-Based Processing for Speech Recognition
	Pavel Ni	Automatic speech recognition has been dominated by technique using hidden Markov models to model time varying aspects of the acoustics. This method allows for a generalization of the observed data as long as the distribution estimated by the model is a reasonable description of the unseen data. In many cases, such a description must be simplified to allow reliable estimates of all free parameters in the model, and as a result, fine details in the model are lost. Exemplar based models have the potential to address this deficiency by building an instance of model based only on the relevant exemplars selected, exploiting sparse coding and compressive sensing technique.
24	2013-06-04	A cell-phone-based brain-computer interface for communication in daily life
	Soogil Woo	In this paper, their study aims to integrate a mobile and wireless electroencephalogram (EEG) system and a signal processing platform based on a cellphone into a wearable and wireless online BCI. They implemented and tested online signal processing methods in both time and frequency domains for detecting steady-state visual evoked potential (SSVEP). They study to demonstrate a portable, cost-effective and miniature cell-phone-based platform.
25	2013-06-25	Supervised Machine Learning: A review of Classification Techniques
	Evgenii Kim	Supervised machine learning is wildly used algorithm in different fields of science. This paper describes a basic idea of various supervised machine learning classification techniques. The author’s hope is to guide the researcher in interesting research directions and to give suggestion possible bias combinations that have yet to be explored.

26	2013-07-09	Digital holography for quantitative phase-contrast imaging
	Nitin Rawat	The paper provides simultaneously an amplitude-contrast image and a quantitative phase-contrast image. The technique uses a CCD camera for recording of a Fresnel off-axis hologram and a numerical method for hologram reconstruction.
27	2013-07-16	A new (semantic) reflexive brain–computer interface: In search for a suitable classifier
	Younghak Shin	The goal of the current study is to find a suitable classifier for electroencephalogram (EEG) data derived from a new learning paradigm which aims at communication in paralysis. A reflexive semantic classical (Pavlovian) conditioning paradigm is explored as an alternative to the operant learning paradigms, currently used in most brain–computer interfaces (BCIs).
28	2013-07-23	Conditions for practicing compressive Fresnel Holography
	Sangjun Park	Recently, compressive sensing based on Fresnel wave propagation and sparsity is sued for promoting imaging reconstruction from a hologram. In this talk, we aim to understand the theoretical bounds on the performance of compressive imaging system based on Fresnel wave propagation.
29	2013-07-30	Random-Frequency SAR Imaging Based on Compressed Sensing
	Jin-Taek Seong	In this paper, a random-frequency SAR imaging scheme based on compressed sensing is proposed. If the targets are sparse or compressible, it is sufficient to transmit only a small number of random frequencies to reconstruct the image of the targets. This means that the limitations of the stepped-frequency technique for SAR can be overcome. The available imaging range width can be enlarged significantly, while the range and azimuth resolutions are both maintained
30	2013-08-07	Optimizing the Channel Selection and Classification Accuracy in EEG-Based BCI
	Seung-Chan Lee	Multichannel EEG is generally used in brain–computer interfaces (BCIs). This paper proposes a novel sparse common spatial pattern (SCSP) algorithm for EEG channel selection. The proposed SCSP algorithm is formulated as an optimization problem to select the least number of channels within a constraint of classification accuracy. The proposed SCSP algorithm is evaluated using two motor imagery datasets, one with a moderate number of channels and another with a large number of channels. The proposed SCSP algorithm yielded an average improvement of 10% in classification accuracy compared to the use of three channels (C3, C4, and Cz).

31	2013-08-14	Compressive Sensing in Photoaccoustic Tomography
	Pavel Ni	The data acquisition speed in photoacoustic computed tomography (PACT) is limited by the laser repetition rate and the number of parallel ultrasound detecting channels. Reconstructing an image with fewer measurements can effectively accelerate the data acquisition and reduce the system cost. We adapt compressed sensing (CS) for the reconstruction in PACT. CS-based PACT is implemented as a nonlinear conjugate gradient descent algorithm and tested with both phantom and in vivo experiments.
32	2013-08-21	Toward Brain-Actuated Humanoid Robot: Asynchronous Direct Control Using an EEG-Based BCI
	Soogil Woo	The brain–computer interface (BCI) technique is a novel control interface to translate human intentions into appropriate motion commands for robotic systems. The aim of this study is to apply an asynchronous direct-control system for humanoid robot navigation using an electroencephalograph (EEG), based active BCI. The experimental procedures consist of offline training, online feedback testing, and real-time control sessions. For the performance test, five healthy subjects controlled a humanoid robot navigation to reach a target goal in an indoor maze by using their EEGs based on real-time images obtained from a camera on the head of the robot. In experimental results, the subjects successfully controlled the robot in the indoor maze.
33	2013-08-28	Temporal classification of multichannel near-infrared spectroscopy signals of motor imagery for developing a brain-computer interface
	Evgenii Kim	in this paper, they describe a study conducted to test the feasibility of using multichannel NIRS in the development of a BCI. They used a continuous wave 20-channel NIRS system over the motor cortex of 5 healthy volunteers to measure oxygenated and deoxygenated hemoglobin changes during left hand and right-hand motor imagery. They applied two different pattern recognition algorithms separately, Support Vector Machines (SVM) and Hidden Markov Model (HMM), to classify the data offline. SVM classified left-hand imagery from right hand imagery with an average accuracy of 73% for all volunteers, while HMM performed better with an average accuracy of 89%. Their results indicate potential application of NIRS in the development of BCIs.

34	2013-09-10	Digital Image information encryption based on compressive sending and double random phase encoding technique
	Nitin Rawat	An image information encryption method based on compressive sensing and double random-phase encoding is proposed. Considering that natural image tends to be compressible in a transform domain, the characterstics of Compressive sensing, dimensional reduction and random projection, are utilized to sample or encrypt a digital image firstly. The double-encrypted information is dispersed and embedded into the host image. At the received terminal, original image information is reconstructed approximately via Orthogonal Matching Pursuit algorithm.
35	2013-09-24	Sparsity driven ultrasound imaging
	Jin-Taek Seong	The framework involves the use of a physics-based forward model of the ultrasound observation process, the formulation of image formation as the solution of an associated optimization problem, and the solution of that problem through efficient numerical algorithms. The sparsity-driven, model-based approach estimates a complex-valued reflectivity field and preserves physical features in the scene while suppressing spurious artifacts. It also provides robust reconstructions in the case of sparse and reduced observation apertures.
36	2013-10-08	An auditory brain–computer interface evoked by natural speech
	Younghak Shin	In this study, they present a novel fully auditory EEG-BCI based on a dichotic listening paradigm using human voice for stimulation. This interface has been evaluated with healthy volunteers, achieving an average information transmission rate of 1.5 bits min−1 in full-length trials and 2.7 bits min−1 using the optimal length of trials, recorded with only one channel and without formal training. This novel technique opens the door to a more natural communication with users unable to use visual BCIs, with promising results in terms of performance, usability, training and cognitive effort.
37	2013-10-15	Temporal classification of multichannel near-infrared spectroscopy signals of motor imagery for developing a brain-computer interface
	Evgenii Kim	In this paper, they describe a study conducted to test the feasibility of using multichannel NIRS in the development of a BCI. They used a continuous wave 20-channel NIRS system over the motor cortex of 5 healthy volunteers to measure oxygenated and deoxygenated hemoglobin changes during left hand and right-hand motor imagery. They applied two different pattern recognition algorithms separately, Support Vector Machines (SVM) and Hidden Markov Model (HMM), to classify the data offline. SVM classified left-hand imagery from right hand imagery with an average accuracy of 73% for all volunteers, while HMM performed better with an average accuracy of 89%. Their results indicate potential application of NIRS in the development of BCIs.

38	2013-10-22	A measurement-domain beamforming approach for ultrasound instrument based on distributed compressed sensing: initial development
	Pavel Nee	In this paper author applied distributed compressed sensing to ultrasound medical imaging and proposed Measurement-domain adaptive beamforming (MABF) to directly reconstruct ultrasound image without reconstructing transducer signals.
39	2013-10-29	A novel BCI based on ERP components sensitive to configural processing of human faces
	Seungchan Lee	This study introduces a novel brain–computer interface (BCI) based on an oddball paradigm using stimuli of facial images with loss of configural face information (e.g., inversion of face). With the proposed novel paradigm, we investigate the effects of ERP components N170, VPP and P300 on target detection for BCI. An eight-class BCI platform is developed to analyze ERPs and evaluate the target detection performance using linear discriminant analysis without complicated feature extraction processing. The online classification accuracy of 88.7% and information transfer rate of 38.7 bits min−1 using stimuli of inverted faces with only single trial.
40	2013-11-05	Securing information by use of digital holography
	Nitin Rawat	An information security method that uses a digital holographic technique is proposed in this paper. An encrypted image is stored as a digital hologram. The decryption key is also stored as a digital hologram. The encrypted image can be electrically decrypted by use of the digital hologram of the key. This security technique provides secure storage and data transmission. Experimental results are presented to demonstrate the proposed method.
41	2013-12-03	A Head-Up Display-Based P300 Brain–Computer Interface for Destination Selection
	Soogil Woo	In this paper, they propose a P300 brain–computer interface (BCI) with visual stimuli presented on a head-up display and we apply this BCI for selecting destinations of a simulated vehicle in a virtual scene. To improve the usability of the selection system, we analyze the effects of the number of electroencephalogram (EEG) rounds on system performance. This paper lays a foundation for developing vehicles that use a BCI to select a desired destination from a list of predefined destinations and then use an autonomous navigation system to reach the desired destination.
42	2013-12-10	Some fundamental properties of speckle
	Hwanchol Jang	A probabilistic modeling for speckle pattern is introduced. Ways to suppress the speckle pattern is also presented.

Digital holography for quantitative phase-contrast imaging

Authors: Etienne Cuche, Frederic Bevilacqua, and Christian Depeursinge

Publication: Optics Letters March 1,1999

Speaker: Nitin Rawat

Short summary:

In the paper, they have presented a new application of digital holography for phase-contrast imaging. The technique uses a CCD camera for recording of a digital Fresnel off-axis hologram and a numerical method for hologram reconstruction. The method simultaneously provides an amplitude-contrast image and a quantitative phase-contrast image.

I. INTRODUCTION

The holographic process is described mathematically as follows:

$$O(x,y) = o(x,y)\,\mathrm{e}^{i\varphi_o(x,y)} \qquad \ldots (1.1)$$

Is the complex amplitude of the object wave with real amplitude o and phase φ_o and

$$R(x,y) = r(x,y)\,\mathrm{e}^{i\varphi_R(x,y)} \qquad \ldots (1.2)$$

Is the complex amplitude of the reference wave with real amplitude r and phase φ_R

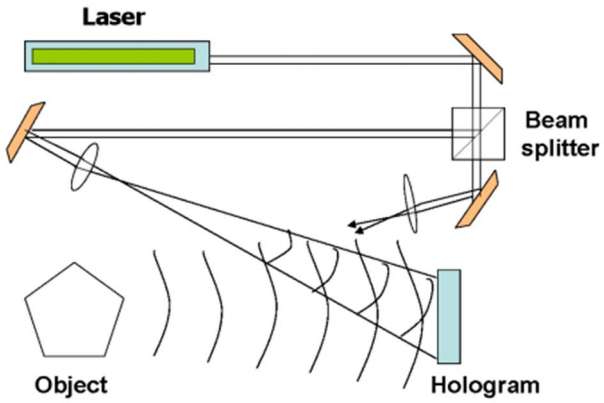

Fig. 1 Construction of a hologram

Both waves interfere at the surface of the recording medium. The intensity is calculated by

$$I_H(x,y) = \left|O(x,y) + R(x,y)\right|^2$$

$$= (O(x,y) + R(x,y))(O(x,y) + R(x,y))^*$$

$$= R(x,y)R^*(x,y) + O(x,y)O^*(x,y)$$
$$+ O(x,y)R^*(x,y) + R(x,y)O^*(x,y) \quad \ldots (1.3)$$

$$I_H(x,y) = |R|^2 + |O|^2 + R^*O + RO^* \quad \ldots (1.4)$$

Digital Recording

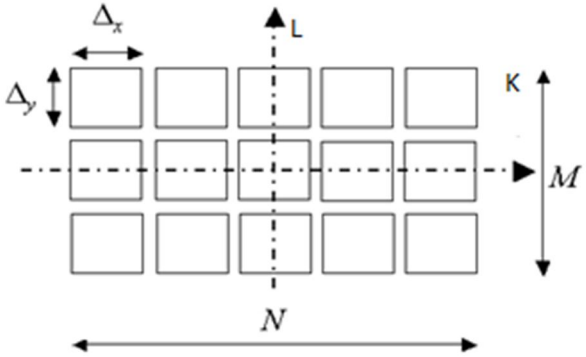

Fig. 2 Concept diagram of a surface-pixel sensor

The digital recording will (depending on the directions x and y on the recording plane) consist of M x N pixels. Each of these pixels is of a dimension $\Delta_x \times \Delta_y$. In CCD sensors, Matrices made up of photosensitive elements called pixels are generally square-shaped. In our case it is $12 \times 12 \mu m$

In their case, the hologram intensity was recorded by a standard black and white CCD camera (Hitachi Denshi KP-M2).

The two neutral-density filters allow the adjustment of the object and the reference intensities.

A square image of area LxL (Sensor size) = 4.83mm X 4.83mm containing N x N= 512 x 512 pixels is acquired in the center of the CCD sensor, and a digital hologram is transmitted to a computer via a frame grabber.

The digital hologram $I_H(k,l)$ results from two-dimensional spatial sampling of $I_H(x,y)$ by the CCD:

$$I_H(k,l) = I_H(x,y)\,rect\left(\frac{x}{L},\frac{y}{L}\right) \times \sum_{k}^{N} \sum_{l}^{N} \delta(x - k\Delta x, y - l\Delta y) \quad \ldots (1.5)$$

Where k and l are integers $(-N/2 \le k,l \le N/2)$ and Δx and Δy are the sampling intervals in the hologram plane i.e. pixel size: $\Delta x = \Delta y$ =L/N

II. NUMERICAL RESULTS

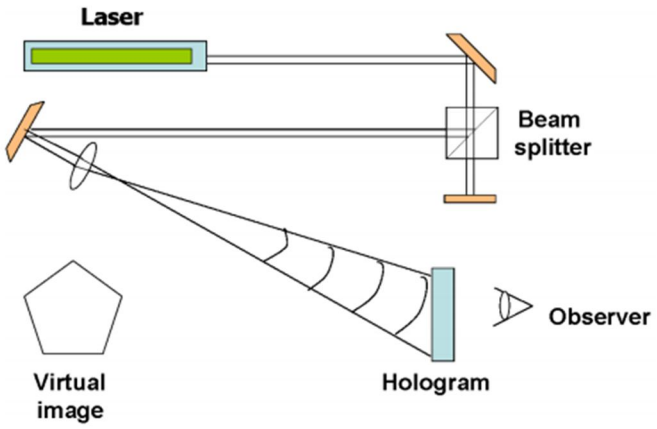

Fig.3 Reconstruction of a hologram

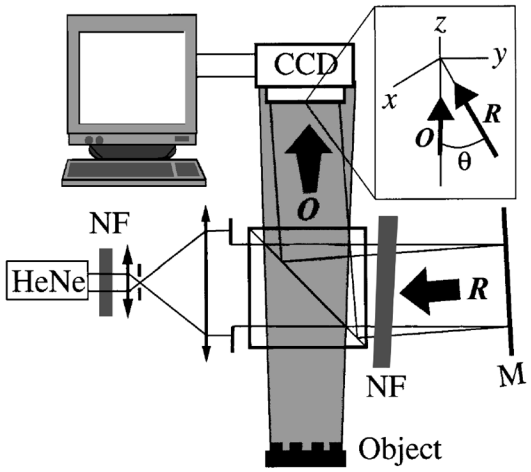

Fig.4 Experimental setup

A wave front $\psi_H(x,y) = R(x,y)I(x,y)$ is transmitted by a hologram and propagates toward an observation plane, where a three-dimensional image of the object can be observed.

For reconstructing a digital hologram, a digital transmitted wave front $\psi_H(k\Delta x, l\Delta y)$ is computed by multiplication of digital hologram $I_H(k,l)$ by a digital computed reference wave, $R_D(k,l)$,called the digital reference wave.

If we assume that mirror M reflects a plane wave of wavelength λ then R_D can be calculated as follows:

$$R_D(k,l) = \underbrace{A_R}_{1} \exp\left[i\frac{2\pi}{\lambda}(k_x k\Delta x + k_y l\Delta y) \right] \quad \text{... (1.6)}$$

Where k_x and k_y are the two components of the wave vector and A_r is the amplitude.
$k_x = -3.12\times10^{-3}$ and $k_y = -5.34\times10^{-3}$

Taking into account the definition of hologram intensity [Eq. 1.4], we have

$$\psi\ (k\Delta x, \Delta y) = R_D(k,l)I_H(k,l) \quad \text{... (1.7)}$$

$$= \underbrace{R_D|R|^2 + R_D|O|^2}_{Zero\ order\ of\ diffraction} + \underbrace{R_D R^* O}_{Twin\ image} + \underbrace{R_D R O^*}_{real\ image}$$

To avoid an overlap of these three components of ψ during reconstruction, they recorded the hologram in the so-called off-axis geometry. For this purpose the mirror in the reference arm, M is oriented such that the reference wave **R** reaches the CCD at an incidence angle θ.The value θ must be sufficiently large to ensure separation between the real and the twin images in the observation planes. However, θ must not exceed a given value so that the spatial frequency of the interferogram does not exceed the resolving power of the CCD.

$$\theta \le \theta_{\max} = arc\ \sin\left(\frac{\lambda}{2\Delta x}\right) \qquad \text{... (1.8)}$$

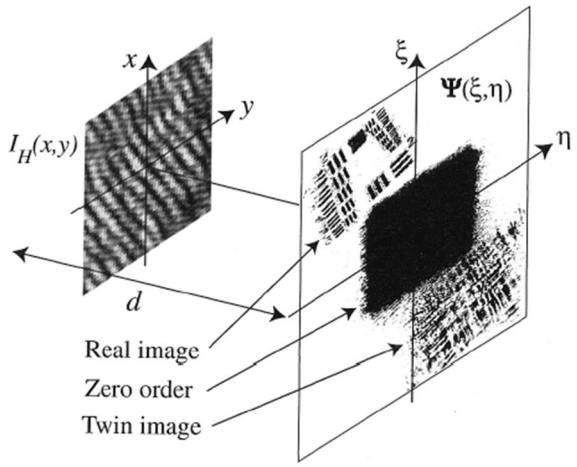

Geometry for hologram reconstruction. *0xy*, hologram plane; *0*ξη, observation plane; *d*, reconstruction distance; **Ψ**(ξ, η), reconstructed wave front.

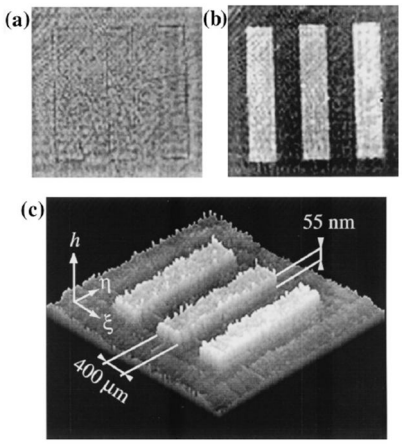

Reconstructed images obtained with a pure phase object: (a) amplitude contrast, (b) phase contrast, (c) three-dimensional perspective of the reconstructed height distribution (the vertical scale is not equal to the transverse scale).

The reconstructed wave front $\psi(m\Delta\xi, n\Delta\eta)$, at a distance d from the hologram plane, is computed by use of a discrete expression of the Fresnel integral:

$$\psi(m\Delta\xi, n\Delta\eta) = A\exp\left[\frac{i\pi}{\lambda d}(m^2\Delta\xi^2 + n^2\Delta\eta^2)\right] \times FFT\left\{R_D(k,l)I_H(k,l)\exp\left[\frac{i\pi}{\lambda d}(k^2\Delta x^2 + l^2\Delta y^2\right]\right\}_{m,n} \qquad \text{... (1.9)}$$

Where m and n are integers $(-N/2 \le m,n \le N/2)$, FFT is the fast Fourier transform operator, and $A = \exp(i2\pi d/\lambda)/(i\lambda d)$

$\Delta\xi$ and $\Delta\eta$ are the sampling intervals in the observation plane and define the transverse resolution of the reconstructed image.

This transverse resolution is related to the size of the CCD (L) and to the distance d by,

$$\Delta\xi = \Delta\eta = \lambda d / L \qquad \text{... (1.10)}$$

The reconstructed wave front is an array of complex numbers. The amplitude and the phase contrast images can be obtained by calculation of the square modulus.

References

[1] M.Pluta, Non-standard techniques for phase contrast microscopy, Vol. 6 of Advances in Optical and Electron Microscopy

[2] U.Schnars and W. Juptner, Appl. Opt. 33, 179 (1994)

[3] E. Cuche, P. Poscio, and C. Depeursinge, Proc. SPIE 2927, 61 (1996)

INFONET, GIST
Journal Club

Compressed sensing with off-axis frequency-shifting holography

Authors: Marcio M. Marim, Michael Atlan, Elsa Angelini, and Jean-Christophe Olivo-Marin
Publication: Optics letters/ vol. 35, no. 6/ March 2010
Speaker: Hwanchol Jang

Short summary: This work reveals an experimental microscopy acquisition scheme successfully combining compressed sensing (CS) and digital holography in off-axis and frequency-shifting conditions. The authors propose a CS-based imaging scheme for sparse gradient images, acquiring a diffraction map of the optical field with holographic microscopy and recovering the signal from as little as 7% of random measurements.

I. COMPRESSED SENSING

- A signal $g \in R^N$ has a sparse representation if it can be written as a linear com bination of a small set of vectors taken from some basis Ψ, such as $g = \sum_{i=1}^{N} c_i \Psi_i$, with $\|c\|_1 \approx S$ where $S << N$.
- If such a sparsifying transform Ψ exists in the spatial domain, it is possible to reconstruct an image g from partial knowledge of its Fourier spectrum [1].

II. SYSTEM OVERVIEW

- g represents the local optical intensity in the object plane.
- We denote by $f \in C^N$ the associated complex optical field, satisfying $g = |f|^2$.
- The radiation field propagates from the object to the detector plane in Fresnel dif fraction conditions $(d>>(x,y)_{max})$.
- Thus, the optical field in the object plane f is linked to the field F in the detect ion plane by a Fresnel transform, expressed in the discrete case as

$$F = \mathrm{F}(f) : C^N \to C^N,$$
$$F_p = \frac{1}{N}\sum_{n=1}^{N} f_n e^{i(\alpha n^2 - 2\pi np/N)} \quad (1),$$

where p and n denote pixel indices and $\alpha \in R^+$ is the parameter of the quadratic phase factor $e^{i\alpha n^2}$ describing the curvature in the detection plane of a wave emitted by a point source in the object plane.

III. Optical configuration [2]

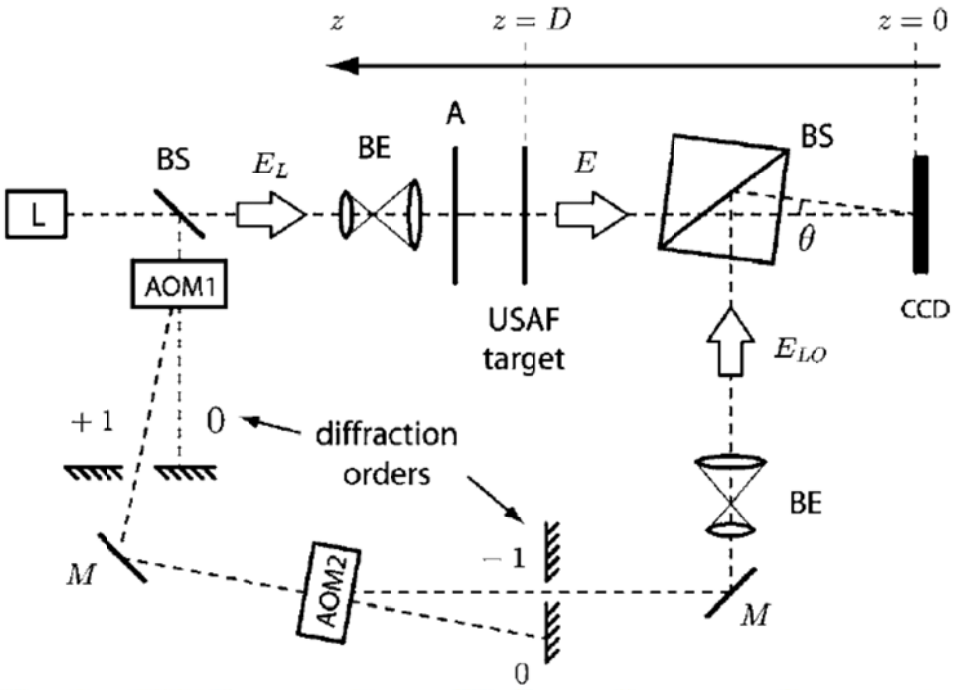

Fig. 1. USAF target digital holography setup: L, main laser; BS, beam splitter; AOM1 and AOM2, acousto-optic modulators; BE, beam expander; M, mirror; A, light attenuator; USAF, transmission target; CCD, CCD camera.

- It consists of an off-axis frequency-shifting digital holography scheme.
- The interfered object beam by the reference beam is recorded at the array detector.
- $F \in C^M$ is calculated from a four-phase measurement.

Phase-shifting digital holography [3].

- The reference beam is dynamically phase shifted with respect to the signal field; the phase shift in the experiment is linear in time (frequency shift).
- It is then possible to obtain the two quadratures of the field in an on-axis configuration even though the conjugate image alias and the true image overlap, because aliases can be removed by taking image differences.
- This shift produces time-varying interferograms on a two dimensional sensor.
- Intensity in the detector plane results from the interference of the signal field with the δf -shifted reference field:

$$I(t) = \left| E_s + E_r \exp i(2\pi \cdot \delta f \cdot t) \right|^2$$

where Es and Er represent the complex amplitudes of the signal and the reference fields, respectively; here E_s=F.

- L intensity $I_l = \left| E_s + E_r \exp i(\frac{2\pi l}{L}) \right|^2$ measurements are performed at $t_l = \frac{l}{\delta f \cdot L}$, $l = 0,...,L-1$; $I_l = |E_s|^2 + |E_r|^2 + E_s^* E_r \exp i(\frac{2\pi l}{L}) + E_s E_r^* \exp -i(\frac{2\pi l}{L})$.
- Obtain Es by demodulating I:

$$E_s = \frac{1}{L \cdot E_r^*} \sum_{l=0}^{L-1} I_l \exp i(\frac{2\pi l}{L}).$$

- The CCD camera records the hologram of the interference with frame rate f_{CCD} =12.5Hz, acquisition time T=1/12.5=80ms. They $\delta f = f_{CCD} / L$ shift the reference beam by combining two acousto-optic modulator (Crystal Technology: $f_{\mathrm{AOM}} \cong 80\mathrm{MHz}$), AOM1 and AOM2, working at $\Delta f + \delta f$ and $-\Delta f$, respectively, with Δf =80MHz. δf =3.125Hz is equal to one quarter of the CCD image frequency (L=4).

The k-space hologram at z=D from the CCD

- $\tilde{E}_s(k_x, k_y, z) = \tilde{K}(k_x, k_y, z)\tilde{E}_s(k_x, k_y, z = 0)$ where $\tilde{K}(k_x, k_y, z)$ is the k-space kernel function that describes the propagation from 0 to z.
- $\tilde{K}(k_x, k_y, z) = e^{iz(k_x^2 + k_y^2)/k}$ where $k = 2\pi / \lambda$ is the optical wave vector.

- Consider the Fresnel propagation of Es from z=0 to z=D, which can be formally expressed as an x and y convolution product (symbol $\otimes$):

$$E_s(x,y,z) = P(x,y,z) \otimes E_s(x,y,z=0),$$

where $P(x,y,z) = \frac{e^{i\cdot kz}}{i\lambda z}\exp\left[i\frac{k}{2z}(x^2+y^2) \right]$.

Combination of "Off axis" and "phase shift".

- With off-axis holography, it is possible to record with a single hologram, the two quadratures of the object complex filed. However, the object field of view is reduced, since one must avoid the overlapping of the image with the conjugate image alias.
- With phase-shifting holography, it is possible to obtain the two quadratures of the field even though the conjugate image alias and the true image overlap, because aliases can be removed by taking image differences.
-

IV. CONVENTIONAL APPROACH

- F can be backpropagated numerically to the target plane with the standard convol ution method when all measurements $F \in C^N$ are available.
- In this case, the complex filed in the object plane f is retrieved from a discrete i nverse Fresnel transform of F; $f = \mathrm{F}^{-1}(F)$,

$$f_p = \frac{1}{N}\sum_{n=1}^{N} F_n e^{-i(\alpha n^2 - 2\pi np/N)} \qquad (2).$$

V. PROPOSED CS APPROACH

- In the CS, the signal reconstruction consists of solving a convex optimization pro blem that finds the candidate $\hat{g}$ of minimal complexity satisfying $\hat{F}|_\Gamma = F|_\Gamma$, whe re $F|_\Gamma \subseteq F$ is a partial subset of measurements in the set Γ.
- We want to recover the intensity image of the object $g = \left\{ |f|^2 : f \in C^N \right\}$ from a small number of measurements $F|_\Gamma \in C^M$, where $M << N$.

- Partial measurements in the detection plane can be written as $F|_\Gamma = \Phi f$, where th e sampling matrix Φ models a discrete Fresnel transformation and a random und ersampling with a flat distribution.
- To find the best estimator $\hat{g}$, we solve the following convex optimization proble m:

$$\hat{g} = \arg\min_{g \in R^N} \|\Psi g\|_1 \text{ subject to } \hat{F}|_\Gamma = F|_\Gamma .$$

- Since the test image is piecewise constant with sharp edges (such as most micros copy images), it can be sparsely represented computing its gradient.
- In image processing, a suitable norm to constrain the gradient of an image was i ntroduced as the total variation (TV) which measures the l-1 norm of the gradien t magnitudes over the whole image, $\|g\|_{TV} = \|\nabla g\|_1$.
- The incoherence property holds for the two bases adopted here which are the Fre snel spectrum and the TV. Moreover, random measurements in the spectral domai n satisfy the RIP condition.
- Hence for an overwhelming percentage of Fresnel coefficients sets Γ with cardin ality obeying $|\Gamma| = M \geq KS \log N$, for some constant *K*, $\hat{g}$ is the unique solution to the problem,

$$\hat{g} = \arg\min_{g \in R^N} \|\nabla g\|_1 \text{ subject to } \hat{F}|_\Gamma = F|_\Gamma .$$

- The reconstruction of g with robustness to noise:

$\hat{g} = \arg\min_{g \in R^N} \|\nabla g\|_1$ subject to $\left\|\hat{F}|_\Gamma - F|_\Gamma\right\|_2 \leq \delta$, for some $\delta \leq C\varepsilon$,
which depends on the noise energy.

VI. RESULTS

Standard convolution method (eq. 2) and CS approach.

- For the CS approach, Fresnel coefficients are undersampled randomly
- Figure 3(b) shows the CS reconstruction result from only 7% of the pixels used in the standard approach.
- Figure 3(d) illustrates the residual (Euclidean distance $|\hat{g} - g|$) from standard holographic and CS reconstructions. The global normalized error is $\|\hat{g} - g\|_2$ =0.005.

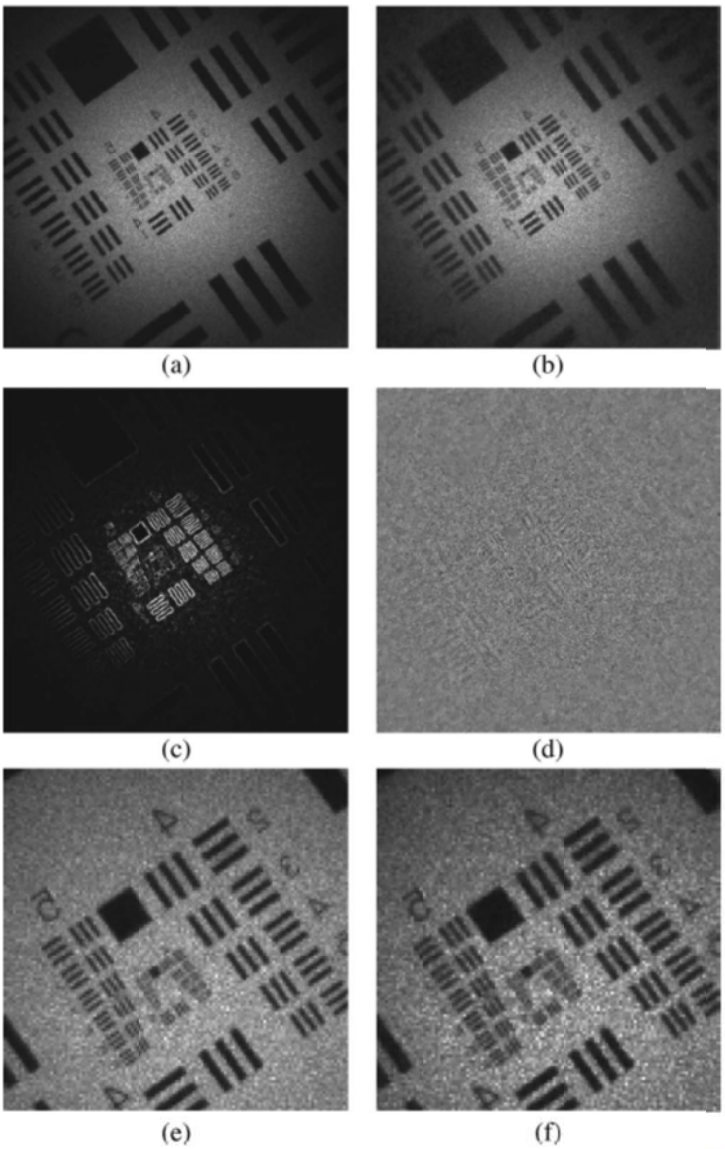

Fig. 3. (a) Standard holography, as described in Eq. (1). (b) CS reconstruction, using 7% of the Fresnel coefficients. (c) Gradient of g. (d) Residual from (a) and (b). (e), (f) Magnified views from (a) and (b).

Reference

[1] E. Candes and J. Romberg, “Practical signal recovery from random projections,” Proc. SPIE, 5674, Jan. 2005.
[2] M. Gross and M. Atlan, “Digital holography with ultimate sensitivity,” Opt. Lett., Vol. 32, no. 8, Apr. 2007.
[3] F. Le Clerc and L. Collot, “Numerical heterodyne holography with two-dimensional photodetector arrays,” Opt. Lett., vol. 25, no. 10, May 2000.

VII. FURTHER DISCUSSION

- How do they check $\hat{F}|_\Gamma = F|_\Gamma$ where $\hat{F}|_\Gamma = \Phi\hat{f}$ and $F|_\Gamma = \Phi f$; it looks difficult as they estimate $g = |f|^2$ not f.

An EEG-Based BCI System for 2-D Cursor Control by Combining Mu/Beta Rhythm and P300 Potential

Yuanqing Li et al.

IEEE Trans. Biomedical Eng. (2010.10)

Presenter : Younghak Shin

GIST, Dept. of Information and Communication, INFONET Lab.

Gwangju Institute of Science and Technology

Background

- P300

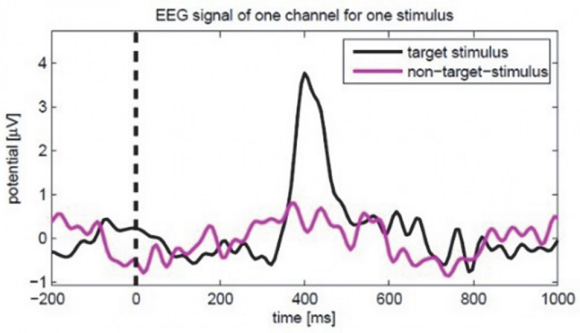

- Motor imagery (Mu/Beta Rhythm)

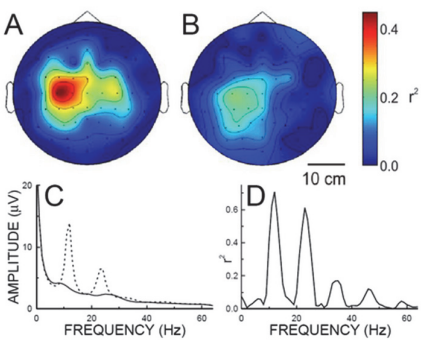

Introduction & Motivation

- Brain computer interface is a communication and control pathway to directly translate brain activities into computer control signals.
- An important issue in BCI research is cursor control: to map brain signals to movements of a cursor on a computer screen.
- Cursor control is a basic and necessary application in BCIs.
- In the EEG-based BCI field, most related studies were focused on 1-D cursor control using motor imagery feature. (our experiment)
- Multidimensional cursor control enables enhanced interfacing between the user and the machine (much wider range of applications)

Introduction & Motivation

- The development of 2-D control BCI is impeded by the difficulty in obtaining two independent control signals from the noisy EEG data of poor spatial specificity.
- The first EEG-based 2-D cursor control BCI is remarkable [Wolpaw 2004]: two independent control signals could be derived from combinations of the rhythmic powers(mu and beta).
- However, the downside of this approach is the required intensive user training (some weeks or months).
- Also other forms of 2-D BCI were reported that adopted a discrete control paradigm using the steady-state visual evoked potential (SSVEP) and P300.

Introduction & Motivation

- P300 and SSVEP based BCI cursor control system

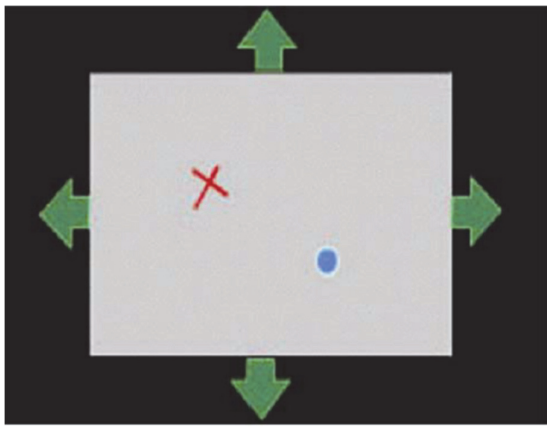

- For each update of the position, the cursor takes only one of a few fixed directions (discrete).
- This leads to unsmooth, zigzag like moves of the cursor.

Introduction & Motivation

- More efficient 2-D control is required for real world application
- This could be implemented through the combination of two independent control signal for vertical and horizontal movements
- In this paper, they propose a new paradigm for 2-D cursor control by simultaneously detecting two brain signals; P300 and motor imagery (hybrid BCIs)
- The user control the vertical movement by using a P300.
- At the same time, the user also use a motor imagery to control the horizontal movement.

Introduction & Motivation

- The P300 allows to select one of the three states: moving upwards, moving downwards, or no vertical movement.
- The motor imagery translates motor imagery into a continuous value that determine the direction and the velocity of the horizontal movement.
- Through selecting the vertical movement state and manipulating the horizontal speed with direction, users will move the cursor along any direction in a self-paced manner.
- Since the neural mechanism of motor imagery differs largely from that of P300, the two signals can be independently controlled by the user.

Method

- Experimental Procedure

- To evaluate the proposed method, they conduct an online experiment involving six subjects.
- After a short calibration(training) session for subject-specific P300 and motor imagery modeling,
- the subjects undergo a few sessions of feedback training using the GUI, and subsequently perform cursor control tasks in test sessions.
- In particular, the feedback training emphasizes on learning of motor imagery control.

Method

- GUI and Control Mechanism

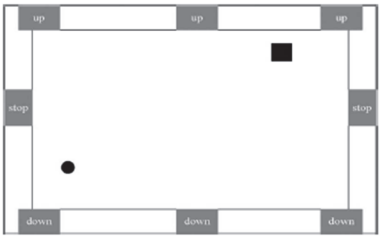

- The ball and the square, respectively, represent a cursor and a target.
- the GUI has a dimension of 1166 pixels ×721pixels.

- In each trial, the initial cursor and target randomly appear inside a rectangular workspace.
- Eight flashing buttons are located at the side, which would generate P300 potentials when the user focus attention on one of them.
- The main objective for the arrangement of three “up” and “down” buttons is for user’s convenient use.
- For example, if the cursor is now in the right-hand side, then the user can choose the “up” or “down” button located in the same side
- The horizontal movement of the cursor is controlled by motor imagery.

Method

- Test trial

- A trial begins when a target and a cursor appear.
- At 100 ms later, the eight buttons begin to flash alternately in a random order.
- Each button is intensified for 100 ms, while the time interval between two consecutive button flashes is 120 ms.
- The trial ends when the cursor hits the target or when the 60-s timeout limit occurs.
- The interval between two consecutive trials is 2 s.
- The cursor’s position is updated every 200 ms; the user is able to control the cursor’s movement at any time at will (self-paced)

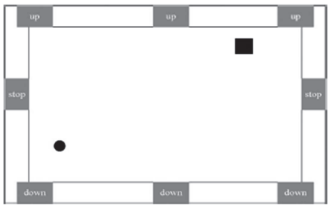

Method

- Control of Vertical Movement Based on P300 Potential

- Let $c(k) \in \{1, -1, 0\}$ represents the output: 1 for "down," −1 for "up," and 0 for "stop" (applied to vertical movement only).
- The vertical movement model: $y(k + 1) = y(k) + c(k)v_0$
- where $y(k)$ represents the vertical position at the k-th update, at a fixed interval of 200 ms and v_0 is a positive speed constant.
- If the output $c(k)$ is 0, the cursor stops vertical movement; if the output is 1 or −1, the cursor moves up or down at a speed of 10 pixels every 200 ms.

Method

- Algorithm (vertical)

1. Feature extraction
   I. 30 channel EEG signals are filtered in the range of 0.1–20 Hz
   II. Extract a segment from 0 to 600 ms after a button flashes
   III. The obtained data vector is denoted as $P_{ai,j,q}$, where $i, j,$ and q represent the i th channel, the j th button associated with this flash, and the q th round,
   IV. Construct a feature vector corresponding to the j th button and the q th round by concatenating the vectors $P_{ai,j,q}$ from all channels, i.e.,

$$F_{ej,q} = [P_{a1,j,q}, \ldots, P_{a30,j,q}].$$

2. Train a support vector machine (SVM) classifier.
   I. Using the feature vectors of the training dataset $\{F_{ej,q}, j = 1, \ldots, 8; q = 1, \ldots, 64\}$ and their corresponding labels, we train an SVM classifier.
   II. If the subject is focusing on the j th button in the q th round,
   then the label of $F_{ej,q}$ is 1 (p300 presence),
   while the labels of $F_{eu,q}$ ($u \neq j$) is −1 (p300 absence).

Method

3. P300 detection with SVM scores

I. For the l th round, we extract feature vectors $Fe_{j,l}$ (j = 1, . . . , 8)

II. Applying the trained SVM to $Fe_{j,l}$, we obtain eight scores denoted as $s_{j,l}$

III. P300 detection requires discriminating between non-P300(idle state) and P300 rounds ➡ self-paced

IV. The detection of P300 is accomplished by a threshold mechanism

- Calculate the sum of SVM scores for each button obtained from l accumulated rounds
- Find maximum and the second maximum of the eight summed scores

$$ss_j = s_{j,1} + \cdots + s_{j,l},\ j = 1, \ldots, 8$$
$$ss_{j_0} = \max\{ss_1, \ldots, ss_8\}$$
$$ss_{j_1} = \max\{\{ss_1, \ldots, ss_8\} \backslash \{ss_{j_0}\}\}$$

- where the j_1 th button is obviously different from the j_0 th button
- define a threshold condition : $1 - \frac{ss_{j_1}}{ss_{j_0}} > \theta_0$
- where the threshold θ_0 is a predefined positive constant, and is empirically set at 0.3
- If the threshold condition is satisfied, then the system makes a decision that P300 potential occurs at the j_0 th button

Method

4. Movement Decision

I. when P300 is detected for the l th round at the j_0 button

II. if the j_0 button is one of the three “up” buttons, set c(k) = −1 (the cursor will go up);

III. if the j_0 button is one of the two “stop” buttons, set c(k) = 0 (the cursor will have no vertical movement).

IV. If P300 is not detected for the l th round, i.e., the threshold condition is not satisfied,

V. then the system does not change the direction of the vertical movement of the cursor, i.e., c(k) = c(k − 1).

Method

- Control of the Horizontal Movement Through Motor Imagery

- The horizontal movement model:

$$x(k+1) = x(k) + \frac{a}{3}(f(k-2) + f(k-1) + f(k)) + b$$

- where *k* represents the *k* th update of the cursor position, *x*(*k*) is the horizontal coordinate of the cursor, *f*(*k*) is the continuous output (score) of the SVM classifier, and *a* and *b* are two constants.
- They introduce delays into the control model to make the cursor move smoothly
- The score *f*(*k*) is generated by an SVM classifier at every 200 ms.
- pre-processing steps
  - spatial filtering with common average reference (CAR)
  - bandpass filtering in specific mu rhythm band (8–13 Hz)
  - spatial filtering based on a common spatial pattern (CSP) matrix W.
- The feature vector is fed into an SVM classifier that is trained using the training data to separate the two classes of feature vectors

Method

- In motor imagery, the cursor shall not move, if the user is in idle state.
- This is accomplished by the introduction of the two parameters: *a* and *b*
  - An EEG dataset is collected when the user is in idle state. This dataset contains N time segments of 200 ms (N = 600), i.e., lasts 2 min.
  - They calculate the SVM scores f(1), . . . , f(N).
  - Set

$$m = \frac{1}{N}\sum_{k=1}^{N} f(k)$$

$$mi = \min\{f(k),\ k = 1, \ldots, N\}$$

$$ma = \max\{f(k),\ k = 1, \ldots, N\}.$$

  - Then we calculate *a* and *b* as $a = \dfrac{h}{\max\{ma - m, m - mi\}}$ $b = -am.$
  - The parameter *h* is used for adjusting the velocity of the cursor. *h* is fixed to 8 for all the subjects.
  - Considering the model : $x(k+1) = x(k) + \frac{a}{3}(f(k-2) + f(k-1) + f(k)) + b$
  - and the parameter setting of *a* and *b*, the average horizontal movement during the idle state $\frac{1}{N}\sum_{k=1}^{N-1}(x(k+1) - x(k))$ Is close to zero.
  - Thus, the cursor almost does not change its horizontal position, if the subject is in the idle state. This has been demonstrated during the online experiments.

Method

- Combining the algorithms for vertical and horizontal movement control, they obtain the algorithm for 2-D cursor control

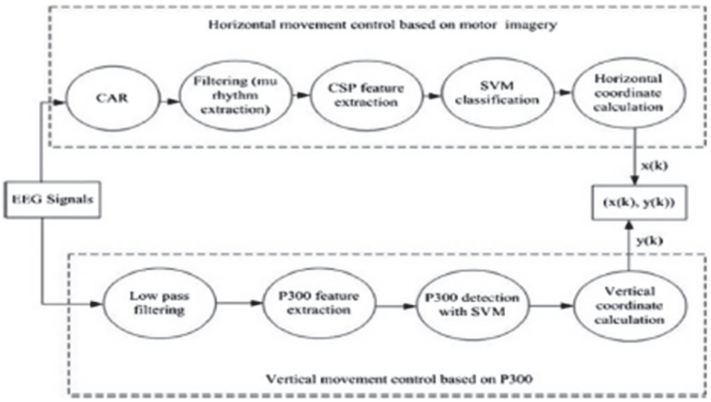

[Diagram of the algorithm for 2-D cursor control]

- The horizontal movement control based on motor imagery and the vertical movement control based on P300 are performed simultaneously

results

	Number of trials	Hit rate (%)	Average time (s)
Subject A	80	97.5	24.8
Subject B	80	91.25	25.0
Subject C	80	86.25	30.7
Subject D	80	84.5	28
Subject E	80	92.5	31.8
Subject F	80	92.5	25.6

- we can find out that the accuracy rates of all the six subjects are satisfactory. However, the control time of each trial was not short (about 28 s in average).
  - The relative small size of the cursor and the target.
  - The ratios of the size of the cursor, target, and the workspace are fixed to be 0.00084:0.003:1.
  - Triggering and effectively detecting P300 are time consuming to some degree (repeated round).

Data Analysis and Discussions

- For efficient 2-D control, the two control signals need to be as independent as possible.
- First, analyze the data collected from online experiment and assess the independence between the two control signals by correlation method.
- There exist horizontal and vertical control variables with values $f(k)$, $c(k)$
- Here, $f(k)$ is an SVM score from motor imagery, while $c(k)$ with value of 1, −1, or 0 is determined by the button
- The button at which P300 occurs is determined by $ss_{j0}(k)$, the maximum of 8 SVM scores corresponding to the eight buttons.
- Since $ss_{j0}(k)$ is generally positive, they let $c(k)ss_{j0}(k)$ to be a new vertical control variable with signs and amplitude.
- For each trial, they also define two position variables representing the relative position of the cursor and the target

$$\bar{x}(k) = x_t - x_c, \quad \bar{y}(k) = y_t - y_c$$

- where t and c means the target and the cursor (at its initial position)

Data Analysis and Discussions

- Calculate the correlation coefficients for each pair of control variable ($f(k)$ or $c(k)ss_{j0}$ (k)) and position variable ($\bar{x}(k)$ or $\bar{y}(k)$)
- and the correlation coefficient for the two control variables.

Subject	$C_{mu,\bar{x}}$	$C_{mu,\bar{y}}$	$C_{P300,\bar{x}}$	$C_{P300,\bar{y}}$	$C_{P300,mu}$
A	0.685	0.016	0.038	0.653	0.042
B	0.521	0.008	0.044	0.566	0.004
C	0.432	0.048	0.013	0.407	0.028
D	0.443	0.019	0.041	0.506	0.021
E	0.501	0.001	0.024	0.321	0.001
F	0.411	0.035	0.008	0.417	0.012

- From the result, each control variable correlates strongly with its own dimension of target cursor position
- and does not correlate with the other variables' dimension
- and also does not correlate with the other variable.
- Hence, such results support the independence of the horizontal and vertical control variables.

Data Analysis and Discussions

- Next, they present their data analysis results to show that the subjects truly used P300 and motor imagery in the 2-D cursor control.

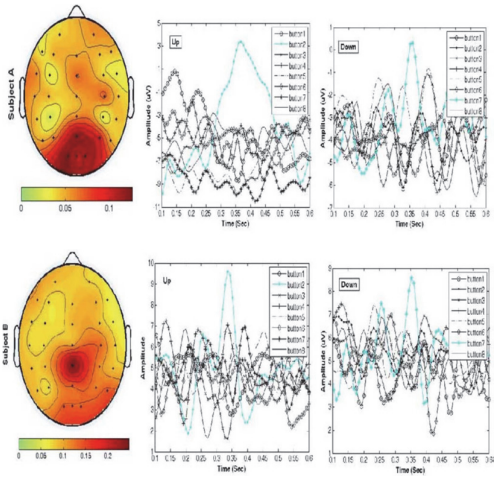

- P300 detection is mainly based on those channels located in the occipital and parietal areas rather than the frontal area (considered EOG).
- we can see P300 potentials elicited by the two chosen buttons and no P300 potentials elicited by other buttons.

Data Analysis and Discussions

- They also plot the topographies of CSP filters and the power spectra of two channels of raw EEG signals calculated based on the training dataset.

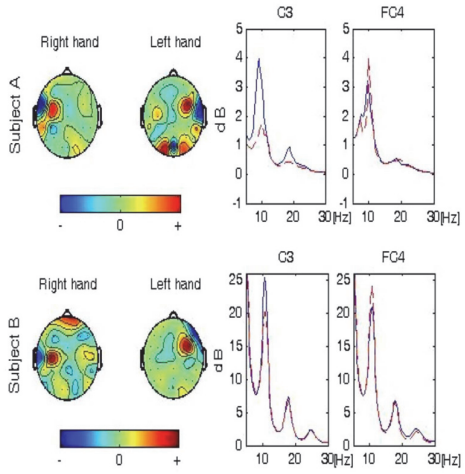

- CSP filters (the first and the last rows of **W**) are displayed which are easily related to the motor imageries of right and left hands
- The discriminability of the brain signals corresponding to the right and left hands is demonstrated.

TWO SUPPLEMENTARY EXPERIMENTS

- In order to show the average trajectory of the cursor based on desired movements, the trajectories of the cursor starting at the center of the GUI and moving to one of the four fixed targets at four corners

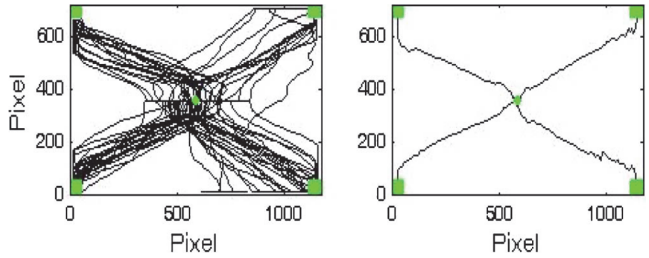

Left: trajectories of the cursor obtained in 80 trials. Right: four average trajectories

- The hit rate and the average control time are 97.5% and 24.7 s
- The trajectories of single trials and the average trajectories for four target positions are quite smooth.

TWO SUPPLEMENTARY EXPERIMENTS

- Second experiment, to show P300 and motor imagery control work simultaneously.

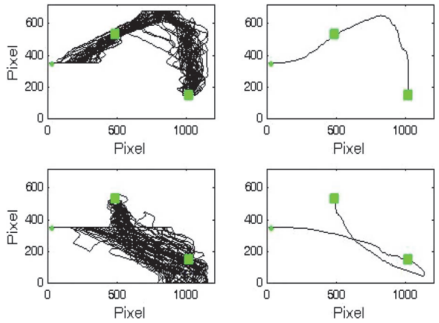

- fix two targets, and fix the initial position of the cursor at the middle left
- In each trial, the subject needs to move the cursor to hit these two targets sequentially without stop. (two classes of trial)
- first class, the subject move the cursor to first hit the target at the middle of upper part and then hit the target at down-right corner
- second class, the subject move the cursor to first hit the target at down right corner and then hit the target at the middle of upper part.

TWO SUPPLEMENTARY EXPERIMENTS

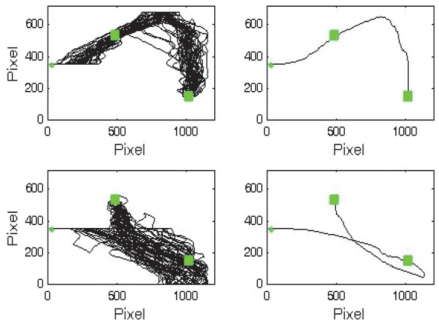

- 80 trials were collected for two classes of trials (40 trials for each class)
- The hit rate and the average control time are 98.75% and 49.1 s
- for each trial, the direction of vertical movement of the cursor is changed while the cursor simultaneously moves to the right.
- Thus, the cursor can be simultaneously controlled (no zigzag) by the two control signals of P300 and motor imagery.

Conclusion

- They have presented a new BCI and its implementation for 2-D cursor-control by combining the P300 potential and motor imagery.
- Two independent signals have been obtained for controlling two degrees of movements of a cursor simultaneously.
- Through an online experiment involving six subjects performed 2-D cursor control tasks.
- The six subjects successfully carried out 2-D cursor control with satisfactory accuracies (>80%).

Thank you

Robust Face Recognition via Sparse Representation

Authors:	J. Wright, Allen, Y. Yang, A. Ganesh, S. Shankar, and Yi Ma
Publication:	IEEE Trans. On Pattern Analysis and Machine Intelligence, Feb.2009
Speaker:	Woongbi Lee

Short summary: In this paper, sparse signal representation is investigated for recognizing human faces from frontal views with varying expression and illumination, as well as occlusion and disguise. Based on a sparse representation computed by l^1-minimization, this face recognition problem is cast as a general classification among multiple linear regression models. Even with severe occlusion and corruption, their algorithms show high performance classification of high dimensional data.

I. INTRODUCTION

In this paper, the discriminative nature of sparse representation for classification is exploited. Instead of using the generic dictionaries, the test sample is represented in an overcomplete dictionary whose base elements are the training samples themselves. If sufficient training samples are available from each class, it will be possible to represent the test samples as a linear combination of just those training samples from the same class. This representation is naturally sparse, involving only a small fraction of the overall training database. In many problems of interest, it is actually the sparsest linear representation of the test sample in terms of this dictionary and can be recovered efficiently via l^1-minimization.

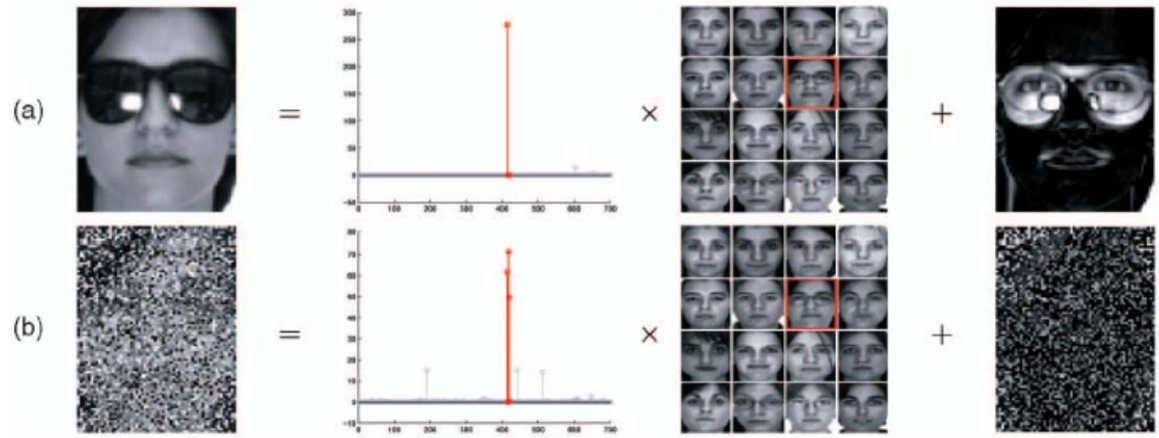

Fig. 1 Simple Example of face recognition: (a) occluded (b) corrupted

There are 700 training images of 100 individuals (7 each). A test image (left) is represented as a sparse linear combination of all the training images plus sparse errors due to occlusion or corruption. Red coefficients correspond to training images of the correct individual.

The theory of sparse representation and compressed sensing yields new insights into two crucial issues in automatic face recognition: the role of feature extraction and the difficulty due to occlusion.

The role of feature extraction: Which low-dimensional features of an object image are the most relevant or informative for classification is a central issue in face recognition. As conventional methods, there exist Eigenfaces (PCA), Fisherfaces (LDA), Laplacianfaces, and a host of variants. The theory of compressed sensing implies that the precise choice of feature space is no longer critical: Even random features contain enough information to recover the sparse representation and hence correctly classify any test image. What is critical is that the dimension of the feature space is sufficiently large and that the sparse representation is correctly computed.

Robustness to occlusion: Occlusion brings about significant troubles in face recognition. This is due to the unpredictable nature of the error occurred by occlusion. Typically, this error corrupts only a small part of the image pixels and therefore is sparse in the standard basis given by individual pixels. The sparse representation of an occluded test image naturally separates the component of the test image arising due to occlusion from the component arising from the identity of the test subject.

II. Classification Based on Sparse Representation

In this section, they introduce classification using sparse representation and show that the sparse representation can be computed by l^1-minimization and can be used for classifying and validating any given test sample.

Object recognition aims to use labeled training samples from *k* distinct object classes to correctly determine the class to which a new test sample belongs. n_i training samples from the *i*-th class form a matrix $A_i \doteq \left[v_{i,1}, v_{i,2}, \cdots, v_{i,n_i} \right] \in \mathbb{R}^{m \times n_i}$ whose columns are the training face images of the *i*-th subject. The image is represented by $w \times h$ gray scale with the vector $v \in \mathbb{R}^m$ ($m = wh$).

A. Test Sample as a Sparse Linear Combination of Training Samples

For the structure of the A_i for recognition, one particularly simple and effective approach models the samples from a single class as lying on a linear subspace. Given sufficient training samples of the *i*-th object class, $A_i = \left[v_{i,1}, v_{i,2}, \cdots, v_{i,n_i} \right] \in \mathbb{R}^{m \times n_i}$, any new test sample $y \in \mathbb{R}^m$ from the same class will approximately lie in the linear span of the training samples associated with object *i*:

$$y = \alpha_{i,1} v_{i,1} + \alpha_{i,2} v_{i,2} + \cdots + \alpha_{i,n_i} v_{i,n_i}$$

for some scalars, $\alpha_{i,j} \in \mathbb{R}$, $j = 1, 2, \ldots, n_i$.

A new matrix **A** is defined for entire training set as the concatenation of the *n* training samples of all *k* object classes:

$$A_i \doteq \left[A_1, A_2, \cdots, A_k \right] = \left[v_{i,1}, v_{i,2}, \cdots, v_{i,n_k} \right]$$

Then, the linear representation of y can be written as

$$y = A x_0 \in \mathbb{R}^m$$

where $x_0 = \left[0, \cdots, 0, \alpha_{i,1}, \alpha_{i,2}, \cdots, \alpha_{i,n_i}, 0, \cdots, 0 \right]^T \in \mathbb{R}^n$ is a coefficient vector whose entries are zero except those associated with the *i*-th class.

Obviously, if $m > n$, the system of equations $y = Ax$ is over-determined, and the correct x_0 can usually be found as its unique solution. In robust face recognition, the system $y = Ax$ is

typically under-determined, and so, its solution is not unique. Conventionally, this difficulty is resolved by choosing the minimum l^2-norm solution.

$$\left(l^2\right): \hat{x}_2 = \arg\min \|x\|_2 \quad \text{subject to} \quad Ax = y$$

While this optimization problem can be easily solved by the pseudo-inverse of A, the solution $\hat{x}_2$ is not especially informative for recognizing the test sample y. To resolve this difficulty, they instead exploit the following optimization problem:

$$\left(l^0\right): \hat{x}_0 = \arg\min \|x\|_0 \quad \text{subject to} \quad Ax = y$$

where $\|\cdot\|_0$ denotes the l^0-norm, which counts the number of nonzero entries in a vector. However, the problem of finding the sparsest solution of an underdetermined system of linear equations is NP-hard and difficult even to approximate.

B. Sparse Solution via l^1-Minimization

If the solution x_0 sought is sparse enough, the solution of the l^0-minimization problem is equal to the solution to the following l^1-minimization problem.

$$\left(l^1\right): \hat{x}_1 = \arg\min \|x\|_1 \quad \text{subject to} \quad Ax = y$$

This problem can be solved in polynomial time by standard linear programming methods.

1) Dealing with Small Dense Noise

Since real data are noisy,

$$y = Ax_0 + z$$

where $z \in \mathbb{R}^m$ is a noise term with bounded energy $\|z\|_2 < \varepsilon$. The sparse solution x_0 can be approximately recovered by solving the following stable l^1-minimization problem:

$$\left(l_s^1\right): \hat{x}_1 = \arg\min \|x\|_1 \quad \text{subject to} \quad \|Ax - y\|_2 \le \varepsilon$$

This convex optimization problem can be efficiently solved via second-order cone programming.

C. Classification Based on Sparse Representation

Given a test sample y from one of the classes in the training set, the sparse representation $\hat{x}_1$ is computed. Noise and modeling error may lead to small nonzero entries associated with

multiple object classes. Based on the global sparse representation, one can design many possible classifiers to resolve this. By using linear structure, we instead classify *y* based on how well the coefficients associated with all training samples of each object reproduce y. For each class *i*, let $\delta_i : \mathbb{R}^n \to \mathbb{R}^n$ be the characteristic function that selects the coefficients associated with the *i*-th class. For $x \in \mathbb{R}^n$, $\delta_i(x) \in \mathbb{R}^n$ is a new vector whose only nonzero entries are the entries in *x* that are associated with class *i*. Using only the coefficients associated with the *i*-th class, one can approximate the given test sample y as $\hat{y}_i = A\delta_i(\hat{x}_1)$. We then classify y based on the these approximations by assigning it to the object class that minimizes the residual between y and $\hat{y}_i$:

$$\min_i r_i(y) \doteq \left\| y - A\delta_i(\hat{x}_1) \right\|_2$$

The recognition procedure is summarized in Algorithm 1. Implementation is done by minimizing the l^1-norm via a primal-dual algorithm for linear programming.

Algorithm 1: Sparse Representation-based Classification (SRC)
1: **Input**: a matrix of training samples $A = [A_1, A_2, \cdots, A_k] \in \mathbb{R}^{m \times n}$ for *k* classes, a test sample $y \in \mathbb{R}^m$, (and an optional error tolerance $\varepsilon > 0$.)
2: Normalize the columns of A to have unit l^2-norm.
3: Solve the l^1-minimization problem: $\hat{x}_1 = \arg\min_x \|x\|_1$ subject to $Ax = y$. (Or alternatively, solve $\hat{x}_1 = \arg\min_x \|x\|_1$ subject to $\|Ax - y\|_2 \le \varepsilon$.)
4: Compute the residuals $r_i(y) \doteq \left\| y - A\delta_i(\hat{x}_1) \right\|_2$ for $i = 1, \cdots, k$.
5: **Output**: identity $(y) = \arg\min_i r_i(y)$.

Example 1. Original image: 192 x 168, downsampled: 12 x 10, size of matrix *A* is 120 x 1207, 38 classes

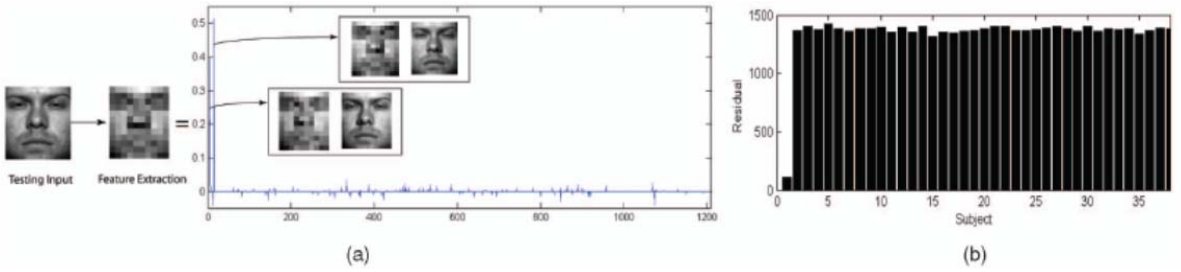

Fig. 2 A valid test image: (a) coefficients (b) residuals

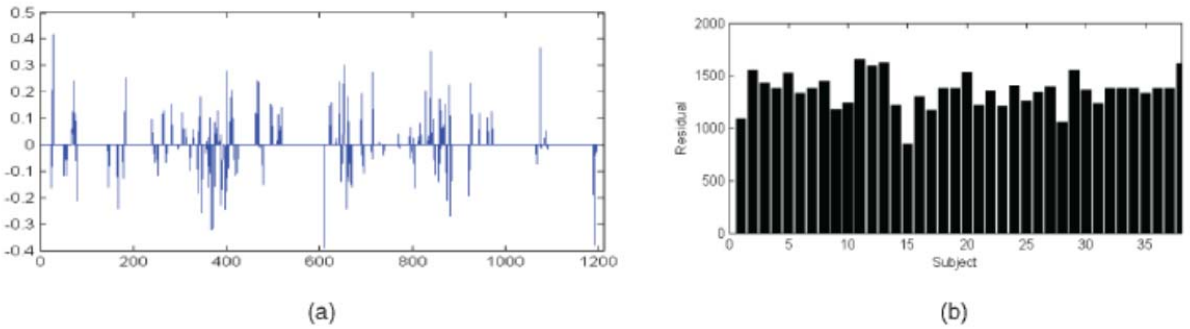

Fig. 3 Non-sparsity of the l^2-minimizer: (a) coefficients (b) residuals

D. Validation Based on Sparse Representation

Before classifying a given test sample, test for validity of the sample is necessary.

Example 2. Randomly selecting an irrelevant image from Google and downsample it to 12 x 10 in the example 1

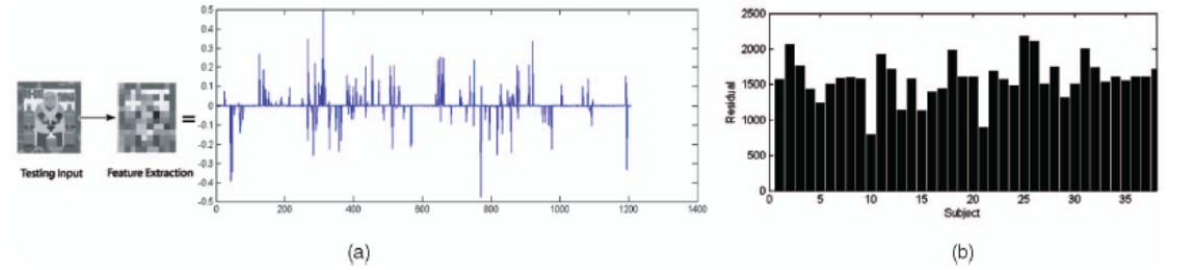

Fig. 4 Example of an invalid test: (a) coefficients (b) residuals

Definition 1 (sparsity concentration index (SCI))

$$SCI(x) \doteq \frac{k \cdot \max_i \left\|\delta_i(x)\right\|_1 / \|x\|_1 - 1}{k-1} \in [0,1]$$

If $SCI(\hat{x}) = 1$, the test image is represented using only images from a single object, and if $SCI(\hat{x}) = 0$, the sparse coefficients are spread evenly over all classes. So, we can choose a threshold $\tau \in (0,1)$ and do the validity test.

If $SCI(\hat{x}) \geq \tau$, then the test image is valid.

III. Two Fundamental Issues in Face Recognition

A. The Role of Feature Extraction

One benefit of feature extraction, which carries over to the proposed sparse representation framework, is reduced data dimension and computational cost. Conventionally, on class of methods extract holistic face features such as Eignefaces, Fisherfaces, and Laplacianfaces. Another class of methods tries to extract meaningful partial facial feature such as patches around eyes or nose.

Since most feature transformations involve only linear operations, the projection from the image space to the feature space can be represented as a matrix $R \in \mathbb{R}^{d \times m}$ with $d \ll m$.

$$\tilde{y} \doteq Ry = RAx_0 \in \mathbb{R}^d$$

The system of equations $\tilde{y} = RAx \in \mathbb{R}^d$ is underdetermined in the unknown $x \in \mathbb{R}^n$. By solving the following l^1-minimization problem,

$$(l_r^1): \hat{x}_1 = \arg\min \|x\|_1 \quad \text{subject to} \quad \left\|RAx - \tilde{y}\right\|_2 \leq \varepsilon$$

for a given error tolerance $\varepsilon > 0$.

For the sparse representation approach to recognition, it is important how the choice of the feature extraction R affects the ability of the l^1-minimization to recover the correct sparse solution x_0. There is remarkable analysis: if the solution x_0 is sparse enough, then with overwhelming probability, it can be correctly recovered via l^1-minimization from any sufficiently

large number d of linear measurements $\tilde{y} = RAx_0$. In other words, if x_0 has $t << n$ nonzeros, then with overwhelming probability, $d\left(\geq 2t\log\left(n/d\right)\right)$ random linear measurements are sufficient for l^1-minimization to recover the correct sparse solution x_0. Random features can be regarded as a less-structured counterpart to classical face features such as Eignefaces or Fisherfaces. The linear projection generated by a Gaussian random matrix is called Randomfaces.

Definition 2. Randomfaces.

- a transform matrix $R \in \mathbb{R}^{d\times m}$ whose entries are independently sampled from a zero mean normal distribution, and each row is normalized to unit length.

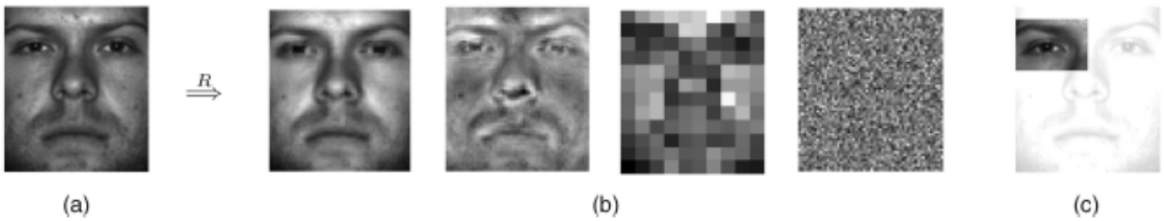

Fig. 5 Examples of feature extraction (a) Original face image (b) 120D representations in terms of four different features: Eigenfaces, Laplacianfaces, downsampled (12 x 10 pixel) image, and random projection (c) The eye is a popular choice of feature for face recognition. In this case, the feature matrix R is simply a binary mask.

B. Robustness to Occlusion or Corruption

In many practical face recognition scenarios, the test image y could be partially corrupted or occluded. The linear model can be modified as

$$y = y_0 + e_0 = Ax_0 + e_0$$

where $e_0 \in \mathbb{R}^m$ is a vector of errors – a fraction, ρ_r of its entries are nonzero. The nonzero entries of e_0 model which pixels in y are corrupted or occluded.

Let us assume that the corrupted pixels are a relatively small portion of the image. Then, the above equation can be written as

$$y = \begin{bmatrix} A & I \end{bmatrix} \begin{bmatrix} x_0 \\ e_0 \end{bmatrix} \doteq Bw_0$$

where $B = \begin{bmatrix} A & I \end{bmatrix} \in \mathbb{R}^{m \times (n+m)}$, so the system $y = Bw$ is always underdetermined and does not have a unique solution for w. From the analysis of sparsity of x_0 and e_0, the correct generating w_0 has at most $n_i + \rho m$ nonzeros. We want to recover w_0 as the sparsest solution to the system $y = Bw_0$.

$$\left(l_e^1\right): \hat{w}_1 = \arg\min \|w\|_1 \text{ subject to } Bw = y$$

Once the sparse solution $\hat{w}_1 = \begin{bmatrix} \hat{x}_1 & \hat{e}_1 \end{bmatrix}$ is computed, setting $y_r \doteq y - \hat{e}_1$ recovers a clean image of the subject with occlusion or corruption compensated for. To identify the subject, we slightly modify the residual $r_i(y)$, computing it against the recovered image y_r

$$r_i(y) = \left\| y_r - A\delta_i\left(\hat{x}_1\right) \right\|_2 = \left\| y - \hat{e}_1 - A\delta_i\left(\hat{x}_1\right) \right\|_2$$

IV. Experimental Verification

A. *Feature Extraction and Classification Methods*

SRC algorithm using several conventional holistic face features, namely, Eigenfaces, Laplacianfaces, and Fisherfaces, and compare their performance with two unconventional features: randomfaces and downsampled images. They compare the SRC algorithm with three classical algorithms, namely, NN, and NS, discussed in the previous section, as well as linear SVM (support vector machine).

Solving $\left(l_r^1\right): \hat{x}_1 = \arg\min \|x\|_1$ subject to $\left\| RAx - \tilde{y} \right\|_2 \le \varepsilon$ with the error tolerance $\varepsilon = 0.05$.

1) Extended Yale B Database

The Extended Yale B database consists of 2,414 frontal-face images of 38 individuals. The copped and normalized 192 x 168 face images were captured under various laboratory-controlled lighting conditions. For each subject, they randomly select half of the images for training (about

32 images per subject) and the other half for testing. They compute the recognition rates with the feature space dimensions 30, 56, 120, and 504, whose numbers corresponding to downsampling ratios of 1/32, 1/24, 1/16, and 1/8, respectively.

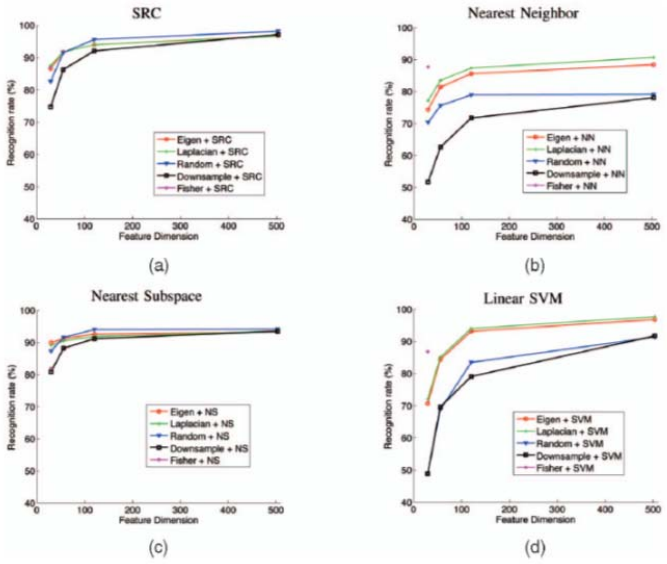

Fig. 6 Recognition rates on Extended Yale B database, for various feature transformation and classifiers. (a) SRC (b) NN (c) NS (d) SVM

2) AR Database

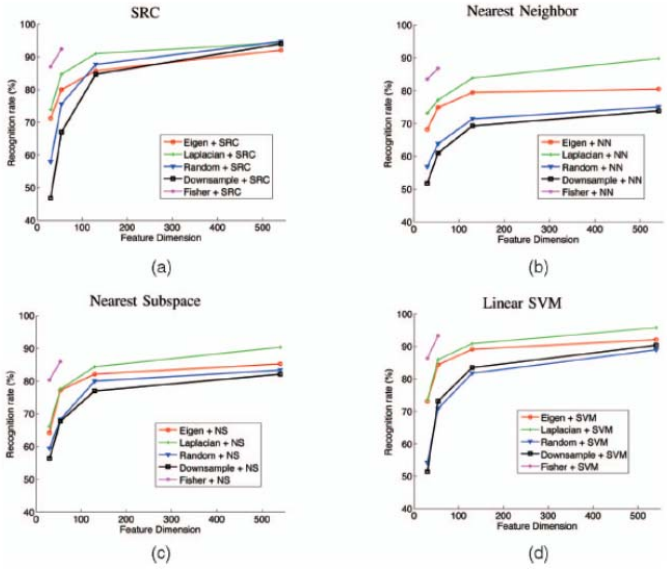

Fig. 7 Recognition rates on AR database, for various feature transformation and classifiers. (a) SRC (b) NN (c) NS (d) SVM

B. Partial Face Features

(a)

(b)

Features	Nose	Right Eye	Mouth & Chin
Dimension (d)	4,270	5,040	12,936
SRC	**87.3%**	**93.7%**	**98.3%**
NN	49.2%	68.8%	72.7%
NS	83.7%	78.6%	94.4%
SVM	70.8%	85.8%	95.3%

Fig. 8 Recognition with partial face features (a) example features, (b) recognition rates of SRC, NN, NS, and SVM on the Extended Yale B database.

C. Recognition Despite Random Pixel Corruption

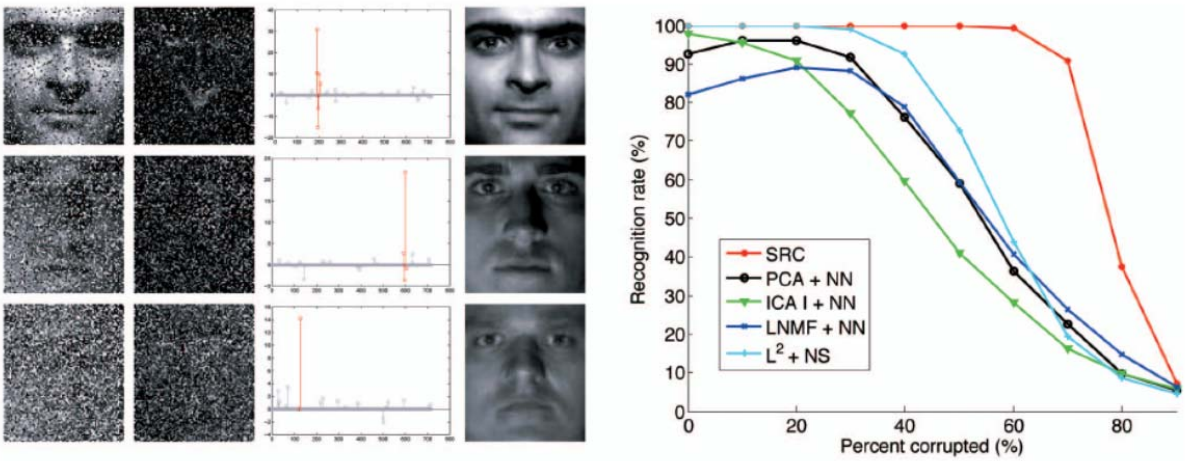

Percent corrupted	0%	10%	20%	30%	40%	50%	60%	70%	80%	90%
Recognition rate	100%	100%	100%	100%	100%	100%	99.3%	90.7%	37.5%	7.1%

D. Recognition Despite Random Block Occlusion

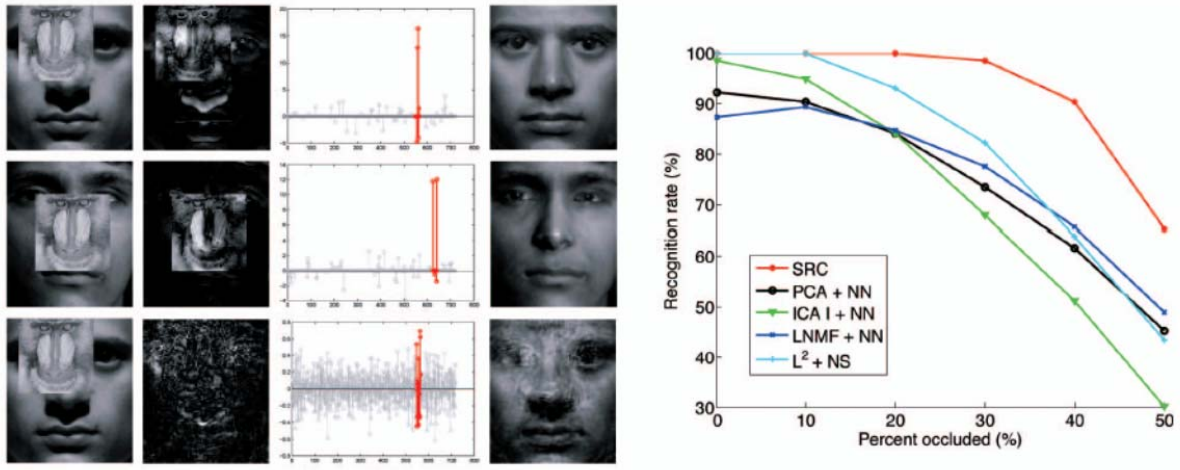

Percent occluded	0%	10%	20%	30%	40%	50%
Recognition rate	100%	100%	99.8%	98.5%	90.3%	65.3%

V. CONCLUSIONS

In this paper, exploiting sparsity can be used for the high-performance classification of high-dimensional data such as face images. The number of features is more important than the choice of features. With occluded and corrupted images, their classification algorithm shows still high-performance.

VI. DISCUSSION

※ Sparse error expression (Occlusion or corruption)

- Can we utilize the sparse error expression of this paper to hologram, microscopy, or spectrometer experiments?

※ BCI experiments

- need to increase classes (multi-class classification)

- applying Gaussian random matrix

Gaming control using a wearable and wireless EEG-based brain-computer interface device with novel dry foam-based sensors.

Lun-De Liao et al.

Journal of Neuroengineering and Rehabilitation. (2012)

Presenter : SeungChan Lee
GIST, Dept. of Information and Communication, INFONET Lab.

Gwangju Institute of Science and Technology

Background

- Wireless BCI systems

Emotiv EPOC neuro-headset

Neurosky Mindset

Introduction & Motivation

- Limitations of wet- and MEMS-type EEG sensors
  - Skin abrasion
  - The required used of conductive gel
  - Time-consuming, uncomfortable, and often painful
  - Degraded signal quality due to skin regeneration and drying of the conductive gel
- Goals
  - They developed a wearable, EEG-based BCI device with a novel dry foam-based sensor for gaming control.
  - A real-time focusing detection algorithm was implemented in their device to detect the real-time cognitive state of the user.

System Design

- Dry EEG sensors

- Dry electrodes are designed by using conductive polymer foam made of a urethane material.
- Conductive foam was covered with a 0.2mm thick taffeta material.
- This was made from an electrically conductive polymer fabric and was coated with Ni/Cu on all of its surfaces.
- A 0.2-mm layer of Cu was used as an adhesion layer that was then connected to the wireless EEG acquisition module.

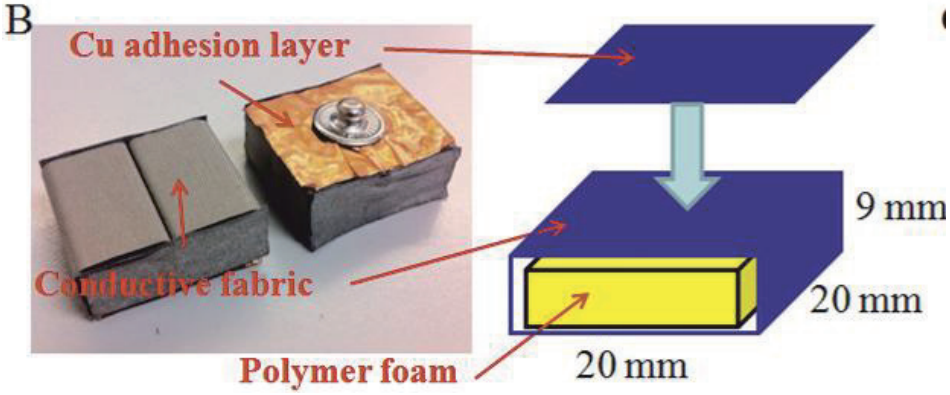

System Design

- Wireless EEG acquisition module

- This module was designed for acquiring EEG signals from the dry EEG sensors.
- Included components : INA2126(Texas Instruments opamp), AD8609(Analog Device opamp), MSP430(Texas Instruments microprocessor), BM0403(Unigrand Ltd., Bluetooth module)

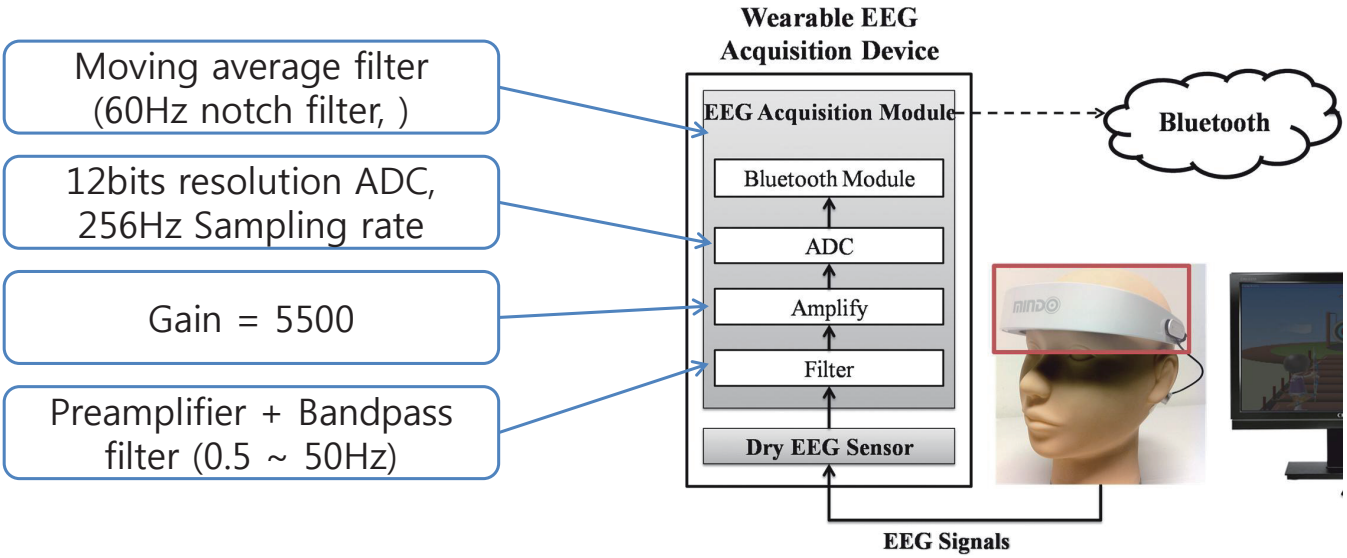

System Design

- Wireless EEG acquisition module

- Size : 4.5 x 3 x 0.6cm3
- Power consumption : 31.58mA with a 3.7V DC power supply
- Battery life : 23 hours using a commercial 750mAh Li-ion battery.

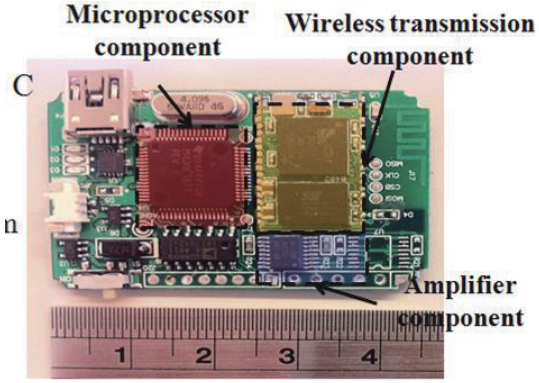

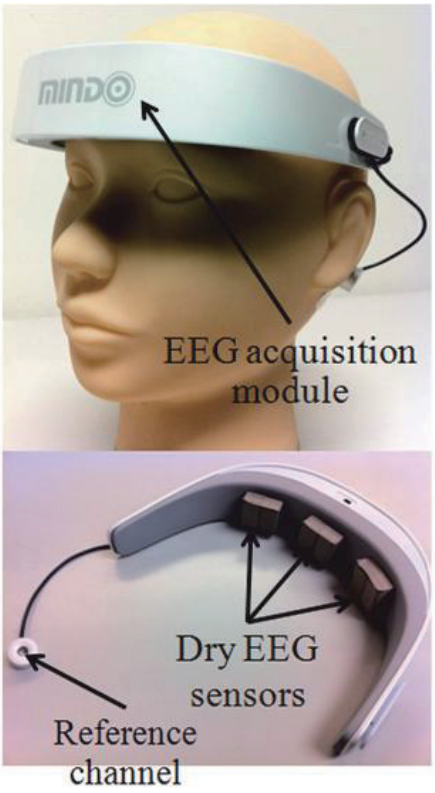

Application Design

- Archery game design

- They designed the archery game controlled by users via mental focusing feature.
- To measure the mental focusing level, they utilized the principle that the power of the alpha rhythm has a negative relationship with the mental focusing level.
- Using the focusing level(FL), they control the aiming of allows.
  - High FL : the shot was close to the center of the target – high score
  - Low FL : the shot was far from the center of the target – low score
- Game design
  - Total ten trials
  - Each trial persisted for ten seconds
  - The FL was initialized to zero for every shot.
  - The FL values were calculated every 2s.

Application Design

- Game interface

A

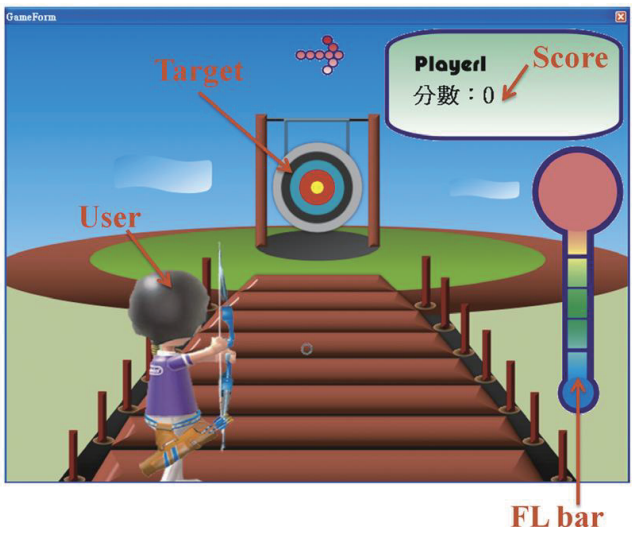

B

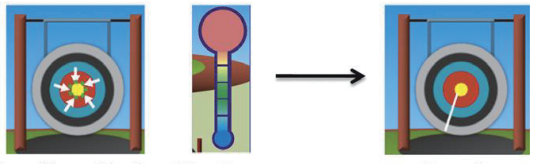

Smaller Circle FL Bar Result

C

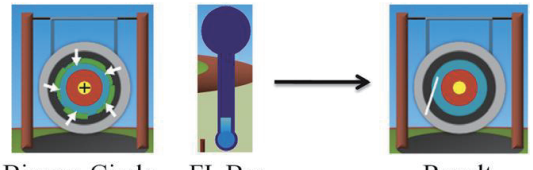

Bigger Circle FL Bar Result

Application Design

- Focusing level detection algorithm

$$X = [X_1 \quad X_2 \quad \cdots \quad X_{512}]$$
$$Y = FFT(X) = [Y_1 \quad Y_2 \quad \cdots \quad Y_{256}]$$
$$P_\alpha = \frac{1}{5}\sum_{n=8}^{12} Y_n \quad \text{(Feature extraction \& Averaging)}$$
$$FF = 1/P_\alpha \quad \text{(Inverse)}$$

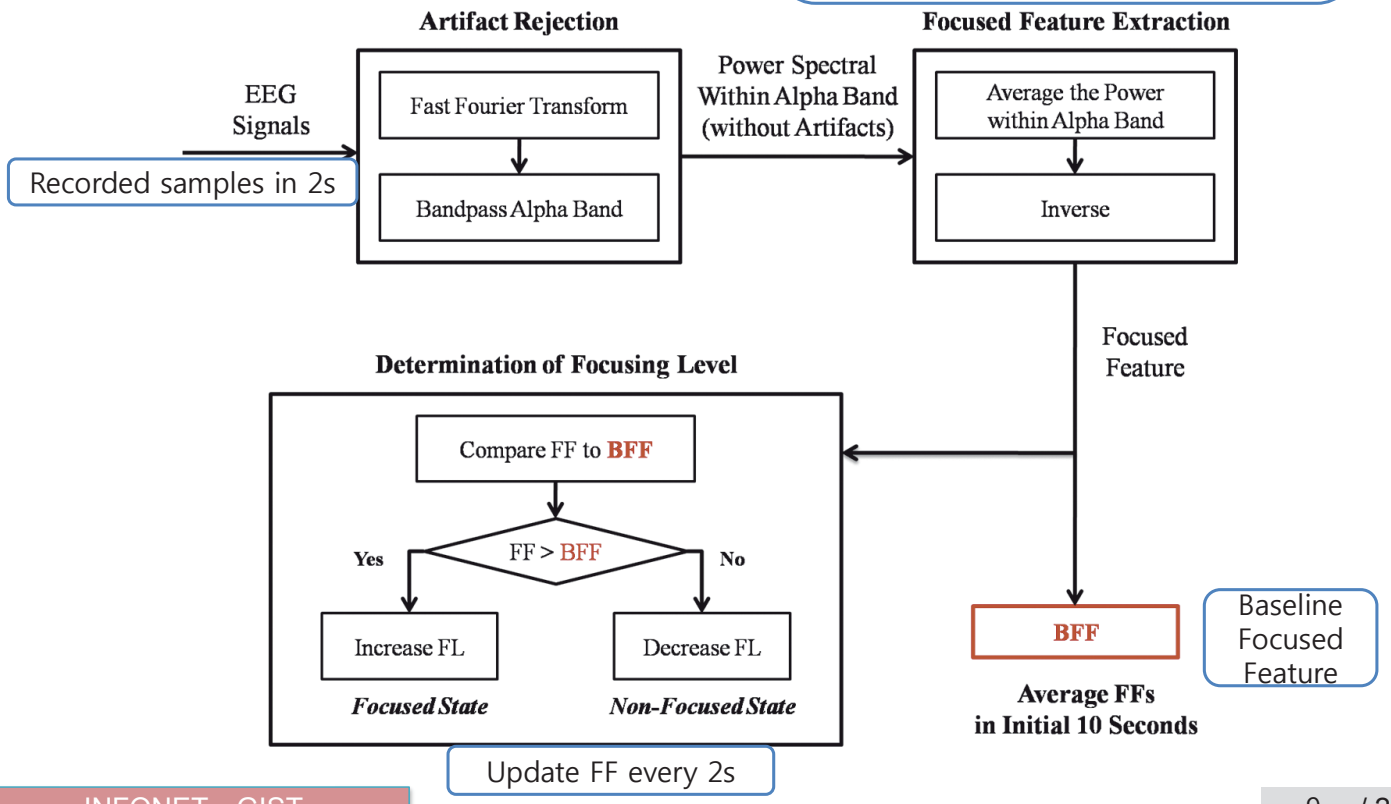

Method

- Total system schematic

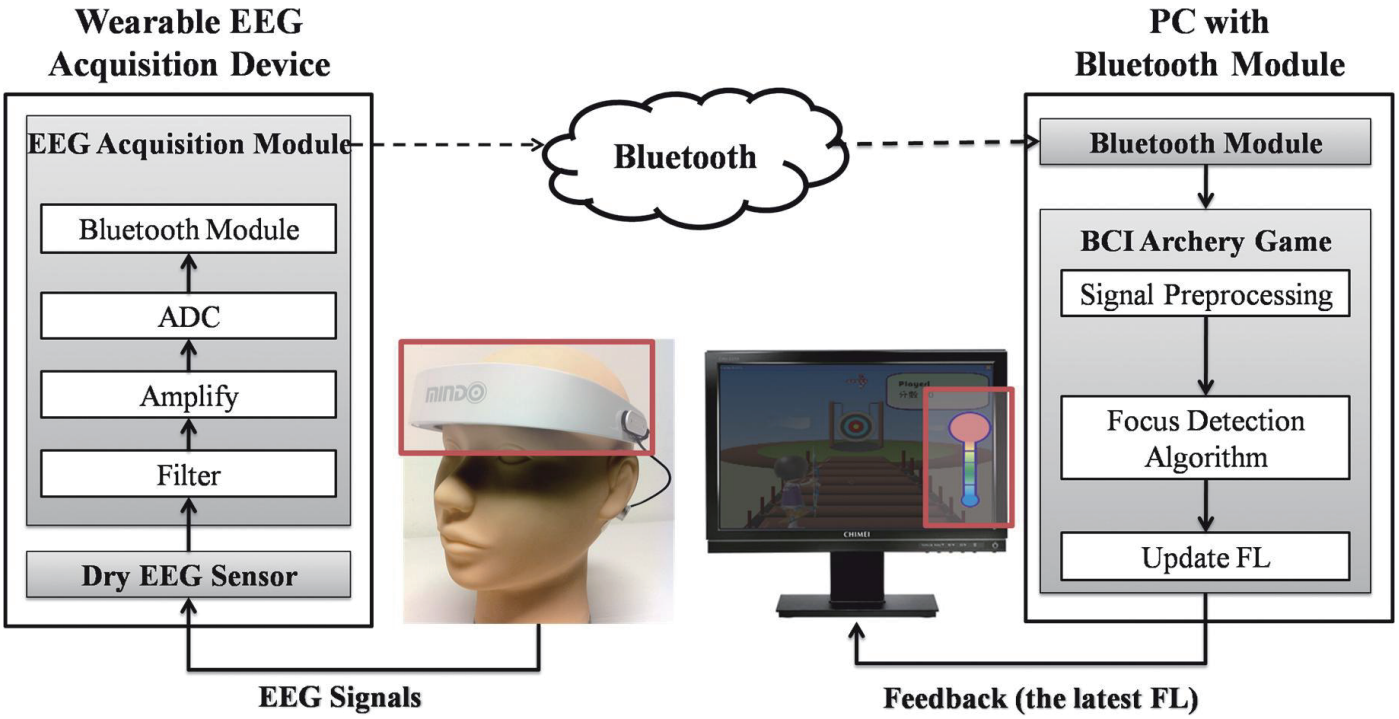

Method

- Verification of the FL algorithm

- Do the FL algorithm indicated the user's focusing level well?
- Short-term memory test
  - The user watches a rapid series of pictures over a few seconds
  - A picture is shown and the user indicate whether of not this picture had been shown before
  - Accuracy high(focused) – test in silence
  - Accuracy low(unfocused) – test under noise
- Experiment procedures
  - Six numbers were presented sequentially, each number lasts for 400ms
  - A number was presented and the user had to indicate whether or not the number had been shown before by using a mouse click
  - Trial was repeated and total 3 min
  - Quite condition vs. noisy condition
  - Average accuracy are used as an indicator to determine the user's focus level.

Method

- Verification of the FL algorithm

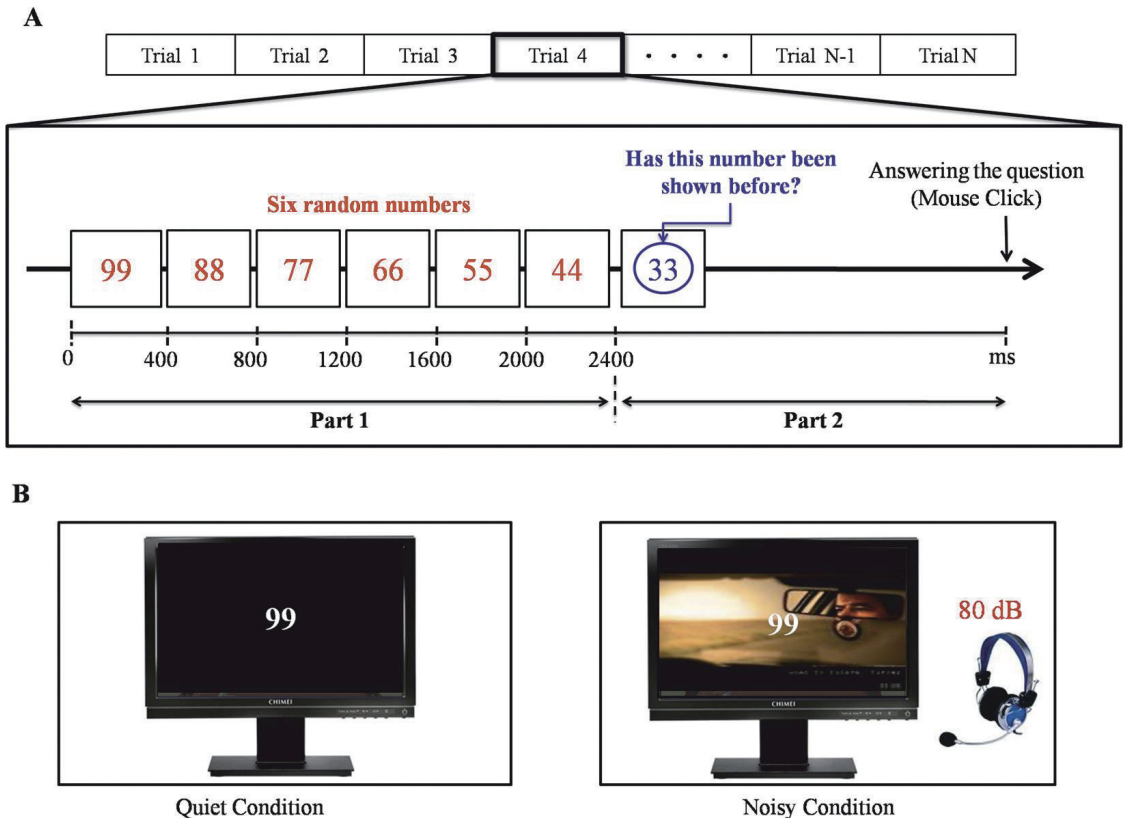

Results

- Verification of the signal quality of the proposed dry sensor

- Experiment procedure
  - The EEG data were prerecorded using standard EEG sensors with conductive gel and were stored in a computer.
  - the EEG data were fed into a programmable function generator and were passed through a voltage divider to generate simulated human EEG signals.
  - Compare the pre-recorded EEG data and the measured EEG data using dry sensor.
- Correlation level : 97.68%

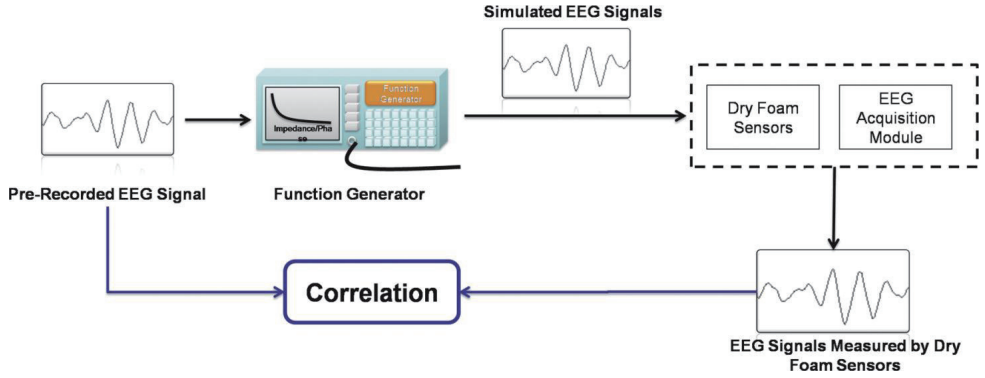

Results

- The correlation between the conventional wet EEG sensor and the dry EEG sensor

- Correlation level : typically in excess of 95.56%
- The performance of the EEG signal measurement using the dry foam-based EEG sensor was identical to that of the conventional wet EEG sensors.

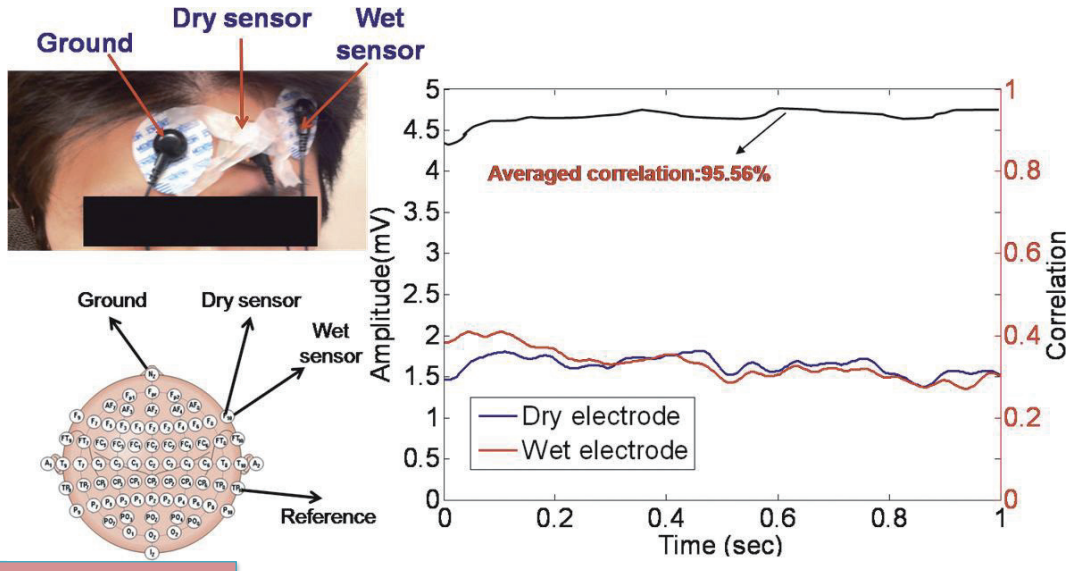

Results

- Comparison of the impedance at the sensor-skin contact interfaces
  - The impedance levels between the dry EEG sensors without skin preparation and conventional wet EEG sensors with skin preparation is similar.
- Comparison of the long-term impedance variation
  - The dry sensor is more stable than wet sensor because the conductive gels are easy to dry during long-term monitoring

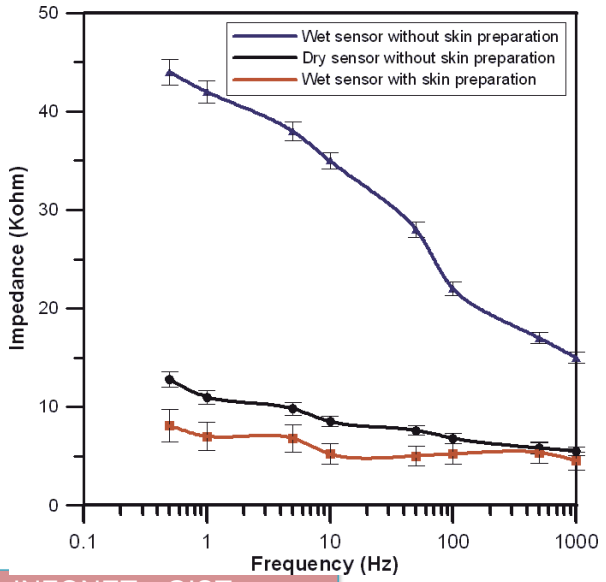

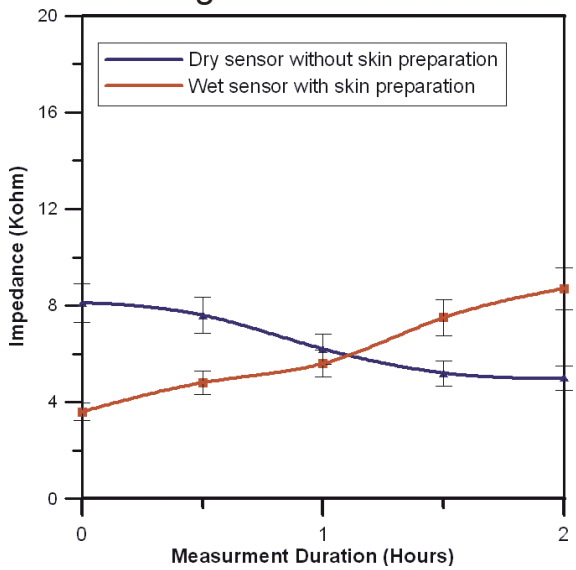

Results

- Relationships between short-term memory testing, FF values and gaming scores under quiet and noisy conditions

- The average accuracy of short-term memory test under two different conditions : 69.0% and 59.8%

Table 1 Results of the short-term memory experiment under quiet and noisy conditions.

	Quiet Condition			Noisy Condition			
	Total	Correct	Accuracy	Total	Correct	Accuracy	*p*-value*
Subject 1	32	24	0.750	22	14	0.636	
Subject 2	44	34	0.773	42	28	0.667	
Subject 3	41	25	0.610	47	27	0.574	
Subject 4	36	24	0.667	38	21	0.553	
Subject 5	58	35	0.603	55	32	0.582	
Subject 6	53	38	0.717	51	25	0.490	
Subject 7	53	36	0.679	54	31	0.574	
Subject 8	54	35	0.648	55	29	0.527	
Subject 9	48	35	0.729	46	31	0.674	
Subject 10	50	36	0.720	47	33	0.702	
			0.690			0.598	0.001

* Paired *t*-test.

Results

- Relationships between short-term memory testing, FF values and gaming scores under quiet and noisy conditions

- The average FF values under two different conditions : 6.94 vs. 4.64
- The users maintained a lower FF under noisy conditions than under quiet conditions because of the presence of distractions.

- Correlation test 1

- The measured FF values were significantly positively correlated to the results of the short-term memory experiment.
  - The measured FF values truly represented the user's mental focusing level.

Table 2 Results of the FF values and gaming scores under quiet and noisy conditions.

	FF			Game Score		
	Quiet	Noisy	*p*-value*	Quiet	Noisy	*p*-value*
Subject 1	8.0	4.9		9.6	7.4	
Subject 2	8.7	4.5		8.4	7.0	
Subject 3	5.4	4.4		9.2	7.6	
Subject 4	6.1	4.2		9.0	8.2	
Subject 5	4.5	3.5		9.0	7.6	
Subject 6	8.9	4.1		9.1	6.9	
Subject 7	7.1	3.9		9.1	6.1	
Subject 8	5.9	4.6		9.1	8.1	
Subject 9	8.0	6.6		8.7	7.9	
Subject 10	6.8	5.6		9.1	7.1	
	6.940	4.642	0.0005	9.013	7.393	0.00004

* Paired *t*-test.

Results

- Correlation test 2

- The game scores are positively correlated to the measured FF values.
  - the game scores are lower if the user performs the test under two different conditions.
- The FF values are an indicator of the focused state and the FL algorithm is a reliable method for measuring the user's focusing level.

Conclusion

- They proposed a wearable EEG-based BCI device with dry EEG sensors for cognitive state monitoring and demonstrated its use during EEG-based gaming control.
- Using their wearable EEG-based BCI device without conductive gel will allow users to monitor their EEG states more comfortably during daily life.
- This wearable EEG-based BCI device and the focusing level detection algorithm can be reliably used to control outside-world applications for general users or researchers.

Thank you

Discussion

- Prof. Lee
  - Check the design of our wireless BCI system?
  - What can we design the application using wireless BCI system?
- Jinteak Seong
  - How to measure the system specifications such as noise level, CMRR, and power consumption?
- Evgenii
  - How to focus in the game application?

Brain-computer interface using a simplified functional near-infrared spectroscopy system

Coyle SM et al.

J. Neural Eng.4 (2007)

Presenter : Evgenii Kim

GIST, Dept. of Information and Communication.

Gwangju Institute of Science and Technology

Outline

- Introduction
- Methods
  - NIRS-the optical signal
  - Functional NIRS measurement and instrumentation
  - Functional NIRS-BCI system design
  - Optode design and placement
  - Software
  - Experimental procedure
  - Data processing and classification
- Results
- Conclusions

Introduction

fMF

Functional near –infrared spectroscopy system

ECoG

Method

Infrared light is composed of a broad range of electromagnetic waves from 770 nm to 1 mm.

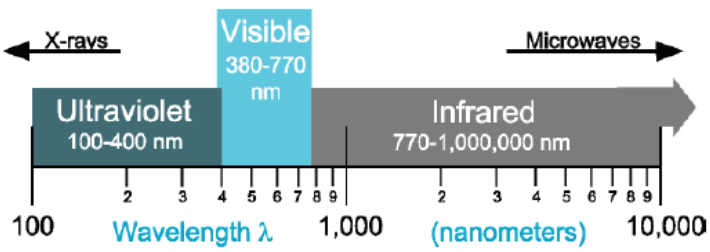

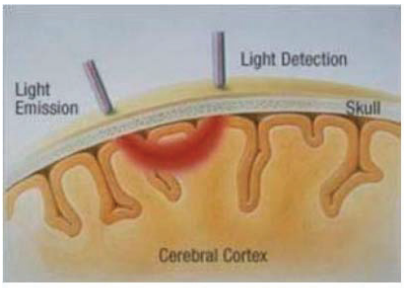

Light propagation through brain

The main principle is based on two physical phenomena. When light enters a tissu e, its propagation in mainly governed by light *absorption* and *scattering*.

Method

- Beer-Lambert law

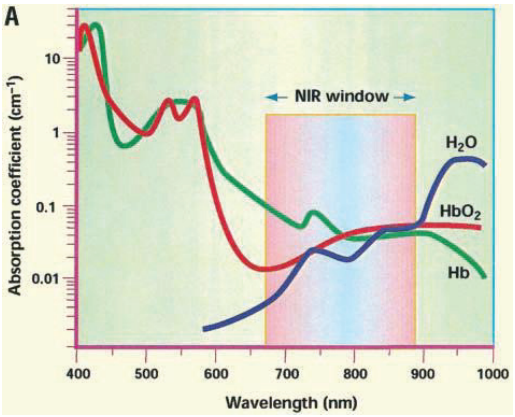

$$A = \log_{10}\frac{I_o}{I} = \mu_a L$$

where I_o is incident light intensity

I is the transmitted light intensity

A is attenuation

L is the optical path length

$\mu_a = \varepsilon.c.$ is the absorption coefficient

$$\mu_a{}^{\lambda 1} = \varepsilon_{Hb}^{\lambda 1} Hb + \varepsilon_{HbO2}^{\lambda 1} HbO2$$

ε is the specific extinction coefficient of the absorber

c is the concentration of absorbing compound in solution

$$\begin{pmatrix} Hb \\ HbO2 \end{pmatrix} = \frac{1}{L}\overline{\begin{pmatrix} \varepsilon_{Hb}^{\lambda 1} & \varepsilon_{HbO2}^{\lambda 1} \\ \varepsilon_{Hb}^{\lambda 2} & \varepsilon_{HbO2}^{\lambda 2} \\ \vdots & \vdots \\ \varepsilon_{Hb}^{\lambda n} & \varepsilon_{HbO2}^{\lambda n} \end{pmatrix}}^{-1} \overline{\begin{pmatrix} A^{\lambda 1} \\ A^{\lambda 2} \\ \vdots \\ A^{\lambda n} \end{pmatrix}}$$

Method

- fNIRS measurement and instrumentation

Functional NIRS measurements are made using one of the three methods:

- Continuous wave (CW)
- Time-resolved (TR)
- Frequency domain (FD)

In CW systems, light is emitted at constant amplitude. Light coming out from the tissue is collected by a detector or detectors.

If more than one wavelenght is used, a relative change of chromophore concentrations can be calculated.

CW systems are comparatively easy to build and acquire data fast.

Method

- fNIRS-BCI system design

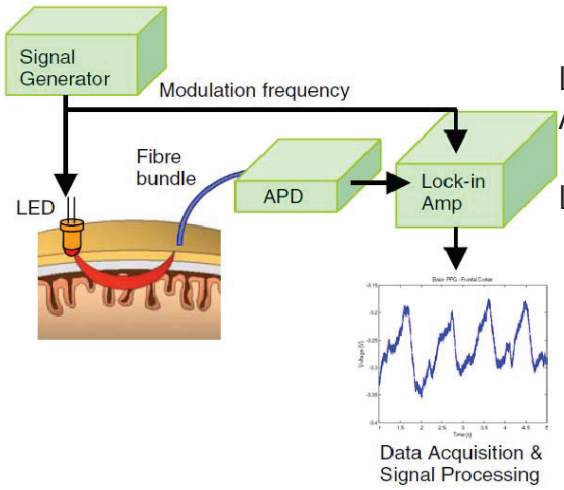

LEDs: 760nm and 880 nm
Avalanche Photodiode (APD): Hamamatsu C5460-01
Lock-in amplifier: Signal recovery m.7265

The data are recorded at a sampling rate of 100 Hz

Figure 1. Components of a continuous wave NIR system.

Lock-in amplifier is a type of amplifier that can extract a signal with a known carrier wave from an extremely noisy environment

Method

The challenge is to ensure rigid optode positioning while still allowing for subject comfort.

Solutions to date include modified cycle helmets, thermoplastic moulded to the contours of each subject's head, spring-loaded fibres attached to semirigid plastic forms and fibres embedded in rubber forms.

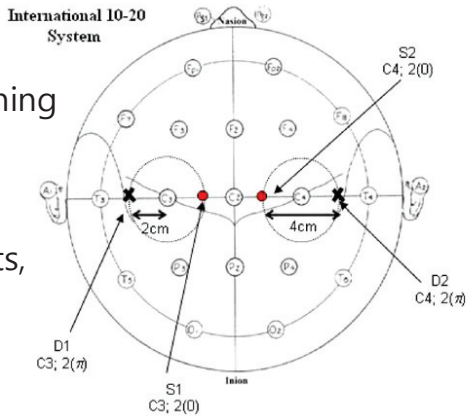

The positions of a source (S1) and detector (D1) placed 4 cm Apart.

Method

Experimental procedure

In this work, they applied fNIRs to MI-based BCI

Three healthy subjects participated in this experiment.

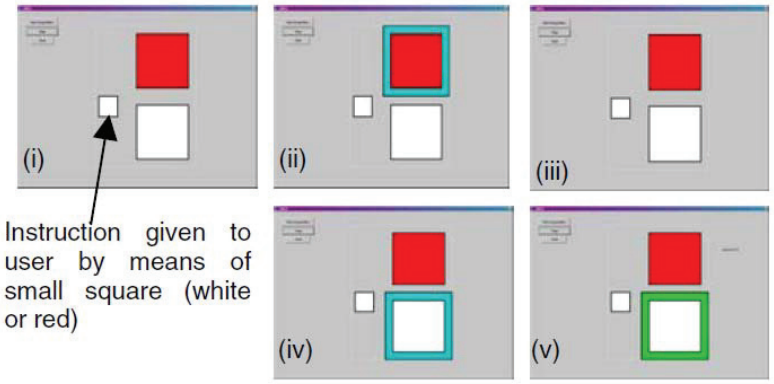

Figure 3. (i)–(v) Sequence of operations in Mindswitch.

Method

Experimental procedure

The total time of a target takes 1 min:

- The first 15 s is a resting period, establishing a baseline condition. In the last 5 s of this period, a command is given to the user by means of a sm all coloured square indicating which target must be selected.
- In the next 15 s the upper target, the red square, is highlighted. If the us er wishes to select the highlighted target, he/she must perform imagery tasks during this time.
- The following 15 s is another rest state allowing the HbO signal to return to baseline if necessary.
- During the next 15 s the lower target is highlighted, and again the user may perform imagery if the highlighted target is desired.
- Rest follows, with the decision being presented to the user and the score updated (number of correct trials/total number of trials).

Results

		Red target red selected ✓	Red target white selected ×	White target white selected ✓	White target red selected ×	Accuracy
Subject 1 Exp. 1	Avg.	0.74	–	0.40	0.33	90%
	St. Dev.	0.36	–	0.22	–	
	No. of trials	4	0	5	1	
Exp. 2	Avg.	0.62	0.39	0.41	–	80%
	St. Dev.	0.50	0.48	0.19	–	
	No. of trials	2	2	6	0	
Exp. 3	Avg.	0.41	–	0.52	0.57	80%
	St. Dev.	0.19	–	0.20	0.27	
	No. of trials	2	0	6	2	
Exp. 4	Avg.	0.24	0.22	0.34	0.22	70%
	St. Dev.	0.02	0.13	0.19	–	
	No. of trials	2	2	5	1	
Exp. 5	Avg.	0.08	0.22	0.34	0.22	70%
	St. Dev.	0.04	0.13	0.19	–	
	No. of trials	2	2	5	1	
Exp. 6	Avg.	0.79	–	0.22	0.01	80%
	St. Dev.	0.49	–	0.07	–	
	No. of trials	4	0	5	1	
Subject 2 Exp. 1	Avg.	0.47	0.41	0.43	–	90%
	St. Dev.	0.40	–	0.29	–	
	No. of trials	3	1	6	0	
Subject 3 Exp. 1	Avg.	0.35	0.25	0.16	0.17	70%
	St. Dev.	–	0.12	0.09	–	
	No. of trials	1	2	6	1	
Exp. 2	Avg.	1.11	–	0.66	0.67	90%
	St. Dev.	0.24	–	0.45	–	
	No. of trials	3	0	6	1	

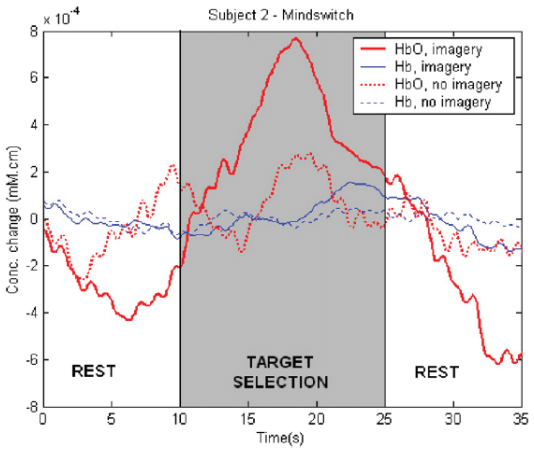

Figure 5. Subject 2—haemodynamic response measured at the right motor cortex during target selection trials. Signal has been low-pass filtered to reduce pulse artefact. Average response is shown for ten trials, i.e. one experimental run. The thicker line is the average of the ten imagery tasks and the thinner line the average of the ten epochs when no imagery was performed.

Conclusion

They have shown how a simplified fNIRS device designed to detect hemodynamic responses arising from mental imagery processes can be used in BCIs.

- The advantages of optical systems: safety
  accessibility
  non-invasiveness.

Discussion

Because, in this work, they didn't consider location of source, the special resolution is not high. But maybe using the source localization technique we can increase a performance of fNIR system.

THANK YOU

INFONET Seminar Application Group

Two-dimensional ultrasound detection with unfocused frequency-randomized signals

Gregory T. Clement

Presenter Pavel Ni

Outline

- Background
- Introduction
- Theory
- Simulation model
- Results
- Conclusion

Background

General US imaging use bandwidth and frequency to determine image resolution

- High frequency –> narrower beam –> better resolution
- High frequency –> higher beam attenuation –> lack of deep imaging

Therefor present US technique turned to increasingly grows of frequency range. Current frequencies for medical imaging is 2-20 MHZ

Introduction

Technique should be turned from focused to unfocused to escape frequency grows

- For each element randomly selected individual frequencies, resulting signal is includes large bandwidth.
- Single point is used to record time history
- Reconstruction of ROI is performed from analysis of acquired signal from single element
- Process is repeated with different frequency patterns to increase performance of reconstruction
- Signal analysis consists of a Fourier-based approach

Theory

- First emitter approximated as an array of simple sources radiating on unique frequency.
- Another approximation that we can describe pressure at any point in a homogeneous space given by

$$p_w(r,t) = -ic_0 k_0 \rho_0 S_w g_w(r_{s_w} | r_0), \quad (1)$$

- Acoustic pressure for wave encounters a varying density may be described

$$\rho \nabla \left(\frac{1}{\rho} \nabla p_w\right) + \frac{w^2}{c^2} p_w = 0$$

- To improve SNR process with new random frequency distribution can be repeated M-times. With M signal strength will increase linearly while noise N will further randomized

$$\tilde{\tilde{p}}_M(r', w) = Mq(r') + \sum_{m=1}^{M} N_m(r', w)$$

Theory

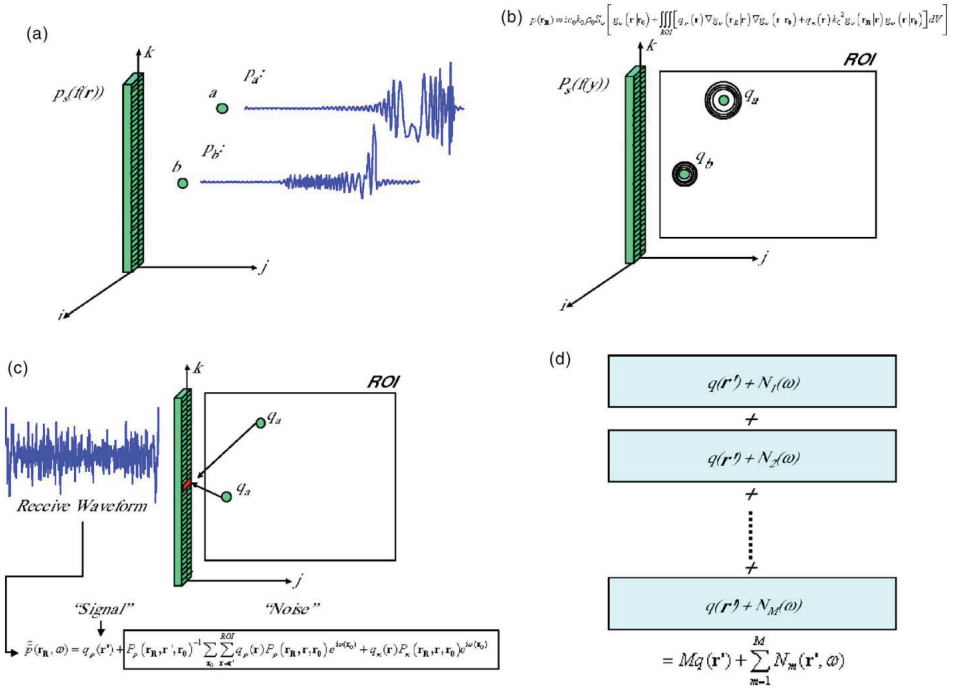

$$p(r_R, w) = q_p(r') + Pp(r_R, r', r_0)^{-1} \sum_{x_0} \sum_{x \to x^{-1}}^{ROI} q_p(r) P_\rho(r_R, r, r_0) e^{iw(x_0)} + q_k(r) P_x(r_R, r, r_0) e^{iw(x_0)}$$

'Signal' 'Noise'

Simulation model

- An operating frequency range between 0.1 – 1.25 MHz
- Simulated array is 40 mm in length and 10 mm in width
- Array segmented in to 202 linear sources with no kerf
- A linear distribution of 202 frequencies between 0.1-1.25 MHz with a frequency resolution of 5.7 kHz
- Each time randomly only one frequency assigned to element
- Also randomly single element selected to record signal
- Scattering field is placed within ROI
- Scattering signal at the receiver is discrete approximation of Eq. (10)

Results

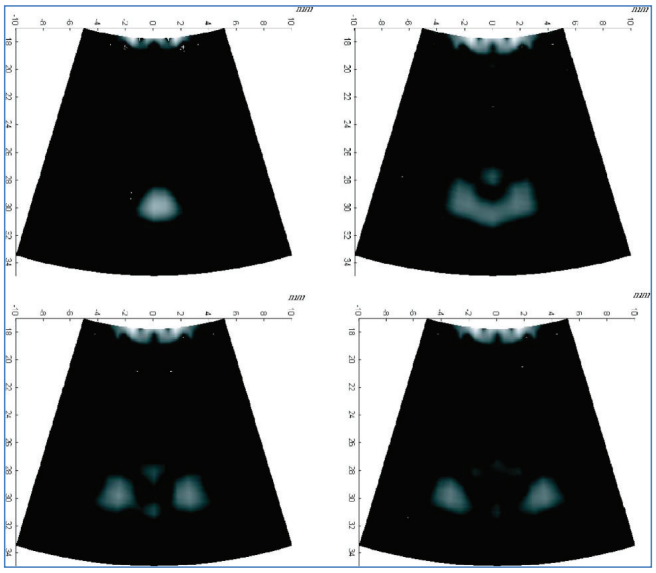

Simulated B-scan images f_c=0.67MHz. Two wires with (diam=0.2mm) separated by a) 2mm, b) 4mm, c) 6mm, d) 8mm.

- Simulated B-scan via k-space projection algorithm using 200 ns resolution. Simulation was repeated for each of 21 scan directions
- ROI 40x40 mm
- Two objects with diameter 0.2mm was given sound speed of 3500 m/s
- Only on 8mm separation objects are clearly separated

Results

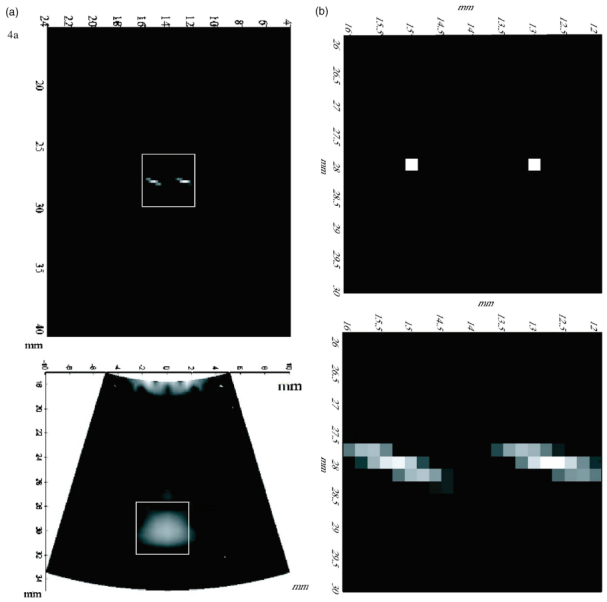

Comparison a) random frequencies (top) B-scan (bottom) b) more magnified view

- Comparing with B-scan method with randomized frequencies has better performance.
- Two objects can be imaged separately with 1.35 mm distance. Vertical 0.5mm
- Simulation was repeated with 15 randomized signals

Results

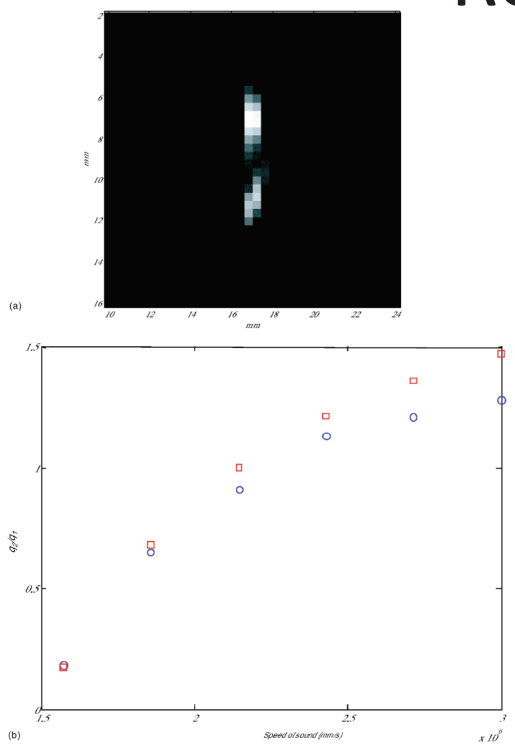

Two reconstructed objects in the ROI with scattering strengths q1= 0.51 and q2=0.62 (top) Scattering ratio of q2/q1 is plotted as fn of frequencies (squares). Reconstructed values (cycles)

- Object placed 4 mm apart and 17 mm distance from transducer
- The plot shows trend of increased distortion with higher sound speed. Corresponding error ranged from 4.3% at 1857 m/s to 13% at 3000 m/s

Results

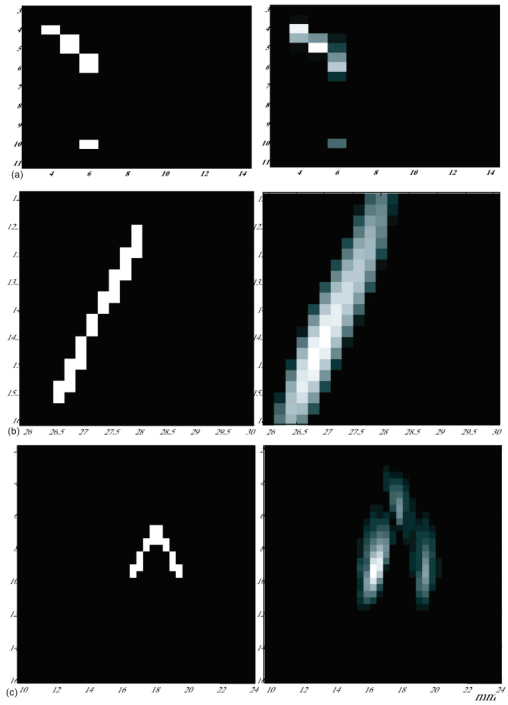

Simulation with multiple scatters (left column) and their reconstructions (right column). Distance from transducer a) 3-14 mm b) 10-24 mm c) 26-30 mm

- Object placed 4 mm apart and 17 mm distance from transducer
- The plot shows trend of increased distortion with higher sound speed. Corresponding error ranged from 4.3% at 1857 m/s to 13% at 3000 m/s
- Three scatterers placed diagonally in 8x8 ROI and additional object 4 mm apart
- Object as an inverted “V” was situated 18 mm from the ultrasound source.

Conclusion

- Large variation in image field makes it possible to localize the position of targets
- In numeric investigation objects where better defined and more spatially localized
- Small objects, which can be hard to detect, and even hard to localize using present methods may be both detected and localized.
- Only single receive channel was used.

Discussion

Thank you

Probabilistic Reconstruction in Compressed Sensing : Algorithms, Phase Diagrams, and Threshold Achieving Matrices

Authors: Florent Krzakala, Marc Mezard, Francois Sausset, Yifan Sun and Lenka Zdeborova

Publication: ArXiv:1206.3953v1 [Cond-mat.stat-mech] 18 Jun 2012

Speaker: Hyeong-ho, Baek

Short summary: In this paper, they present the probabilistic approach to reconstruction and discuss its optimality and robustness. And they detail the derivation of the message passing algorithm for reconstruction. Moreover, they further develop the asymptotic analysis of the corresponding phase diagrams with and without measurement noise, for different distribution of signals.

I. INTRODUCTION

The CS problem can be posed as follows: given an $N-$component signal $\mathbf{s}$, one makes M measurements that are grouped into an $M-$component vector $\mathbf{y}$, obtained from $\mathbf{s}$ by a linear transformation using $M \times N$ matrix $\mathbf{F}$, given by $y_\mu = \sum_{i=1}^{N} F_{\mu i} s_i$ with $\mu = 1, 2, ..., M$ .The aim is to reconstruct the signal $\mathbf{s}$ from the knowledge of $\mathbf{F}$ and $\mathbf{y}$. This amounts to inverting the linear system $\mathbf{y = Fs}$. However, we want to have M as small as possible and when $M < N$ there are fewer equations than unknowns. The system is under-determined and the inverse problem is ill-defined. However, CS deals with sparse signals. In the noiseless case, an exact reconstruction case, an exact reconstruction is possible for such signals as soon as $M > K$.

Candes, Tao, Donoho and collaborators proposed to find the vector satisfying the constraints $\mathbf{y = Fx}$ which has the smallest l_1 norm. This optimization problem is convex and can be solved using efficient linear programming techniques. For any signal with density $\rho = K / N$, the l_1 reconstruction gives indeed the exact result $\mathbf{x = s}$ with probability one only if

$\alpha = M/N > \alpha_{l_1}(\rho)$ is, however, larger than ρ. The l_1 reconstruction is thus sub-optimal: it requires more measurements than theoretically necessary.

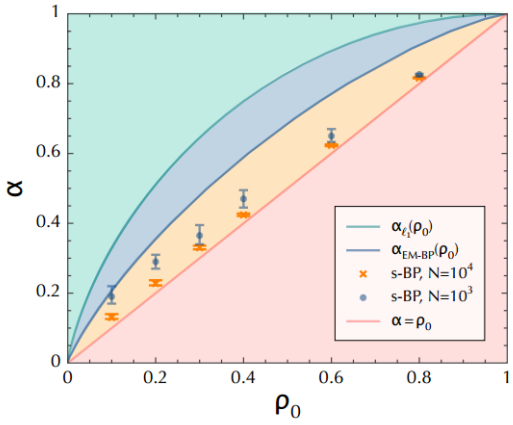

II. PROBABILISTIC RECONSTRUCTION IN COMPRESSED SENSING

The definition of the compressed sensing problem is as follows

$$y_\mu = \sum_{i=1}^{N} F_{ui} s_i + \xi_u \quad \mu = 1,...,M\,, \tag{1}$$

Where s_i are the signal elements, out of which only K are non-zero. F_{ui} are the elements of a known measurement matrix, y_μ are the known result of measurements, and ξ_u is Gaussian white noise on the measurement with variance Δ_μ. The goal of CS is to find an approach that allows reconstruction with as low values of α as possible.

We shall adopt a probabilistic inference approach to reconstruct the signal.

$$\hat{P}(\mathbf{x}) = \frac{1}{Z}\prod_{i=1}^{N}[(1-\rho)\delta(x_i) + \rho\phi(x_i)]\prod_{\mu=1}^{M}\frac{1}{\sqrt{2\pi\Delta_\mu}} e^{-\frac{1}{2\Delta_\mu}(y_\mu - \sum_{i=1}^{N} F_{\mu i} x_i)^2}\,, \tag{2}$$

Where Z, the partition function, is a normalization constant. Here we model the signal as stochastic with iid entries, the fraction of non-zero entries being $\rho > 0$ and their distribution being ϕ.

We stress that in general the signal properties are not known and hence we do not assume that the signal model matches the empirical signal distribution, $\rho = \rho_0, \Delta = \Delta_0, \phi = \phi_0$. One crucial point in our approach is using $\rho < 1$ which includes the fact that on searches a sparse signal in the model of the signal.

A. The Bayesian optimality and the Nishimori condition

The probabilistic approach can also be recovered from a Bayesian point of view. Indeed, given $\mathbf{F}$ and $\mathbf{y}$, from Bayes theorem, we have

$$P(\mathbf{x}\,|\,\mathbf{F},\mathbf{y}) = \frac{P(\mathbf{x}\,|\,\mathbf{F})P(\mathbf{y}\,|\,\mathbf{F},\mathbf{x})}{P(\mathbf{y}\,|\,\mathbf{F})} \tag{3}$$

The value of measurements $\mathbf{y}$ given the knowledge of the matrix $\mathbf{F}$ and the signal $\mathbf{x}$ is, by definition of the problem, given by $P(\mathbf{y}\,|\,\mathbf{F},\mathbf{x}) = \prod_{\mu=1}^{M} \delta(y_\mu - \sum_{i=1}^{N} F_{\mu i} x_i)$ in the noiseless case, and by

$$P(y\,|\,F,x) = \prod_{\mu=1}^{M} \frac{1}{\sqrt{2\pi\Delta_\mu}} e^{-\frac{1}{2\Delta_\mu}(y_\mu - \sum_{i=1}^{N} F_{\mu i} x_i)^2} \tag{4}$$

With random Gaussian measurement noise of variance Δ_μ, for measurement μ. To express the probability $P(\mathbf{x}\,|\,\mathbf{F})$ we consider that the signal dose not depend on the measurement matrix. And we model the signal as an iid:

$$P(x\,|\,F) = \prod_{i=1}^{N} \left[(1-\rho)\delta(x_i) + \rho\phi(x_i) \right] \tag{5}$$

Thus the posterior probability of $\mathbf{x}$ after the measurement of $\mathbf{y}$ is given by

$$P(\mathbf{x}\,|\,\mathbf{F},\mathbf{y}) = \frac{1}{Z(\mathbf{y},\mathbf{F})}\prod_{i=1}^{N}\left[(1-\rho)\delta(x_i)+\rho\phi(x_i)\right]\prod_{\mu=1}^{M}\frac{1}{\sqrt{2\pi\Delta_\mu}}e^{-\frac{1}{2\Delta_\mu}(y_\mu-\sum_{i=1}^{N}F_{\mu i}x_i)^2}, \tag{6}$$

Where $Z(\mathbf{y},\mathbf{F}) = P(\mathbf{y}\,|\,\mathbf{F})$ is again the normalization constant.

An estimator $\mathbf{x}^*$ that minimizes mean-squared error with respect to the original signal $\mathbf{s}$, defined as $E = \sum_{i=1}^{N}(x_i - s_i)^2 / N$, is then obtained from averages of x_i with respect to the probability measure $P(\mathbf{x}\,|\,\mathbf{F},\mathbf{y})$, i.e.,

$$x_i^* = \int dx_i x_i v_i(x_i), \tag{7}$$

Where $v_i(x_i)$ is the marginal probability distribution of the variable i

$$v_i(x_i) \equiv \int_{\{x_j\}_{j\neq i}} P(\mathbf{x}\,|\,\mathbf{F},\mathbf{y}). \tag{8}$$

III. THE BELIEF PROPAGATION RECONSTRUCTION ALGORITHM FOR COMPRESSED SENSING

Exact computation of the averages $x_i^* = \int dx_i x_i v_i(x_i)$ requires exponential time and is thus intractable. To approximate the expectations we will use a variant of the belief propagation(BP) algorithm. Indeed, message passing has been shown very efficient in terms of both precision and speed for the CS problem.

A. Belief Propagation recursion

The canonical BP equation for the probability measure $P(\mathbf{x}\,|\,\mathbf{F},\mathbf{y})$ are expressed in terms of $2MN$ "messages", $m_{\mu\to j}(x_j)$ and $m_{j\to\mu}(x_j)$, which are probability distribution functions.

$$m_{\mu\to i}(x_i)=\frac{1}{Z^{\mu\to i}}\int\prod_{j\neq i}dx_j e^{-\frac{1}{2\Delta_\mu}\left(\sum_{j\neq i}F_{\mu j}x_j+F_{\mu i}x_i-y_\mu\right)^2}\prod_{j\neq i}m_{j\to\mu}(x_j), \tag{9}$$

$$m_{i\to\mu}(x_i)=\frac{1}{Z^{i\to\mu}}\left[(1-\rho\delta(x_i)+\rho\phi(x_i)\right]\prod_{\gamma\neq\mu}m_{\gamma\to i}(x_i), \tag{10}$$

Where $Z^{\mu\to i}$ and $Z^{i\to\mu}$ are normalization factors ensuring that $\int dx_i m_{\mu\to i}(x_i)=1$, $\int dx_i m_{i\to\mu}(x_i)=1.$

Using the Hubbard-Stratonovich transformation

$$e^{-\frac{w^2}{2\Delta}}=\frac{1}{\sqrt{2\pi\Delta}}\int d\lambda e^{-\frac{\lambda^2}{2\Delta}+\frac{i\lambda w}{\Delta}} \tag{11}$$

For $w=\left(\sum_{j\neq i}F_{\mu j}x_j\right)$ we can simplify Eq.(9) as

$$m_{\mu\to i}(x_i)=\frac{1}{Z^{\mu\to i}\sqrt{2\pi\Delta}}e^{-\frac{1}{2\Delta_\mu}(F_{\mu i}x_i-y_\mu)^2}\int d\lambda e^{-\frac{1}{2\Delta_\mu}}\prod_{j\neq i}\left[\int dx_j m_{j\to\mu}(x_j)e^{\frac{F_{\mu j}x_j}{\Delta_\mu}(y_\mu-F_{\mu i}x_i+i\lambda)}\right] \tag{12}$$

The integration over scalar x_j takes the form of the moment generating function. Therefore,

$$m_{\mu\to i}(x_i)=\frac{1}{Z^{\mu\to i}\sqrt{2\pi\Delta}}e^{-\frac{1}{2\Delta_\mu}(F_{\mu i}x_i-y_\mu)^2}\int d\lambda e^{-\frac{\lambda^2}{2\Delta_\mu}}\prod_{j\neq i}E_{X_j}\left[e^{\frac{F_{\mu j}x_j}{\Delta_\mu}(y_\mu-F_{\mu i}x_i+i\lambda)}\right] \tag{13}$$

By assuming that each scalar X_j is Gaussian distributed, the moment generating function is expressed using means and variance. Thus, introducing means and variances as “messages”

$$a_{i\to\mu}\equiv\int dx_i x_i m_{i\to\mu}(x_i), \tag{14}$$

$$v_{i\to\mu}\equiv\int dx_i x_i^2 m_{i\to\mu}(x_i)-a_{i\to\mu}^2 \tag{15}$$

We obtain

$$m_{\mu\to i}(x_i)=\frac{1}{Z^{\mu\to i}\sqrt{2\pi\Delta}}e^{-\frac{1}{2\Delta_\mu}(F_{\mu i}x_i-y_\mu)^2}\int d\lambda e^{-\frac{\lambda^2}{2\Delta_\mu}}\prod_{j\neq i}\left[e^{\frac{F_{\mu j}a_{j\to\mu}}{\Delta_\mu}(y_\mu-F_{\mu i}x_i+i\lambda)+\frac{F_{\mu j}^2 v_{j\to\mu}}{2\Delta_\mu^2}(y_\mu-F_{\mu i}x_i+i\lambda)}\right] \tag{16}$$

Performing the Gaussian integral over λ, we obtain

$$m_{\mu\to i}(x_i)=\frac{1}{\widetilde{Z}^{\mu\to i}}e^{-\frac{x_i^2}{2}A_{\mu\to i}+B_{\mu\to i}x_i},\quad \widetilde{Z}^{\mu\to i}=\sqrt{\frac{2\pi}{A_{\mu\to i}}}e^{\frac{B_{\mu\to i}^2}{2A_{\mu\to i}}} \tag{17}$$

Where

$$A_{\mu\to i}=\frac{F_{\mu i}^2}{\Delta_\mu+\sum_{j\neq i}F_{\mu j}^2 v_{j\to\mu}} \tag{18}$$

$$B_{\mu\to i}=\frac{F_{\mu i}(y_\mu-\sum_{j\neq i}F_{\mu j}a_{j\to\mu})}{\Delta_\mu+\sum_{j\neq i}F_{\mu j}^2 v_{j\to\mu}} \tag{19}$$

To close the equation on messages $a_{i\to\mu}$ and $v_{i\to\mu}$ we notice that

$$m_{i\to\mu}(x_i)=\frac{1}{\widetilde{Z}^{i\to\mu}}[(1-\rho)\delta(x_i)+\rho\phi(x_i)]e^{-\frac{x_i^2}{2}\sum_{\gamma\neq\mu}A_{\gamma\to i}+x_i\sum_{\gamma\neq\mu}B_{\gamma\to i}} \tag{20}$$

Message $a_{i\to\mu}$ and $v_{i\to\mu}$ are respectively the mean and variance of the probability distribution $m_{i\to\mu}(x_i)$. It also useful to define the local beliefs a_i and v_i as

$$a_i\equiv\int dx_i x_i m_i(x_i) \tag{21}$$

$$v_i\equiv\int dx_i x_i^2 m_i(x_i)-a_i^2, \tag{22}$$

Where

$$m_i(x_i) = \frac{1}{\widetilde{Z}^i}[(1-\rho)\delta(x_i) + \rho\phi(x_i)]e^{-\frac{x_i^2}{2}\sum_\gamma A_{\gamma\to i} + x_i\sum_\gamma B_{\gamma\to i}} \tag{23}$$

Let us define the probability distribution

$$\mathrm{M}_\phi\left(\sum{}^2, R, x\right) = \frac{1}{\widehat{Z}(\sum{}^2, R)}[(1-\rho)\delta(x) + \rho\phi(x)]\frac{1}{\sqrt{2\pi\sum}}e^{-\frac{(x-R)^2}{2\sum{}^2}}, \tag{24}$$

$$\sum{}^2 := \frac{1}{\sum_{\gamma\neq\mu} A_{\gamma\to i}}, \quad R := \frac{\sum_{\gamma\neq\mu} B_{\gamma\to i}}{\sum_{\gamma\neq\mu} A_{\gamma\to i}}$$

Where $\widehat{Z}(\sum{}^2, R, x)$ is normalization. We define the average and variance of M_ϕ as

$$f_a(\sum{}^2, R) \equiv \int dx x \mathrm{M}(\sum{}^2, R, x) \tag{25}$$

$$f_c(\sum{}^2, R) \equiv \int dx x^2 \mathrm{M}(\sum{}^2, R, x) - f_a^2(\sum{}^2, R) \tag{26}$$

The closed form of the BP update is

$$a_{i\to\mu} = f_a\left(\frac{1}{\sum_{\gamma\neq\mu} A_{\gamma\to i}}, \frac{\sum_{\gamma\neq\mu} B_{\gamma\to i}}{\sum_{\gamma\neq\mu} A_{\gamma\to i}}\right), \quad a_i = f_a\left(\frac{1}{\sum_{\gamma} A_{\gamma\to i}}, \frac{\sum_{\gamma} B_{\gamma\to i}}{\sum_{\gamma} A_{\gamma\to i}}\right), \tag{27}$$

$$v_{i\to\mu} = f_c\left(\frac{1}{\sum_{\gamma\neq\mu} A_{\gamma\to i}}, \frac{\sum_{\gamma\neq\mu} B_{\gamma\to i}}{\sum_{\gamma\neq\mu} A_{\gamma\to i}}\right), \quad v_i = f_c\left(\frac{1}{\sum_{\gamma} A_{\gamma\to i}}, \frac{\sum_{\gamma} B_{\gamma\to i}}{\sum_{\gamma} A_{\gamma\to i}}\right) \tag{28}$$

For a general signal model $\phi(x_i)$ the functions f_a and f_c can be computed using a numerical integration over x_i. Eqs. (14-15) together with (18-19) and (20) lead to closed iterative message passing equation, which can be solved by iterations. There equation can be used for any signal $\mathbf{s}$, and any matrix $\mathbf{F}$. When a fixed point of the BP equations is reached, the

elements of the original signal are estimated as $x_i^* = a_i$, and the corresponding variance v_i can be used to quantify the correctness of the estimate. Perfect reconstruction is found when the message converge to a fixed point such that $a_i = s_i$ and $v_i = 0$.

IV. DISCUSSION

After meeting, please write discussion in the meeting and update your presentation file.

Reference

[1] Krzakala F., Mezard M., Sausset F., Sun Y. & Zdeborova L. Statistical physics-based reconstruction in compressed sensing. Phys. Rev. X 021005 (2012).

[2] Candes E. J. & Wakin M. B. An Introduction To Compressive Sampling. IEEE Signal Processing Magazine 25, 21-30 (2008).

[3] Donoho D., Maleki A. & Montanari A. Message passing algorithms for compressed sensing: I. motivation and construction. In Information Theory Workshop (ITW), 2010 IEEE, 1 {5 (2010).

[4] Donoho D. L., Javanmard A. & Montanari A. Information-Theoretically Optimal Compressed Sensing via Spatial Coupling and Approximate Message Passing (2011). ArXiv:1112.0708v1 [cs.IT]

[5] Montanari A. & Bayati M. Message-passing algorithms for compressed sensingThe dynamics of message passing on dense graphs, with applications to compressed sensing (2010). ArXiv:1001.3448.

[6] Rangan S. Estimation with random linear mixing, belief propagation and compressed sensing. In Information Sciences and Systems (CISS), 2010 44th Annual Conference on, 1-6 (2010).

[7] Montanari A. & Bayati M. Message-passing algorithms for compressed sensingThe dynamics of message passing on dense graphs, with applications to compressed sensing (2010). ArXiv:1001.3448

[8] Bayati M., Lelarge M. & Montanari A. Universality in message passing algorithms (2012). In preparation.

[9] Wu Y. & Verdu S. Renyi information dimension: fundamental limits of almost lossless analog compression. IEEE Transactions on Information Theory 56, 37213747 (2010).

[10] Wu Y. & Verdu S. Optimal Phase Transitions in Compressed Sensing (2011). ArXiv:1111.6822v1 [cs.IT].

[11] Wu Y. & Verdu S. MMSE Dimension. IEEE Transactions on Information Theory 57, 4857 - 4879 (2011).

[12] Baron D., Sarvotham S. & Baraniuk R. Bayesian Compressive Sensing Via Belief Propagation. IEEE Transactions on Signal Processing 58, 269 - 280 (2010).

[13] Rangan S., Fletcher A. & Goyal V. Asymptotic Analysis of MAP Estimation via the Replica Method and Applications to Compressed Sensing. arXiv:0906.3234v2 (2009).

[14] Donoho D. L., Johnstone I. & Montanari A. Accurate Prediction of Phase Transitions in Compressed Sensing via a Connection to Minimax Denoising (2011). ArXiv:1111.1041v1 [cs.IT].

DASHER - An Efficient Writing System for Brain Computer Interfaces?

Sebastian A. Wills and David J. C. MacKay

IEEE Trans. Neural systems and Rehabilitation Engineering. (2006.06)

Presenter : Soogil Woo
GIST, Dept. of Information and Communication, INFONET Lab.

Gwangju Institute of Science and Technology

Background

- The P300 (P3) wave is an event related potential (ERP) component elicited in the process of decision making.
- In neurology, Steady State Visually Evoked Potentials (SSVEP) are signals that are natural responses to visual stimulation at specific frequencies. When the retina is excited by a visual stimulus ranging from 3.5 Hz to 75 Hz, the brain generates electrical activity at the same (or multiples of) frequency of the visual stimulus.
- Dasher is a computer accessibility tool which enables users to write without using a keyboard, by entering text on a screen using a pointing device such as a mouse, a touchpad, a touch screen, a roller ball, a joystick, a Push-button, or even mice operated by the foot or head.

Introduction

- DASHER is a human computer interface for entering text using continuous or discrete gestures.
- DASHER efficiently converts bits received from the user into text, and has been shown to be a competitive alternative to existing text-entry methods in situations where an ordinary keyboard cannot be used. (PDAs, mobile phones, for handicapped person)
- DASHER is free, open-source software.
- In DASHER, the size of each box within its parent box is determined by the corresponding letter's probability according to a language model.
- As result, sequences of characters that are well predicted by the language model take less time to zoom into.
- Improbable sequences of characters are always possible to write, but take longer.

Introduction & Overall Users' View

- They first describe how Dasher is used to enter the word 'the'.
- Figure (a) show the initial configuration, with an alphabet of 27 characters displayed in a column.
- There are 26 lower case letters and the symbol '_'(under bar) represents a space.
- The user writes the first letter by making a gesture towards the letter's rectangle.
- The trails show the user moving the mouse towards the letter 't'.

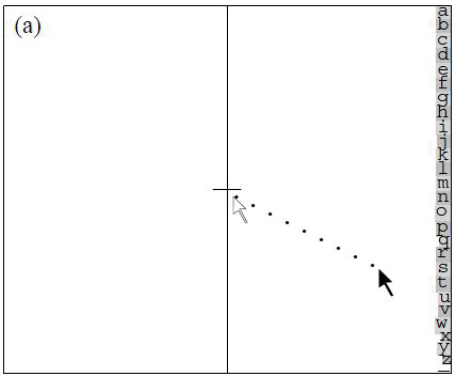

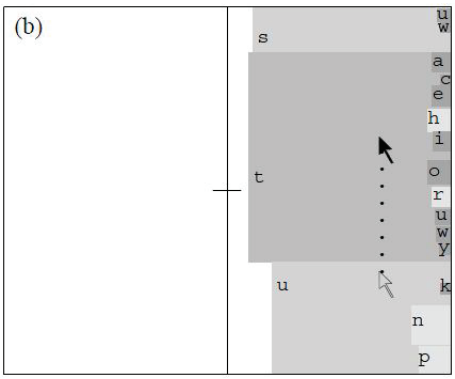

Introduction & Overall Users' View

- The point of view zooms towards this letter (figure (b)).
- As the rectangles get larger possible extensions of the written string appear within the rectangle that they are moving towards.
- If they are moving into the 't', rectangles corresponding to 'ta', 'tb',…, 'th',…,'tz' appear in a vertical line like the first line.
- The heights of the rectangles correspond to the probabilities of these strings, given the languages.

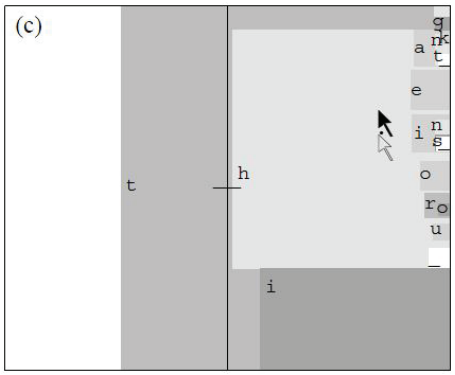

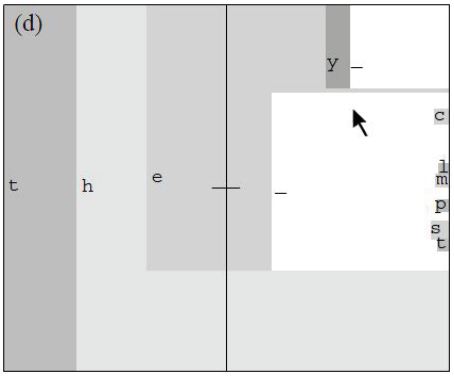

Introduction & Overall Users' View

- In English, 'ta' is quite probable; 'tb', is less so; 'th' is very probable.
- It is easy to gesture our point of view into 'th' (figure (c)), and from there into 'the' (figure (d)).

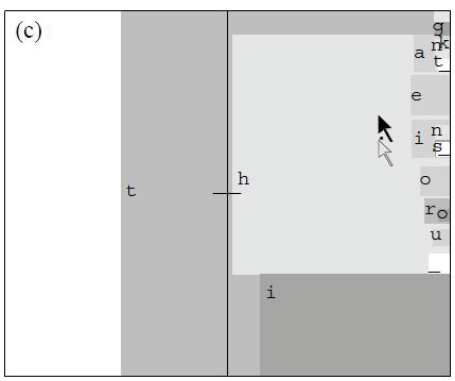

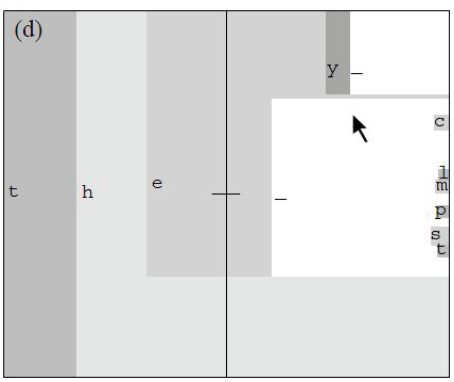

Introduction & Probabilistic Model Determines

- In a given context, they display the alphabet of possible continuations as a column of characters as shown in figure 2.
- The division of the right-hand vertical is analogous to arithmetic coding.
- Let their alphabet be $A_X = \{a_1, a_2, ..., a_I\}$.
- They divide the real line[0,1) into I intervals of lengths equal to the probabilities $P(x_i = a_i)$.
- They subdivide the interval a_i into intervals denoted $a_i a_1, a_i a_2, a_i a_3, ..., a_i a_I$ such that the length of the interval $a_i a_j$ is

$$P(x_1 = a_1, x_2 = a_2) = P(x_1 = a_i) P(x_2 = a_j \mid x_1 = a_i)$$

- They use a language model. (PPM and PPM5D+)

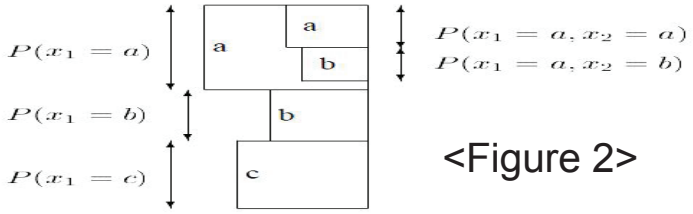

<Figure 2>

Input Devices currently used with DASHER

A. 2-D Continuous Input

- DASHER was first developed to be driven by continuous two-dimensional (2-D) gestures by directly controlling the position of a pointer on the screen.
- If the user moves the pointer away from the origin, the interface zooms in towards the location pointed to by the vector from the origin to the pointer.
- 2-D input devices used with DASHER include mouse, touch-screen, gaze tracker, and head mouse.
- Under mouse control, novice users can reach writing speeds of 25 words/min after 1 h of practice; expert users can write at 35 words/min.
- Under eye control alone users familiar with DASHER can write at 25 words/min, faster than any other gaze-writing system they are aware of.

Input Devices currently used with DASHER

A. 2-D Continuous Input (Example)

Input Devices currently used with DASHER

B. 1-D Continuous Input

- For input devices offering a single continuous dimension of control, DASHER maps the one-dimensional (1-D) input onto a continuous curve within the normal 2-D control space.
- Midrange values of the input control the direction in which to zoom.
- Values towards the extremes of the available range allow the user to zoom out and pause the interface.

C. Discrete Inputs

- Users who can activate buttons (virtual or physical) but cannot reliably provide a continuous output can use one of DASHER's "button modes". (The direct 2-button mode maps 1 button to the action of zooming in one the top half of the visible DASHER land-scape, and the second button to zooming in on the bottom half.)

Input Devices currently used with DASHER

C. Discrete Inputs

- In button mode, DASHER converts bits from the user into written text at exactly the compression rate achieved by the language model.
- DASHER's current language model PPMD5 compresses English text to around 2 bits per character.
- DASHER outputs one character for every two bits provided by the user's button presses.

DASHER as a BCI user interface

A. Motivation

- Current brain computer interface (BCI) systems extract data from the user at a lower information transfer rate than typical physical user interfaces.
- DASHER offers an efficient method for converting the output of a BCI into text.
- DASHER can also use information about the reliability if the signals generated by the user.
- DASHER's language model can be initialized using text that is biased towards a limited set of phrases and words that the user is likely to wish to communicate.
- The user will be able to write these phrases, or variants of them, extremely quickly, while retaining the ability to write any other phrase should they wish to.

DASHER as a BCI user interface

B. Continuous Control

- Many BCI systems output a continuous 1- or 2-D signal which could be used to drive DASHER directly.
- DASHER is well-suited to a BCI signal which is likely to be under imperfect control of the user.
- In DASHER, users write by navigating to what they want to say, not by selecting letters or words.
- If the user accidentally steers in the wrong direction, they can correct their mistake by subsequent compensatory action.
- As with all navigation, all that matters is the final location arrived at.

DASHER as a BCI user interface

C. Discrete Control

- BCI systems that emit discrete events fall into two categories.
- The first category contains systems which internally convert a continuous variable into discrete outputs
- Systems in which the user makes selections by driving a cursor to one of two or more on-screen targets fall into this category.
- They suggest that the best strategy for using DASHER with BCI systems in this category may be to use the continuous variable to drive DASHER directly, without an intermediate conversion into discrete options.
- The second category contains systems which are intrinsically discrete in nature.
- For example, both P300 and steady-state visually evoked potential (SSVEP) interfaces determine which of several discrete visual targets the user is attending to.

DASHER as a BCI user interface

C. Discrete Control

- A natural way to use these techniques would be to paint P300 targets or SSVEP regions onto the DASHER landscape.
- For example, in the case of SSVEP, the right-hand half of the DASHER landscape could be covered by two or more regions flickering at different frequencies (Fig. 3).

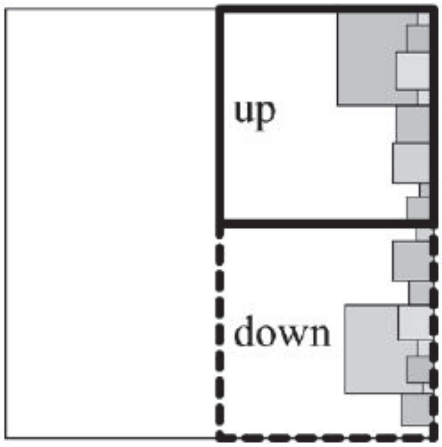

Depending on which region the user attends to, DASHER zooms in on the top or bottom half of the screen. <Figure 3>

DASHER as a BCI user interface

C. Discrete Control

- To zoom into one of these regions, the user attends to that region.
- The BCI system detects which region the user is attending to and causes DASHER to zoom in appropriately, and the cycle repeats. Likewise, P300 targets could be arranged down the right-hand side of the DASHER landscape, instead of in the commonly used speller grid.
- If the accuracy of the BCI system is high, then the optimal strategy for dealing with the rare errors that do occur may be to simply provide an additional target which instructs DASHER to undo the previous action (i.e., zoom out).
- Such a target needs to be present anyway, in case the user makes a mistake in selecting which region of the DASHER landscape contains the text they are trying to write.
- This is similar to the strategy of adding a “delete” node to a binary decision tree.

DASHER as a BCI user interface

C. Discrete Control

- However, if the BCI misclassification rate is high, they suggest that the optimal strategy is to model the BCI system as a noisy communication channel between the user and the computer, and to use information theory to inform the choice of an error-correcting code to use.
- For example, instead of accumulating evidence that the user is attending to a particular target over a single, long trial, it may be more efficient to run several shorter trials, each one individually less reliable.
- By varying the SSVEP frequencies on each target in each trial according to the coding scheme specied by the error-correcting code, the overall information transfer rate may be improved.

Conclusion

- They wish to make the best possible use of the bits of information content that can be generated by severely disabled people.
- DASHER offers a paradigm for efficiently converting these bits to communication symbols.
- DASHER has proved its effectiveness for people able to use a gaze tracker or make other motor actions.
- DASHER will be equally useful to users who retain functioning vision but are limited to communication through a BCI.

Idea

- DASHER + SSVEP (Continuous Control) (Mouse Control)

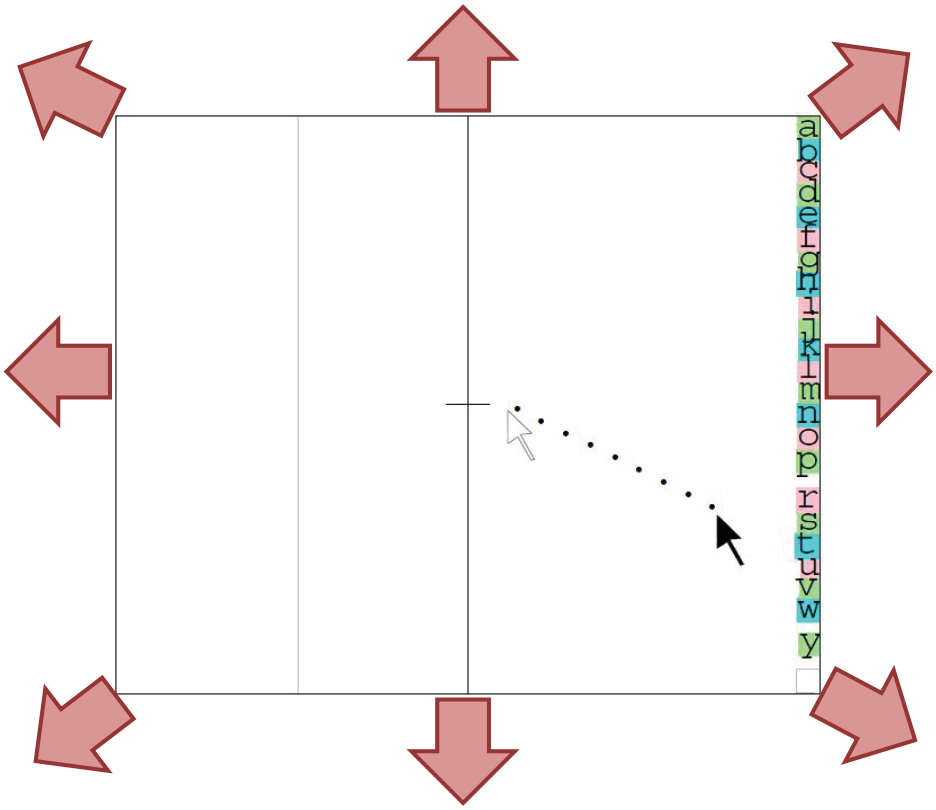

Thank you!

Title: Speckle field digital holographic microscopy

Wonshik Choi, YongKeun Park, Zahid Yaqoob, Ramachandra Dasari, Kamran Badizadegan, and Michael S. Feld

Speaker: Nitin Rawat

Brief Summary:

I. General Overview.

II. Experimental setup

III. Hologram reconstruction

This material is presented at the INFONT's Compressive Sensing Seminar

Lab Homepage: http://infonet.gist.ac.kr

Seminar Homepage: http://infonet.gist.ac.kr/twiki/bin/view/Main/CompressiveSensing

Advisor: Prof. Heung-no Lee

Speckle-field digital holographic microscopy

Conventional Holographic phase microscopy (HPM) uses a plane wave illumination that has very limited aperture in a condenser lens. This leads to poor spatial resolution compared with diffraction-limited resolution of conventional bright field microscopy.

Speckle field digital holographic microscopy (SFDHM), an interferometry-based light microscopic technique for sensing complex electric field (E-field) which utilizes the speckle field for illumination.

Principle

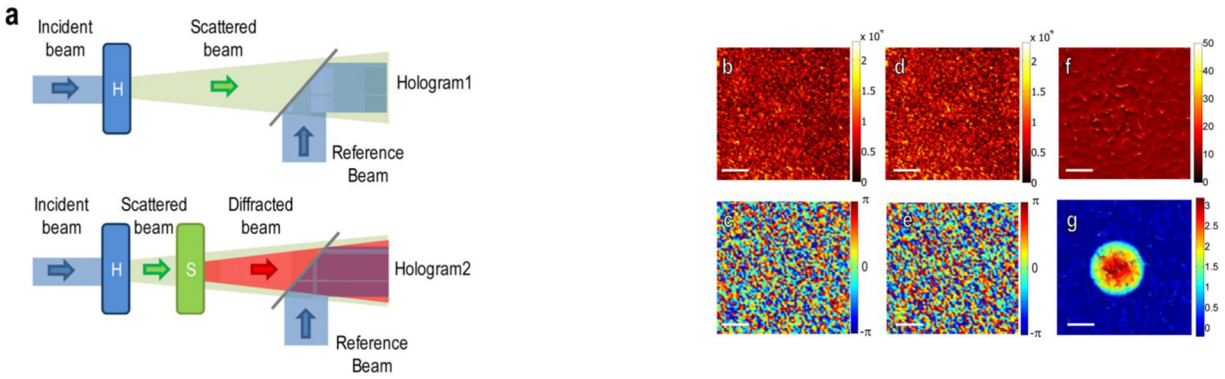

Figure. 1

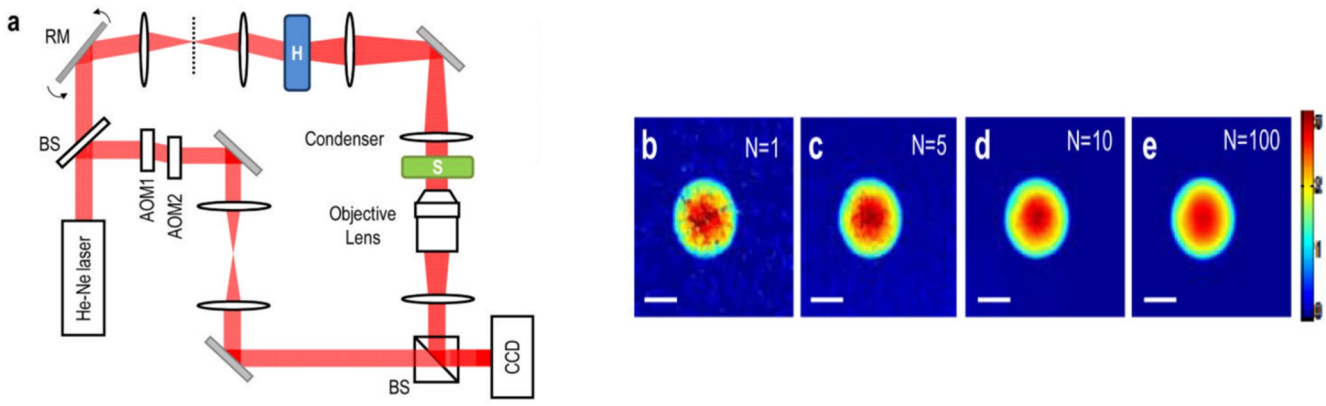

Figure.2

They generated a speckle field by illuminating a holographic diffuser with a He-Ne laser. The speckle field traveled through a microscope and was imaged on a detector. The hologram of the speckle field was generated by imposing a plane-wave reference beam on the detector. Using a heterodyne Mach-Zehnder interferometer, a complex E-field of the speckle was retrieved, as shown in figure 1b-c.

Then a sample was inserted on the sample stage with the same speckle field illumination. Introducing the sample modified the original speckle pattern.

Next, the E-field of the modified speckle was recorded in the same way as the recording of the original speckle pattern (Figs. 1d-e). The sample is almost invisible in these images since its image is overlapped with the complex pattern of the speckle field.

The background speckle field can be removed and the sample-induced complex field image can be retrieved from the speckle field (Fig. 1b-c) by dividing it by the field without the sample (Fig. 1d-e).

As a result, the sample becomes clearly visible, as shown in figs. 1f-g.

Speckle illumination not only reduces diffraction noise but also enhances the resolution in comparison with conventional HPM.

Holographic process

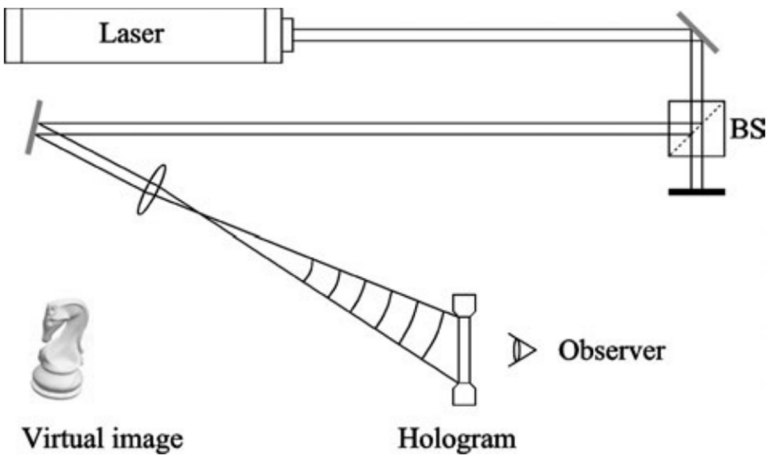

Light with sufficient coherence length is split into two partial waves by a beam splitter (BS). One wave illuminates the object, is scattered and reflected to the recording medium, e.g. a photographic plate.

The second wave, called the reference wave, illuminates the plate directly. Both waves are interfering. The recorded interference pattern is called hologram.

The holographic process is described mathematically as follows:

$$O(x,y) = o(x,y)\exp(i\varphi_o(x,y)) \quad \text{... (1.1)}$$

Is the complex amplitude of the object wave with real amplitude o and phase φ_o and

$$R(x,y) = r(x,y)\exp(i\varphi_R(x,y)) \quad \text{... (1.2)}$$

Is the complex amplitude of the reference wave with real amplitude r and phase φ_R

Both waves interfere at the surface of the recording medium (CCD). The intensity is calculated by

$$I(x,y) = \left|O(x,y) + R(x,y)\right|^2$$

$$= (O(x,y) + R(x,y))(O(x,y) + R(x,y))^*$$

$$= R(x,y)R^*(x,y) + O(x,y)O^*(x,y)$$

$$+ O(x,y)R^*(x,y) + R(x,y)O^*(x,y) \quad \text{... (1.3)}$$

Where $*$ denotes the conjugate complex.

The amplitude transmission *h(x,y)* of the developed photographic plate (or CCD) is proportional to *I(x,y)* :

$$h(x,y) = h_o + \beta\tau I(x,y) \quad \text{... (1.4)}$$

Where β is a constant, τ is the exposure time and h_o is the amplitude transmission of the unexposed plate. $h(x,y)$ is also called the hologram function.

In digital holography using CCD's as recording medium h_o can be neglected.

For hologram reconstruction the amplitude transmission has to be multiplied with the complex amplitude of the reconstruction (reference) wave:

$$R(x,y)h(x,y) = [h_o + \beta\tau(r^2 + o^2)]R(x,y) + \beta\tau r^2 O(x,y) + \beta\tau R^2(x,y)O^*(x,y) \quad \text{... (1.5)}$$

$$R(x,y)h(x,y) = \underbrace{[h_o + \beta\tau(r^2 + o^2)]R(x,y)}_{\text{reference wave multiplied by a factor}} + \underbrace{\beta\tau r^2 O(x,y)}_{\text{reconstructed object wave, forming the virtual image}} + \underbrace{\beta\tau R^2(x,y)O^*(x,y)}_{\text{distorted real image of the object}}$$

The first term on the right side of this equation is the reference wave, multiplied by a factor. It represents the un-diffracted wave passing through the hologram (zero diffraction order).

The second term is the reconstructed object wave, forming the virtual image. The factor $\beta\tau r^2$ only influences the brightness of the image.

The third term produces a distorted real image of the object.

For off-axis holography the virtual image, the real image and the un-diffracted wave are spatially separated.

Optical Path change

The hologram is reconstructed by illumination with the reference wave. As a result of the superposition of the two holographic recordings with slightly different object waves only one image superimposed by interference fringes is reconstructed.

The complex amplitude of the object wave in the initial state is

$$O_1(x,y) = o(x,y)\exp[i\varphi(x,y)] \quad \text{... (1.6)}$$

Where $o(x,y)$ is the real amplitude and $\varphi(x,y)$ is the phase of the object wave.

Optical path changes due to deformations of the object surface can be described by a variation of the phase from $\varphi \; to \; \varphi + \Delta\varphi$. $\Delta\varphi$ is the difference between the initial and actual phase, and is called the *interference phase*. The complex amplitude of the actual object wave is therefore denoted by:

$$O_2(x,y) = o(x,y)\exp[i(\varphi(x,y) + \Delta\varphi(x,y))] \quad \text{... (1.7)}$$

The intensity of a holographic interference pattern is described by the square of the sum of the complex amplitudes. It is calculated as follows:

$$I(x,y) = |O_1 + O_2|^2 = (O_1 + O_2)(O_1 + O_2)^* \quad \text{... (1.8)}$$

Equation (1.8) describes the relation between the intensity of the interference pattern and the interference phase, which contains the information about the deformation.

Several techniques have been developed to determine the interference phase by recording additional information. The most commonly used techniques are the various phase-shifting methods.

The interference phase is the key to calculate quantities representing the object under investigation. These are the displacement vector field of the surface in the case of opaque bodies.

The interference phase is the key to calculate quantities representing the object under investigation. These are the displacement vector field of the surface in the case of opaque bodies or refractive index changes within transparent media.

Yet to explore

General Principles

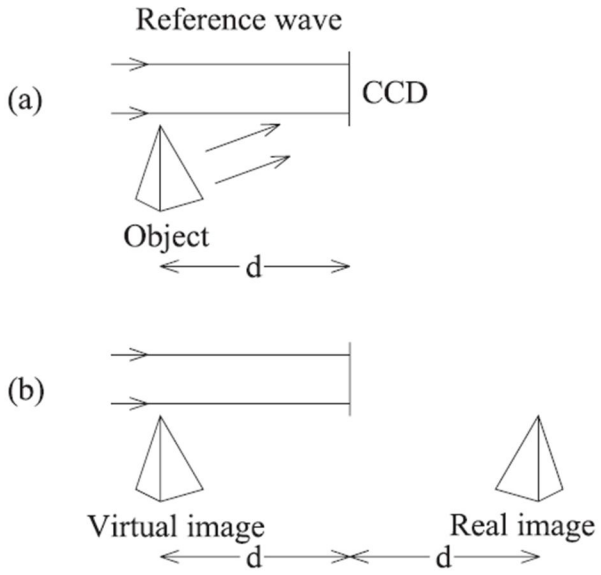

A general set-up for digital recording of off-axis holograms is shown in above above figure. A plane reference wave and the wave reflected from the object are interfering at the surface of a CCD. The resulting hologram is electronically recorded and stored.

The object is, in general, a three-dimensional body with diffusely reflecting surface, located at a distance *d* from the CCD.

In optical reconstruction the virtual image appears at the position of the original object and the real image is formed also at a distance *d*, but in the opposite direction from the CCD, see figure (b).

The diffraction of a light wave at an aperture (in this case a hologram) which is fastened perpendicular to the incoming beam is described by the Fresnel-Kirchhoff integral

$$\Gamma(\xi,\eta)=\frac{i}{\lambda}\int_{-\infty}^{\infty}\int_{-\infty}^{\infty}h(x,y)R(x,y)\frac{\exp(-i\frac{2\pi}{\lambda}\rho)}{\rho}\times(\frac{1}{2}+\frac{1}{2}\cos\theta)dx\,dy \quad \text{... (2.1)}$$

With $\rho=\sqrt{(x-\xi)^2+(y-\eta)^2+d^2}$ ... (2.2)

Where $h(x,y)$ is again the hologram function and ρ is the distance between a point in the hologram plane and a point in the reconstruction plane, see figure 5.

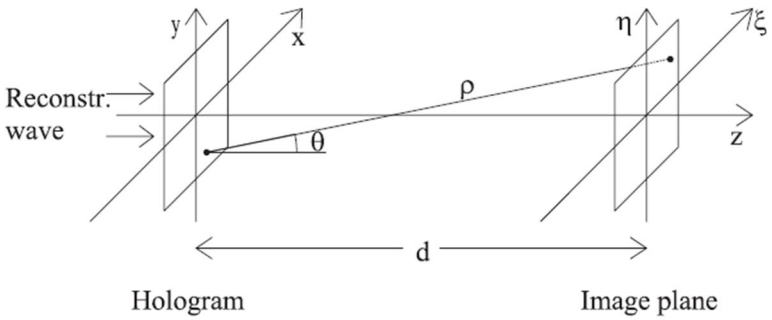

For a plane reference wave $R(x, y)$ is simply given by the real amplitude:

$$R = r + i0 = r \quad \text{... (2.3)}$$

The diffraction pattern is calculated at a distance *d* behind the CCD plane, which means it reconstructs the complex amplitude in the plane of the real image.

Equation (2.2) is the basis for numerical hologram reconstruction. Because the reconstructed wave-field $\Gamma(\xi, \eta)$ is a complex function, both the intensity as well as the phase can be calculated.

Also the real amplitude $O(x, y)$ of the object wave can be measured from the intensity by blocking the reference wave.

Example

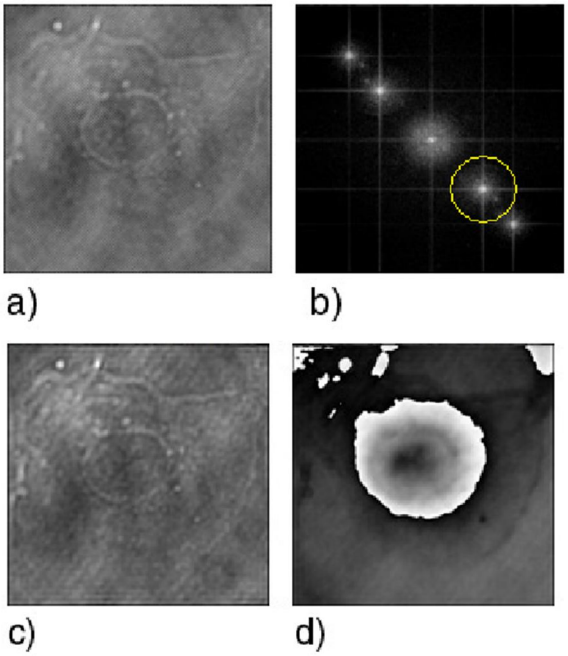

Figure 4

Figure 4 illustrates the implementation of the numerical algorithms in the reconstruction of an ovarian cell.

The area is $60 \times 60 \mu m^2$ with 424 x 424 pixels.

Figure 4(a) is the holographic interference pattern recorded by the CCD camera, and its Fourier transform in figure 4(b) is the angular spectrum.

A propagation phase factor $(z = 1.0 \mu m)$ is multiplied, and finally inverse-Fourier transformed to obtain the amplitude image in figure 4(c) and the phase image in figure 4(d).

The physical thickness of the cell can be calculated from

$$d = \lambda(\Delta\varphi / 2\pi) / (n - n_0) \quad \text{... (2.3)}$$

Where λ is the wavelength, $\Delta\varphi$ is the phase step and $(n - n_0)$ is the index difference between the film and air.

For example the layer of a cell is found to be about 110nm, assuming n=1.375.

Compressive multiple view projection incoherent holography

Authors: Yair Rivenson, Adrian Stern, and Joseph Rosen
Publication: Optics Express, 2011
Speaker: Sangjun Park

Short summary: In this seminar, the principles of the multiple view projection (MVP) holography technique are given. After understanding the principles, the intuition of the paper is shortly given. Finally, the new technique so called compressive multiple view projection (CMVP) holography is presented and the numerical simulations are also demonstrated.

I. INTRODUCTION

1. Holography is a classical method to store three dimensional information of a scene.
2. Acquisition methods of traditional holography are required high coherence and high powered sources such as lasers.
3. Without using the sources, the multiple view projection (MVP) holography technique is proposed.
4. The authors have pointed the drawback of the MVP holography technique, and then they have remedied the drawback by adopting the compressive sensing (CS) approach.

II. THE MULTIPLE VIEW PROJECTION (MVP) HOLOGRAPHY TECHNIQUE

1. According to the paper, the MVP holography technique appears to solve the traditional Holography technique that requires the sources such as lasers.

2. The process of the MVP holography technique:
   A. While a digital camera moves, it captures many view of the same scene from different angles.
   B. Each captured scene is projected into the CCD plane.
   C. Then, the different projections are used to synthesize a digital hologram.

3. Any ordinal digital camera can be used to store a three dimensional information of a scene.
4. The drawback of the MVP holography technique requires a significant scanning effort.
   A. For example, to generate a hologram whose size is 256×256, $256 \times 256 = 65536$ projections are acquired.

5. To remedy the drawback, techniques [Rosen07][Kim10] have been proposed.
   A. The first one is to employ a lenslet array instead of the CCD plane. But, this approach gives a low resolution hologram. [Kim10]
   B. The second one is to reduce scanning times by recording only a small number of the projections and synthesizing the rest using a view synthesis stereo algorithm. But, this approach faces with some difficulties in handling multiple scenes. [Rosen07]
   C. Please, read the papers if you have interested in them (They are not covered in this seminar). According to the authors, the proposed technique in this paper remedies the drawbacks presented in the papers.

6. The process of obtaining a digital hologram using the MVP technique is divided into optical and digital stages according to the paper.
   A. In the optical stage, different perspectives of the scene obtaining from a digital camera are recorded.

i. The perspective can be characterized by a pair of angles (φ_m, θ_n).

ii. The $(m,n)^{th}$ projection is denoted to $p_{mn}(x_p, y_p)$, where x_p and y_p are the coordinates in the projection domain.

B. In the digital stage, we multiply each acquired projection by a complex phase function $f_{mn} = \exp\{-j2\pi b(x_p \sin\varphi_m + y_p \sin\theta_n)\}$, where b is a real constant.

C. Obtaining a Fourier hologram. It is done by integrating the product of p_{mn} and f_{mn} as following: $h(m,n) = \iint p_{mn}(x_p, y_p) f_{mn} dx_p dy_p$. Then, we obtain a complex scalar for every projection (φ_m, θ_n).

i. By taking a Fourier transform on $h(m,n)$, we will get a reconstruction which corresponds only to $z = 0$ plane of the scene.

ii. In general, to obtain a reconstruction corresponding to z_i, we should multiply the hologram by a quadratic phase function. Viz.

$$u_i(x,y) = \mathcal{F}^{-1}\left\{h(v_x, v_y)\exp\left[-j\pi\lambda z_i\left(v_x^2 + v_y^2\right)\right]\right\}, \quad (1)$$

where u_i is the reconstructed plane, both v_x and v_y indicate spatial frequencies, λ denotes the central wavelength and $\mathcal{F}$ represents the Fourier transform.

D. Since digital holograms are considered, (1) becomes

$$u_i(x,y) = \sum_m \sum_n h(m,n)\exp\left\{-j\pi\lambda z_i\left[(\Delta v_x m)^2 + (\Delta v_y n)^2\right]\right\}\exp\left\{j2\pi\left(\frac{mp}{N_x} + \frac{nq}{N_y}\right)\right\}, \quad (2)$$

where N_x and N_y are the number of pixels in the x and y directions respectively. For simplicity, $N_x = N_y = N$. (2) can be rewritten as a matrix-vector multiplication form as following:

$$\mathbf{u}_i = \mathbf{F}^{-1}\mathbf{Q}_{-\lambda^2 z_i}\mathbf{h}, \tag{3}$$

where $\mathbf{u}_i$ is a $N^2 \times 1$ vector corresponding to z_i plane. Let F be a $N \times N$ discrete Fourier transform matrix whose elements are $F_{m,p} = \exp(-j2\pi mp/N)$. Then, $\mathbf{F} = F \otimes F \in \mathbb{C}^{N^2 \times N^2}$, where $\otimes$ is the Kronecker product. The matrix $\mathbf{Q}_{-\lambda^2 z_i} \in \mathbb{C}^{N^2 \times N^2}$ is a diagonal matrix with quadratic phase elements along its diagonal.

E. Shortly, reconstructing $\mathbf{u}_i$ is easy. $\mathbf{F}$ is given, $\mathbf{Q}_{-\lambda^2 z_i}$ is determined the angles, and $\mathbf{h}$ is obtained by integrating the product of p_{mn} and f_{mn}.

F. To understand how to get $\mathbf{h}$ from an experiment, we need to read the following papers.[Rosen01][Rosen03]…

III. Compressive Sensing approach for reducing the number of projections

1. The idea is very simple and intuitive.
   A. To reconstruct a hologram, what things do we need? They are $\mathbf{F}$, $\mathbf{Q}_{-\lambda^2 z_i}$ and $\mathbf{h}$.
   B. Among them, what is the measured factor in an experiment? It is $\mathbf{h}$.
2. The authors assume that the synthesized Fourier hologram $\mathbf{h}$ can be sparse. Then, this assumption allows us to reduce the size of $\mathbf{h}$. It is the main idea of this paper.
3. Let us denote $\mathbf{h}^M$ to the subsampled Fourier hologram. By solving the below equation

$$\hat{\mathbf{u}}_i = \arg\min_{\mathbf{u}_i} \left\{ \left\| \mathbf{u}_i - \mathbf{F}^{-1}\mathbf{Q}_{-\lambda^2 z_i}\mathbf{h}^M \right\|_2^2 + \gamma \left\| \Psi_i \mathbf{u}_i \right\|_1 \right\}, \tag{4}$$

we can reconstruct an object plane $\mathbf{u}_i$ at distance z_i from $z=0$ plane. In the paper, the authors recommend Ψ_i such as Haar wavelet or total variation and the authors name it compressive multiple view projection (CMVP) holography.

IV. SUMMARY OF THE CMVP HOLOGRAPHY

1. Instead of $N^2 = N_x \times N_y$ projections, only $\Omega(K \log N)$ random projections of the scene are taken.
2. Multiply each taken projection p_{mn} by its corresponding phase function f_{mn}.
3. Then, we get a single Fourier hologram by doing $h(m,n) = \int\int p_{mn}(x_p, y_p) f_{mn} dx_p dy_p$.
4. After obtaining an under-sampled Fourier hologram $\mathbf{h}^M$, we can reconstruct each plane of the scene by solving (4).

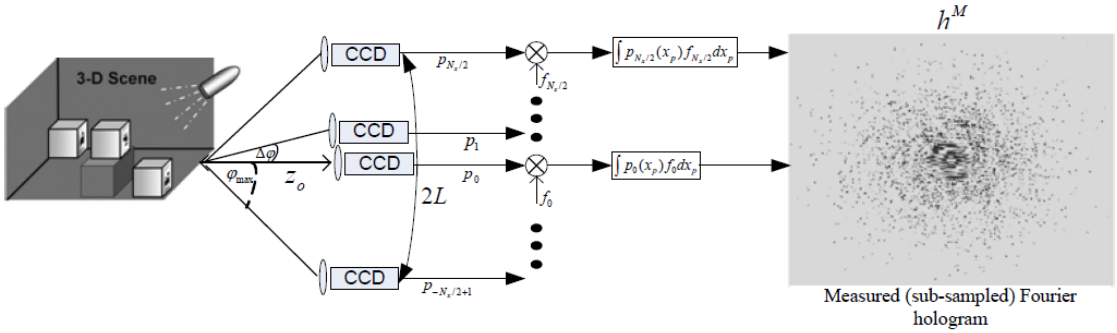

Fig. 1. Illustration of CMVP hologram acquisition. Acquisition of only $\approx K log N_x$ projections results in a heavily undersampled Fourier hologram. Each sample in the hologram plane corresponds to a nonuniformly randomly picked projection.

In the above Fig. 1, the CMVP hologram acquisition is shown. For simplicity, only a scan along the *x*-axis is shown. The minimal angular distance between two adjacent projections is $\Delta\varphi$, and z_0 is the distance between the imaging system and the object. The length of the CCD's translation trajectory is $2L$.

V. NUMERICAL RESULTS

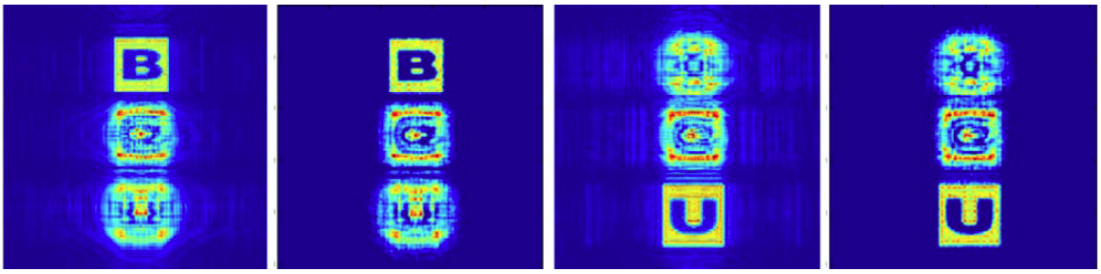

(a) (b) (c) (d)

Fig. 2. Reconstruction examples of the B and U planes of simulated data. (a) Reconstruction of the B plane from 100% of the projections. (b) CS reconstruction of the B plane from 6% of the projections. (c) Reconstruction of the U plane from 100% of the projections. (d) CS reconstruction of the U plane from 6% of the projections.

In both (a) and (c), 256×256 projections are required.

In both (b) and (d), $256 \times 256 \times 0.06$ projections are acquired.

In the CMVP method, Haar wavelet transform is used and TwIST solvers is used to solve (4).

VI. CONCLUSION

1. In this paper, the authors shortly have summarized about the multiple view projection (MVP) holography technique (See Section 2). Then, the authors have proposed the compressive multiple view projection (CMVP) technique (See Section 3).
2. The strong advantages of the proposed technique are that 1) it does not require changing a sensing hardware, 2) it gives a high resolution hologram compared to the previous technique [Kim10], and 3) it does not require a distinct anchor point problem arisen in [Rosen07].

   (In the paper, the authors have made a part System's Resolution Analysis for the theoretical analysis of the system's resolution limit. If you have interested in it, please carefully read the paper)

   (The distinct anchor point problem is that the technique [Rosen07] requires the distinct anchor points to interpolate the different perspectives of the scene. Thus, if the scene is changed, then the distinct anchor points are also changed. However, the CMVP technique is free from this)

VII. DISCUSSION

After meeting, please write discussion in the meeting and update your presentation file.

Reference

[Rosen01] Y. Li, D. Abookasis, and J. rosen, “Computer-generated holograms of three-dimensional realistic objects recorded without wave interference,” Appl. Opt. 40(17), 2864 – 2870 (2001).

[Rosen03] D. Abookasis, and J. Rosen, “Computer-generated holograms of three-dimensional objects synthesized from their multiple angular viewpoints, “J. Opt. Soc. Am. A 20(8), 1537 – 1545 (2003).

[Rosen07] B. Katz, N. T. Shaked, and J. Rosen, “Synthesizing computer generated holograms with reduced number of perspective projections,” Opt. Express 15(20), 13250 – 13255 (2007).

[Kim10] N. Chen, J.-H. Park, and N. Kim, “Parameter analysis of integral Fourier hologram and its resolution enhancement,” Opt. Express 18(3), 2152 – 2167 (2010).

Compressed Sensing of EEG for Wireless Telemonitoring with Low Energy Consumption and Inexpensive Hardware

Authors: Zhilin Zhang, Tzyy-Ping Jung, Scott Makeig, Bhaskar D. Rao,

Publication: IEEE TRANSACTIONS ON BIOMEDICAL ENGINEERING, 2012

Speaker: Younghak Shin

Short summary: Telemonitoring of electroencephalogram (EEG) through wireless body-area networks (WBAN) is an evolving direction in personalized medicine. However, there are important constraints such as energy consumption, data compression, and device cost. Recently, Block Sparse Bayesian Learning (BSBL) was proposed as a new method to the CS problem. In this study, they apply the technique to the telemonitoring of EEG. Experimental results show that its recovery quality is better than state-of-the-art CS algorithms. These results suggest that BSBL is very promising for telemonitoring of EEG and other non-sparse physiological signals.

I. INTRODUCTION

Telemonitoring of electroencephalogram (EEG) via WBANs is an evolving direction in personalized medicine and home-based e-Health. Equipped with the system, patients need not visit hospitals frequently. Instead, their EEG can be monitored continuously and ubiquitously.

However, there are many constraints

A. The primary one is energy constraint. Due to limitation on battery life, it is necessary to reduce energy consumption as much as possible.

B. Another constraint is that transmitted physiological signals should be largely compressed.

C. The third constraint is hardware costs. Low hardware costs are more likely to make a telemonitoring system economically feasible and accepted by individual customers

It is noted that many conventional data compression method such as wavelet compression cannot satisfy all the above constraints at the same time.

Compared to wavelet compression, Compressed Sensing (CS) can reduce energy consumption while achieving competitive data compression ratio.

However, current CS algorithms only work well for sparse signals or signals with sparse representation coefficients in some transformed domains (e.g., the wavelet domain).

Since EEG is neither sparse in the original time domain nor sparse in transformed domains, current CS algorithms cannot achieve good recovery quality.

This study proposes using Block Sparse Bayesian Learning (BSBL) [1] to compress/recover EEG. The BSBL framework was initially proposed for signals with block structure. This study explores the feasibility of using the BSBL technique for EEG, which is an example of a signal without distinct block structure.

II. COMPRESSED SENSING AND BLOCK SPARSE BAYESIAN LEARNING

CS is a new data compression paradigm, in which a signal of length N, denoted by $\mathbf{x} \in \mathbb{R}^{M \times N}$, is compressed by a full row-rank random matrix, denoted by $\mathbf{\Phi} \in \mathbb{R}^{M \times N}$ $\left(M \ll N\right)$,i.e.,

$$\mathbf{y} = \mathbf{\Phi x}, \tag{1}$$

where $\mathbf{y}$ is the compressed data, and $\mathbf{\Phi}$ is called the *sensing matrix*. CS algorithms use the compressed data $\mathbf{y}$ and the sensing matrix $\mathbf{\Phi}$ to recover the original signal $\mathbf{x}$. Their successes rely on the key assumption that most entries of the signal x are zero (i.e., $\mathbf{x}$ is sparse).

When this assumption does not hold, one can seek a dictionary matrix, denoted by $\mathbf{D} \in \mathbb{R}^{M \times M}$, so that $\mathbf{x}$ can be expressed as $\mathbf{x} = \mathbf{Dz}$ and $\mathbf{z}$ is sparse.

$$\mathbf{y} = \mathbf{\Phi D z}. \tag{2}$$

When CS is used in a telemonitoring system, signals are compressed on sensors according to (1). This compression stage consumes on-chip energy of the WBAN. The signals are recovered by a remote computer according to (2). This stage does not consume any energy of the WBAN.

Despite of many advantages, the use of CS in telemonitoring is only limited to a few types of signals, because most physiological signals like EEG are not sparse in the time domain and not sparse enough in transformed domains.

The issue now can be solved by the BSBL framework [1], [2].

It assumes the signal **x** can be partitioned into a concatenation of non-overlapping blocks, and a few of blocks are non-zero. Thus, it requires users to define the block partition of **x**.

However, it turns out that user-defined block partition does not need to be consistent with the true block partition [3]. Further, in this work, they found even if a signal has no distinct block structure, the BSBL framework is still effective.

This makes feasible using BSBL for the CS of EEG, since EEG has arbitrary waveforms and the representation coefficients **z** generally lack block structure.

Currently, there are three algorithms in the BSBL framework. In this experiment, they chose a bound-optimization based algorithm, denoted by BSBL-BO. Details on the algorithm and the BSBL framework can be found in [1].

III. EXPERIMENTS OF COMPRESSED SENSING OF EEG

The following experiments compared BSBL-BO with some representative CS algorithms in terms of recovery quality.

Two performance indexes were used to measure recovery quality. One was the Normalized Mean Square Error (NMSE). The second was the Structural SIMilarity index (SSIM) [4]. SSIM measures the similarity between the recovered signal and the original signal, which is a better performance index than the NMSE for structured signals.

In the first experiment **D** was an inverse Discrete Cosine Transform (DCT) matrix, and thus **z** $\left(\mathbf{z}=\mathbf{D}^{-1}\mathbf{x}\right)$ are DCT coefficients. In the second experiment **D** was an inverse Daubechies-20 Wavelet Transform (WT) matrix.

In both experiments the sensing matrices $\mathbf{\Phi}$ were sparse binary matrices, in which every column contained 15 entries equal to 1 with random locations while other entries were zeros.

A. Experiment 1: Compressed Sensing with DCT

This example used a common dataset (‘eeglab data.set’) in the EEGLab. This dataset contains

EEG signals of 32 channels with sequence length of 30720 data points, and each channel signal contains 80 epochs each containing 384 points.

To compress the signals epoch by epoch, they used a 192 ×384 sparse binary matrix as the sensing matrix $\mathbf{\Phi}$, and a 384×384 inverse DCT matrix as the dictionary matrix **D**.

Two representative CS algorithms were compared in this experiment. One was the Model-CoSaMP, which has high performance for signals with known block structure. The second was an L1 algorithm (CVX toolbox) to recover EEG.

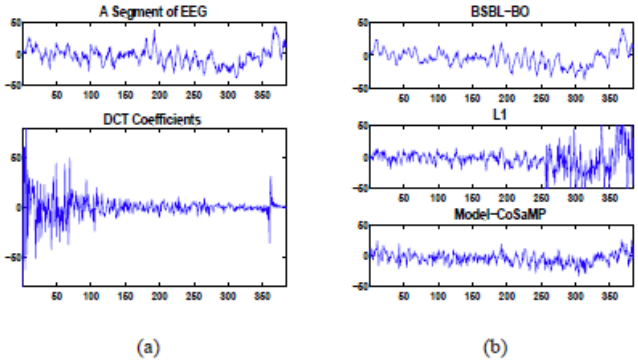

Fig. 1. (a) An EEG epoch, and its DCT coefficients. (b) The recovery results by BSBL-BO, ℓ_1, and Model-CoSaMP when using the model (2).

Figure 1(a) shows an EEG epoch and its DCT coefficients. Clearly, the DCT coefficients were not sparse and had no block structure. Figure 1(b) shows the recovery results of the three algorithms. BSBL-BO recovered the epoch with good quality.

Table I shows the averaged NMSE and SSIM of the three algorithms on the whole dataset.

TABLE I
AVERAGED PERFORMANCE IN EXPERIMENT 1.

	NMSE (mean ± std)	SSIM (mean ± std)
DCT-based BSBL-BO	**0.078 ± 0.046**	**0.85 ± 0.08**
BSBL-BO without DCT	0.116 ± 0.066	0.81 ± 0.09
DCT-based ℓ_1	0.493 ± 0.121	0.48 ± 0.11
DCT-based Block-CoSaMP	0.434 ± 0.070	0.45 ± 0.10

The DCT-based BSBL-BO evidently had the best performance.

B. Experiment 2: Compressed Sensing with WT

The second experiment used movement direction dataset. It consists of multiple channel signals, each channel signal containing 250 epochs for each of two events ('left direction' and 'right direction'). BSBL-BO and the previous L1 algorithm were compared.

The sensing matrix $\mathbf{\Phi}$ had the size of 128 × 256, and the dictionary matrix D had the size of 256 × 256.

For each event, they calculated the ERP by averaging the associated 250 recovered epochs.

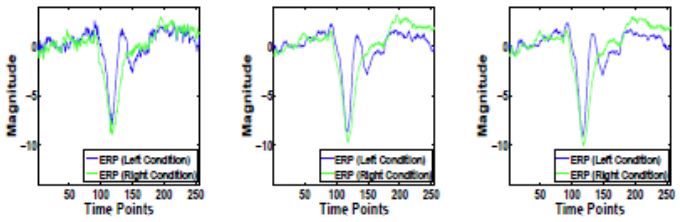

Fig. 3. The ERPs corresponding to two event conditions ('left' and 'right') averaged (a) from the recovered epochs by the ℓ_1 algorithm, (b) from the recovered epochs by BSBL-BO, and (c) from the original dataset.

Figure 3 (a) shows the ERP for the 'left direction' and the ERP for the 'right direction' averaged from the dataset recovered by the L1 algorithm. Figure 3 (b) shows the ERPs from the recovered dataset by BSBL-BO. Figure 3 (c) shows the ERPs from the original dataset.

Clearly, the resulting ERPs by the L1 algorithm were noisy.

The ERPs averaged from the recovered by BSBL-BO maintained all the details of the original ERPs with high consistency. The SSIM and the NMSE of the resulting ERPs by the L1 algorithm were 0.92 and 0.044, respectively. In contrast, the SSIM and the NMSE of the resulting ERPs by BSBL-BO were 0.97 and 0.008, respectively.

IV. DISCUSSIONS

Using various dictionary matrices, the representation coefficients of EEG signals are still not sparse. Therefore, current CS algorithms have poor performance, and their recovery quality is not suitable for many clinical applications and cognitive neuroscience studies.

Instead of seeking optimal dictionary matrices, this study proposed a method using general dictionary matrices achieving sufficient recovery quality for typical cognitive neuroscience studies.

The empirical results suggest that when using the BSBL framework for EEG compression/recovery, the seeking of optimal dictionary matrices is not very crucial.

V. CONCLUSIONS

This study proposed to use the framework of block sparse Bayesian learning, which has superior performance to other existing CS algorithms in recovering non-sparse signals. Experimental results showed that it recovered EEG signals with good quality. Thus, it is very promising for wireless telemonitoring based cognitive neuroscience studies.

VI. DISCUSSION & COMMENTS

This method can be applied other research area with non-sparse signal.

Appendix

Experiment codes can be downloaded at:

https://sites.google.com/site/researchbyzhang/bsbl.

Reference

[1] Z. Zhang and B. D. Rao, "Extension of SBL algorithms for the recovery of block sparse signals with intra-block correlation," IEEE Trans. On Signal Processing (submitted), 2012.

[2] ——, "Sparse signal recovery with temporally correlated source vectors using sparse Bayesian learning," IEEE Journal of Selected Topics in Signal Processing, vol. 5, no. 5, pp. 912–926, 2011.

[3] Z. Zhang, T.-P. Jung, S. Makeig, and B. D. Rao, "Low energy wireless body-area networks for fetal ECG elemonitoring via the framework of block sparse Bayesian learning," IEEE Trans. on Biomedical Engineering (submitted), 2012.

[4] Z. Wang and A. Bovik, "Mean squared error: Love it or leave it? a new look at signal fidelity measures," IEEE Signal Processing Magazine, vol. 26, no. 1, pp. 98–117, 2009.

Compressive sensing in medical ultrasound (Invited paper)

H. Liebgott et al.

IEEE Intl. Ultrasonics Symp. (2012. July)

Presenter : Jin-Taek Seong

GIST, Dept. of Information and Communications, INFONET Lab.

Gwangju Institute of Science and Technology

Introduction

- Compressed sensing can be applied for two main purposes:
  - *i*) it can lower the amount of data needed and thus allows to speed up acquisition.
  - An example in the field of medical imaging of such application is dynamic MRI [4].
  - *ii*) it can improve the reconstruction of signals/images in fields where constraints or the physical acquisition set up yields very sparse data sets.
  - A typical example is seismic data recovery in geophysics [5].
- The objective of this paper is
  - to give the reader an overview of the different attempts to show the feasibility of CS in medical ultrasound.
- The classification of the studies is done according to the data that are considered to be sparse.
  - the scatterer distribution itself, the pre-beamforming channel data, the beamformed RF signal and even Dopple data.

Introduction

- The way that how to be sparse in some domains is a key idea to apply the inverse problem to the CS problem.
- In this paper, they show several schemes that expand data into sparse signals.

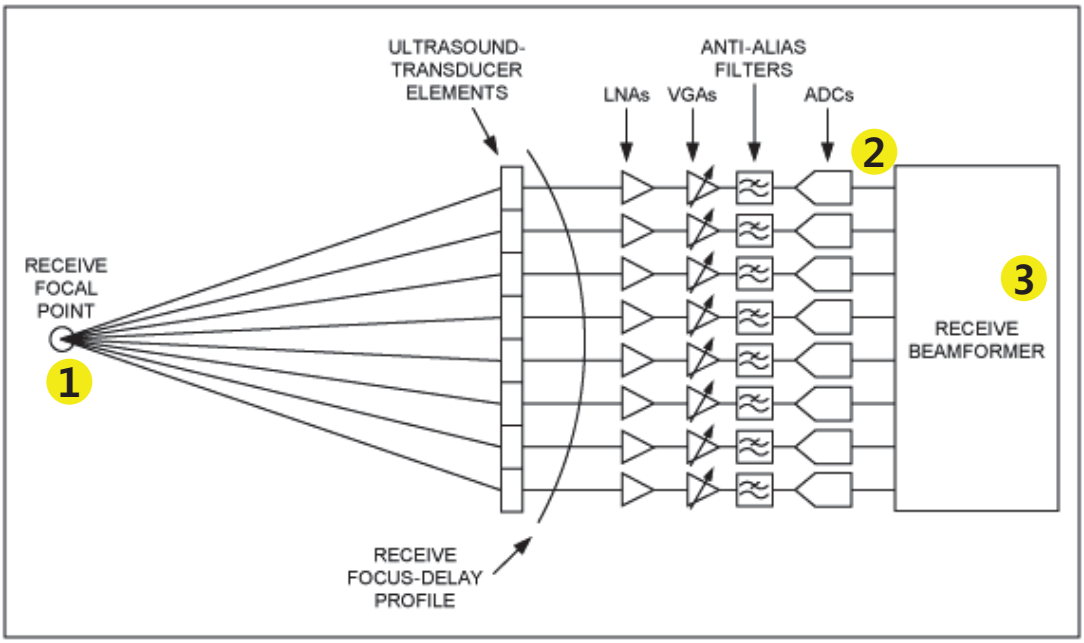

Application to Ultrasound Imaging

- A central concern in CS is that the data under consideration should have sparse expansion in some dictionaries.
  - Fourier basis, wavelet basis, dictionary learned from data, etc...
  - i.e., the number of non-zero coefficients of the image or signal in this representation basis should be as small as possible.
- One of the main features of the existing studies is the type of signal/image to be reconstructed and the choice of the representation where the US data are assumed to be sparse.
- We overview the following models in the sparse domains
  - Sparse diffusion map
  - Sparse Raw RF
  - Sparse assumption of the RF images Fourier transform
  - Doppler imaging

Sparse diffusion map

- Several groups of authors [12-18] have chosen to model the medium under investigation itself as a sparse distribution of scatters.
- However, considering that most of the scatters have an echogenecity close to zero is more unusual.
- The basic idea [12-13] is to write the direct scattering problem and solve the inverse problem under the constraint that the scatter distribution is sparse.

$$\boldsymbol{p}^{sc}\left(e_\theta\right)=\boldsymbol{G}\left(e_\theta\right)\gamma_K$$

  - With $\boldsymbol{p}^{sc}\left(e_\theta\right)$ the scattered pressure received by the transducer elements after transmission of a plane wave in direction θ, $\boldsymbol{G}\left(e_\theta\right)$ represents propagation and interaction with the scatters and γ_K is the scatter distribution lying on a regular grid.
- If γ_K is assumed to be sparse, this problem is equivalent to the CS problem.

Sparse diffusion map

- Figure shows a result from a simple phantom consisting in four isolated scatters obtained with this approach.

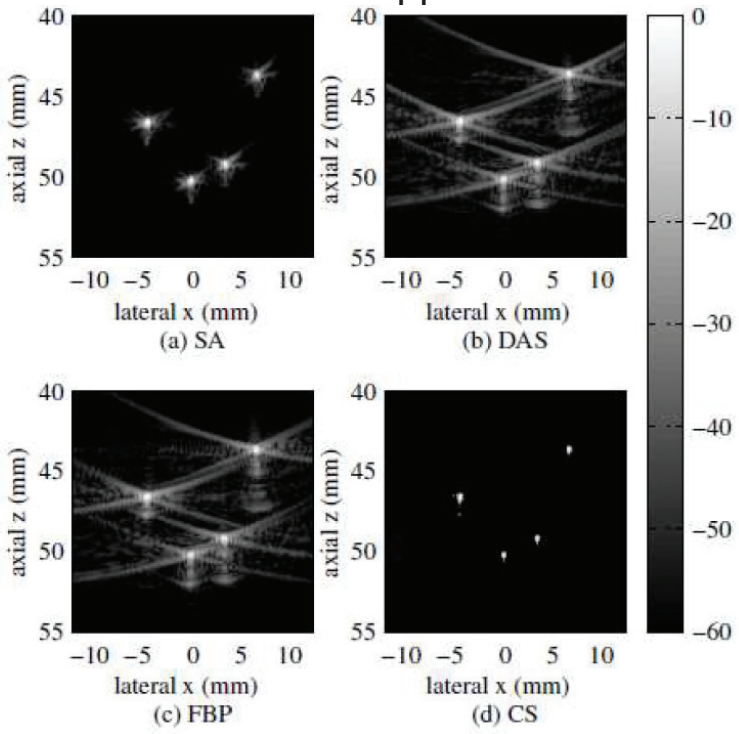

  - The CS result (d) is compared with synthetic aperture (a), delay and sum (b) and Fourier propagation (c).

Sparse diffusion map

- With the same assumption [14, 15] proposed another approach based on finite rate of innovation and Xampling.

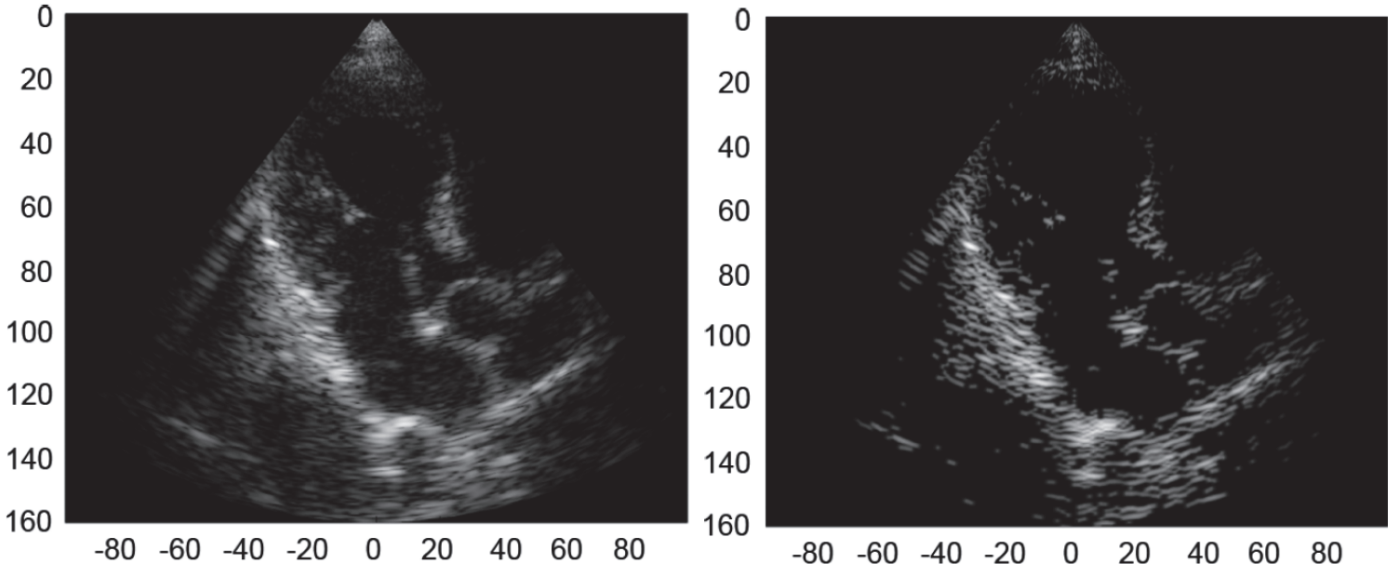

- The edges are well reconstructed but the speckle is close to be completely lost in some parts of the images.
- This is consistent assumption of scatter map sparsity.

Sparse Raw RF

- Another group of authors [21-24] consider that the raw channel data gathered at each transducer element during receive have a sparse decomposition in some basis.
- The objective of such an approach is to reduce the quantity of pre-beamformed data acquired and evaluate the ability of this approach to reconstruct B-mode images of good quality.

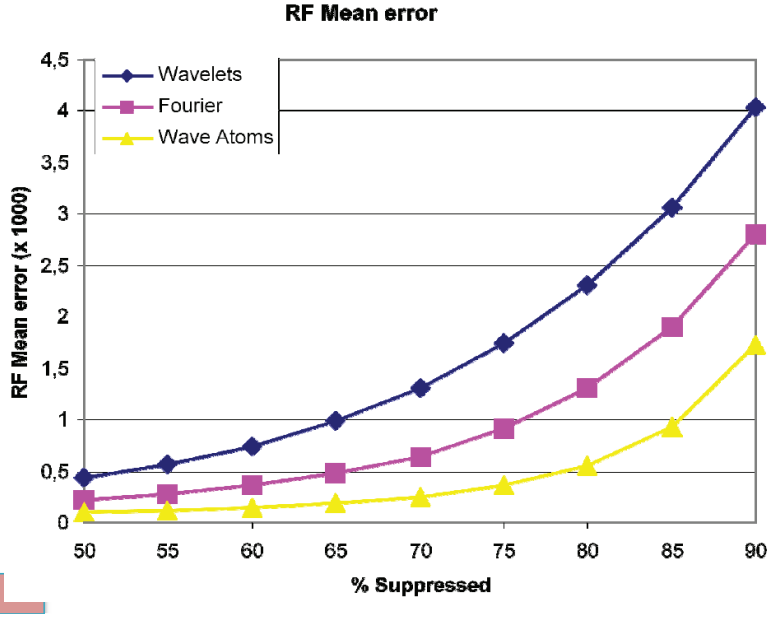

Sparse Raw RF

- Figure shows experimental results obtained from only 20% of the original data using CS and wave atoms.

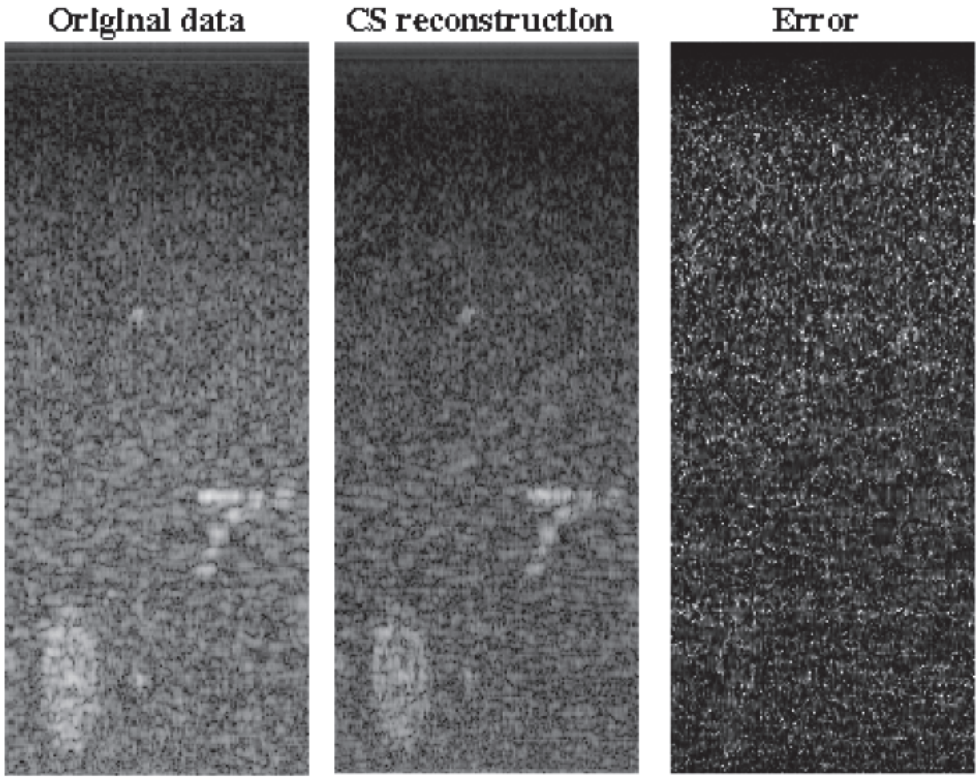

Sparse assumption of the RF images Fourier transform

- The reconstruction of post-beamforming 2D RF images via CS technique is addressed.
- The sparsity assumption is related to the assumption of bandlimited RF signal acquisition.
- The 2D Fourier transform of RF images is assumed to be sparse.

$$y = \Phi \Psi x$$

  - Φ denotes the sampling mask, Ψ is the 2D Fourier Transform.

Random post-beamforming RF sampling mask

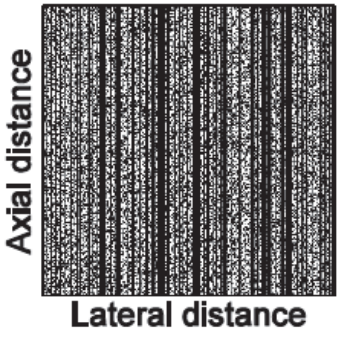

Sparse assumption of the RF images

- (a) original simulated RF image, (b) RF samples used for reconstruction, (c) reconstructed RF image using a reweighted conjugate gradient optimization, (d) reconstructed RF image using the Bayesian framework proposed in [20].

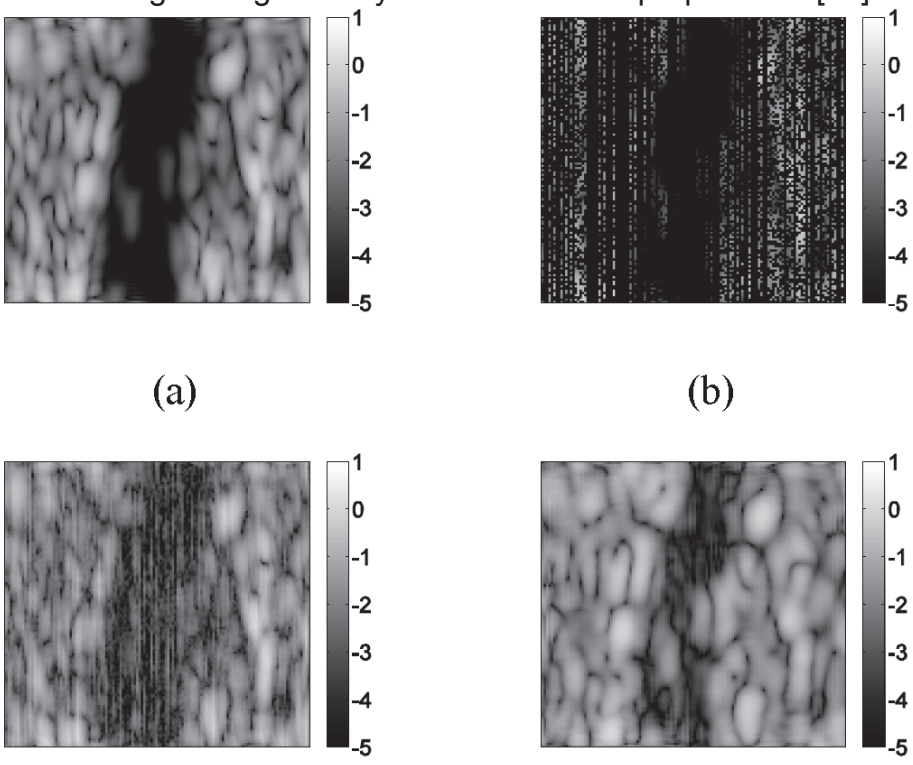

Doppler imaging

- CS has also been proposed for Doppler imaging [32, 33].
- The authors [32] made the assumption that the Fourier transform of the Doppler signal is sparse.

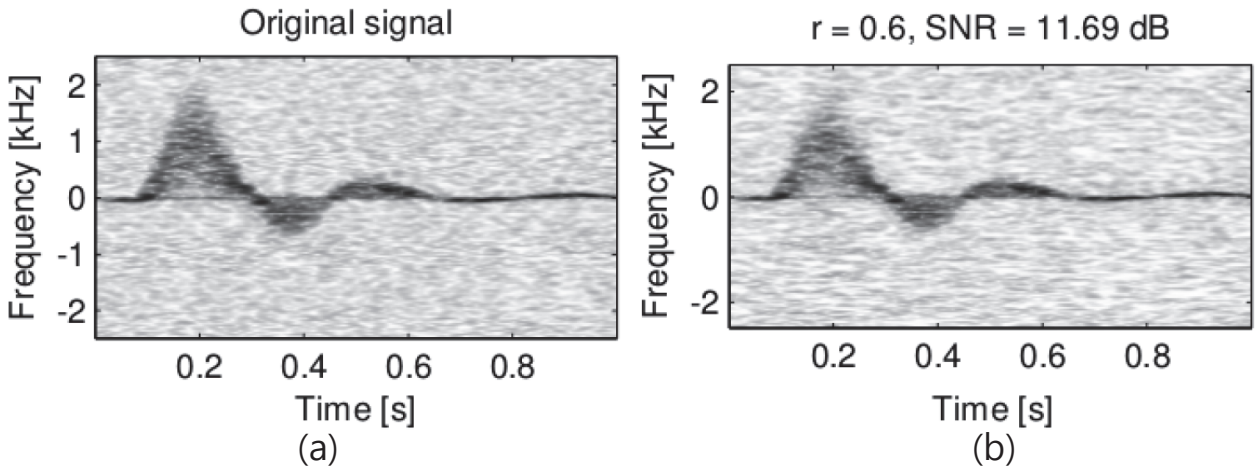

- In vivo Doopler result from a femoral artery. (a) real sonogram; (b) reconstructed sonogram based on CS, where r is the ratio of the number of Doppler samples to the total number of samples.

Conclusion

- Compressed sensing medical ultrasound is a very recent field of research that can lead to drastic modifications in the way ultrasound scanners are developed.
- The technique is feasible but far from its technological applicability.
- The key points for CS to work are
  - A sparsifying basis
  - A measure basis in coherent with the sparsifying basis
  - Dedicated acquisition material
  - Fast and robust reconstruction algorithms
- Improvements are necessary for all of these concerns.
- Efforts should be made in order to maintain the real-time characteristic of medical ultrasound.

Reference

- [4] M. Lustig, D. Donoho, and J. M. Pauly, “Sparse MRI: The application of compressed sensing for rapid MR imaging,” Magnetic Resonance in Medicine, vol. 58, pp. 1182-1195, 2007.
- [5] F. J. Herrmann and G. Hennenfent, “Non-parametric seismic data recovery with curvelet frames,” Geophysical Journal Intl., vol. 173, pp. 223-248, 2008.

Enhanced performance by a hybrid NIRS–EEG brain computer interface.

Siamac Fazli et al. (Benjamin Blankertz*)

NeuroImage (2012)

Presenter : SeungChan Lee

GIST, Dept. of Information and Communication, INFONET Lab.

Gwangju Institute of Science and Technology

Background

- NIRS
  - Near-infrared spectroscopy (NIRS) is a spectroscopic method that uses the near-infrared region of the electromagnetic spectrum.
  - NIRS measures the concentration changes of oxygenated and deoxygenated hemoglobins ([HbO] and [HbR]) in the superficial layers of the human cortex.
  - While concentration of [HbO] is expected to increase after focal activation of the cortex due to higher blood flow, [HbR] is washed out and decreases.

Introduction & Motivation

- Hybrid BCI approach
  - For increasing information transfer rates and robustness of the classification
  - Combination of EEG features from multiple domains such as movement related potentials (MRPs) and event-related desynchronizations (ERD).
  - Combinations of EEG and peripheral parameters such as electromyography(EMG), electrooculogram(EOG)
- Limitation in neuroimaging techniques
  - EEG : spatial resolution
  - NIRS, fMRI : temporal resolution
- Goals
  - Implement a hybrid BCI by extracting relevant NIRS features to support and complement high-speed EEG-based BCI.
  - Evaluate the time delay and spatial information content of the hemodynamic response and show enhance and robust BCI performance during a SMR-based BCI paradigm.

Experiment design

- Data acquisition
  - NIRS system : NIRScout 8–16 (NIRx Medizintechnik GmbH, Germany)
    - 24 optical fibers (8 sources with wavelengths of 850 nm and 760 nm, 16 detectors convolving to 24 measurement channels)
    - The sampling rate is 6.25Hz
  - EEG system : BrainAmp (Brain Products, Munich, Germany)
    - 37 Ag/AgCl electrodes, 2 bipolar EMG, 2 bipolar EOG
    - The sampling rate is 1kHz and downsampled to 100 Hz.
  - The optical probes are constructed such that they fit into the ring of standard electrodes.

Experiment design

- Locations of electrodes

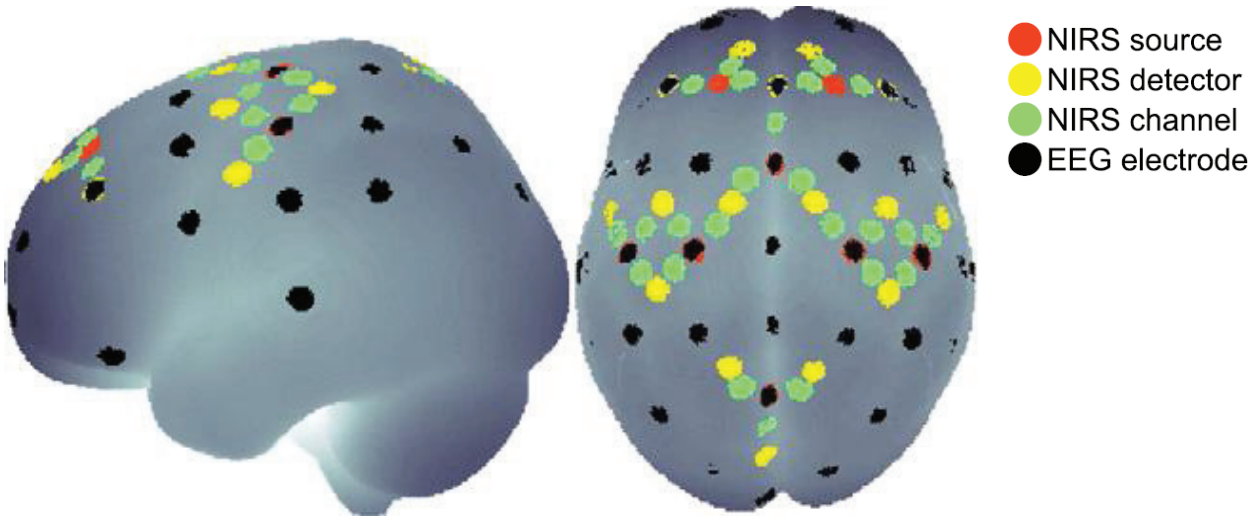

Experiment design

- Experiment design
  - 14 healthy, right-handed volunteers (aged 20 to 30)
  - 2 class motor function(left vs. right hand movements)
  - 2 blocks of motor execution by means of hand gripping (24 trials per block per condition) and 2 blocks of real-time EEG-based, visual feedback controlled motor imagery (50 trials per block per condition)
    - first 2s : trial began with a black fixation cross
    - 2 ~ 6s : visual cue an arrow appeared pointing to the left or right
    - 2 ~ 6s motor imagery : the fixation cross started moving for 4 s according to the classifier output
    - After 4s : blank screen for 10.5±1.5 s.

Data analysis

- EEG analysis
  - Offline analysis + Motor imagery of feedback session based on ***coadaptive calibration***
  - First block of 100 trials : subject-independent classifier (band power estimates of laplacian filtered from motor-related EEG channels)
  - Second block of 100 trials : subject-dependent spatial and temporal filters were estimated from the data of the first block and combined with some subject-independent features
  - Feedback features(moving cross) were calculated every 40 ms with a sliding window of 750 ms.

Data analysis

- NIRS analysis
  - Only offline analysis based on Lamber-beer law
  - Low-pass filtered at 0.2Hz(3rd order Butterworth-filter)
  - A mean of baseline interval(−2s ~ 0s) subtracted from each trial.
  - Average over the time length of the moving window width

Data analysis

- Classification
  - -6 ~ 15 seconds data and moving window (width 1 s, step size=500 ms) are used for classification.
  - 8-fold cross validation with Linear discriminant analysis (LDA).

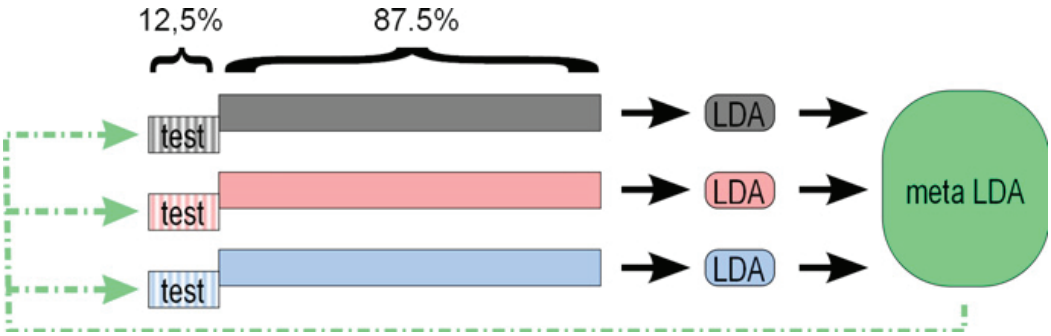

  - 78 training data and 18 test data (real movements)
  - An individual LDA classifier is computed for EEG, [HbO] and [HbR]
  - A meta-classifier is estimated for optimally combining the three LDA outputs.
  - All LDA classifiers are then applied to the test set

Results

- Comparison of classification accuracies and peak classification time
  - For showing the physiological reliability of NIRS feature classification both in time and location.

Accuracies	Real	Imagery
EEG	90.8%	78.2%
HbO	71.1%	71.7%
HbR	73.3%	65.0%

Peak clas.	Real	Imagery
EEG	1680±1014ms	1430±707ms
HbO	7430±2201ms	6501±1579ms
HbR	6966±2484ms	6109±1339ms

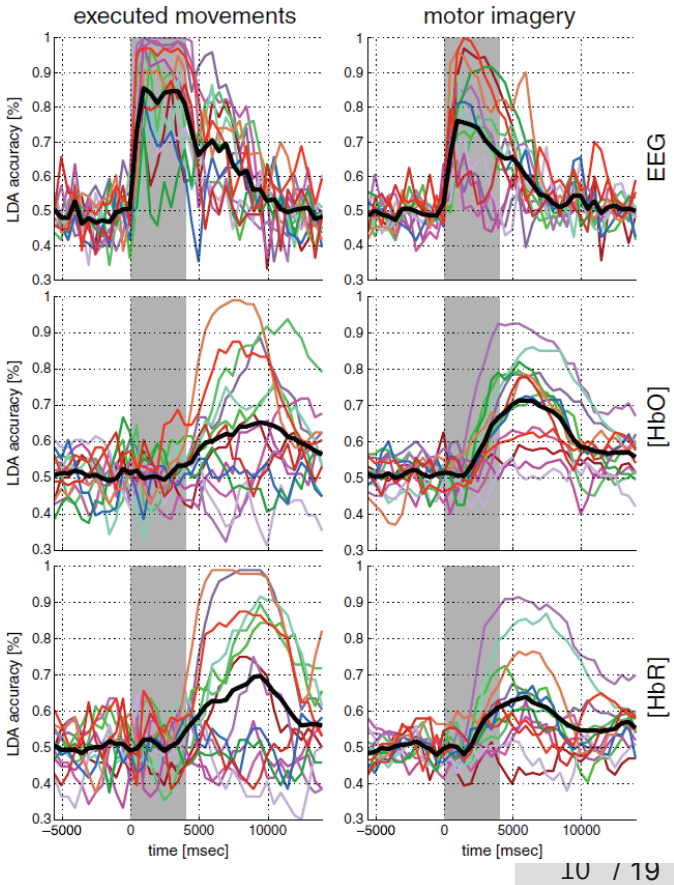

Results

- Topology of significant EEG and NIRS features
  - Motor execution

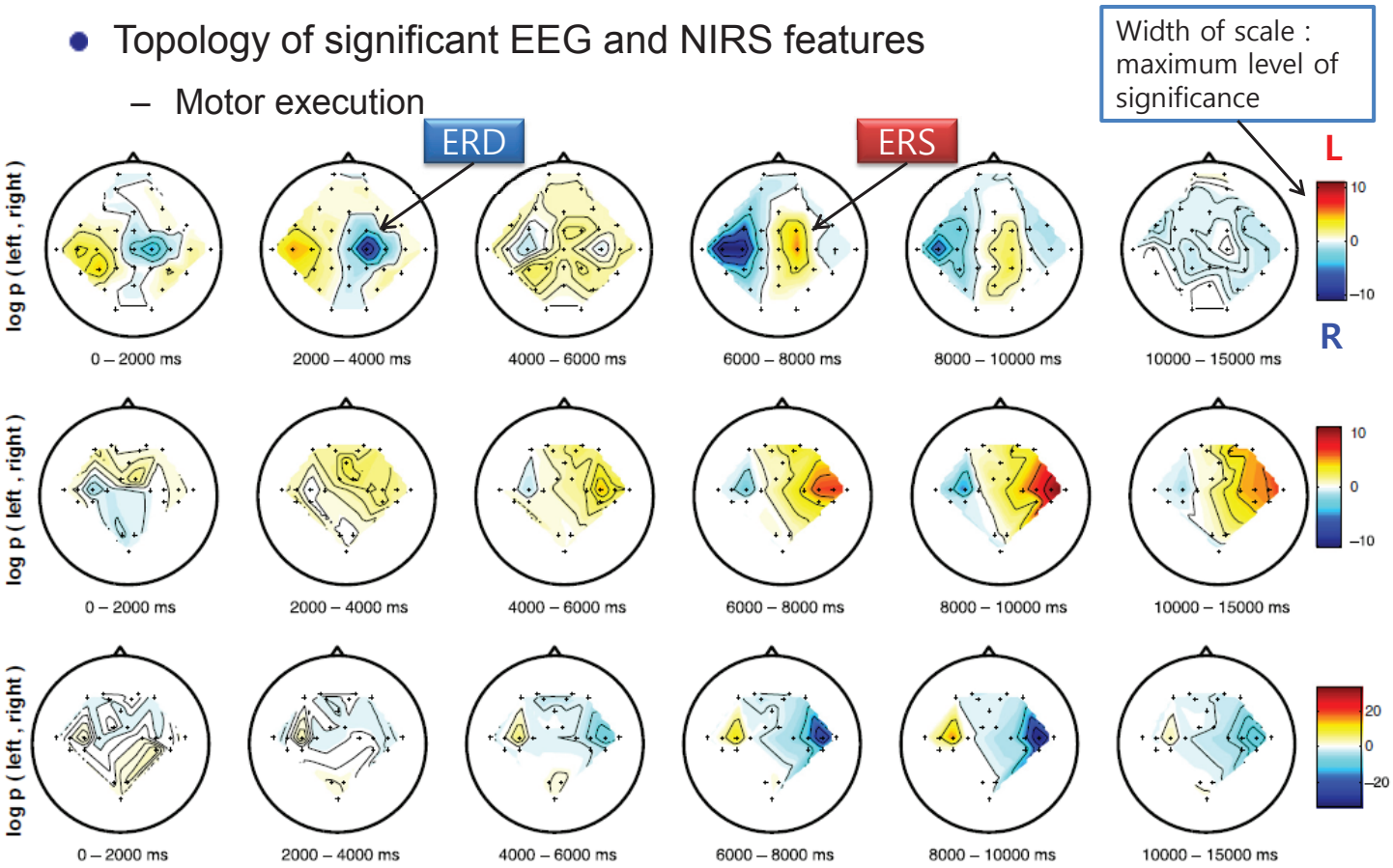

Results

- Topology of significant EEG and NIRS features
  - Motor imageries

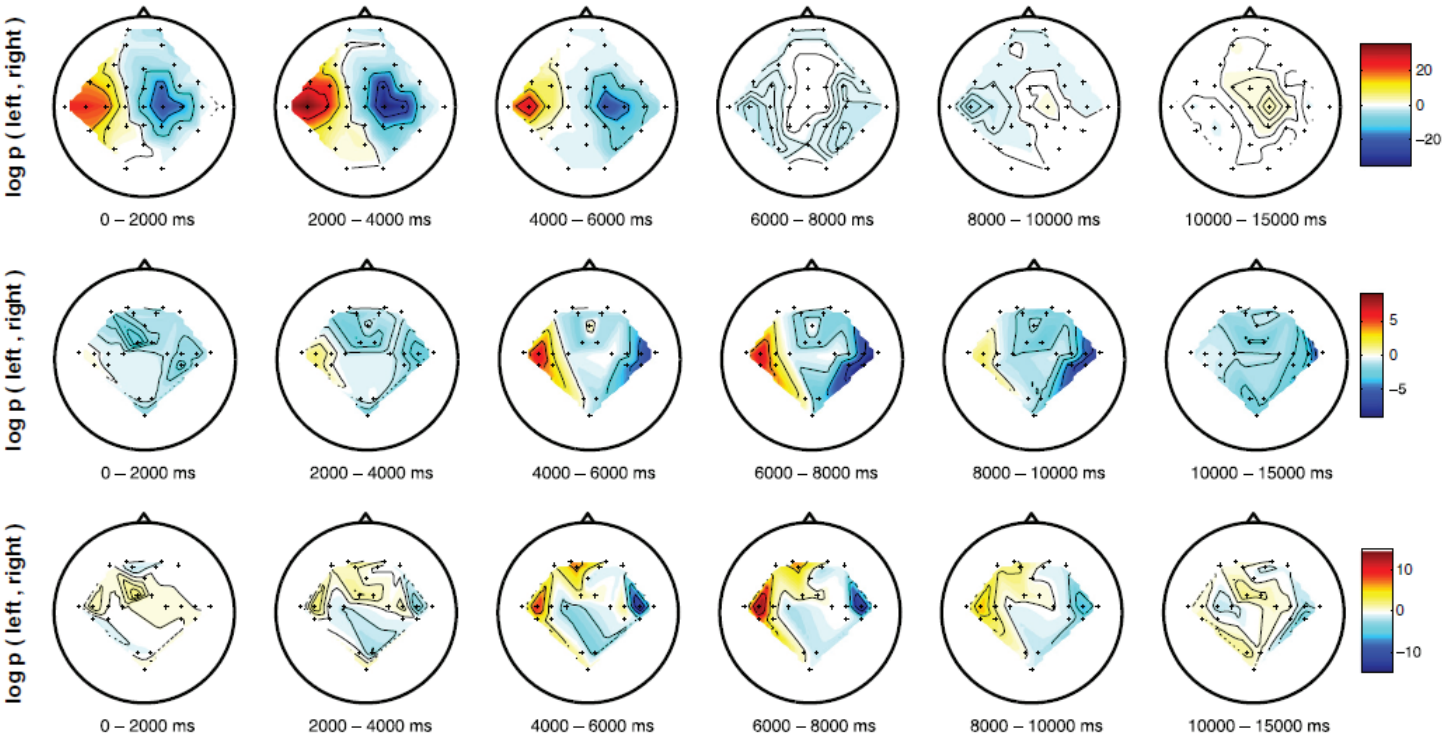

Results

- Topology of significant EEG and NIRS features
  - They found higher significance levels of [HbR] in both paradigms, but [HbO] yielded higher accuracies for motor imagery.
  - They found the inverted polarity of [HbO] for motor imagery.

Results

- Individual LDA classification accuracies for each measurement methods with a meta-classifier
  - A meta classifier was derived for combining the individual signals.
  - Only combinations of measured features for motor imagery score shown (highly) significant improvements.
    - When comparing EEG with combined EEG/[HbO] for motor imagery, there was an average 5% classification accuracy increase across all subjects.

Mean Accuracies	Real	Imagery
EEG	90.8%	78.2%
HbO	71.1%	71.7%
HbR	73.3%	65.0%
EEG+HbO	92.6%	83.2%
EEG+HbR	93.2%	80.6%
EEG+HbO+HbR	87.4%	83.1%

Red latter : Highly significant improvements based on paired t-test

Results

- Scatter plot comparing classification accuracies and significance values of various combination methods
  - Hybrid approaches are effective for motor imagery

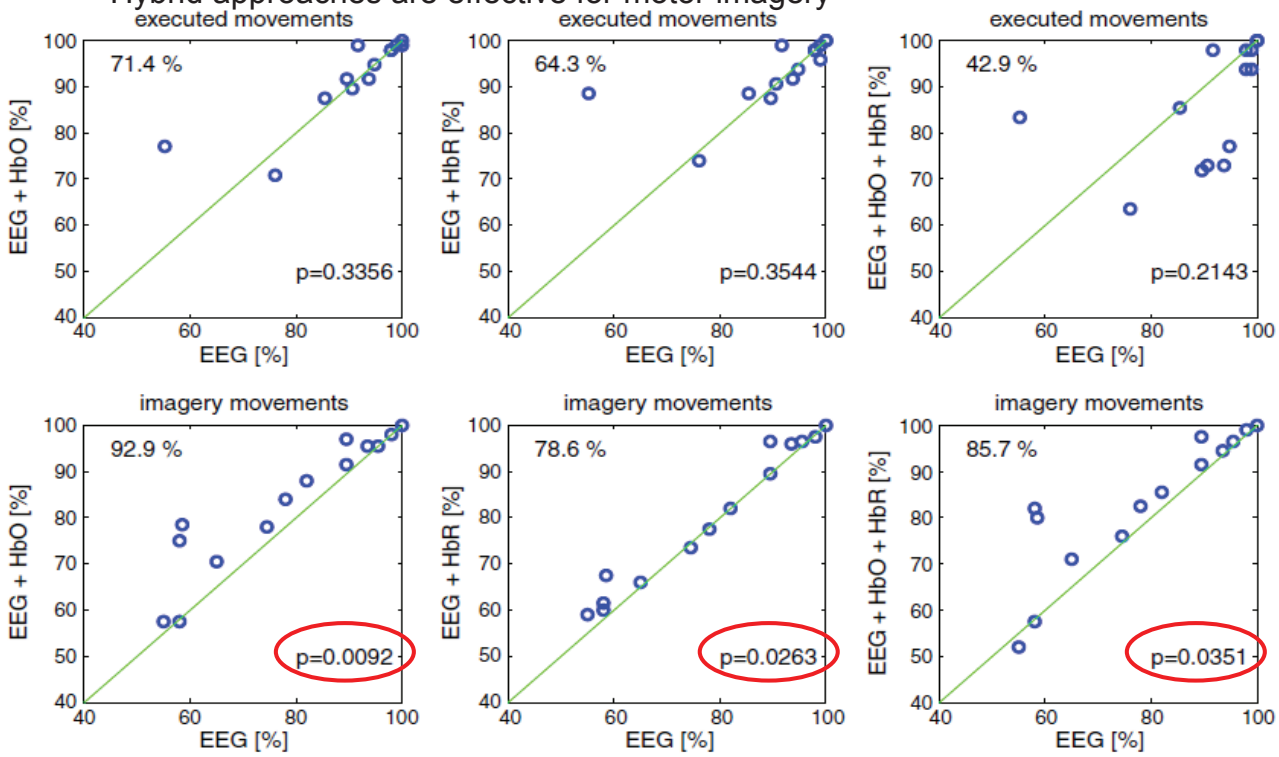

Results

- Mutual information vs. accuracy

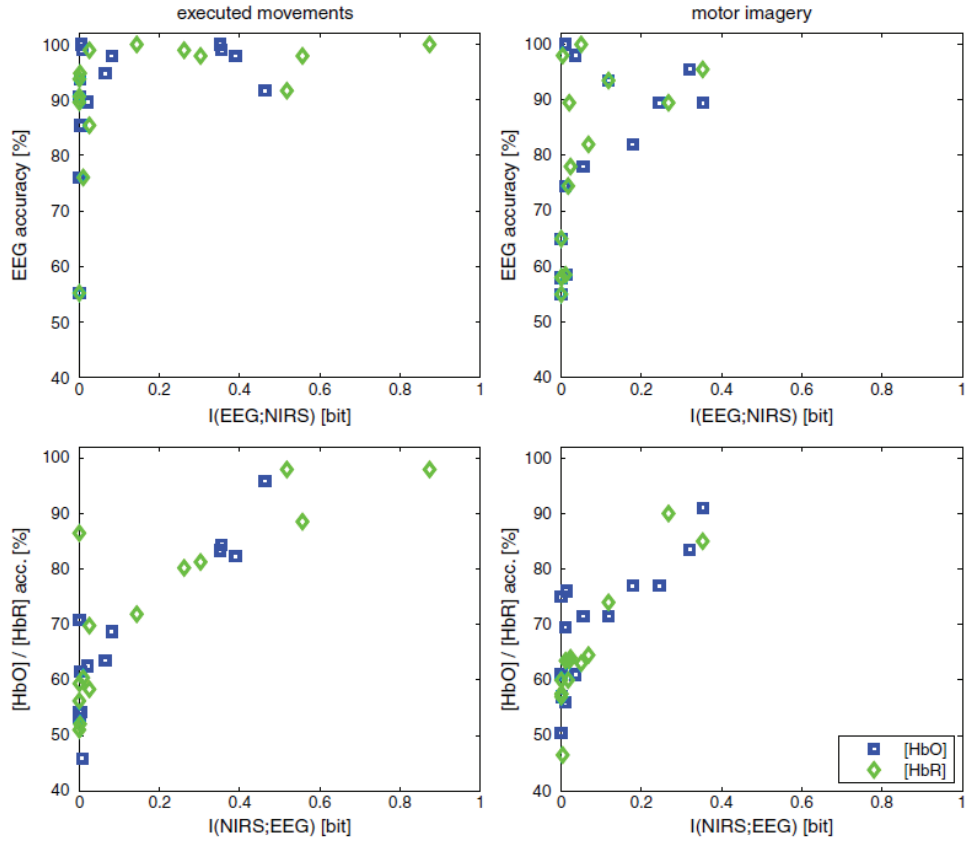

Results

- Mutual information vs. accuracy
  - Relation of the classification performance (y-axes) of the individual measurement methods (EEG, [HbO] and [HbR]) in relation to their mutual information content (I(EEG; [HbO]) and I(EEG; [HbR]) (x-axes).
  - Generally, mutual information is directly proportional to accuracy
    - If for a given subject method X scores a low classification accuracy, one would expect the conditional entropy H(X|Y) to be of similar magnitude as H(X) and therefore the mutual information content is very low.
  - While the classification accuracy of a given method is high, we observe a low mutual information content.
    - the other classification method does not work well
    - their information content is complementary
  - Average mutual information over all subjects

Mutual information	Real	Imagery
I(EEG:HbO)	0.125±0.177bit	0.096±0.127bit
I(EEG:HbR)	0.194±0.277bit	0.067±0.110bit

Conclusion

- In a combination with EEG, they find that NIRS is capable of enhancing event-related desynchronization (ERD)-based BCI performance significantly.
- Behaviors of HbO and HbR
  - Typical behavior of hemoglobin oxygenation during brain activation consists of an increase in [HbO] approximately mirrored by a decrease of [HbR]
  - For motor imagery, only [HbR] clearly showed the typical behavior but [HbO] there seems to be an initial drop followed by a subsequent rise
- Limitation of NIRS based BCI
  - long time delay of the hemodynamic response
  - Advantages
    - For subjects (and patients) which are not able to operate a BCI, solely based on EEG, this combination presents a viable alternative.
    - One could imagine a feedback scenario, where a secondary NIRS-derived classifier is only turned on in particular trials, when the 'primary' EEG-based classification is likely to fail.

Discussion

- Evaluation of hybrid NIRS–EEG brain computer interface
  - Hybrid measurement is helpful in classification of SMR based BCI
  - Classification of NIRS response is not higher than EEG based BCI
  - Long time delay of the hemodynamic response lead to lower information transfer rate
  - There is no benefit with hybrid NIRS-EEG based BCI yet
- Probable research direction
  - Hybrid NIRS-EEG based BCI with real time classification
  - Zero training classifier and adaptive calibration with real time experiment

INFONET Seminar Application Group

Frequency Domain Compressive Sensing for Ultrasound Imaging

Celine Quinsac, Adrian Basarab

Advances in Acoustic and Vibration April 2012

Presenter Pavel Ni

Gwangju Institute of Science and Technology

Introduction

Conventional Ultrasound imaging systems rely on Shannon-Nyquist theorem. Often US devices use a sampling rate that is at least four times the central fr equency.
Consequently large amount of data imply problems in:

- Real-time imaging (especially 3D)
- Data-transfer
- Grows of machinery size

Compressive sensing allows reduce volume of data directly acquiring compre ssed signal. Recently CS framework was adopted to ultrasound imaging [10-1 5] (all paper except one are conference papers), Ultrasound Doppler [16-17] or Photoacoustic [18]

Sampling a signal

Sampling can be summarized by measuring linear combination of an analog signal

$$y_k = \langle \varphi_k, f \rangle, \quad \text{for } k = 1,\ldots,m, \quad (1)$$

Where y_k are the measurements, φ_k are sampling vectors, and m is the number o f measurements. The most common sampling protocol consist of vectors of Dirac's at equal time. The measurements then simple discretization of $f(t)$.

In CS, the number of measurements is m << n. However, when the number of mea surements is smaller then the signal size, then it is ill-posed inverse problem.
If Φ is a matrix of size $m \times n$, concatenating the sampling vectors φ_k, then $y = \Phi f$. T he signal $\hat{f}$ corresponding to the measurements y has infinity many solutions.

CS shows that $\hat{f}$ can be reconstructed if it has sparse representation in a given basi s and that the measurements are incoherent with that basis.

Concept of Sparsity

Sparsity is the idea that signal may have a concise representation in a given basis.

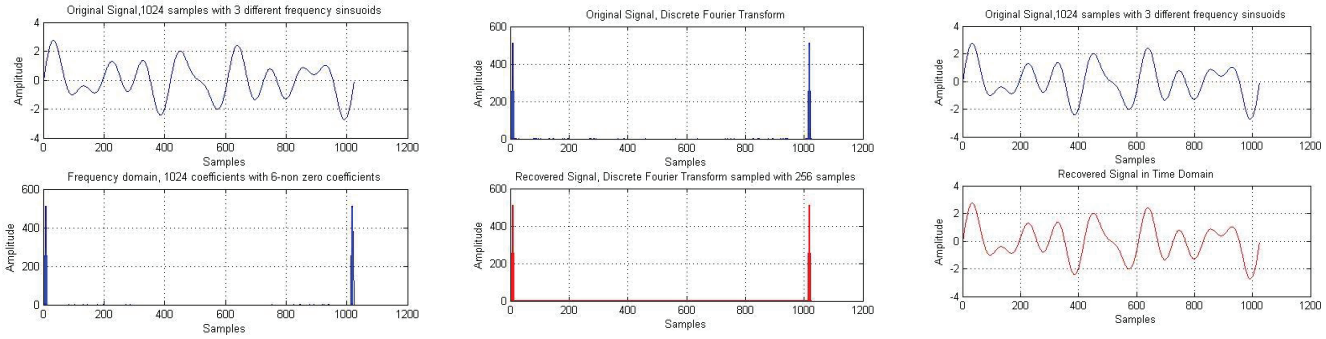

Hence a dense signal in the time domain can be coded with only a few samples. Mathe matically it translates as follows:

$$f(t) = \sum_{i=1}^{n} x_i \psi_i(t) \quad (2)$$

Where $f(t)$ is the original signal, x_i are the coefficients of the signal in sparse basis, and $\psi i(t)$ is an orthonormal basis. The S largest coefficients x_i are noted x_S, and t he corresponding signal $f_S(t)$ If $f(t)$is sparse in the basis Ψ composed of the vect ors ψ_i, then $f = \Psi x$ and the error $\|f - f_S\|_2$ is small.

Concept of Sparsity

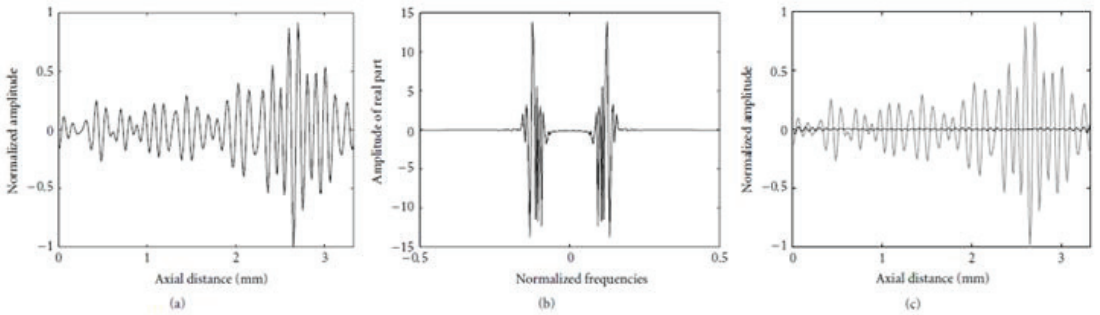

FIGURE 1: (a) A full US RF signal and (b) its sparse representation via Fourier transform. Most of the coefficients are equal or close to zero. (c) Compressed US RF signal (gray), corresponding to 30% of the largest Fourier coefficients, the rest of them being set to zero. The difference between the full and compressed US RF signal (black) is minimal.

- Sparsity therefore leads to compressive nature of signal: if signal has sparse rep resentation, then the information coding that signal can be compressed on a fe w coefficients.
- However directly acquire only significant coefficients without knowing their po sitions is impossible.
- CS overcomes this issue via an incoherent sampling.

Incoherent Sampling

The term Incoherent sampling conveys the idea that the sampling protocol φ_k in (1) has to be as little correlated as possible with sparse representation ψ_i in (2).

$$y_k = \langle \varphi_k, f \rangle, \quad \text{for } k = 1, \ldots, m, \quad (1) \qquad f(t) = \sum_{i=1}^{n} x_i \psi_i(t) \quad (2)$$

The mathematical definition of incoherence is:

$$\mu(\Phi, \Psi) = \sqrt{n} \max_{1 \le k, j \le n} \left| \langle \phi_k, \psi j \rangle \right|, \quad (3)$$

Where Φ is the sampling basis and Ψ is the sparsifying basis. If the two bases are strongly correlated, then μ will be close to $\sqrt{n}$, and if the are not correlated, then it will be close 1.

- CS requires incoherence .
- If the sampling basis completely random , then it will be maximally incoherent with sparsifying fixed basis.

Incoherent Sampling

- (a) A full US RF signal
- (b) its sparse representation FT
- When sampling is incoherent with the sparsifying basis then the meas urements in that basis are dense (c, d)
- When the sampling basis and the s parsifying basis are coherent (e,f), t he measurements in the sparsifying basis are themselves sparse. There i s significant information missing
- Knowing sparsifying basis and incoh erent measurements in cs make it p ossible to reconstruct original signal using optimization.

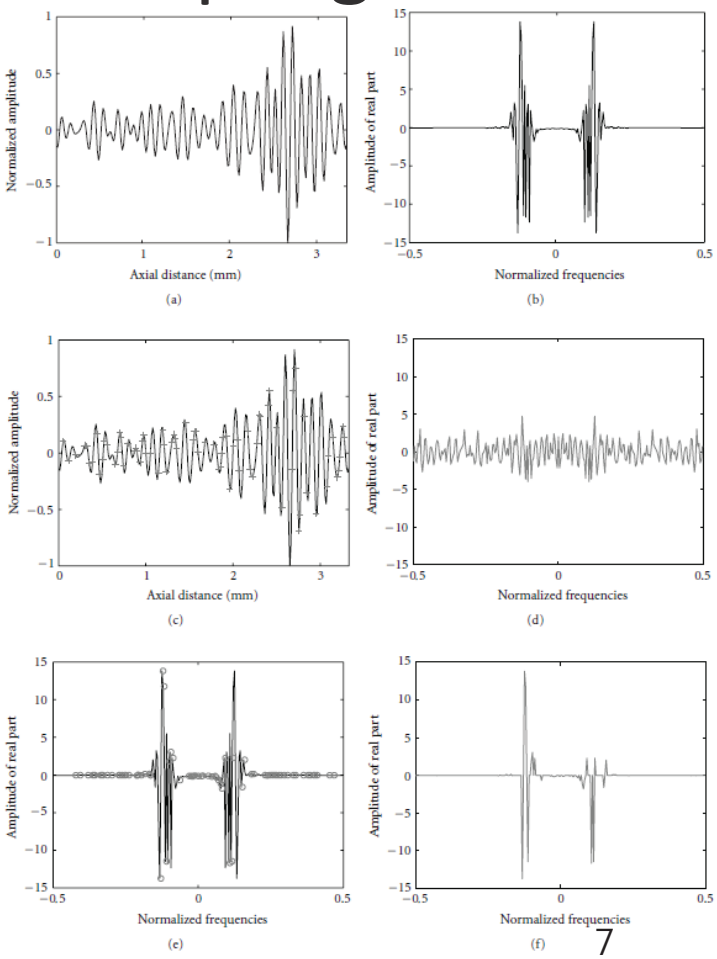

Signal Reconstruction through Optimization

Reconstruction performed via convex optimization:

$$\min \|\hat{x}\|_1 \quad \text{subject to } y=\Phi f = \Phi\Psi\hat{x}, \quad (4)$$

$\hat{x}$ is the reconstructed sparse signal.

The optimization searches amongst all the signals that verify the measurements y , the one with the smallest l1 norm, that is the sparsest.
Optimization removes the interferences caused incoherent under sampling from t he sparse representation of the measurements.

Sampling Protocols in Ultrasound

The data acquisition in US is performed in spatial domain. The sampling basis has to be in coherent with sparsifying basis. There are several sampling protocols adapted and incohe rent with sparsifying basis. Basically they all consist in taking samples at random locations (taking samples at specific times on RF signal or taking some RF lines at specific locations) .

- Eight different protocols are proposed:

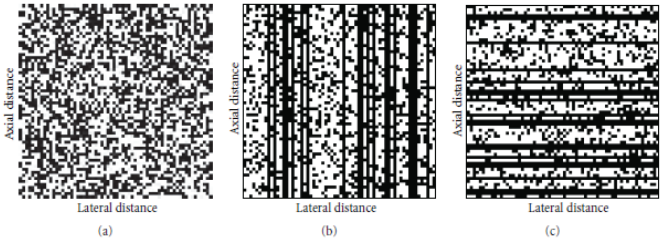

FIGURE 6: Sampling masks Φ_1 (a), Φ_2 (b), and Φ_3 (c) adapted to a spatial sampling of the US images. The white pixels correspond to the samples used for CS. The proportion of samples here is 50% of the original image.

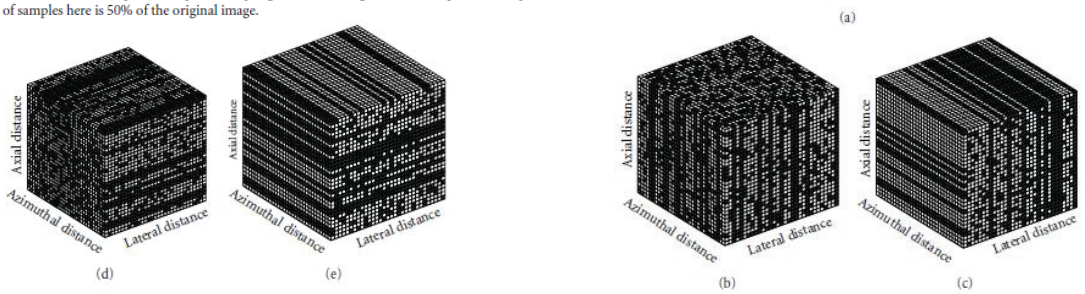

FIGURE 7: Sampling masks Θ_1 (a), Θ_2 (b), Θ_3 (c), Θ_4 (d), and Θ_5 (e) adapted to a spatial sampling of the 3D US volumes. The white pixels correspond to the samples used for CS. The proportion of samples here is 50% of the original volume.

Reconstruction of Ultrasound Images

The acquisition consist in taking samples of the RF signals. This sampling protocol is simila r to a basis of Diracs. Basis incoherent with Diracs and where US images are sparse is need ed. Fourier basis is maximally incoherent with Diracs and because the US image k-space is sufficiently sparce. The function to minimize is

$$\arg\min_{M} \left\| AM - y \right\|_2 + \lambda \left| M \right|_1, \quad (8)$$

where M is the k-space of the US RF image m (M= Fm), and A is the sampling scheme (A = ΦF), y are the RF US image measurements and λ is a coefficient weighting for sparsi ty.

Results on a 2D Simulation Image

The proposed CS method was used to reconstruct the k-space of an RF image simulated using the Field ii simulation program. Map of kidney used with linear transducer. Sampli ng frequency 20 MHz.

The sampling Φ_1, Φ_2, Φ_3 were studied to compare CS recons truction using a fixed optimal set to 0.005 and the reweight ed λ minimization ℓ_1

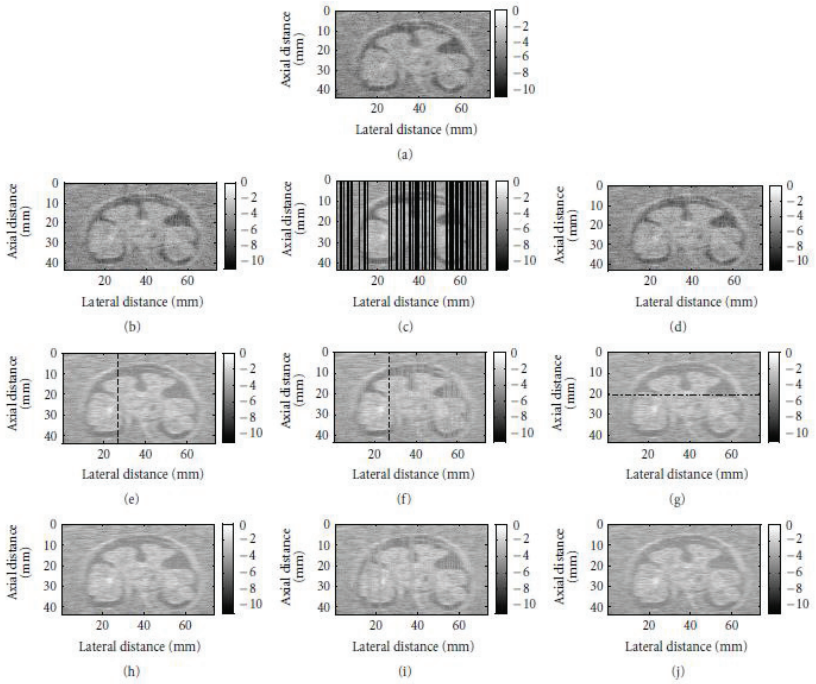

Results on a 2D Simulation Image

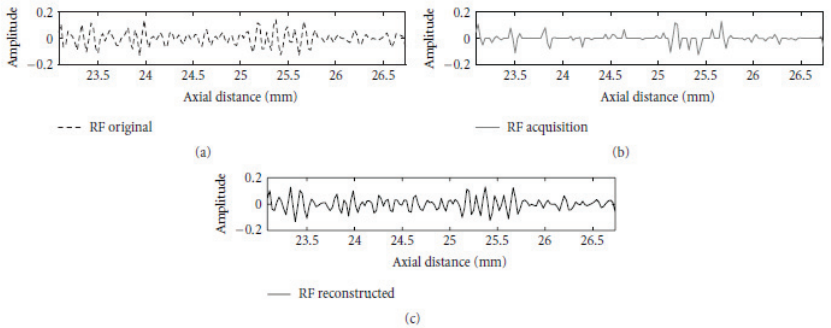

FIGURE 9: An example of a local region of an RF line after CS reconstruction using Φ_1 sampling pattern, corresponding to the dotted line in Figure 8(e).

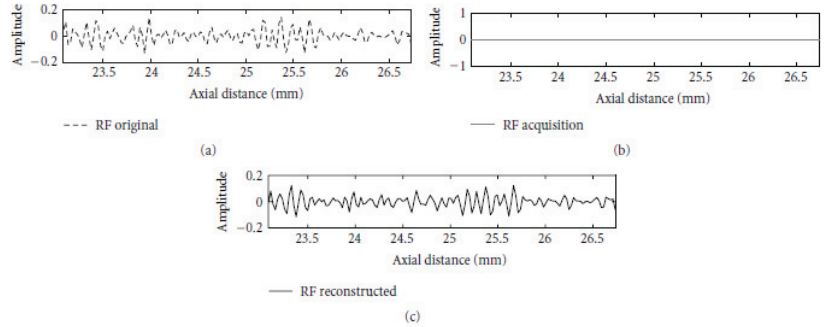

FIGURE 10: An example of a local region of an RF line after CS reconstruction using Φ_2 sampling mask, corresponding to the dotted line in Figure 8(f). This line was not sampled at all.

Results on a 2D Simulation Image

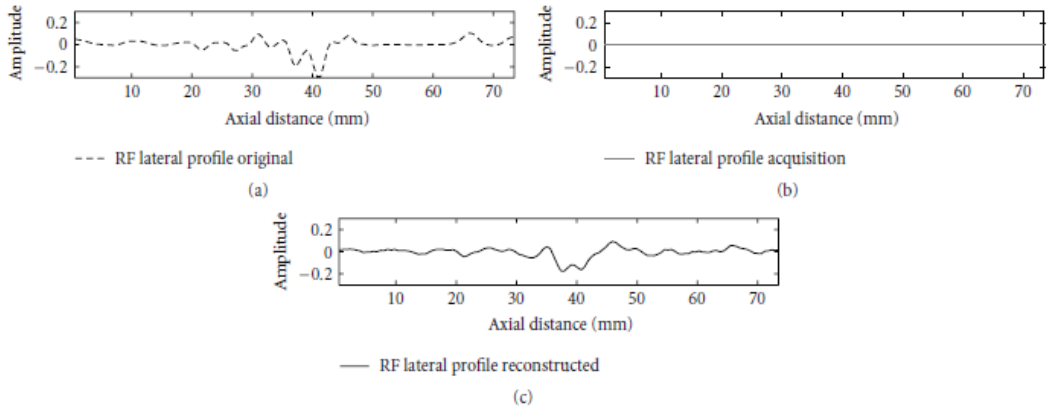

FIGURE 11: An example of a lateral profile of aN RF image after CS reconstruction using Φ_3 sampling mask, corresponding to the dotted line in Figure 8(g). This lateral profile was not sampled at all.

TABLE 1: NRMSE between the CS-reconstructed RF US image and the original simulated image of a kidney for different sampling ratios and patterns.

		Φ_1	Φ_2	Φ_3
Classic ℓ_1 minimization ($\lambda = 0.005$)	25%	0.48	0.58	0.6
	33%	0.33	0.45	0.49
	50%	0.15	0.28	0.29
Reweighted ℓ_1 minimization	25%	0.51	0.56	0.64
	33%	0.36	0.47	0.49
	50%	0.17	0.24	0.3

Discussion and Conclusion

Sampling using high sampling rate is neither easy nor cost-effective in high frequency a pplications.
It was showed potential of CS to reduce data volume and wrap acquisition at the price of a reconstruction using the ℓ_1 norm.

Future work

- Better sparsity basis
- Investigation of several optimization routines
- The aim is to reach fastest and most reliable reconstruction from as little amount of data as possible.

Thank you

Brain Computer Interface-Based Smart Living Environmental Auto-Adjustment Control System in UPnP Home Networking

Chin-Teng Lin, Bor-Shyh Lin, Fu-Chang Lin, Che-Jui Chang

IEEE SYSTEMS JOURNAL. (2012.04)

Presenter : Soogil Woo

GIST, Dept. of Information and Communication, INFONET Lab.

Gwangju Institute of Science and Technology

Background

- Wired BCI system

- Wireless BCI system

Introduction

- Recently many studies are trying to develop commercial products to bring the convenience to people in their usual life.
- Some environmental control systems in a smart house employed radio frequency identification (RFID), external sensor modules, and voice recognition as the controlled signals.
- By combining with universal plug and play (UPnP) home networks, users could send out service requests from their personal digital assistant, mobile phones, a wearable appliance, or external sensors to home server, graphic user interface, or motion.
- With the development of BCI, it is an new option to apply the physiological signals as the stimulus of environmental control system in a smart house.
- However, Most of the existing BCI-based environmental control systems require the user's active mental command to control external device.

Introduction

- These systems lack the capability to control devices automatically and adaptively according to the user's current cognitive state.
- Most of current BCI-based environmental control system are inconvenient because bulky and expensive EEG machines and computer are both required for signals acquisition and backend analysis, which will limit the flexibility and portability of these systems.
- The goal of this paper is to propose a cost-effective, simply extendable and easy to use BCI-based smart living environmental auto-adjustment control system (BSLEACS) to control electric home appliances based on the change of user's cognitive state (drowsiness or alertness).
- Their proposed wireless physiological signal acquisition module and embedded signal processing module contain the advantages of small volume and low power consumption, and are more suitable for practical application.

System Architecture

- (1) is designed to acquire and transmit an EEG signal to the embedded signal processing module via Bluetooth.
- (2) is designed to estimate the user's cognitive state from his or her EEG, and provides the estimated cognitive state to the host system.
- (3) is designed for data storage /display, and is also served as an UPnP control point to manage the request from UPnP control device.

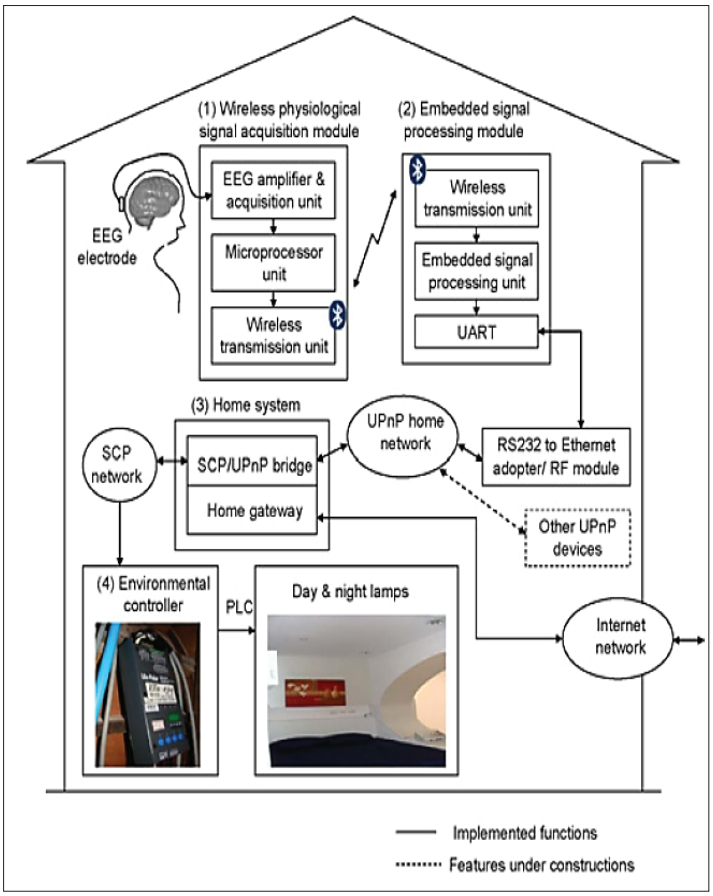

System Architecture

A) Wireless Physiological Signal Acquisition Module

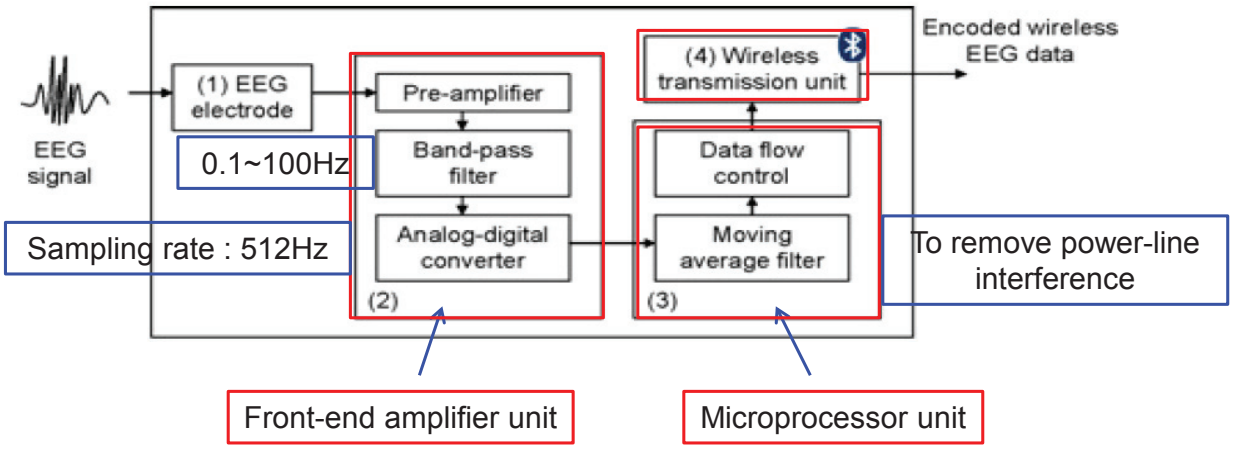

- EEG data digitized by ADC will be stored into memory.
- This module operates at 31 mA with 3.7V DC power supply, and continuously operate over 33 h with a commercial 1100mAh Li-ion batter.
- The volume is about 4 cm * 2.5 cm * 0.6 cm.

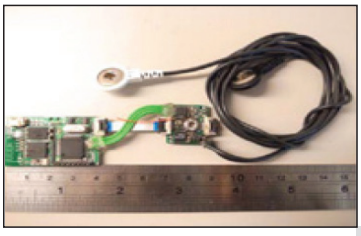

System Architecture

B) Embedded Signal Processing Module

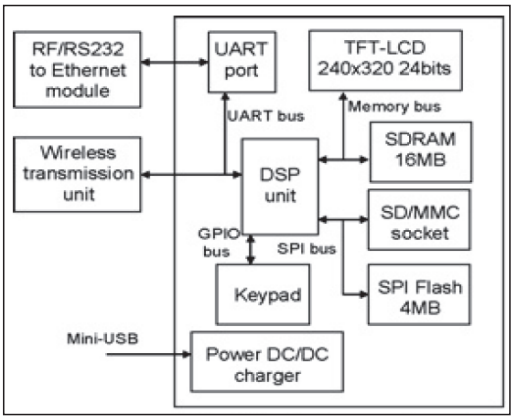

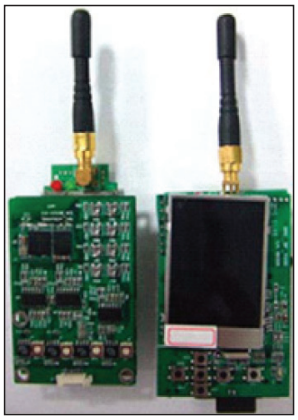

3.7V DC power

Over 45 h

6.4cm*4.4cm*1cm

- This module contains a powerful computation capability and can support various peripheral interface.
- This module is developed to perform the real-time cognitive state detection algorithm.
- This module is also evaluated as the UPnP control device to send out the estimated cognitive state and EEG signal to host system to drive environmental controller via UPnP home networking.

System Architecture

B) Embedded Signal Processing Module

- The received EEG data will be real-time processed, analyzed and displayed by the embedded signal processing module.
- When the change of cognitive state of the user is detected, the corresponding command will be transmitted either by RF module or by Ethernet through UPnP.

C) Host System and Environmental Controller

- The host system is an UPnP/SCP bridge and is also served as the home gateway to internet network.
- A SCP-based environmental controller with four-channel AC/DC power line control output is used to control home equipment.
- The SCP-based environmental controller is used to control the day and night lamps in the showroom.

Methods

A) Real-Time Cognitive state Detection

- When alert person is becoming drowsy, his or her EEG power in both theta and alpha rhythms will increase.
- If the subject remains alert, his or her EEG spectra in theta and alpha rhythms should match the alert model. Otherwise, his or her EEG spectra will diverge from the alert model if the subject is under drowsy state.
- They observe that the alpha and theta rhythm of EEG spectra in the occipital midline (the location Oz in the international 10-20 EEG system) can provide discriminating power and they have high correlation with cognitive state.
- A single EEG channel is used in their system to monitor EEG signal in the occipital midline.

Methods

A) Real-Time Cognitive state Detection

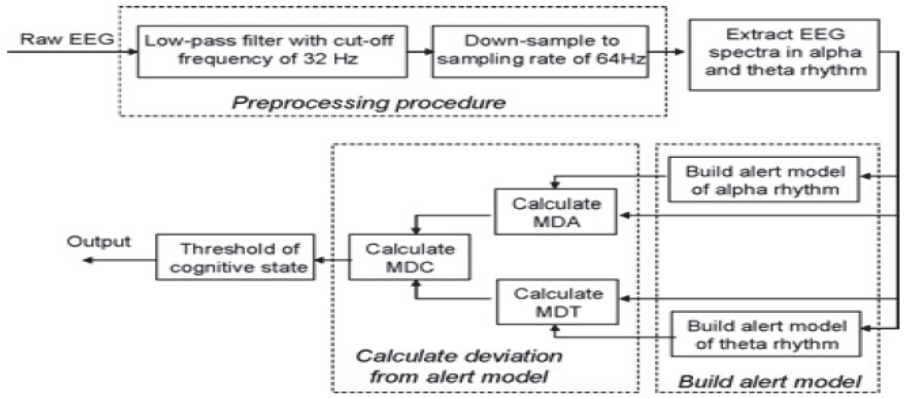

- A 512-point FFT with 448-point overlap is used to obtain the EEG spectra, and then the EEG spectra in alpha and theta rhythms are extracted to build up the alert model.
- A new alert model will be constructed separately.
- The distribution of power spectrum in the alert state can be modeled by a multivariate normal distribution $N(\mu, \Sigma^2)$. μ : mean vector

Σ^2: variance-covariance

Methods

A) Real-Time Cognitive state Detection

- (μ_A, Σ_A^2): alpha rhythms, (μ_T, Σ_T^2): theta rhythms.
- After building the alert mode, the Mahalanobis distance from the alert mode of the alert mode of alpha rhythm (MDA) and that of theta rhythm (MDT) will be calculated.
- Mahalanobis distance is a distance measure based on correlations between variables by which different patterns can be identified and analyzed. It takes into account the correlations of the data set and is scale-invariant.

$$MDA(x_A) = \sqrt{(x_A - \mu_A)^T (\Sigma_A^2)^{-1} (x_A - \mu_A)} \quad , MDT(x_T) = \sqrt{(x_T - \mu_T)^T (\Sigma_T^2)^{-1} (x_T - \mu_T)}$$

$$MDC = \alpha \times MDA + (1-\alpha) \times MDA, 0 \le \alpha \le 1$$

- They use the linear combination MDC of MDT and MDA to estimate the user's cognitive state.
- If the value of MDC is larger than the threshold, the subject can be treated as his or her cognitive state trends to drowsy state; otherwise, it trends to alert state.

Methods

B) Performance Evaluation

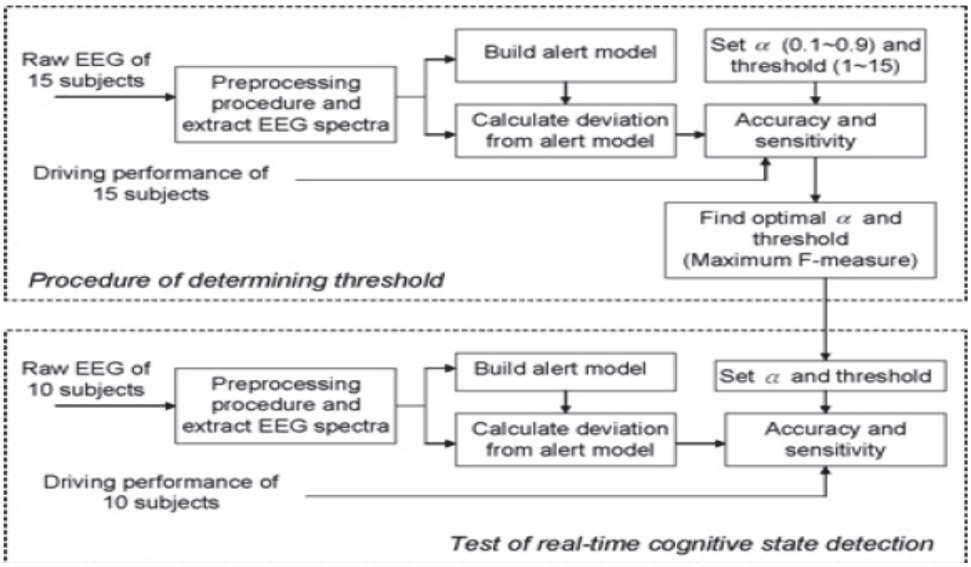

- F-measure, the harmonic mean of precision [positive predictive value (PPV)] and recall (sensitivity), is used to find out the threshold of Mahalanobis distance to decide the cognitive state.

$$F = 2 \times \frac{precision \times recall}{precision + recall}$$

Results

A) Performance of BSLEACS for cognitive state Detection

Subject	F-measure (%)	PPV (%)	Sensitivity (%)
1	77.7	75.5	80
2	72.2	78.8	66.7
3	89.1	80.4	100
4	87.5	77.8	100
5	87.4	77.6	100
6	88.9	80	100
7	83.5	78.7	88.9
8	81.1	77.9	84.6
9	66.1	65.5	66.7
10	86.8	76.6	100
Average	82	76.9	88.7

- A total of 1370-trial response time and Mahalanobis distances from 15 subject were analyzed to determine the maximum F-measure value. $(\alpha = 0.1-0.9, threshod = 1-15)$
- The maximum value 77.6% of F-measure (PPV=69.2% & sensitivity = 88.3%) was determined with $(\alpha = 0.9, threshod = 7.5)$
- 1000-trial response times and Mahalanobis distances from ten subjects for testing session were used to test the performance of this system.

Results

B) Performance of BSLEACS for controlling Home Application

- BSLEACS is used to control day and night lamps.
- Criterion 1) when the trend of cognitive state is alert, the major day lamp is on and the night lamp is off.
- Criterion 2) when the trend of cognitive state is drowsy, the major day lamp is off and the night lamp is on.
- A total of 75-trial system responses and questionnaire results from 15 subjects were cross referenced and analyzed.
- The F-measure of system control performance is 75.27% (PPV = 70% & sensitivity = 81.4%).<effectively control home appliance>

		System Control Output	
		Control Criterion 1	Control Criterion 2
Cognitive state (questionnaire)	Drowsy	8 (FN)	35 (TP)
	Alert	17 (TN)	15 (FP)

Conclusion

- In this paper, they proposed a BCI-based smart living environmental auto-adjustment control system (BSLEACS).
- BSLEACS only needs single EEG channel to recognize cognitive state by monitoring EEG signal in the location of Oz.
- BSLEACS has been verified in a practical environment and shows that the light/lamp can be adjusted in real time based on the change of the user's cognitive state.
- BSLEACS provides a system prototype for environmental control, and can be generalized for other applications and constructed in an UPnP-based smart house.

Thank you!

Diffuse optical imaging of brain activation: approaches of optimizing image sensitivity, resolution and accuracy
David A. Boas *et al.*

NeuroImage (2004)

Presenter : Evgenii Kim

GIST, Dept. of Information and Communication

Gwangju Institute of Science and Technology

Outline

- Introduction
- Diffuse optical imaging forward and inverse problem basics
- Optimum wavelengths and cross-talk in estimating hemoglobin concentrations
- Systemic physiological signal interference
- Improving image resolution with overlapping measurements
- MRI structural and functional spatial priors for improving quantitative accuracy of DOI
- Conclusion

Introduction

- Near – infrared spectroscopy (NIRS) and diffuse optical imaging (DOI) are techniques applied to study neural activity in the brain.
- Infrared light is composed of a broad range of electromagnetic waves from 770 nm to 1 mm.

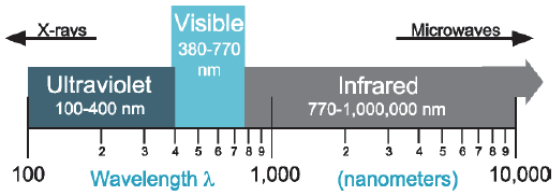

http://www. en.wikipedia.org/

Introduction

- Optical Window

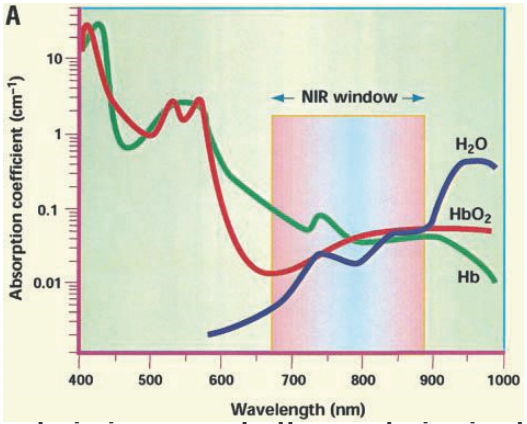

Hemoglobin is the iron-containing metalloprotein in the red blood cells.

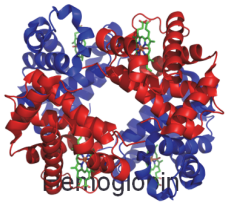

http://www. en.wikipedia.org/

Introduction

- Using NIRS we can get:
  - concentrations of oxyhemoglobin (HbO_2)
  - concentrations of deoxyhemoglobin (HbR)
  - regional blood volume
  - blood flow
  - metabolic rate of oxygen consumption
- This ability is potentially important for a brain studies particularly

Introduction

- Limitation:
  - Estimation of HbO_2 and HbR concentrations is sensitive to random measurement and systematic errors appeared from incorrect model parameters.
  - The sensitivity to brain activation is able to decrease due to contamination from several systemic physiological signals

Diffuse optical imaging forward and inverse problem basics

- Diffusion Equation

$$\nabla \cdot D(r)\nabla\Phi(r,t) - v\mu_a(r)\Phi(r,t) + vS(r,t) = \frac{\partial\Phi(r,t)}{\partial t}$$

where $\Phi(r,t)$ photon fluence rate

$$\Phi(r,t) = vU(r,t)$$

D(r) photon diffusion coefficient

$$D = v/3(A = \mu'_s + \mu_a);\ \mu'_s = (1-g)\mu_s$$

S(r,t) isotropic source

Monte Carlo Simulation

For REF

- Monte Carlo methods are a class of computational algorithms that rely on repeated random sampling to compute their results.
- The path of each photon packet is determined by the sampling of random numbers and a set of functions or probability distributions describing the likeliness of for example the step length and scattering angles.
- This way of stochastic simulation relies on the simulation of a large number of photon packets and the solutions provided are more or less noisy depending on the number of photons simulated.

Solutions of the Diffusion Equation for Comparison with Monte Carlo

For REF

$$\Phi(r_s, r_d, t) = \frac{vS}{4\pi D}\left[\exp\left(-\frac{|r_s - r_d|^2}{(4Dt)}\right) - \exp\left(-\frac{|r_{s,i} - r_d|^2}{(4Dt)}\right)\right]\exp(-v\mu_a t)$$

where r_d the detector position at time t, generated by a point source of amplitude S at position r_s. The position of the image source is indicated by $r_{s,i}$.

The modified Beer-Lamber law

- $\Delta OD_i(t,\lambda) = -\log\left(\frac{\Phi(t,\lambda)}{\Phi_0(\lambda)}\right) = \sum_{j=1}^{N_{vox}} \Delta\mu_{a,j}(t,\lambda) L_{i,j}(\lambda)$

where OD is the attenuation measured in optical densities; Φ_0 is average detected photon fluence; $L_{i,j}$ is the effective pathlength of detected photons for *i*th measurement in the *j*th voxel.

$$\mu_a(\lambda) = \varepsilon_{HbO_2}(\lambda)[HbO_2] + \varepsilon_{HbR}(\lambda)[HbR]$$

$$\begin{pmatrix}\Delta[HbR]\\ \Delta[HbO_2]\end{pmatrix} = \frac{1}{L}\begin{pmatrix}\varepsilon_{HbR}^{\lambda_1} & \varepsilon_{HbO_2}^{\lambda_1}\\ \varepsilon_{HbR}^{\lambda_2} & \varepsilon_{HbO_2}^{\lambda_2}\\ \hdashline \varepsilon_{HbR}^{\lambda_n} & \varepsilon_{HbO_2}^{\lambda_n}\end{pmatrix}^{-1}\begin{pmatrix}\Delta OD^{\lambda_1}\\ \Delta OD^{\lambda_2}\\ \hdashline \Delta OD^{\lambda_n}\end{pmatrix}$$

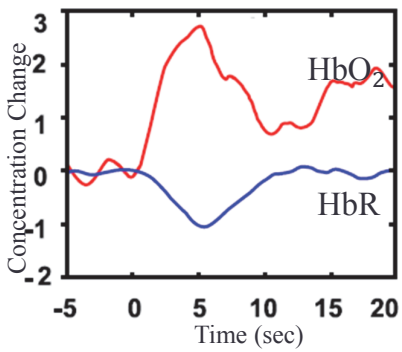

Optimum wavelengths and cross-talk in estimating hemoglobin concentrations

- Most published optical results show us that two wavelengths can provide sufficient accuracy.
- Judicial choice of measurement wavelengths is required, because it can partially reduce random measurement, systematic errors (690 or 750 with 830 nm) and cross-talk in the estimate of the HbO_2 and HbR concentrations (780 and 830 nm).
- It is important to choose a wavelength above and below the hemoglobin isobestic point at 805 nm.

Systemic physiological signal interface

- The system has numerous sources of systemic signal interference that reduce its sensitivity to weaker brain activation signals.
- To improve the optical sensitivity to brain activation it is required to use special signal processing methods that distinguish the different source signals in space and time. Some research used a principle component analysis (PCA)

Principle component analysis

For REF

- PCA is a way of identifying patterns in data, and expressing the data in such a way as to highlight their similarities and differences.
- The main advantage of PCA is that once you have found these patterns in the data, you can compress the data, by reducing the number of dimensions.

Lindsay I Smith, 2002

Using PCA

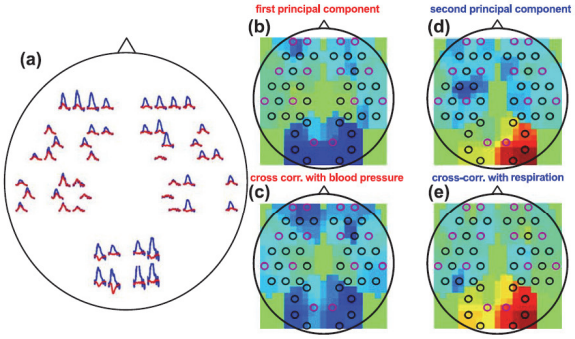

Fig. 3. (a) Spatial-temporal map of brain activation in response to 10 blocks of right hand finger tapping. The blue curves are the ΔOD changes at 830 nm block averaged after a temporal band-pass filter between 0.02 and 0.8 Hz; the red curves are the ΔOD changes obtained after PCA analysis. The x-axis is 35 s long, with the stimulation period lasting for 10 s, followed by 20 s of baseline. The y-axis is from -7% to 7% changes in ΔOD. (b) and (d) Maps of the first and second principal component of the optical data at 830 nm obtained during 300 s of baseline. (c) and (e) Cross-correlation maps of the optical data with the blood pressure (c) and respiration (e) during baseline. The optical data was cross-correlated with blood pressure and respiration with a 2-s lag.

MRI structural and functional spatial priors for improving quantitative accuracy of diffuse optical imaging

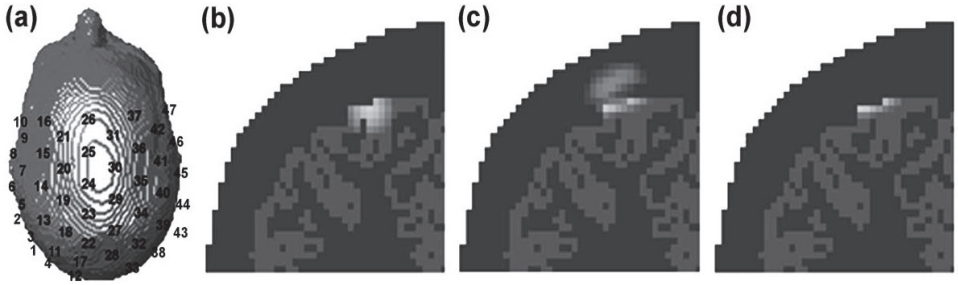

Fig. 5. Comparison of image reconstruction with and without a cortical constraint. (a) Probe geometry on a 3D segmented head. (b) True location of the simulated absorption change. (c) Image reconstructed using DOT and overlapping measurements. (d) Image reconstructed with a cortical constraint.

Temporal correlation of *f*MRI and DOI

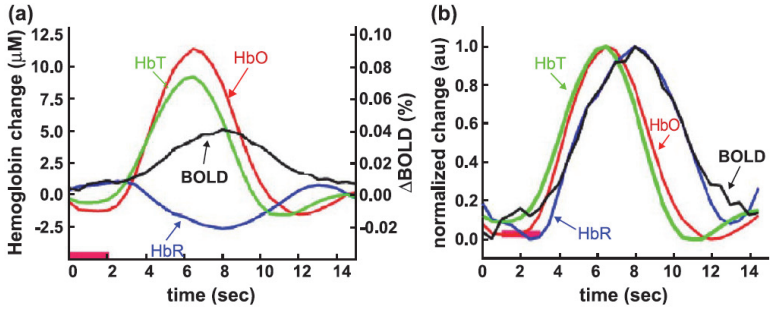

Fig. 6. (a) Response functions of hemoglobin concentrations and BOLD for event-related finger tapping as measured through simultaneously acquired fMRI–BOLD and DOI optical recordings of the primary motor cortex. (b) Normalized and rescaled response functions for the event-related finger tapping to allow visualization of the four variables on the same linear scale. The deoxyhemoglobin data have also been inverted to emphasize the strong correlation between deoxyhemoglobin and BOLD.

Spatial correction of *f*MRI and DOI

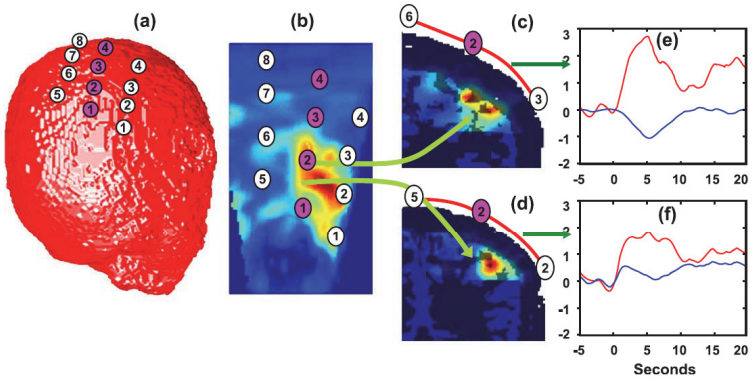

Fig. 7. (a) Coregistration of the position of optical sources (pink) and detectors (white) on the structural MRI of the subject. (b) Maximum intensity radial projection of the fMRI *t* statistic image on to the scalp. The source and detector positions are overlaid to reveal the spatial correlation of the optical signals and the BOLD signal. (c) and (d) Coronal slices through the maximum fMRI response (d) and 1 cm posterior (c). (e) and (f) Hemoglobin concentration time traces measured with source 2 and detectors 3 and 2, respectively, in relative units. Red oxyhemoglobin, blue deoxyhemoglobin. The stimulus starts at $t = 0$ s and lasts 2 s.

Conclusion

- NIRS gives us enough function information about tissue, to be widely used in the study of human brain.
- In addition, the extension of NIRS to DOI will improve the sensitivity, resolution and accuracy of the optical estimates of the hemodynamic response to brain activation

References

- Boas D.A., Dale M., Franceschili M. A., 2004. Diffuse optical imaging of brain activation: approaches of optimizing image sensitivity, resolution and accuracy. NeuroImage 23(2004), 275-288
- Boas, D.A., Culver, J., Stott, J., Dunn, A.K., 2002. Three dimensional Monte Carlo code for photon migration through complex heterogeneous media including the adult head. Opt. Express 10, 159– 170.
- Smith L. I., 2002, A tutorial on Principal Components Analysis.

Title: Direct recording of holograms by a CCD target and numerical reconstruction

U.Schnars and W.Juptner

Presenter: Nitin Rawat
Date: 4/9/2013

Here they introduced a method that uses a charge-coupled device detector (CCD) as a holographic recording medium. However, using CCD's for recording holograms is advantageous and no chemical or physical developing is necessary. Reconstruction can be performed by digital image processing.

In this Note, the mathematical reconstruction is done directly with the digitally sampled Fresnel hologram form the CCD.

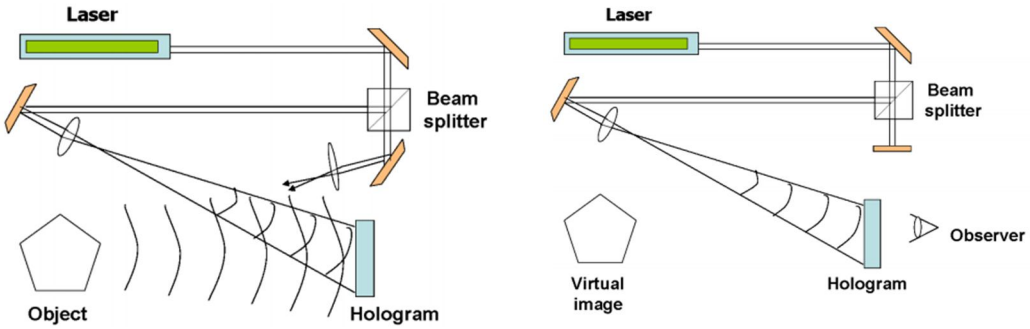

The holographic process is described mathematically as follows:

$$O(x,y) = o(x,y)\,\mathrm{e}^{i\varphi_o(x,y)} \quad \text{... (1.1)}$$

Is the complex amplitude of the object wave with real amplitude o and phase φ_o and

$$R(x,y) = r(x,y)\,\mathrm{e}^{i\varphi_R(x,y)} \quad \text{... (1.2)}$$

Is the complex amplitude of the reference wave with real amplitude r and phase φ_R

$$I_H(x,y) = \left|O(x,y) + R(x,y)\right|^2$$

$$= (O(x,y) + R(x,y))(O(x,y) + R(x,y))^*$$

$$= R(x,y)R^*(x,y) + O(x,y)O^*(x,y)$$

$$+ O(x,y)R^*(x,y) + R(x,y)O^*(x,y) \quad \text{... (1.3)}$$

$$I_H(x,y) = \left|R\right|^2 + \left|O\right|^2 + R^*O + RO^* \quad \text{... (1.4)}$$

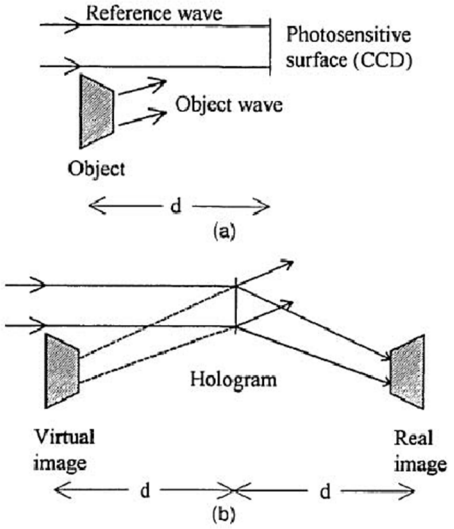

Fig. 1. Off-axis holography with a plane reference wave: (a) recording, (b) reconstruction.

Fig.1 (a) shows the recording geometry. A plane reference wave and the diffusely reflected object wave are interfering at the surface of a photosensitive medium.

In optical holography the object wave can be reconstructed by illumination of the processed hologram with a plane wave, similar to that used in the process of recording.

Looking through the hologram, one notice a virtual image of the object at the position of the original object $[Fig.1(b)]$ .If a screen is placed at a distance *d* behind the hologram, a real image is formed.

Mathematically the amplitude and phase distribution in the plane of the real image can be found by the Fresnel-Kirchhoff integral.

Fresnel integral of the digitized hologram intensity $I_H(k,l)$:-

$$\Psi(m,n) = A\exp\left[\frac{i\pi}{\lambda d}\left(m^2\Delta\xi^2 + n^2\Delta\eta^2\right)\right] \times FFT\left\{R_D(k,l)I_H(k,l)\times\exp\left[\frac{i\pi}{\lambda d}\left(k^2\Delta x^2 + l^2\Delta y^2\right)\right]\right\}_{m,n}$$

Where k, l, m, n $(-N/2 \le k,l \le N/2)$ are integers; FFT is the fast Fourier transform operator; d is the distance between the hologram and the observation plane; and $A = \exp(i2\pi d/\lambda)/(i\lambda d)$ is a constant.

$\Delta x = \Delta y = L/N$ define the sampling intervals in the observation plane ($\Delta\xi$ and $\Delta\eta$) are related to the size of the CCD (L) and to the distance d by the following relation:

$$\Delta\xi = \Delta\eta = \lambda d/L$$

The reconstructed wave front is an array of complex numbers. An amplitude-contrast image and a phase-contrast image can be obtained by calculation of the intensity

$\left[\mathrm{Re}(\psi)^2 + \mathrm{Im}(\psi)^2\right]$ and the argument $\left\{a\tan\left[\mathrm{Re}(\psi)/\mathrm{Im}(\psi)\right]\right\}$ of $\psi(m,n)$, respectively.

$\Psi(m,n)$ is a matrix of N x N points that describes the amplitude and phase distribution of the real image.

$\Delta\xi$ and $\Delta\eta$ are the pixel sizes in the reconstructed image. If only the intensity distribution according to Eq.3 is of interest, the phase factor before the summation can be neglected.

In the experimental investigations a CCD array is placed at the position of the photosensitive surface (Fig.1).

The CCD array consists of 1024 x 1024 pixels. The pixel area(L) is $6.8\mu m \times 6.8\mu m$.

For computation the hologram is stored in a digital image processing system. The object in this experiment was a cube with a side of length of 11 mm, which was placed at a distance of 1 m from the target.

A helium-neon laser was used as a light source.

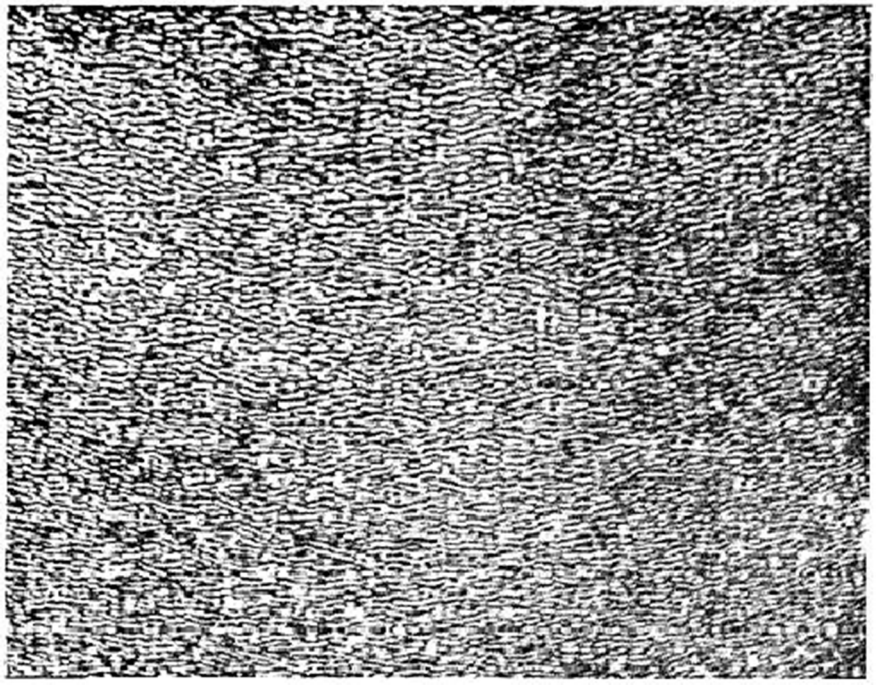

Fig. 2. Digitally sampled off-axis hologram.

Fig. 2 shows a part of a digitally sampled hologram. The original dimensions of the whole hologram were 7mm x 7mm, which are the dimensions of the CCD chip.

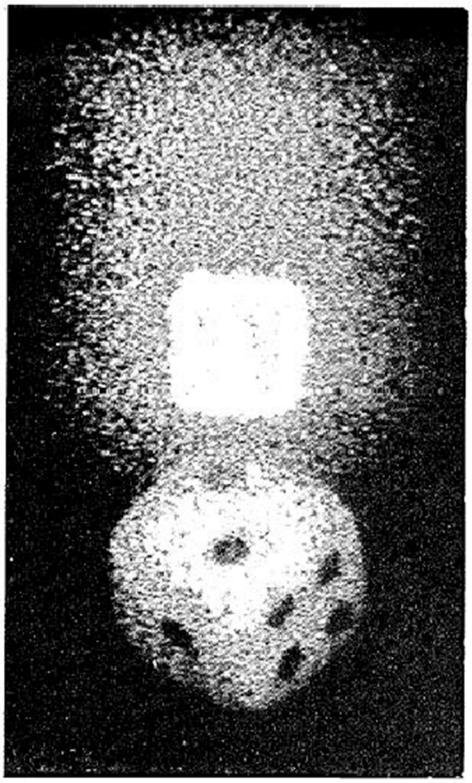

Fig. 3. Numerical reconstruction.

The numerical reconstruction according to $\Psi(m,n)$ is demonstrated in Fig.3. A real image of the cube together with the undiffracted reference wave is noticeable.

Because of the off-axis geometry, these two parts of the real image are separated. Furthermore, a speckle appearance on the reconstructed cube is noticeable. It is a result of the interaction between coherent light and the rough surface of the object.

Localisation of cognitive tasks used in EEG-based BCIs

M. Dyson *, F. Sepulveda, J.Q. Gan

Clinical Neurophysiology (2010.3)

Presenter : Younghak Shin

GIST, Dept. of Information and Communication, INFONET Lab.

Gwangju Institute of Science and Technology

Objective

- In BCIs, motor and non-motor(e.g., auditory) cognitive states are used.
- To provide candidate electrode sites and neurophysiological reference information used in brain–computer interfacing research, they investigate six cognitive tasks.
- This is the first study to provide candidate electrode sites for multiple tasks used in brain–computer interfacing

Methods

- Cognitive tasks

- Six cognitive tasks were tested against the idle state
- The idle state was used as a baseline against each task in order to observe changes in the activation associated

1. Arithmetic

- Subtraction was selected as an arithmetic task
- Generate a three digit number and a single digit number for each trial
- The single digit number was to be repeatedly subtracted from the results of each calculation
- continuing for the duration of the trial.

2. Navigation imagery

- Subjects were instructed to select a familiar route between two locations
- Subjects were required to bring to mind images associated with the route.

Methods

3. Auditory recall

- Auditory recall involved recall of a tune familiar to subjects
- and involved the mental rehearsal of the said song.

4. Phone imagery

- This task was an alternative auditory task
- and involved subjects bringing to mind a familiar telephone bell or ringtone and retain the sound for the duration of the trial
- It was emphasized that this was an auditory task and associations should not be made with motor activities associated with telephone use

5. Motor imagery of the left hand

- A wrist extension was demonstrated to subjects.
- Motor imagery was defined as bringing to mind these associations without performing the task itself

6. Motor imagery of the right hand

- Instructions matched those for left hand motor imagery.

Methods

- Data collection

- Subjects : Seven male subjects (age 24–35) took part in the study. All subjects were able bodied, free from medication and any disorders of, or injuries to the central nervous system.
- Protocol
  - Each run contained 10 trials (randomly ordered)
  - trials within each run were split equally between the active task condition and the idle condition.
  - Each run was repeated six times, producing 30 trials for each mental task and 30 trials of associated idle data.
  - The number of runs per session was dependent on subject preference.
  - Within each run cues appeared after a 60 s pre-trial period

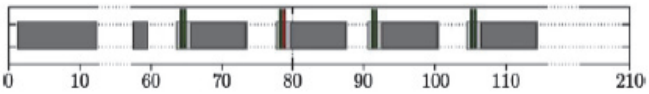

Fig. 1. Outline of an experimental run with time in seconds. A breakdown of the components of a trial are shown in Fig. 2.

Methods

- Protocol
  - A trial began with the presentation of a fixation cross in the centre of the screen.
  - Paired beep sounds were used to cue the active task condition and the idle task.
  - Two 70 ms duration tones were presented
  - The first sound was consistently 1 kHz, the second either 1 or 1.3 kHz.
  - If the two tones were perceived as the same tone the subject performed the given mental task for the run
  - If the tones were different the subject relaxed for the duration of the trial
  - Subjects were instructed to attempt to perform each task until the fixation cross disappeared from the screen

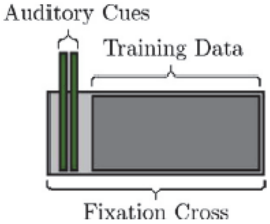

Fig. 2. Breakdown of the components of a trial as used in Fig. 1.

Methods

- Recordings
  - EEG was recorded from 64 electrodes positioned according to the international 10–20 layout using a BioSemi Active2 system.
  - EEG signals were filtered between 0.1 Hz and 100 Hz (Butterworth–Order 5)
  - Data were sampled at a frequency of 256 Hz

- Feature extraction
  - Features were extracted in two representations, band power and reflection coefficients.
  - Band power extraction was performed on 10 frequency bands, corresponding to the delta (0.1–5 Hz), theta (5–8 Hz), alpha (8–12Hz), sigma (12–15 Hz), beta (15–25 Hz) bands and the five bands in the gamma range (25–35, 35–45, 45–55, 55–65, 65–75 Hz).
  - Features were extracted for each band on each channel, giving a total of 640 features based on band power.

Methods

- Feature extraction
  - Reflection coefficients, or partial correlation (PARCOR) coefficients, are obtained via autoregressive analysis and are related to autoregression coefficients
  - An autoregressive model represents a time signal as an output of an all pole filter driven by white noise.
  - Filter coefficients are calculated from a block of samples as input signal

The notation AR(p) indicates an autoregressive model of order p. The AR(p) model is defined as

$$X_t = c + \sum_{i=1}^{p} \varphi_i X_{t-i} + \varepsilon_t$$

where $\varphi_1, \ldots, \varphi_p$ are the parameters of the model, c is a constant, and ε_t is white noise.

Methods

- Feature selection
  - A sequential forward floating search (SFFS) *[Pudil et al. 1994]* algorithm was used to obtain electrode-feature combinations for each subject-task dataset.
  - The algorithm works on the extracted feature space Y, which contains a finite number of features, D: $Y = \{y_j \mid j = 1,\ldots,D\}$.
  - Output is a subset of extracted features X, consisting of the *k* features producing best discrimination in the feature space:

$$X_k = \{x_j \mid j = 1,\ldots,k,\ x_j \in Y\}, \quad k = 0,1,\ldots,D.$$

  - The selected features subset is initialized as an empty set $X_0 = 0$ with no features selected (*k*=0).
  - Halting occurs when *k* reaches the required number of selected features (k = 10).
  - The SFFS algorithm proceeds via two steps.
  - 'Inclusion' step and 'Conditional Exclusion' step.

Methods

- SFFS algorithm
  - 'Inclusion' step
  - the most significant feature with respect to the currently selected feature set X_k, x^+ is determined: $x^+ = \arg\max_{x \in Y - X_k} J(X_k + x)$.
  - This feature is added to the selected features subset $X_{k+1} = X_k + x^+$ and the feature count incremented accordingly *k*=*k*+1
  - 'Conditional Exclusion' step
  - the least significant feature, x^-, of the current selected features subset is determined: $x^- = \arg\max_{x \in X_k} J(X_k - x)$.
  - The least significant feature is removed from the current selected feature set, $X_{k-1} = X_k - x^-$, the feature count is decremented, *k*=*k*-1
  - and the conditional exclusion stage is repeated.
  - if no improvement in discrimination be found, the algorithm returns to the inclusion step.
  - Search terminated at 10 features (k = 10).
  - The function *J* maximized was mean classification accuracy achieved by LDA (10-fold cross-validation)

Methods

- To analyze that which electrode positions and frequency bands were used. They have used electrode maps for different tasks.
- Cross subject electrode frequency(# of counts)
  - electrode site was selected multiple times during a search based on differing features,
  - i.e. a single channel selected at differing frequency bands,
  - each instance would contribute independently towards an electrode frequency count.
- Cross subject electrode maps
  - To visualize the distribution of channels selected across subjects gradient maps are produced based on the frequency count of channels selected.
  - subject group gradient maps of selected channels are obtained by smoothing frequency counts over all channels.

Methods

- Localization with sLORETA
  - To obtain localization results, we used Standardised Low Resolution Brain Electromagnetic Tompography (sLORETA) *[Pascual-Marqui, 2002].*
  - sLORETA is a linear method of computing a statistical map from EEG data which indicates the location of underlying source processes with less error.
  - Underlying sources providing spatial activation with closest correspondence to electrodes selected through feature selection were selected.

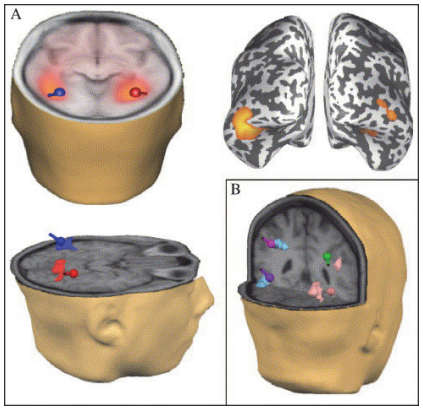

Results

- Classification results derived through cross subject electrode selection are presented in parallel with source localization results.
- Based on activations derived from localization results we obtain closest match Brodmann area and attempt to identify neural structures

1. Motor imagery (left hand)

Table 1
Motor imagery (left hand): frequency of channels selected, ranked descending. Left group features based on band power. Right group features based on reflection coefficients. Highlighting: band power channels highlighted reflect channels in proximity to C4. Reflection coefficient channels highlighted reflect channels in proximity to C4.

Band power						Reflection coefficients					
Site	Freq.	%	Site	Freq.	%	Site	Freq.	%	Site	Freq.	%
C4	**32**	**8.74**	CP3	8	2.19	**CP6**	**25**	**6.98**	**CP4**	**8**	**2.23**
P9	26	7.1	Iz	7	1.91	**CP2**	**25**	**6.98**	P10	8	2.23
AF7	19	5.19	**FC6**	**7**	**1.91**	**C4**	**24**	**6.70**	P04	8	2.23
Cz	17	4.64	P6	7	1.91	P9	23	6.42	P3	7	1.96
P04	16	4.37	AF3	6	1.64	F3	17	4.75	PO7	7	1.96
C2	**14**	**3.83**	FC1	6	1.64	**C2**	**16**	**4.47**	P4	7	1.96
CP6	**14**	**3.84**	C3	6	1.64	P8	15	4.19	AF3	6	1.68
P8	13	3.55	O1	6	1.64	**FC6**	**14**	**3.91**	AFz	6	1.68
PO7	12	3.28	Pz	6	1.64	CP3	13	3.63	FC5	5	1.4
AF4	11	3.01	F7	5	1.37	Fp1	10	2.79	CP1	5	1.4
F8	11	3.01	C1	5	1.37	FC3	10	2.79	AF4	4	1.12
CP4	**11**	**3.01**	TP7	5	1.37	C1	10	2.79	F2	4	1.12
P10	11	3.01	P3	5	1.37	CP5	10	2.79	T8	4	1.12
P08	11	3.01	POz	5	1.37	Cz	10	2.79	P2	4	1.12
FC2	**10**	**2.73**	C6	5	1.37	CPz	9	2.51	FC1	3	0.84
AFz	9	2.46	P2	5	1.37	AF8	9	2.51	Fpz	3	0.84
TP8	9	2.46	F5	3	0.82	C6	9	2.51	F6	3	0.84
P4	9	2.46				F4	8	2.23			

- Table 1 shows the frequency of channels utilized in discrimination of motor imagery of the left hand from idle activity

Results

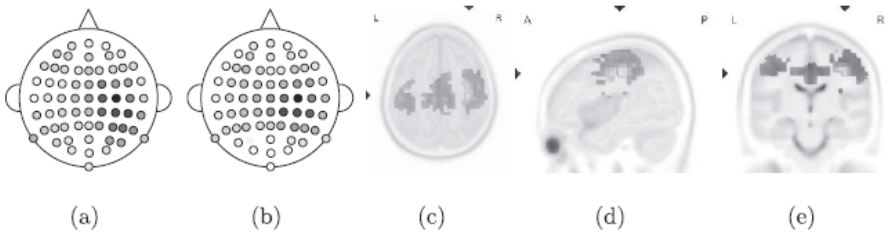

Fig. 3. Motor imagery (left hand). (a) and (b) Gradient maps based on frequency of channels selected by SFFS across subjects. Results based on band power and reflection coefficients, respectively. Darker colour indicates increased frequency. (c)–(e) sLORETA source localisation results corresponding to activation in Brodmann area 4 in the upper alpha/mu band (10.5–12 Hz).

- Fig. 3(a) and (b) shows gradient maps, obtained using band power and reflection coefficients based on the values outlined in Table 1
- For both feature representations electrode C4 achieves the highest frequency value
- Fig. 3(c)–(e) shows localization results with activation most similar to activity displayed in gradient maps.
- The closest match Brodmann area is BA4, the primary motor cortex, located on the precentral gyrus.
- This localization activity was found in the upper alpha/mu band (10.5–12 Hz)

Results

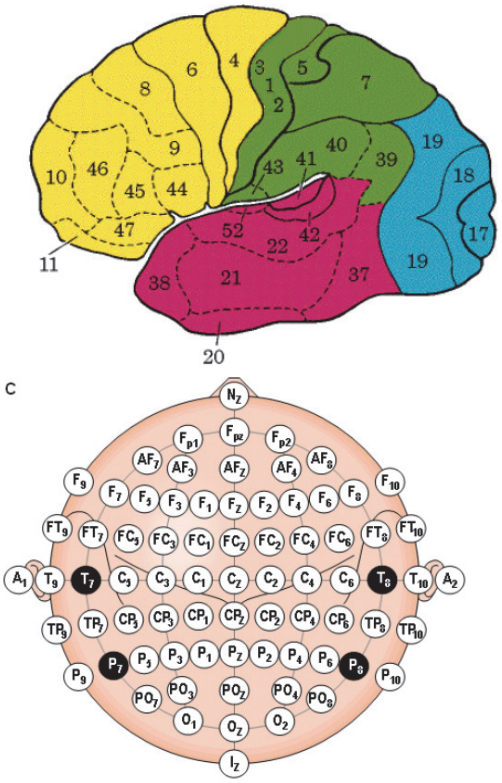

Functional Areas of the Brain

Function	Brodmann Area
Vision	
primary	17
secondary	18, 19, 20, 21, 37
Audition	
primary	41
secondary	22, 42
Body Sensation	
primary	1, 2, 3
secondary	5, 7
Sensation, tertiary	7, 22, 37, 39, 40
Motor	
primary	4
secondary	6
eye mov't	8
speech	44
Motor, tertiary	9, 10, 11, 45, 46, 47

- A Brodmann area is a region of the cerebral cortex defined based on its cytoarchitectonics(세포구축), or structure and organization of neurons.

Results

2. Motor imagery (right hand)

Table 2
Motor imagery (right hand): frequency of channels selected, ranked descending. Left group features based on band power. Right group features based on reflection coefficients. Highlighting: band power channels highlighted reflect channels in proximity to CP1. Reflection coefficient channels highlighted reflect channels in proximity to CP3.

Band power						Reflection coefficients					
Site	Freq.	%	Site	Freq.	%	Site	Freq.	%	Site	Freq.	%
CP3	**27**	**7.20**	FT7	8	2.13	**CP3**	**42**	**12.35**	CPz	7	2.06
P9	26	6.93	PO7	8	2.13	P8	19	5.59	Fp2	7	2.06
CP1	**24**	**6.40**	AFz	8	2.13	FC6	18	5.29	F8	7	2.06
Iz	23	6.13	F4	8	2.13	C4	16	4.71	CP6	7	2.06
C3	**20**	**5.33**	O1	7	1.87	FC5	15	4.41	**C3**	**6**	**1.76**
Oz	18	4.80	O2	7	1.87	**C5**	**13**	**3.82**	PO3	6	1.76
P8	17	4.53	F1	5	1.33	AF8	13	3.82	F4	5	1.47
C6	16	4.27	Fpz	5	1.33	C6	11	3.24	P6	5	1.47
P6	16	4.27	F8	5	1.33	FT7	10	2.94	TP7	4	1.18
Cz	**15**	**4.00**	AF4	4	1.07	C2	10	2.94	FCz	4	1.18
FC3	13	3.47	**C1**	**3**	**0.80**	F3	9	2.65	**P3**	**3**	**0.88**
F5	10	2.67	T7	3	0.80	F7	9	2.65	**P5**	**3**	**0.88**
C5	10	2.67	AF8	3	0.80	FC3	9	2.65	O1	3	0.88
P3	**10**	**2.67**	FC6	3	0.80	Oz	9	2.65	AFz	3	0.88
Pz	**10**	**2.67**	TP7	2	0.53	P10	9	2.65	**CP5**	**2**	**0.59**
CP4	10	2.67	P7	1	0.27	P08	9	2.65	CP4	2	0.59
POz	9	2.40	**CPz**	**1**	**0.27**	Fp1	8	2.35	P04	2	0.59
Fp2	9	2.40	F6	1	0.27	**P1**	**8**	**2.35**	F5	1	0.29
C2	9	2.40	C4	1	0.27	Cz	8	2.35	FC1	1	0.29
						CP2	8	2.35	FC4	1	0.29
						AF7	7	2.06	T8	1	0.29

- Table 2 shows the frequency of channels utilized in discrimination of motor imagery of the right hand from idle activity

Results

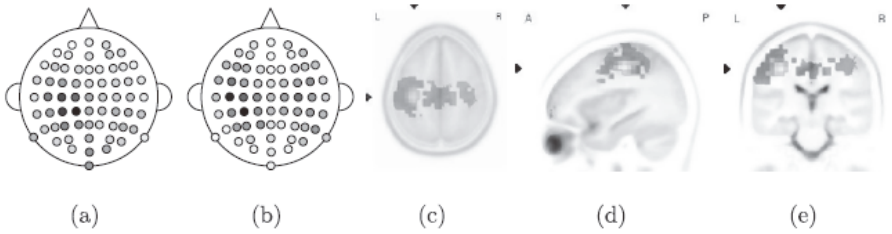

Fig. 4. Motor imagery (right hand). (a) and (b) Gradient maps based on frequency of channels selected by SFFS across subjects. Results based on band power and reflection coefficients, respectively. Darker colour indicates increased frequency. (c)–(e) sLORETA source localisation results corresponding to activation in Brodmann area 3 in the upper alpha/mu band (10.5–12 Hz).

- Fig. 4(a) and (b) shows gradient maps, obtained using band power and reflection coefficients based on the values outlined in Table 2
- For both feature representations electrode CP3(near the C3) achieves the highest frequency value
- Fig. 4(c)–(e) shows localization results with activation most similar to activity displayed in gradient maps (a) and(b).
- The closest match Brodmann area is BA3 located on the primary somatosensory cortex
- This localization activity was found in the upper alpha/mu band (10.5–12 Hz)

Results

3. Auditory recall

Table 3
Auditory recall: frequency of channels selected, ranked descending. Left group features based on band power. Right group features based on reflection coefficients. Highlighting: band power channels highlighted reflect channels in proximity to TP8. Reflection coefficient channels highlighted in regular bold reflect channels in proximity to CP6, channels highlighted in italic bold reflect channels in proximity to F4.

Band power						Reflection coefficients					
Site	Freq.	%	Site	Freq.	%	Site	Freq.	%	Site	Freq.	%
P10	**19**	**6.25**	C6	5	1.64	***AF8***	***24***	***7.16***	Fz	8	2.39
CP6	**18**	**5.92**	P08	5	1.64	***AFz***	***20***	***5.97***	***FC6***	***8***	***2.39***
Fp1	16	5.26	CP5	4	1.32	***F4***	***19***	***5.67***	***FC4***	***7***	***2.09***
P7	15	4.93	P1	4	1.32	FC1	17	5.07	**CP4**	**7**	**2.09**
F5	14	4.61	P5	4	1.32	CP6	17	5.07	FT8	6	1.79
F7	13	4.28	Iz	4	1.32	CP3	14	4.18	Cz	6	1.79
TP8	**13**	**4.28**	POz	4	1.32	**TP8**	**13**	**3.88**	F1	5	1.49
F1	11	3.62	Pz	4	1.32	**P4**	**13**	**3.88**	Fpz	5	1.49
AF8	10	3.29	Oz	3	0.99	F3	12	3.58	**T8**	**5**	**1.49**
C5	9	2.96	Fz	3	0.99	T7	12	3.58	P10	5	1.49
Fp2	9	2.96	FC4	3	0.99	***AF4***	***12***	***3.58***	AF3	4	1.19
AFz	9	2.96	Cz	3	0.99	P08	12	3.58	P5	4	1.19
FC2	9	2.96	P8	3	0.99	C3	11	3.28	CP2	4	1.19
CP2	9	2.96	F3	2	0.66	**C6**	**10**	**2.99**	FT7	3	0.9
02	9	2.96	FT7	2	0.66	FC3	9	2.69	F7	2	0.6
C4	8	2.63	FCz	2	0.66	P1	9	2.69	P04	2	0.6
P6	**8**	**2.63**	P2	2	0.66	***F6***	***9***	***2.69***	Fp1	1	0.3
TP7	7	2.30	AF3	1	0.33	**C4**	**9**	**2.69**	CPz	1	0.3
T8	**7**	**2.30**	CP3	1	0.33	**P6**	**9**	**2.69**	Fp2	1	0.3
PO3	6	1.97	CPz	1	0.33						
F2	6	1.97	FT8	1	0.33						
P04	6	1.97	C2	1	0.33						
P9	5	1.64	CP4	1	0.33						
F6	5	1.64									

- Table 3 lists the frequency of channels used in the discrimination of auditory imagery from idle activity

Results

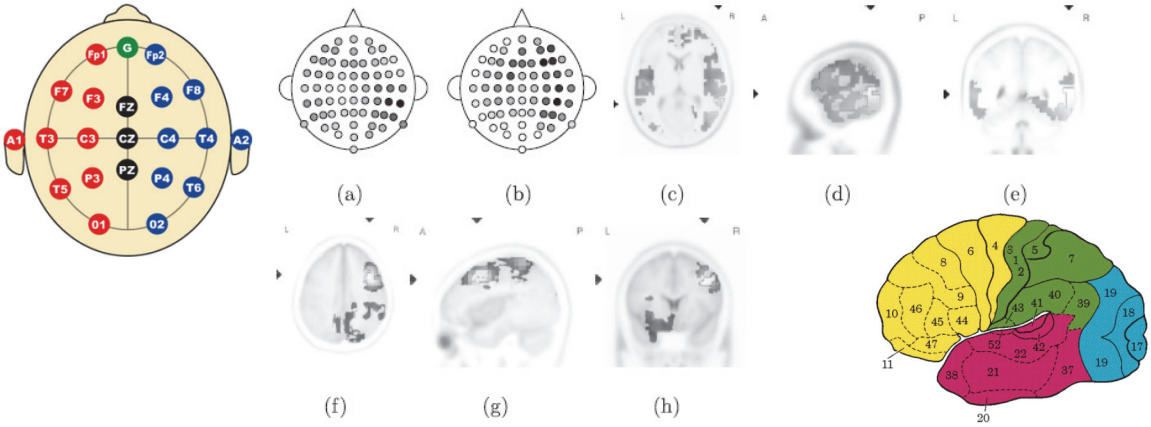

Fig. 5. Auditory recall. (a) and (b) Gradient maps based on frequency of channels selected by SFFS across subjects. Results based on band power and reflection coefficients, respectively. Darker colour indicates increased frequency. (c)–(e) sLORETA source localisation results corresponding to activation in Brodmann area 21 in the high beta (21–30 Hz) range. (f)–(h) sLORETA source localisation results corresponding to activation in Brodmann area 9 in the lower alpha band (8.5–10 Hz).

- Fig. 5(a), the gradient map based on band power, has greatest density of channels selected around TP8
- Fig. 5(b), show a primary area of main density around electrode CP6 with a secondary area commonly selected around FP4
- Fig. 5(c)–(e) has closest match in Brodmann area 21 located in the middle temporal gyrus (high beta (21–30 Hz) range).
- Fig. 5(f)–(h) has closest match is Brodmann area 9 on the precentral gyrus (lower alpha band (8.5–10 Hz)).

Results

4. Phone imagery

Table 4
Phone imagery: frequency of channels selected, ranked descending. Left group features based on band power. Right group features based on reflection coefficients. Highlighting: band power channels highlighted in regular bold reflect channels in proximity to C6, channels highlighted in italic bold reflect channels in proximity to FC5. Reflection coefficient channels highlighted in regular bold reflect channels in proximity to TP7, channels highlighted in italic bold reflect channels in proximity to CP6.

Band power						Reflection coefficients					
Site	Freq.	%	Site	Freq.	%	Site	Freq.	%	Site	Freq.	%
AF4	23	6.55	P5	7	1.99	**P9**	**27**	**7.20**	P10	9	2.4
AF8	20	5.70	P7	7	1.99	AF7	26	6.93	C3	8	2.13
C6	**19**	**5.41**	Pz	7	1.99	***T8***	***20***	***5.33***	**P7**	**8**	**2.13**
FCz	18	5.13	P2	6	1.71	***P8***	***19***	***5.07***	F8	8	2.13
T8	**16**	**4.56**	P04	6	1.71	**P5**	**18**	**4.80**	F3	7	1.87
F7	***14***	***3.99***	***F3***	***5***	***1.42***	Fp2	17	4.53	CPz	7	1.87
T7	***14***	***3.99***	***FC5***	***5***	***1.42***	AF8	15	4	P2	7	1.87
CP5	14	3.99	P9	5	1.42	**CP5**	**14**	**3.73**	O1	6	1.6
C4	**14**	**3.99**	02	5	1.42	Fpz	13	3.47	P1	5	1.33
C5	***13***	***3.70***	Fp1	4	1.14	FT7	12	3.2	FT8	5	1.33
Iz	12	3.42	AF7	4	1.14	**T7**	**12**	**3.20**	***C6***	***5***	***1.33***
CP4	**11**	**3.13**	Fp2	3	0.85	***P4***	***12***	***3.20***	***P6***	***5***	***1.33***
PO7	10	2.85	AFz	3	0.85	Pz	12	3.2	Iz	4	1.07
FT8	**10**	**2.85**	Cz	3	0.85	2	12	3.2	FC2	4	1.07
CP6	**10**	**2.85**	C2	3	0.85	CP1	10	2.67	Cz	4	1.07
P10	10	2.85	Oz	2	0.57	P04	10	2.67	C2	3	0.8
P8	9	2.56	**FC6**	**2**	**0.57**	**TP7**	**9**	**2.40**	CP2	3	0.8
F5	***8***	***2.28***	CP2	2	0.57	***C4***	***9***	***2.40***	POz	1	0.27
FT7	***8***	***2.28***	AF3	1	0.28	***TP8***	***9***	***2.40***			
C1	8	2.28	P1	1	0.28						
Fz	8	2.28	CPz	1	0.28						

- Table 4 lists the frequency of channels used in the discrimination of phone imagery from idle activity

Results

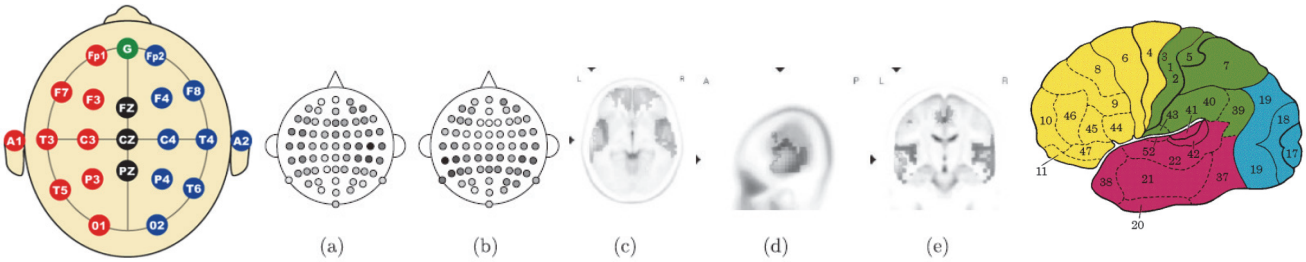

Fig. 6. Phone imagery. (a) and (b) Gradient maps based on frequency of channels selected by SFFS across subjects. Results based on band power and reflection coefficients, respectively. Darker colour indicates increased frequency. (c)–(e) sLORETA source localisation results corresponding to activation in Brodmann area 21 in the mid beta (18.5–21 Hz) range.

- Fig. 6(a), the gradient map based on band power, has greatest density of channels selected around C6, secondary area surrounding FC5.
- Fig. 6(b) which has two areas of density centered around TP7 and CP6
- Fig. 6(c)–(e) shows localization results which best explain the pattern of activation found in gradient maps (Fig. 6(a) and (b)).
- Closest match Brodmann area is BA21 located on the middle temporal gyrus (freq. : mid beta (18.5–21 Hz) range).
- In comparison to the auditory recall results shown in Figs. 5(a) and (b), Figs. 6(a) and (b) show a greater degree of bilateral activity.

Results

5. Arithmetic

Table 5
Arithmetic: frequency of channels selected, ranked descending. Left group features based on band power. Right group features based on reflection coefficients. Highlighting: band power channels highlighted reflect channels in proximity to AF3. Reflection coefficient channels highlighted reflect channels in proximity to CP4.

Band power						Reflection coefficients					
Site	Freq.	%	Site	Freq.	%	Site	Freq.	%	Site	Freq.	%
P9	28	7.89	FC5	6	1.69	**P6**	**24**	**6.40**	T8	8	2.13
P10	21	5.92	PO3	6	1.69	P9	19	5.07	**CP4**	**7**	**1.87**
F3	**20**	**5.63**	Iz	6	1.69	CP3	16	4.27	**CP6**	**6**	**1.60**
F5	**19**	**5.35**	**AFz**	**6**	**1.69**	FC1	15	4	P8	6	1.6
CP2	18	5.07	F4	6	1.69	AF3	14	3.73	2	6	1.6
AF3	**13**	**3.66**	POz	5	1.41	F5	13	3.47	FC5	5	1.33
C5	13	3.66	FT8	5	1.41	**C6**	**13**	**3.47**	POz	5	1.33
Fp2	13	3.66	CP5	4	1.13	TP8	13	3.47	Fpz	5	1.33
TP8	11	3.10	FC2	4	1.13	F8	12	3.2	F4	5	1.33
Fp1	**10**	**2.82**	FCz	4	1.13	C3	11	2.93	FT8	5	1.33
AF7	**10**	**2.82**	T8	4	1.13	AF4	11	2.93	**P4**	**5**	**1.33**
T7	10	2.82	P08	4	1.13	F7	10	2.67	Fp1	4	1.07
C2	10	2.82	TP7	3	0.85	F2	10	2.67	FT7	4	1.07
02	10	2.82	P3	3	0.85	FCz	10	2.67	P1	4	1.07
C3	9	2.54	P7	3	0.85	**C2**	**10**	**2.67**	PO7	4	1.07
P1	9	2.54	AF4	3	0.85	**P2**	**10**	**2.67**	Fp2	3	0.8
Oz	9	2.54	F8	3	0.85	CP5	9	2.4	F6	3	0.8
Pz	9	2.54	**F1**	**2**	**0.56**	O1	9	2.4	P08	3	0.8
CP3	8	2.25	F2	2	0.56	AF8	9	2.4	P5	2	0.53
AF8	8	2.25	F7	1	0.28	**CP2**	**9**	**2.40**	CPz	2	0.53
Fz	8	2.25	FC1	1	0.28	F1	8	2.13	FC6	2	0.53
Fpz	**7**	**1.97**	C1	1	0.28	FC3	8	2.13	TP7	1	0.27
						T7	8	2.13	Oz	1	0.27
						FC4	8	2.13			

- Table 5 lists the frequency of channels used in the discrimination of arithmetic from idle activity
- Table 5 shows greatest frequency at AF3 for band power features, and at CP4 when discrimination is based on reflection coefficients.

Results

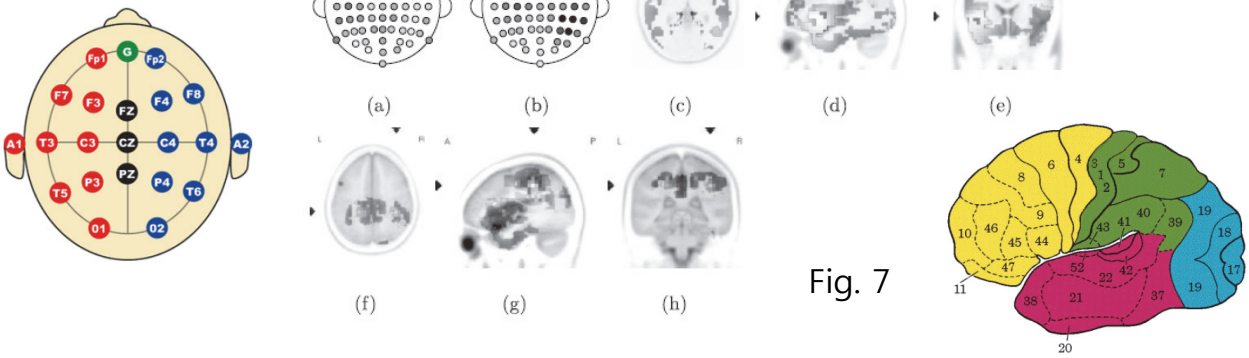

Fig. 7

- Arithmetic mental activity shows distinct differences in classification areas obtained dependent on feature extraction method, band power and AR coefficients.
- Fig. 7(c)–(e) and Fig. 7(f)–(h) represent areas of activation best describing patterns of activation found with Fig. 7(a) and Fig. 7(b) respectively .
- The closest match Brodmann area related to activation was BA46 in the inferior frontal gyrus of the left hemisphere (low beta band (12.5–18 Hz)).
- Fig. 7(f)–(h) shows activation centered on Brodmann area 40, inferior parietal lobe, in the area of the supramarginal gyrus (theta band (6.5–8 Hz)).

Results

6. Navigation

Table 6
Navigation imagery: frequency of channels selected, ranked descending. Left group features based on band power. Right group features based on reflection coefficients. Highlighting: band power channels highlighted in regular bold reflect channels in proximity to AF4, channels highlighted in italic bold reflect channels in proximity to CP2. Reflection coefficient channels highlighted in regular bold reflect channels in proximity to PO4, channels highlighted in italic bold reflect channels in proximity to AFz.

Band power						Reflection coefficients					
Site	Freq.	%	Site	Freq.	%	Site	Freq.	%	Site	Freq.	%
F7	20	6.04	C6	8	2.42	**P04**	**37**	**9.61**	FC1	7	1.82
AF4	**18**	**5.44**	P8	8	2.42	CP1	26	6.75	CP3	7	1.82
F2	**18**	**5.44**	Iz	7	2.11	***AFz***	***21***	***5.45***	F4	7	1.82
Fp1	17	5.14	**Fpz**	7	**2.11**	**CP2**	**20**	**5.19**	FCz	7	1.82
CP2	***17***	***5.14***	**F6**	7	**2.11**	F6	18	4.68	Iz	6	1.56
P1	***16***	***4.83***	CP3	6	1.81	**P2**	17	**4.42**	**P08**	**6**	**1.56**
T8	16	4.83	F8	6	1.81	FT7	16	4.16	FC6	5	1.3
CP1	***14***	***4.23***	T7	5	1.51	FT8	16	4.16	**CP6**	**5**	**1.30**
AF8	13	**3.93**	Oz	5	1.51	***Fpz***	***15***	***3.90***	F5	4	1.04
P04	13	3.93	C4	5	1.51	***Fp2***	***12***	***3.12***	***F2***	***4***	***1.04***
P08	12	3.63	P4	5	1.51	***Fz***	***11***	***2.86***	TP7	3	0.78
P7	11	3.32	F3	4	1.21	***F1***	***10***	***2.60***	PO7	3	0.78
AFz	**11**	**3.32**	FC3	4	1.21	C4	10	2.6	F8	3	0.78
F5	10	3.02	CP5	4	1.21	P1	9	2.34	**P4**	**3**	**0.78**
FT7	9	2.72	**Fp2**	**4**	**1.21**	PO3	9	2.34	P6	3	0.78
C2	***9***	***2.72***	FT8	3	0.91	TP8	9	2.34	***AF3***	***2***	***0.52***
P2	***9***	***2.72***	***C1***	***2***	***0.60***	F3	8	2.08	CPz	2	0.52
P5	8	2.42				FC5	8	2.08	AF7	1	0.26
						T7	8	2.08	C5	1	0.26
						POz	8	2.08	O1	1	0.26
						FC4	8	2.08	C2	1	0.26
						FC3	7	1.82	C6	1	0.26

- Table 6 lists the frequency of channels used in the discrimination of navigation imagery from idle activity

Results

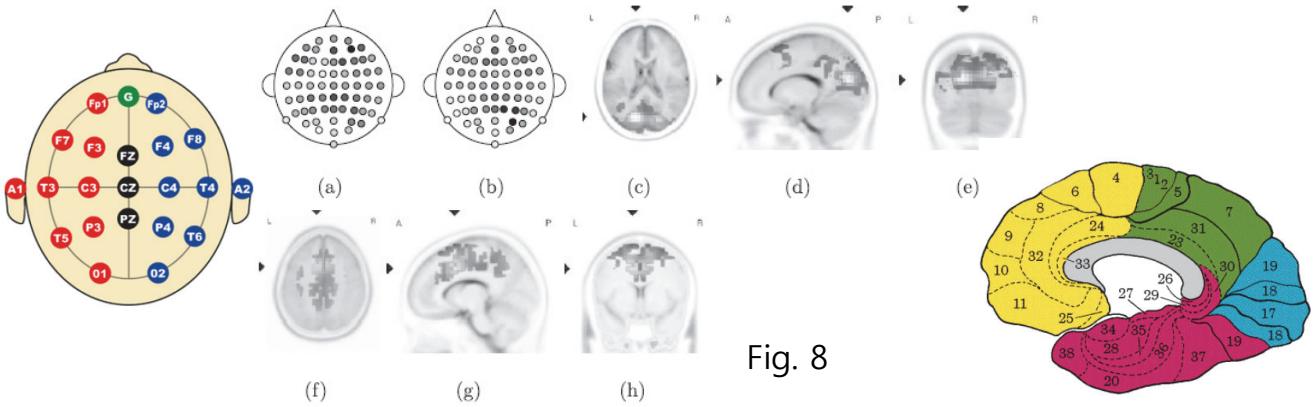

Fig. 8

- Fig. 8(a) shows gradient maps produced from band power features, the greatest density value is centered around AF4 with a second area of increased density located around CP2.
- The equivalent values for Fig. 8(b) are centered at PO4 and AFz.
- Activity centered around CP2 in the case of band power, and PO4 in the case of reflection coefficients is best matched by localization activity shown in Fig. 8(c)–(e).
- The closest matched Brodmann area is BA31, on the parietal lobe in the mid beta band(18.5–21Hz).
- Frontal activation found in Fig. 8(a) and (b), centered around AF4 and AFz is best matched by Fig. 8(f)–(h) in the lower beta band (12.5–18 Hz) at Brodmann area BA32.

Results

Contrast of feature distributions

- they calculate the relative overlap in spatial electrode distributions using two methods.

1. dot product of feature vectors
   - The values in Table 7 show the dot product of feature vectors divided over a fixed electrode count of 64.
   - Higher values indicate greater overlap in the cross subject distribution maps
   - The lowest levels of overlap are associated with contrasts of the distributions produced by motor imagery tasks
   - The highest degree of overlap is found between the auditory imagery and arithmetic task based on reflection coefficients

Table 7
Comparative overlap in spatial electrode distributions: the dot product of normalised electrode distribution vectors, divided over electrode count. Greater values indicate increased overlap. Highlighting: values in italic are based on band power features. Values in standard text are based on reflection coefficients.

Tasks	MoIm:Left	MoIm:Right	Navigation	Arithmetic	Auditory	Phone
MoIm:Left		0.06	0.06	0.09	0.11	0.07
MoIm:Right	*0.07*		0.11	0.11	0.10	0.11
Navigation	*0.08*	*0.07*		0.16	0.15	0.10
Arithmetic	*0.08*	*0.08*	*0.12*		0.17	0.16
Auditory	*0.07*	*0.06*	*0.10*	*0.11*		0.16
Phone	*0.10*	*0.10*	*0.14*	*0.13*	*0.14*	

Results

Contrast of feature distributions

2. distance between the density of features

- The values in Table 8 are the summed absolute distance between paired feature vectors
- providing a measure of the difference in density distributions of features for contrasted cognitive tasks
- The greatest distance in Table 8 is found between motor imagery of the left hand and arithmetic in the band power domain
- The lowest distance, is found between the auditory imagery and arithmetic tasks based on reflection coefficients.

Table 8
Comparative distance between electrode feature density vectors: the sum of absolute distance between electrode distribution vectors. Lower values indicate similarity in feature distribution. Highlighting: values in italic are based on band power features. Values in standard text are based on reflection coefficients.

Tasks	MoIm:Left	MoIm:Right	Navigation	Arithmetic	Auditory	Phone
MoIm:Left		0.44	0.53	0.41	0.49	0.60
MoIm:Right	*0.57*		0.46	0.44	0.47	0.50
Navigation	*0.49*	*0.53*		0.39	0.44	0.59
Arithmetic	*0.72*	*0.54*	*0.51*		0.31	0.47
Auditory	*0.45*	*0.59*	*0.46*	*0.49*		0.68
Phone	*0.52*	*0.58*	*0.41*	*0.53*	*0.36*	

Conclusions

- Primary centers of activity for motor imagery tasks are localized to the pre- and postcentral gyrus
- Auditory-based tasks show activity in the middle temporal gyrus
- Calculation activity was localized to the left inferior frontal gyrus and right supramarginal gyrus
- Navigation imagery produced activity in the praecuneus and anterior cingulate cortex.
- Spatial areas of activation suggest that arithmetic and auditory tasks show promise for pairwise discrimination based on single recording sites.
- sLORETA results suggest that motor imagery tasks will show greatest discrimination from baseline EEG activity(idle state)

Thank you

INFONET, GIST
Journal Club (2013. 4. 30)

Scanner-Free and Wide-Field Endoscopic Imaging by Using a Single Multimode Optical Fiber

Authors: Youngwoon Choi, Changhyeong Yoon, Moonseok Kim, Taeseok Daniel Yang, Christopher Fang-Yen, Ramachandra R. Dasari, Kyoung Jin Lee, and Wonshik Choi
Publication: Physical Review Letters, 109, 203901 (16 Nov. 2012)
Speaker: Hwanchol Jang

Short summary: An endoscopic method is developed to replace the fiber bundle scope by a single multimode fiber. The dispersion in a multimode fiber is reversed by TLI methods. The speckle patterns are reduced by averaging the object images with different speckle illuminations.

I. OPTICAL FIBER FOR ENDOSCOPY

Multimode optical fiber
A multimode optical fiber has drawn interest because numerous independent spatial modes can be used for parallel information transport. However, the single multimode fiber could not be used in itself for the imaging purpose. When a light wave couples to and propagates through the fiber, the wave is distorted into a complex pattern because of mode dispersion.

Mode dispersion
Rays of light enter the fiber with different angles to the fiber axis, up to the fiber's acceptance angle. Rays that enter with a shallower angle travel by a more direct path, and arrive sooner than rays that enter at a steeper angle (which reflect many more times off the boundaries of the core as they travel the length of the fiber). The arrival of different components of the signal at different times distorts the shape.

Moreover, it has been much more challenging to use a single multimode fiber for practical endoscopic imaging in which the imaging operation should be performed in the reflection mode. In such a case, the light wave injected into the fiber is distorted twice, i.e., on the way in for the illumination and on the way out for the detection.

Fiber scope
For this reason, a fiber bundle has been widely used and thus became a standard for commercial endoscopes. In this fiber scope, each fiber constituting the bundle acts as a single pixel of an image, and the number of fibers in the bundle determines the pixel resolution.
Problem: Therefore, the requirement for a large number of fibers for high resolution imaging has posed constraints on the diameter of the endoscope, thereby causing considerable limitation on the accessibility of the device.

II. PROPOSED LENSELESS MICROENDOSCOPY BY A SINGLE FIBER (LMSF)

The multimode fiber is converted into a self-contained 3D imaging device that does not require a scanner or a lens.

Record the transmission matrix
The authors make use of the measured transmission matrix of a multimode optical fiber to reverse the on-the-way-out distortion of the detected light.
The transmission matrix of an unknown complex medium was used for the delivery of an image through the medium. In fact, a multimode optical fiber can also be considered as a complex medium because bending and twisting of the fiber complicate wave propagation through the fiber.

Speckle imaging method
By employing the speckle imaging method, the on-the-way-in distortion was also eliminated.

III. EXPERIMENTAL SET-UP

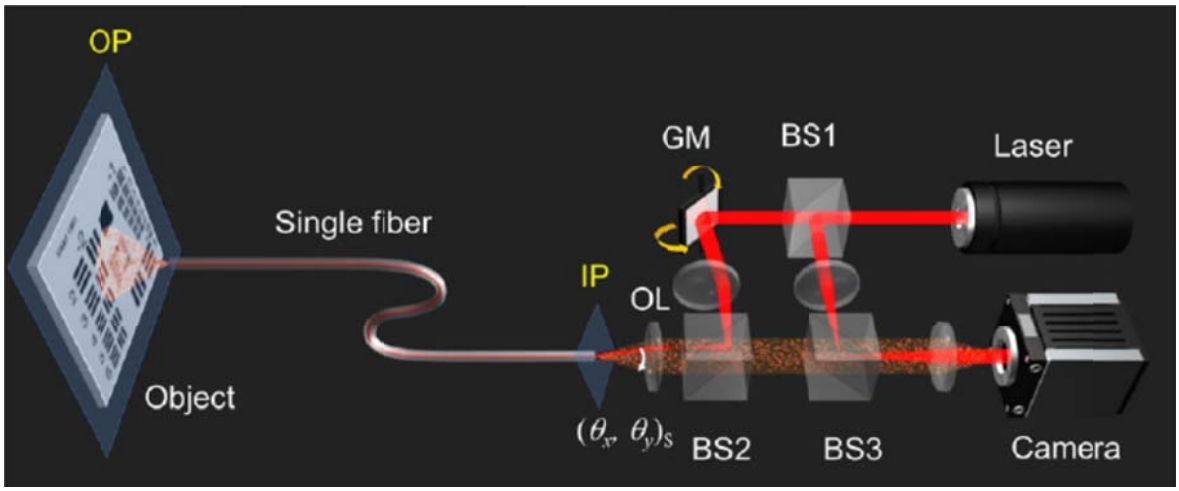

The beam illuminates at the input plane (IP) of the fiber, couples to the fiber, and subsequently propagates toward the object plane (OP) located at the exit of the fiber to illuminate a target object.
The laser beam reflected by BS1 is combined with the beam from the fiber to form an interference image at the camera. Using an off-axis digital holography algorithm, both amplitude and phase of the image from the fiber are retrieved.

IV. TECHNIQUES FOR LMSF

Two sources of the distortion
Two processes mask the object information: (1) distortion of illumination light on the way in (IP to OP) and (2) the scrambling of the light reflected by the object on the way out (OP to IP). In

order to overcome these two distortions, they employ methods of speckle imaging and turbid lens imaging (TLI), respectively.

Descrambling

They first characterize the input-output response of the optical fiber from the object side to the camera side (OP to IP). They scan the incident wave in its angle $(\theta_\xi, \theta_\eta)_T$ to the fiber and record its transmitted image at the camera. A set of these angle-dependent transmission images is called the transmission matrix T. The transmission matrix elements are measured up to 0.22 NA by recording 15000 images.

Once the transmission matrix is recorded, an object image at the OP can be reconstructed from the distorted image recorded at the IP by using the TLI. The process is an inversion of the transmission matrix given by the relation EOP

$$E_{OP}(\xi,\eta) = T^{-1}E_{IP}(x,y)$$

Here EIP and T^{-1} represent the recorded image at the IP and the inversion of the measured transmission matrix, respectively, and EOP is the image at the OP. Using Eq. (1), the distortion from OP to IP is reversed.

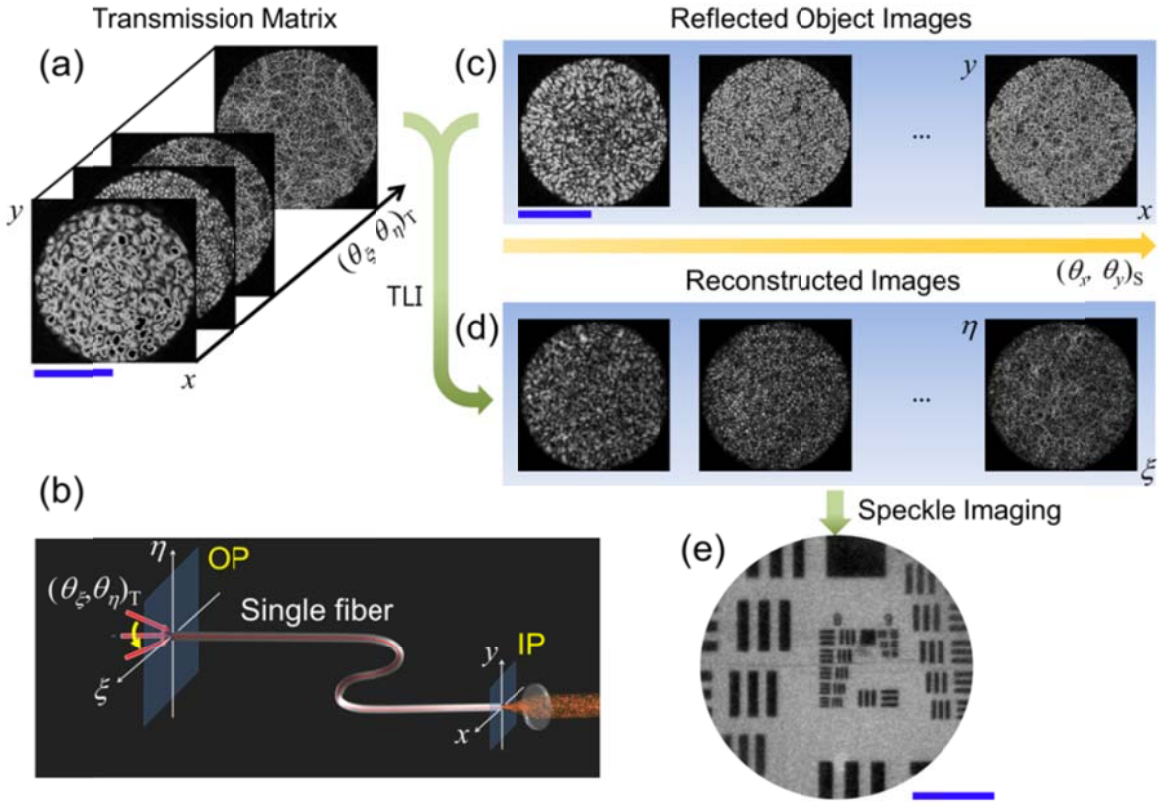

Eliminating the speckle pattern

The transmitted patterns are random speckles and the average size of the speckle decreases as the angle of illumination increases. This is because a high angle of illumination mostly couples to the high-order modes of the fiber.

The reconstructed images remain devoid of object structure because the illumination light is distorted due to the propagation of the illumination from IP to OP.
The change in the illumination angle causes the variation of the illumination light at the target object; in other words, a different speckle field is generated as we vary the angle $(\theta_x, \theta_y)_S$.

According to the speckle imaging method, a clean object image can be acquired if we average sufficient numbers of images recorded at different speckle illuminations.
The complex speckle illumination patterns are averaged out, leaving a clean object image.

Scanning of the fiber end to enlarge the view field.
They measured the transmission matrix of the fiber at an initial position of the fiber end and then used the same matrix to reconstruct object images taken while moving the fiber end.
Although bending induced by the movement of the fiber causes a change of the transmission matrix, many of the matrix elements stay intact and contribute to the image reconstruction.
According to their experiment, the LMSF is working well up to a centimeter-travel of the fiber end, confirming that LMSF has partial flexibility for searching for the view field.

V. CONCLUSION

The same techniques used in turbid medium lens are employed to reverse the distortion of the multimode fiber.
The transmission matrix stays almost the same even with the centimeter changes of the fiber end.

INFONET, GIST
Journal Club (2013. 05. 14)

A Compressive Sensing and Unmixing Scheme for Hyperspectral Data Processing

Authors: Chengbo Li, Ting Sun, Kevin Kelly, Yin Zhang
Publication: IEEE Trans. On Image Processing, March, 2012
Speaker: Woongbi Lee

Short summary: In this paper, a low complexity scheme is proposed for hyperspectral data compression and reconstruction. The data reconstruction minimizes the total variation of the abundance fractions subject to a preprocessed fidelity equation with a significantly reduced size, and other side constraints.

I. INTRODUCTION

Hyperspectral imaging is a technique to identify and quantify distinct material substances(재료물질) from observed spectral data. It employs hyperspectral sensors to collect information as a set of images. Each image represents a range of the electromagnetic spectrum, which is known as spectral bands containing the visible, near-infrared, and shortwave infrared spectral bands. Hyperspectral imaging has a wide range of applications such as terrain classification, mineral detection and exploration, pharmaceutical counterfeiting, environmental monitoring, and military surveillance.

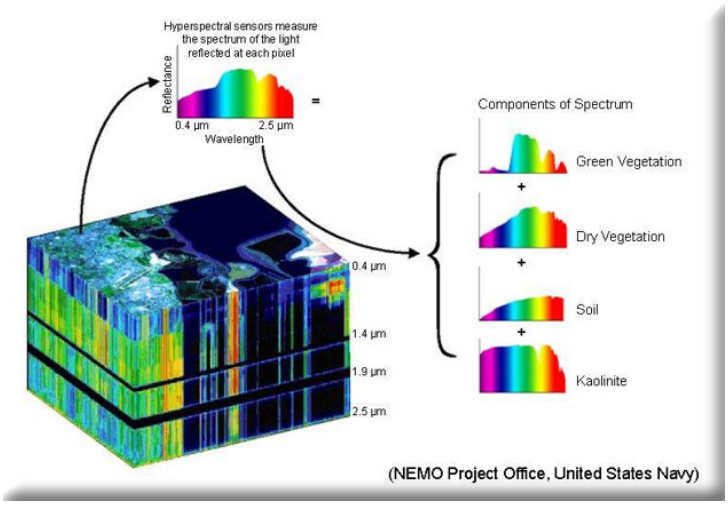

<출처: Google Image>

Hyperspectral imaging is typically low resolution and is a mixture of several different material substances, termed endmembers (pure signature), each possessing a characteristic hyperspectral signature. Hyperspectral unmixing is to decompose each pixel spectrum to identify and quantify the relative abundance of each endmember. The representative endmembers for a given scene are known a priori and their signatures can be obtained from a spectral library or are unknown but the hyperspectral data is fully accessible.

Hyperspectral data cubes have huge volume so that it is difficult to directly process and analyze them in real time. But, the hyperspectral data are highly compressible with two-fold compressibility: 1) each spatial image is compressible, and 2) the entire cube, when treated as a matrix, is of low rank.

In this paper, data are acquired by means of compressive sensing (CS), similar to extension of the single pixel camera. Data reconstruction and unmixing are combined into a single step of much lower complexity. They propose a compressive sensing and unmixing (CSU) scheme which formulates an unmixing model based on total variation (TV) minimization, develops an efficient algorithm to solve it, and provides experimental and numerical evidence to validate the scheme.

II. System Model

A. Notations

n_e	number of significant endmembers
$w_i^T \in \mathbb{R}^{n_b}$, for $i = 1,...,n_e$	spectral signature of an endmember
$n_b \geq n_e$	number of spectral bands
$x_i \in \mathbb{R}^{n_b}$	hyperspectral data vector at the i^{th} pixel
$h_i^T \in \mathbb{R}^{n_e}$	abundance fractions of the endmembers for any $i \in \{1,...,n_p\}$
n_p	number of pixels
$X = \left[x_1,...,x_{n_p} \right]^T \in \mathbb{R}^{n_p \times n_b}$	a matrix representing the hyperspectral cube

$W = \left[w_1, ..., w_{n_e} \right]^T \in \mathbb{R}^{n_e \times n_b}$	mixing matrix containing the endmember spectral signatures
$H = \left[h_1, ..., h_{n_p} \right]^T \in \mathbb{R}^{n_p \times n_e}$	a matrix holding the respective abundance fractions
$\mathbf{1}_s$	column vector of all ones with length s
$A \in \mathbb{R}^{m \times n_p}$	measurement matrix
$F \in \mathbb{R}^{m \times n_b}$	observation matrix
m	number of samples for each spectral band

B. Problem Formulation

The hyperspectral vector x_i at the i-th pixel can be regarded as a linear combination of the endmember spectral signatures, and the weights are gathered in a nonnegative abundance vector h_i.

$$X = HW,\ H\mathbf{1}_{n_e} = \mathbf{1}_{n_p},\ H \geq 0 \tag{1}$$

where $X = \left[x_1, ..., x_{n_p} \right]^T \in \mathbb{R}^{n_p \times n_b}$, $H = \left[h_1, ..., h_{n_p} \right]^T \in \mathbb{R}^{n_p \times n_e}$, and $W = \left[w_1, ..., w_{n_e} \right]^T \in \mathbb{R}^{n_e \times n_b}$.

$$\begin{bmatrix} - & x_1 & - \\ - & x_2 & - \\ & \vdots & \\ - & x_{n_p} & - \end{bmatrix} = \begin{bmatrix} - & h_1 & - \\ - & h_2 & - \\ & \vdots & \\ - & h_{n_p} & - \end{bmatrix} \begin{bmatrix} - & w_1 & - \\ - & w_2 & - \\ & \vdots & \\ - & w_{n_e} & - \end{bmatrix}$$

Since each column of X represents a 2D image corresponding to a particular spectral band, we can collect the compressed hyperspectral data $F \in \mathbb{R}^{m \times n_b}$ by randomly sampling all the columns of X using the same measurement matrix $A \in \mathbb{R}^{m \times n_p}$, where $m < n_p$ is the number of samples for each column.

$$AX = F \tag{2}$$

Combining (1) and (2), we obtain

$$AHW = F,\ H\mathbf{1}_{n_e} = \mathbf{1}_{n_p},\ H \geq 0 \tag{3}$$

Assuming the endmember spectral signatures in W are known, we aim to find the abundance distributions, H in (3), given the measurement matrix A and the compressed hyperspectral data F.

Instead of l_1 minimization of compressive sensing, TV (Total Variation) regularization is generally more advantageous on image problems since it can better preserve edges or boundaries in images. TV regularization puts emphasis on sparsity in the gradient map of the image and is suitable when the gradient of the underlying image is sparse. With assumption that the gradient of each image composed by abundance fractions for each endmember is mostly and approximately piecewise constant, we propose to recover the abundance matrix H by solving the following unmixing model:

$$\min_{H\in\mathbb{R}^{n_p\times n_e}} \sum_{j=1}^{n_e} TV\left(He_j\right) \text{ s.t. } AHW = F, H\mathbf{1}_{n_e} = \mathbf{1}_{n_p}, H \geq 0$$

where e_j is the j-th standard unit vector in $\mathbb{R}^{n_e}$.

$$TV\left(He_j\right) \triangleq \sum_{i=1}^{n_p} \left\| D_i\left(He_j\right)\right\|$$

$\|\bullet\|$ is the 2-norm in $\mathbb{R}^2$, and $D_i \in \mathbb{R}^{2\times n_p}$ denotes the discrete gradient operator at the i-th pixel.

III. SVD PREPROCESSING

In eq. (3), $AHW = F$, the size is $m\times n_b$, where $m << n_p, m << n_b$. In this section, we propose a preprocessing procedure based on singular value decomposition (SVD) of the observation matrix F to decrease the size of eq. (3) from $m\times n_b$ to $m\times n_e$. Typically, $n_e << n_b$.

Let $A\in\mathbb{R}^{m\times n_p}$ and $W\in\mathbb{R}^{n_e\times n_b}$ be full-rank, and $F\in\mathbb{R}^{m\times n_b}$ be rank- n_e with $n_e < \min\left\{n_b, n_p, m\right\}$. Let $F = U_e\sum_e V_e^T$ be the economy-size SVD of F where $\sum_e \in \mathbb{R}^{n_e\times n_e}$ is diagonal and positive definite, $U_e \in \mathbb{R}^{m\times n_e}$ and $V_e \in \mathbb{R}^{n_b\times n_e}$ both have orthonormal columns. Assume that $\text{rank}\left(WV_e\right) = n_e$, then the two linear systems below for $H\in\mathbb{R}^{n_p\times n_e}$ have the same solution set;

$$AHW = F \Leftrightarrow AHWV_e = U_e\sum_e \tag{4}$$

IV. ALGORITHMS

$$\min_{H} \sum_{j=1}^{n_e} TV\left(He_j\right) \text{ s.t. } AHWV_e = U_e \sum_e \tag{5}$$

To separate the discrete gradient operator from the non-differentiable TV term, splitting variables $v_{ij} = D_i\left(He_j\right)$ for $i = 1,...,n_p$ and $j = 1,...,n_e$. Then (5) becomes

$$\min_{H, v_{ij}} \sum_{i,j} \left\| v_{ij} \right\| \text{ s.t. } D_i\left(He_j\right) = v_{ij}, AHWV_e = U_e \sum_e \tag{6}$$

The augmented Lagrangian function for (6) can be written as

$$\begin{aligned} L_A\left(H, v_{ij}\right) \triangleq \sum_{i,j} \left\{ \left\| v_{ij} \right\| - \lambda_{ij}^T \left(D_i\left(He_j\right) - v_{ij} \right) + \frac{\alpha}{2} \left\| D_i\left(He_j\right) - v_{ij} \right\|_2^2 \right\} - \\ \left\langle \Pi, AHW - F \right\rangle + \frac{\beta}{2} \left\| AHW - F \right\|_F^2 - \nu^T \left(H\mathbf{1}_{n_e} - \mathbf{1}_{n_p} \right) + \frac{\gamma}{2} \left\| H\mathbf{1}_{n_e} - \mathbf{1}_{n_p} \right\|_2^2 \end{aligned} \tag{7}$$

where λ_{ij}, Π, ν are multipliers of appropriate sizes, and $\alpha, \beta, \gamma > 0$ are penalty parameters.

V. NUMERICAL RESULTS: SYNTHETIC DATA

In the experiments, we use randomized Walsh-Hadamard matrices as measurement matrices, *A*, considering that they permit fast transformation and easy hardware implementation. A Walsh-Hadamard matrix is randomized by choosing *m* random row from it and applying a random permutation to its columns.

Walsh-Hadamard (WH) Matrix (Matlab – hadamard)
The *N*-by-*N* WH matrices $\mathbf{H}_N$ are defined by $\mathbf{H}_1 = 1$ $\mathbf{H}_N = \begin{bmatrix} \mathbf{H}_{N/2} & \mathbf{H}_{N/2} \\ \mathbf{H}_{N/2} & -\mathbf{H}_{N/2} \end{bmatrix}$

A. Test Results on Synthetic Data

We selected $n_e = 4$ endmembers from the ASTER Spectral Library: nontronite, ferroaxinite, trona, and molybdenite. $n_b = 211$ spectral bands were selected in the range of 0.4 to 2.5 μm. The distributions of abundance fractions (물질별 점유비율) corresponding to 4 endmembers were given with a spatial resolution of $n_p = 64 \times 64$.

Synthetic abundance distributions ($H \in \mathbb{R}^{n_p \times n_e}$)	Endmember spectral signatures
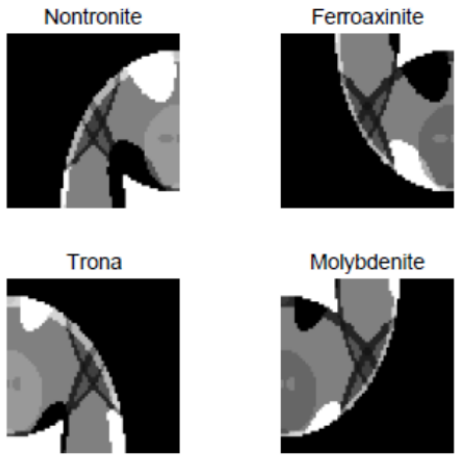	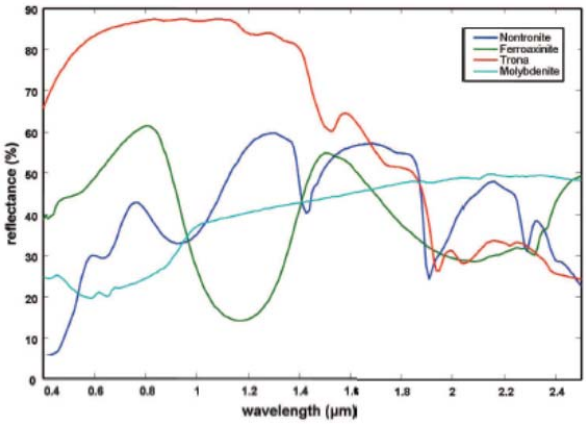
Recoverability for noisy and noise-free cases	
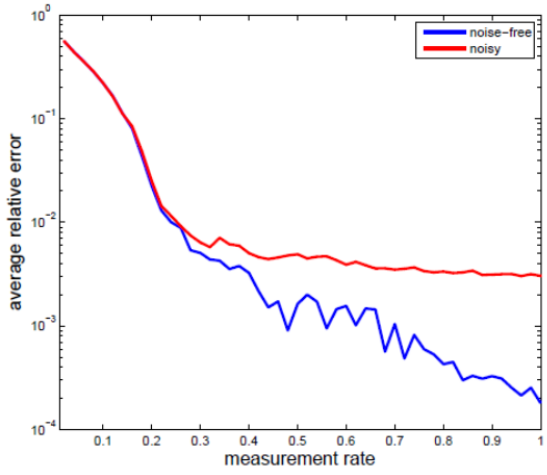	- Relative errors in computed abundance fractions versus measurement rate of compressed data on 100 distinct testing points with or without additive noise. - When measurement rate is greater than 20% in both noisy and noise-free cases, the CSU scheme attains relative error less than 1%.

In the second test, from the publicly available HYDIC Urban hyperspectral data, $n_b = 163$ bands in a range from 0.4 to 2.5 μm, $n_p = 307 \times 307$, $n_e = 6$ significant endmembers: road, metal, dirt, grass, tree, and roof.

"Urban" image and endmember selection	Spectral signatures with water absorption bands abandoned
	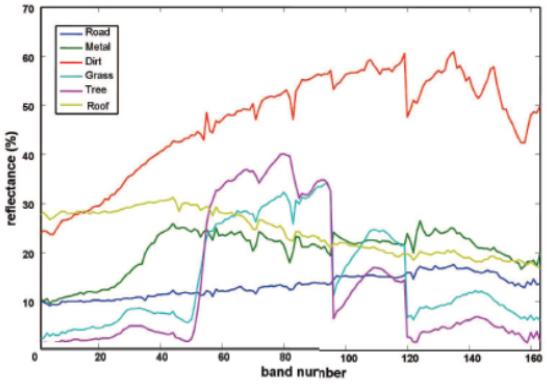

Unmixing results from 25% measurements are given below.

Computed abundance: solution obtained from 25% of measurements

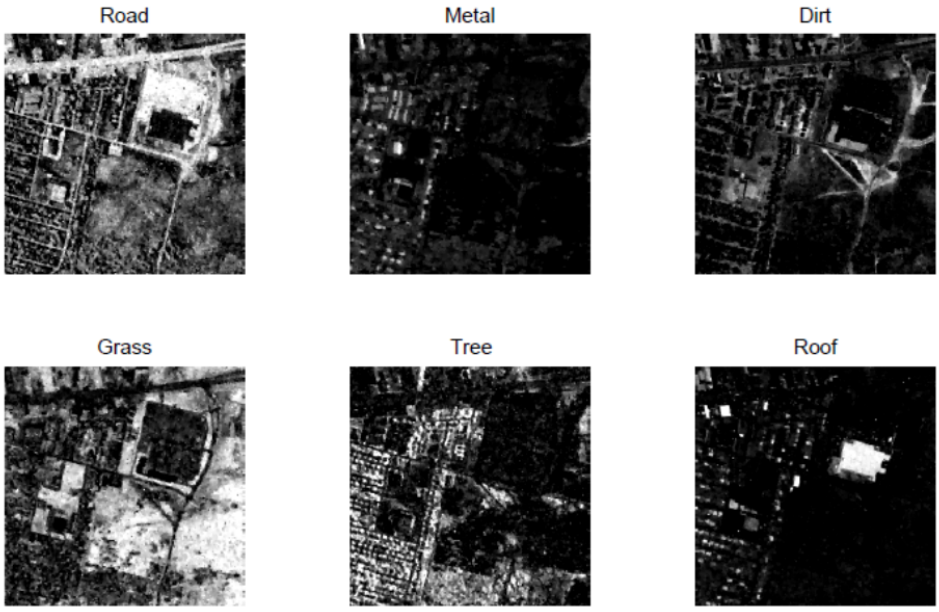

Estimated abundance: least squares solution

from directly solving $AHW = F$ for H with 100% data

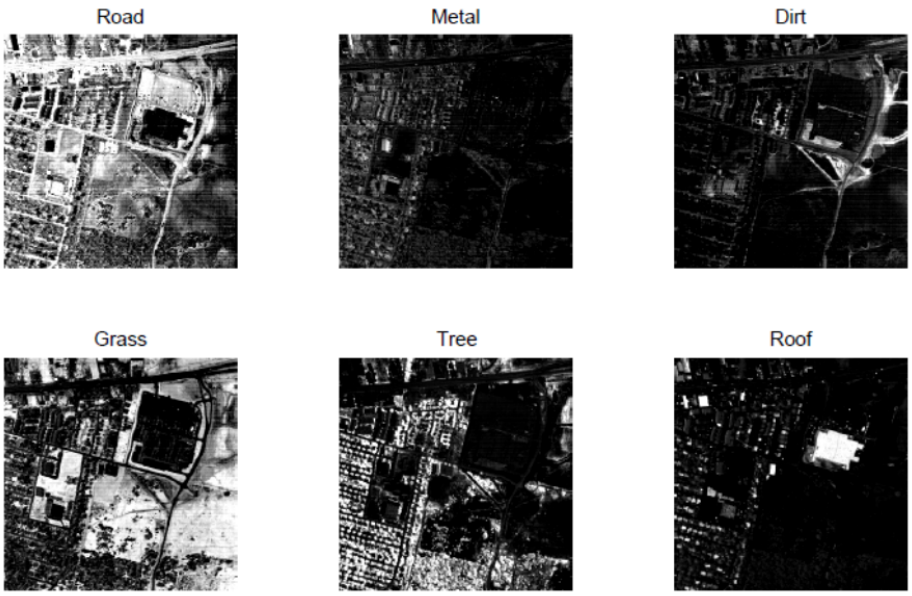

VI. Experimental Results: Hardware-Measured Data

A. Hardware Implementation

A compressive sensing hyperspectral imaging system is implemented based on a digital micro-mirror device (DMD). This system incorporates a micro-mirror array driven by pseudo-random patterns and one spectrometer.

$n_b = 175$ in the range of 0.4 to 0.75 μm, $n_p = 256 \times 256$, $n_e = 3$: yellow, cyan, and magenta

Single-pixel camera schematic for hyperspectral data acquisition	
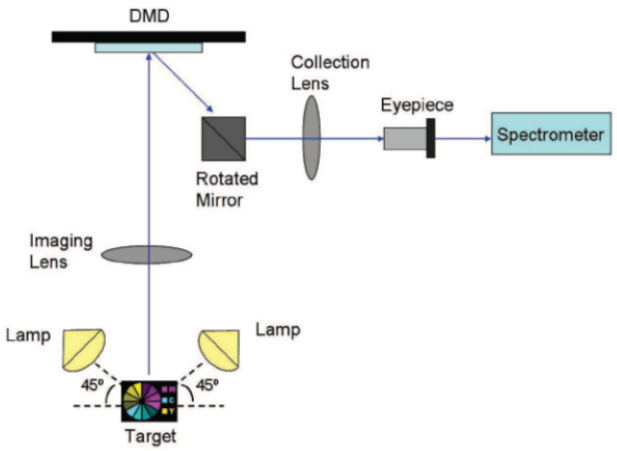	
Target image “Color wheel”	Measured spectral signatures of the three endmembers
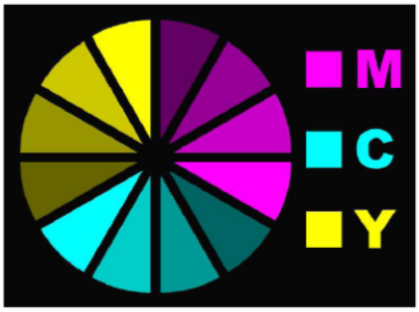	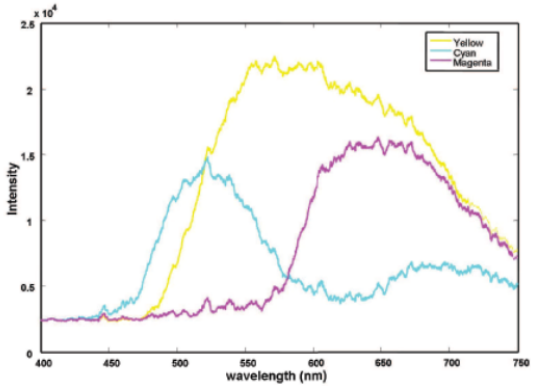

Estimated abundance (H): CS unmixing solution from 10% measurements
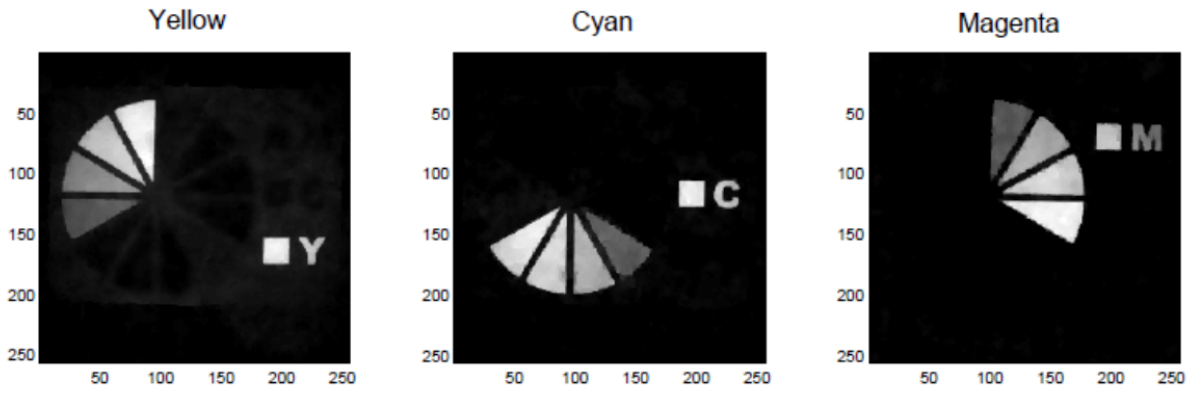

Four slices computed by the proposed approach ($X = HW$)	Four slices computed slice-by-slice by TV minimization
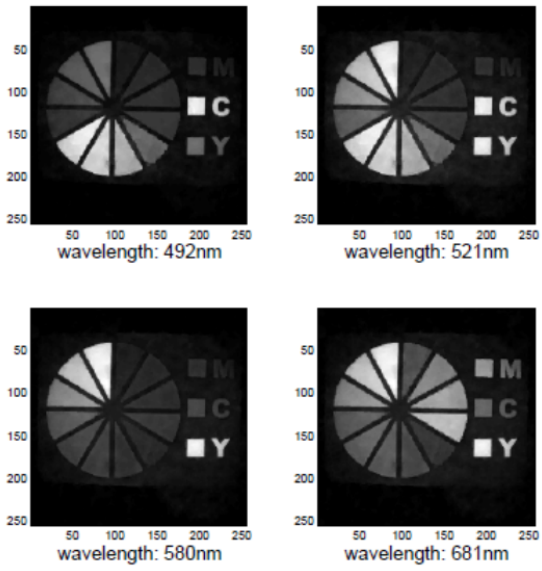	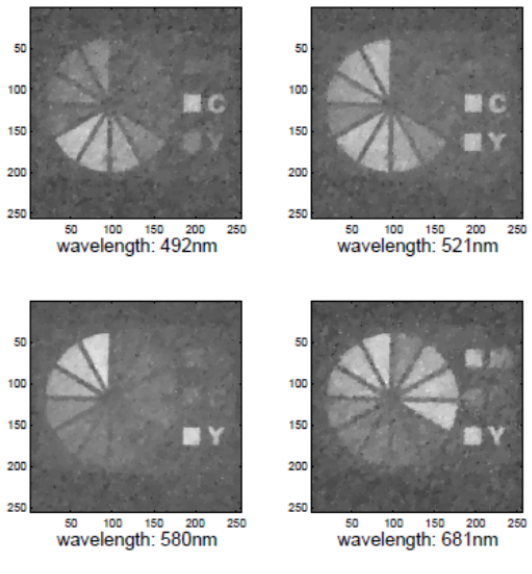

VII. Conclusion

This paper proposes a compressive sensing and unmixing (CSU) scheme for hyperspectral data processing that does not require forming or storing any full-size data cube. The CSU scheme consists of three major steps: 1) data acquisition by compressive sensing; 2) data preprocessing

by SCD; and (3) data unmixing by solving a compressed unmixing model with total-variation regularization on abundance fraction distributions.

VIII. DISCUSSION

After meeting, please write discussion in the meeting and update your presentation file.

Appendix

Reference

[1]
[2]
[3]

Dry and Noncontact EEG Sensors for Mobile Brain-Computer interface.

Yu Mike Chi et al. (Gert Cauwenberghs*)

IEEE Transactions on Neural Systems and Rehabilitation Engineering (2012)

Presenter : SeungChan Lee

GIST, Dept. of Information and Communication, INFONET Lab.

Gwangju Institute of Science and Technology

Background

- Various EEG electrodes

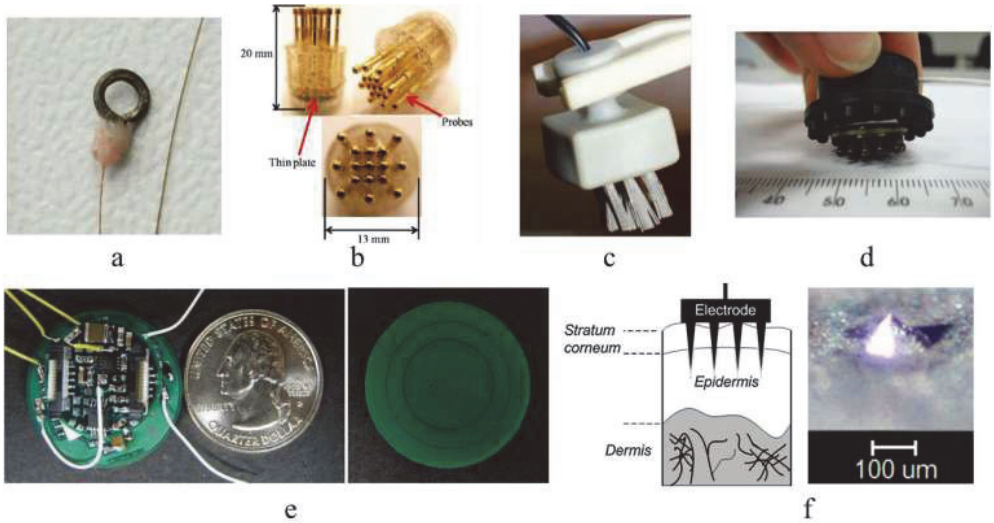

(a) a miniature passive ring electrode (b) a spring-loaded dry electrode (c) a bristle-type dry electrode (d) the Quasar hybrid EEG biosensor (e) a non-contact-type active dry EEG sensor (f) Diagram of a micro-tip electrode and the pyramidal shape of a micro-tip

Introduction

- Introduction
  - In EEG- based BCI systems, conventional BCI systems need extensive preparations such as scalp abrasion, conductive gels for good signal quality. Moreover, multiple wired electrodes are difficult to escape from laboratory scale experiments.
  - To overcome these problems, extensive research produced a variety of dry electrodes.
  - In this paper, they introduced dry and non-contact electrodes and evaluate their performance with SSVEP paradigms.
- Contents
  - Introduction of their dry and non-contact electrodes
  - Offline sensor benchmark with SSVEP paradigm
  - Online decoding test with mobile application

Dry electrodes

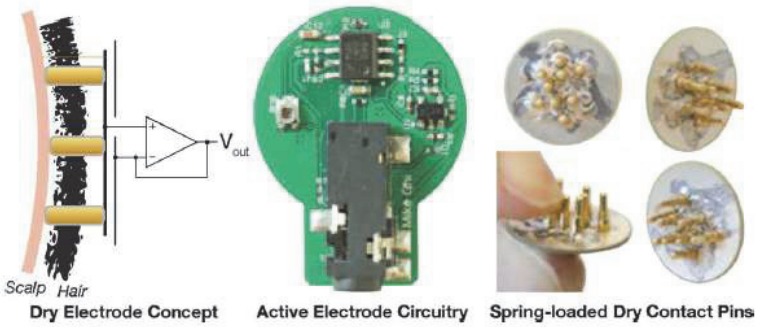

Dry Electrode Concept | Active Electrode Circuitry | Spring-loaded Dry Contact Pins

- Structure
  - Lower plate : a set of spring-loaded pins, a male snap connector
  - Upper PCB : active electrode circuitry (CMOS-input opamp, LMP7702)
  - Unity gain buffer (gain=1) with shielded cable
  - No discomfort, injury hazard

Non-contact electrodes

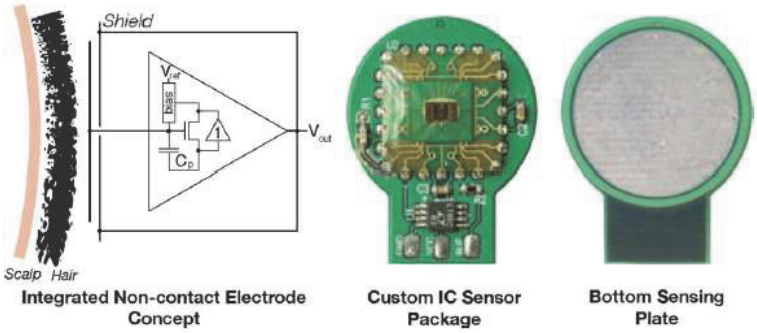

Integrated Non-contact Electrode Concept

Custom IC Sensor Package

Bottom Sensing Plate

- Structure
  - The electrodes operates via capacitive coupling on top of hair.
  - Based on a custom VLSI integrated analog front-end circuit

System design and mobile application

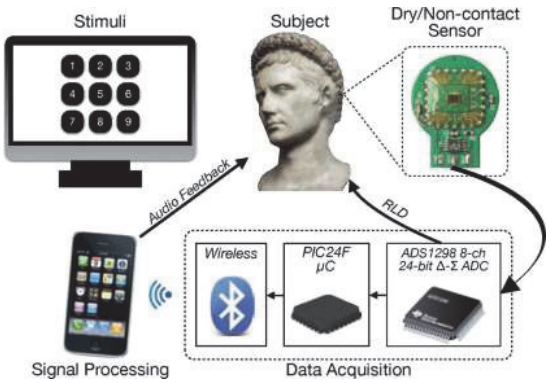

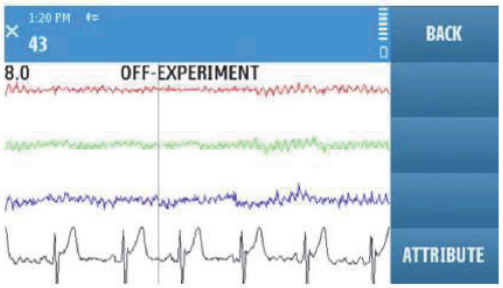

- Data acqusition
  - 24bit delta-sigma ADCs(TI ADS1298), PIC24F low-power microcontroller, onboard Bluetooth module, two AAA batteries (10 hours working time)
- Mobile signal processing
  - Nokia N97 cellular phone (640x360 pixel 3.5 inch touchscreen LCD)
  - Canonical correlation analysis(CCA) : band-pass filter and correlation calculation

CCA

- CCA is a multivariable statistical method used when there are two sets of data, which may have some underlying correlation.
- It finds a pair of linear combinations, for two sets, such that the correlation between the two canonical variables is maximized.
- Consider two multidimensional random variables X, Y and their linear combinations $x = X^T W_x$ and $y = X^T W_y$ respectively.
- CCA finds the weight vectors, Wx and Wy, which maximize the correlation between x and y, by solving the following problem:

$$\max_{W_x, W_y} \rho(x, y) = \frac{E[x^T y]}{\sqrt{E[x^T x]E[y^T y]}} = \frac{E[W_x^T X Y^T W_y]}{\sqrt{E[W_x^T X X^T W_x]E[W_y^T Y Y^T W_y]}}.$$

- The maximum of ρ with respect to Wx and Wy is the maximum canonical correlation. Projections onto Wx and Wy, i.e. x and y, are called canonical variants.

Offline sensor benchmark

- Test setting
  - Comparison electrodes : wet Ag/AgCl electrodes, proposed dry electrodes, proposed non-contact electrodes
  - Three sensors array are attached in a triad over the occipital region as closely together as possible.
  - 10 subjects
  - Each subject gaze at a single SSVEP target stimulus(10Hz) displayed on a CRT monitor for a 1-min duration.
  - Each subject repeated this task three times, and the best dataset was used for analysis.

Offline sensor benchmark

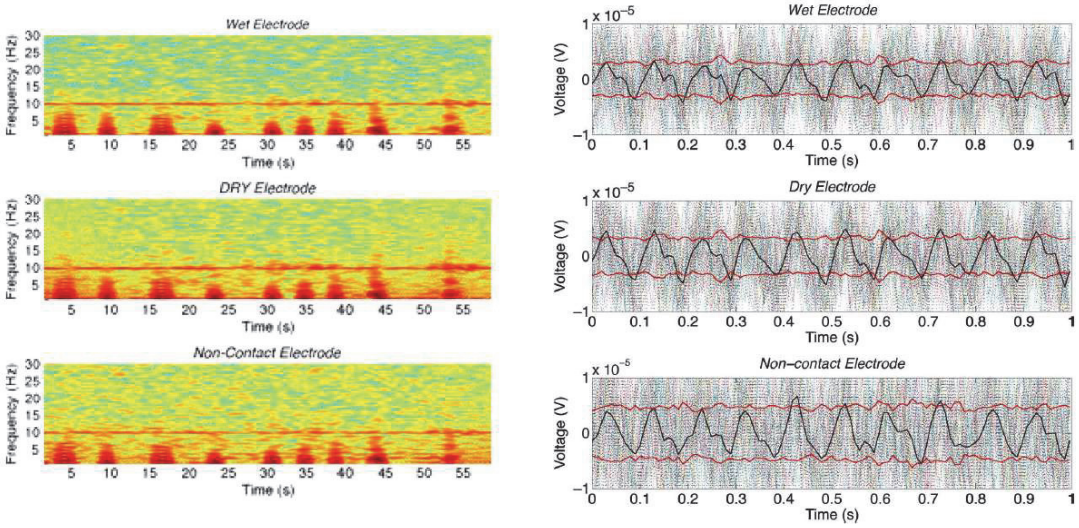

- Result plots
  - Left spectrograms are one of the 60s trials shown 10Hz SSVEP stimulus.
  - Right graphs show detailed signals with the average in black, the standard deviation in red with the raw signals.

Offline sensor benchmark

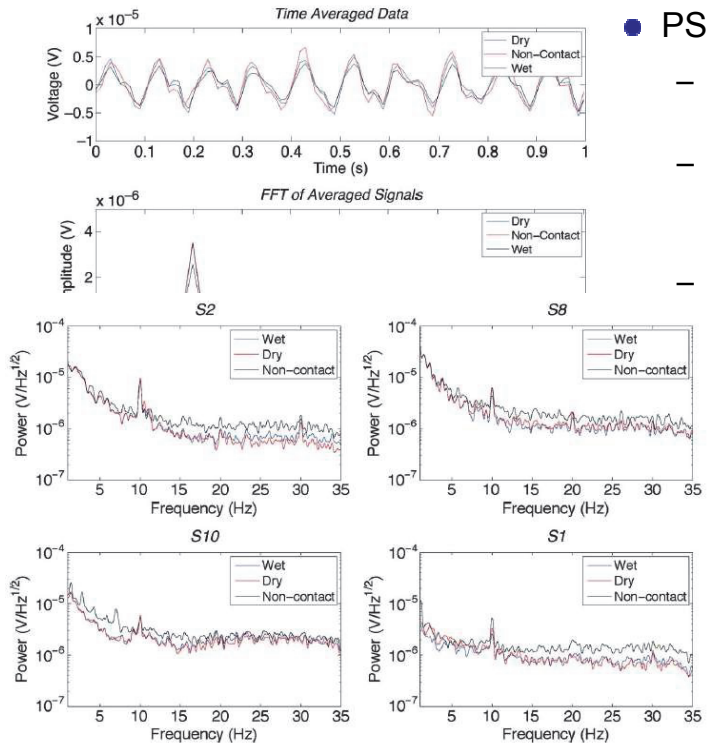

- PSD
  - In the four subjects shown the 10Hz stimulus is clearly visible.
  - PSD from the wet electrode almost perfectly matches that from the dry electrode.
  - The PSD of the noncontact electrode's signals also shows the 10Hz stimulus. But, there is greater amount of broadband noise due to their high coupling impedance.

Offline sensor benchmark

TABLE I
SIGNAL CORRELATION BETWEEN DIFFERENT ELECTRODES

Subject	SSVEP Amplitude (μV)			Sensor Correlation			SNR (dB)		
	Wet	Dry	NC	Wet vs. Dry	Wet vs. NC	Dry vs. NC	Wet	Dry	NC
1	1.1	1.7	2.2	0.88	0.85	0.74	-15.16	-10.97	-10.36
2	3.7	3.7	3.2	0.98	0.88	0.85	-6.49	-7.00	-8.46
3	1.9	2.0	2.1	0.90	0.78	0.70	-11.71	-12.24	-12.96
4	2.2	2.2	2.4	0.97	0.80	0.78	-7.69	-8.09	-8.22
5	1.1	1.1	1.0	0.97	0.96	0.94	-12.24	-11.87	-13.05
6	1.6	1.2	1.4	0.75	0.71	0.55	-6.61	-10.49	-9.67
7	1.6	1.1	1.8	0.91	0.86	0.88	-14.33	-13.61	-10.72
8	2.5	3.4	3.5	0.93	0.73	0.70	-6.85	-5.17	-7.47
9	1.4	0.8	0.8	0.89	0.85	0.85	-13.08	-17.42	-17.64
10	1.4	1.8	1.4	0.95	0.57	0.59	-15.60	-13.29	-18.21
Mean	**1.8**	**1.9**	**2.0**	**0.91**	**0.80**	**0.76**	**-10.98**	**-11.01**	**-11.68**
STD	0.8	1.0	0.9	0.07	0.11	0.13	3.71	3.56	3.78

$$\mathrm{SNR} = 10\ \log_{10} \frac{\bar{X}(10\ \mathrm{Hz})^2_{\mathrm{rms}}}{var(x) - \bar{X}(10\ \mathrm{Hz})^2_{\mathrm{rms}}}.$$

- Correlation and SNR
  - Over half the subjects has a correlation of greater than 0.9 between the wet and dry electrodes.
  - Correlation values of the wet versus noncontact electrode were lower. But, half the subject had correlation values of above 0.8.

Online decoding test

- Test setting
  - Subjects 1 and 2 were recalled to perform an SSVEP phone dialing task using the mobile signal processing platform.
  - Procedure
    - 4s sliding window with 1s increments
    - Two consecutive decisions are constructed as a successful input and trigger an audio feedback to notify the subject
    - Noncontact electrodes
      - 6s sliding window with four consecutive decisions due to degraded SNR
  - Predetermined 12 digit sequence
  - Signal decoding performed using CCA analysis

Online decoding test

TABLE III
RESUL: FROM ONLINE BCI TESTS

		Accuracy			Detection Time (1.)			ITR (bitvmin)		
		Wet	Dry	NC	Wet	Dry	NC	Wel	Dry	NC
Subject 1	Trial 1	0.83	0.92	1.00	6.2	5.7	10.3	23.0	28.1	19.3
	Trial 2	0.83	0.83	1.00	5.9	5.8	9.7	23.9	22.6	20.5
	Trial 3	0.83	1.00	1.00	6.4	5.6	*9A*	20.5	*3-'A*	21.0
Subjecl 2	Trial 1	0.83	0.83	0.50	6.2	5.9	12.8	23.0	23.9	4.0
	Trial 2	0.83	0.92	0.75	5.9	6.3	9.7	23.9	27.3	11.9
	Trial 3	0.92	0.83	0.75	5.7	6.3	11.0	29.2	22.6	10A
	Mean	0.85	0.89	0.83	6.04	5.92	10.49	23.9	26.5	14.5
	STO	0.03	0.07	0.20	0.26	0.31	1.29	2.90	4.52	6.85

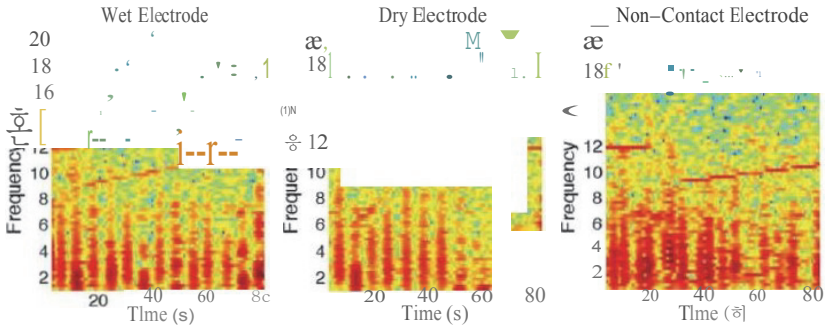

Online decoding test

- Discussion of online test
  - In subject 1's spectrograms for the three different electrodes, the different SSVEP frequencies are clearly visible.
  - The wet and dry electrodes were could both be successfully used for BCI.
  - The dry electrode trials achieved superior performance to the wet electrode trials because the wet electrodes was tested last
  - Noncontact electrodes
    - Subject 1achieve 100% accuracy with noncontact electrodes because of longer detection window. But they achieve lower ITR (19 bits/min).
    - Subject 2 had difficulty with utilizing the noncontact electrodes due to thicker hair.

Conclusion

- Quantitative benchmarking show that dry and noncontact electrodes are capable of resolving SSVEP-type signals.
  - The dry electrode only shows a slight amount of signal degradation.
  - The noncontact electrodes show more signal degradation and susceptibility to movement artifacts.
- However, the online test demonstrate that both electrodes can be successfully utilized in BCI applications.
- The signal quality of noncontact electrodes is possible to still resolved with careful circuit design.

INFONET Seminar Application Group 05/25/2013

Exemplar-Based Processing for Speech Recognition

Tara N. Bhuvana Ramabhadra.
IEEE SIGNAL PROCESSING MAGAZINE

Presenter Pavel Ni

Gwangju Institute of Science and Technology

Introduction

Automatic Speech Recognition is the translation of spoken words in to text.
(Voice dial, Apple Siri, Google One Voice, Samsung S voice)

Recognition and classification of speech requires modeling of speech production and uncertainty in it. Vocal tract complexity noise corruption, and vocal tract variations amongst different people arise uncertainty.

The goal of modeling is to establish a generalization from the set of observed data such that accurate classification can be made about unseen data i.e. speaker independent speech recognition.

Introduction

Construction of the model leads to two categories of approaches for modeling the observed data:

- Global-data model uses all available training data to build a model before the test sample seen
  - allow for a generalization of the observed data only if distribution estimated by the model provides a reasonable description of unseen data.
  - with limited training data unable of representing the fine detail in distribution of the data. Therefore require large amount of training data.

- exemplar based modeling since the model is build from a few relevant training examples for each test sample.
  - Building an instance of the model based only on the relevant and informative exemplars. Doesn't need large data however for each query builds local model.

Speech recognition problem

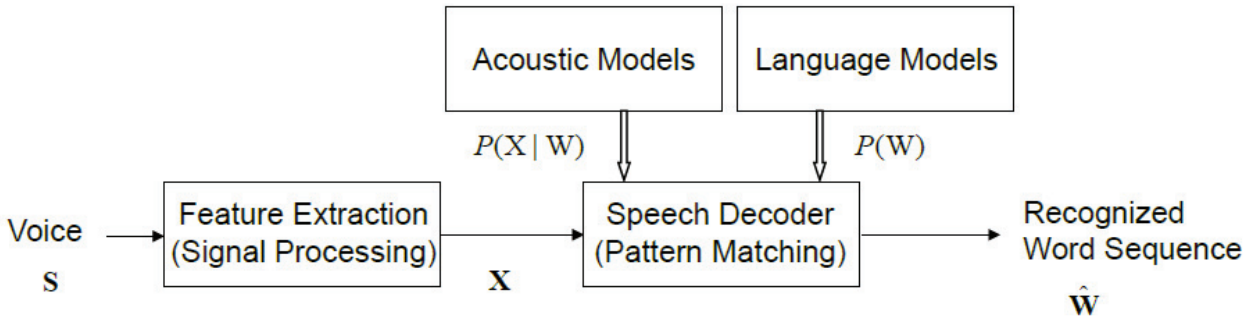

Figure 1. Block diagram of speech recognition system

Where X is a set of observations, W sequence of words.

Acoustic model: physics of sound speech, models of vocal tract
Language model: syntax and semantics

$$\hat{W} = \arg\max_{W} P(W \mid X) = \arg\max_{W} \frac{P(X \mid W)P(W)}{P(X)}$$

In speech recognition we need to find sequence of words $\hat{W}$. The common solution is to find the word sequence that maximizes the posterior probability $P(W \mid X)$

System overview

Features - such as power, pitch, and vocal tract configuration fr om the speech signal.
Frames – fixed length features

3 stages of recognition:
- Exemplar selection
- Instance modeling
- Frame decoding

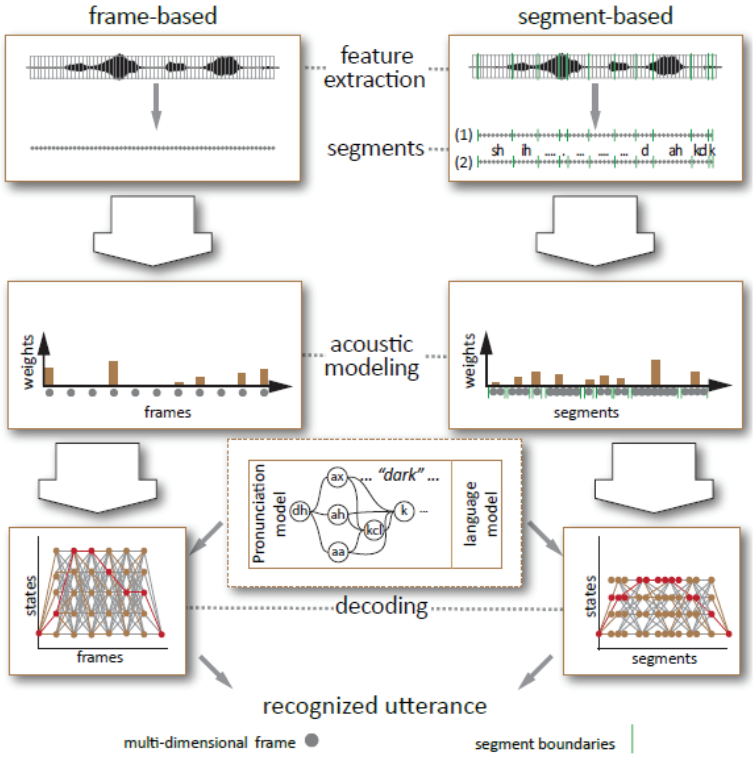

Figure 2. Frame and segment based recognition

System overview

- Exemplar selection

Identifies instances from the training data which are more relevant to test inst ances. Training set selectively downsampled to simplify the search and then appropriate exemplars are taken from this reduced set.

- Instance modeling

Set of training instances which most relevant for test instance is used to mode l the test instance. Weight distribution using k-NN (near neighbors) or sparse r epresentation (SR or compressive sensing)

- Frame decoding

Recognizing an entire sentence.

k-Nearest Neighbors

k-NN algorithm classifies test point based on *k* closest neighbors in the training set.
Exemplar selection: exemplars for individual frames, fixed length sequences of multiple frames

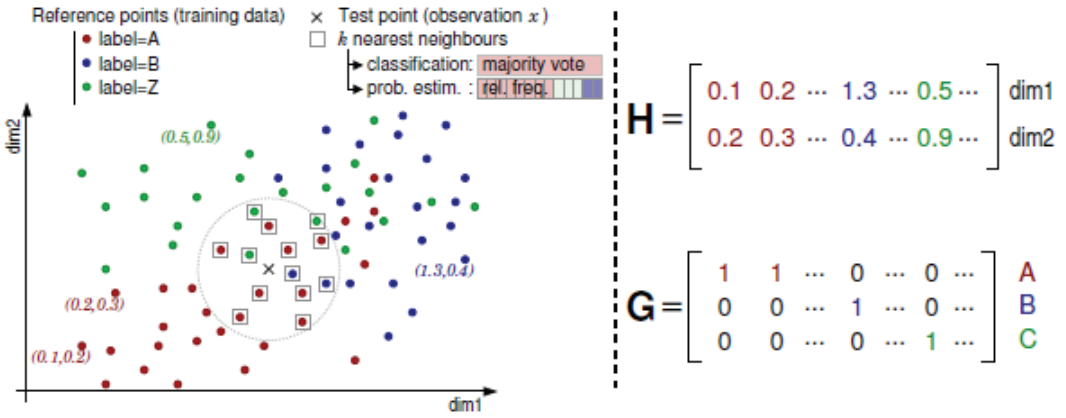

Figure 3. An example of k-NN in a 2-D feature space. In the left panel the distance between an observed feature vector *x* and a set of exemplars are shown, and in the right panel the mathematical description of the exemplars and the exemplar-label association, H and G respectively, is visualized. The columns of H and G correspond to the exemplars in the left panel.

k-Nearest Neighbors

In order to extract useful information for speech recognition or classification exemplars are associated with label. (phone classes and word labels)
Matrix G is a binary matrix that associates each exemplar in H with class labels.

Classification made by maximum likelihood.

Sparse Representation classification

Test vector y, dictionary H with exemplars h_i from training set.
Where H is a $m \times N$ matrix where m is the dimension of each feature vector x and N is the total number of all training examples from all class es. (m<<N)

Then vector y can be written as linear combination of all training examples.

$$y = H\beta$$

β should be sparse with non-zero elements for the elements in H which belong to the same class.

Results: Sparse representation reconstruction features was tested on TIMIT database. Phonetic Error Rate 18.6%. 0.8% improved over a state-of-art GMM/HMM

Thank you

A cell-phone-based brain-computer interface for communication in daily life

Yu-Te Wang, Yijun Wang and Tzyy-Ping Jung

Journal of Neural Engineering (2011.03)

Presenter : Soogil Woo

GIST, Dept. of Information and Communication, INFONET Lab.

Gwangju Institute of Science and Technology

Introduction

- BCI systems acquire EEG signals from the human brain and translate them into digital commands which can be recognized and processed on a computer.
- Although EEG-based BCIs have already been studied for several decades, moving a BCI system from a laboratory demonstration to real-life application still poses severe challenges to the BCI community.
- In real-life applications, BCI systems should not use bulky, expensive, wired EEG acquisition devices and signal processing platforms.
- Several studies have demonstrated the use of portable devices for BCIs.
- Recently, with advances in integrated circuit technology, cellphones combined with DSP and built-in Bluetooth function have become very popular in the consumer market.

Introduction

- If a cell-phone-based BCI proves to be feasible, many current BCI demonstrations (gaming, text messaging) can be realized on cell phones in practice and numerous new applications might emerge.
- This system consists of a four-channel bio-signal acquisition /amplification module, a wireless transmission module and a Bluetooth-enabled cell phone.
- SSVEP is the electrical response of the brain to the flickering visual at a repetition rate higher than 6Hz.
- SSVEP-based BCI, which has recognized advantages of ease of use, little user training and high information transfer rate (ITR), was employed as a test paradigm.
- In an SSVEP BCI, the attended frequency-coded targets of the user are recognized by detecting the dominant frequency of the SSVEP.
- This study implemented and tested both single-channel FFT and multi-channel canonical correlation analysis (CCA) methods for processing SSVEPs induced by attended targets.

System Architecture

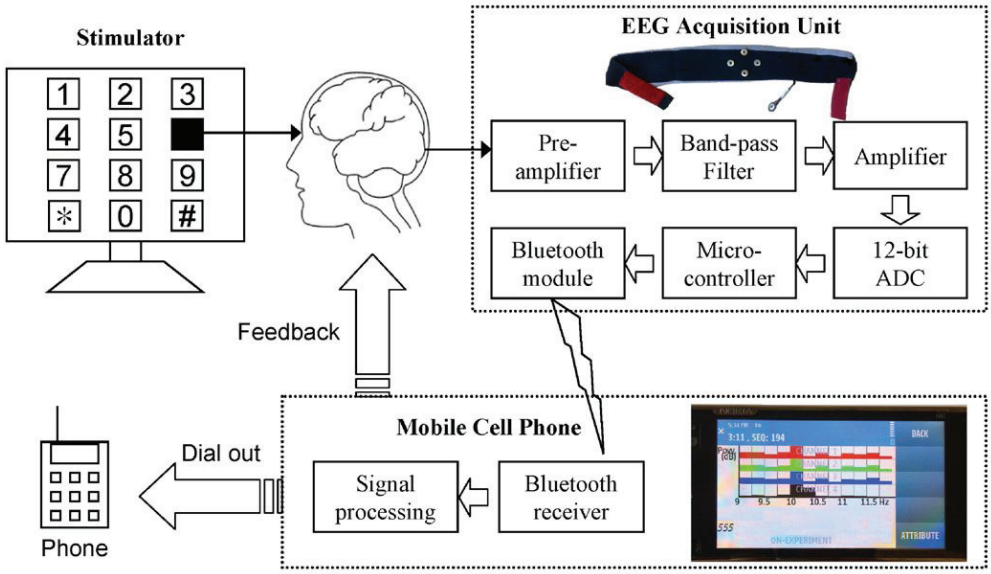

- System hardware diagram
- System software design
- BCI experiment design

System hardware diagram

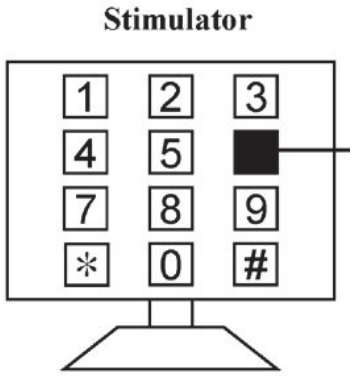

- The visual stimulator comprises a 21 inch CRT monitor with 4*3 stimulus matrix constituting a virtual telephone keypad which includes digits 0-9, BACKSPACE and ENTER.
- The stimulus frequencies ranged from 9 to 11.75 Hz with an interval of 0.25Hz between two consecutive digits.
- The stimulus program was developed in Microsoft Visual C++ using the Microsoft DirectX 9.0 framework.

System software design

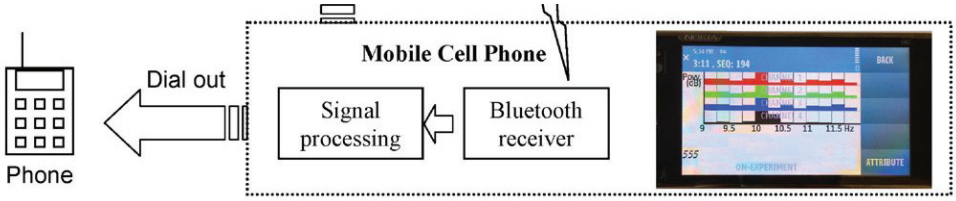

- The signal-processing unit was realized using a Nokia N97 cell phone.
- A J2ME program developed in BorlandJBuilder2005 and Wireless Development Kit 2.2 were installed to perform online procedures including :(1) displaying EEG signals in time-domain, frequency-domain and CCA-domain on the LCD screen of the cell phone, (2) band-pass filtering, (3) estimating the dominant frequencies of the VEP using FFT or CCA, (4) delivering auditory feedback to the user, (5) dialing a phone call
- Users can choose the format of the display btw time-domain and frequency-domain.
- Under the frequency-domain display mode, the power spectral densities of 40channel EEG will be plotted on the screen and updated every second.

System software design

- In the FFT mode, a 512 point FFT is applied to the EEG data using a 4 sec moving window advancing at 1 sec steps for each channel.
- In the CCA mode, it uses all four channels of the EEG with a 2 sec moving window advancing 1 sec steps.
- To improve the reliability, a target is detected only when the same dominant frequency is detected in two consecutive windows.
- At the k and k+1 sec, k≥4 in the FFT mode
- At the k and k+1 sec, k≥2 in the CCA mode
- The subjects were instructed to shift their gaze to the next target once they heard the auditory feedback.

System BCI experiment design

- The experiments were conducted in a typical office room without room without any electromagnetic shielding.
- Subjects were seated in a comfortable chair at a distance of about 60cm from screen.
- Four electrodes on the EEG headband were placed 2cm apart, surrounding a midline occipital (Oz) site, all referred to a forehead midline electrode.
- The FFT- and CCA-based approaches were tested separately.
- All subjects participated in the experiments during which the cell phone used FFT to detect frequencies of SSVEPs, and four subjects were selected to do a comparison study btw using FFT and CCA for SSVEP detection.
- In the FFT mode, the channel with highest SNR, which is based on the power spectra of the EEG data, was selected for online target detection.
- The EEGs in the CCA experiments were feedback codes for an offline comparison study btw FFT and CCA.

Results

- Tables show results of the SSVEP BCI using FFT and CCA.

Subject	Input length	Time (s)	Accuracy (%)	ITR (bits min^{-1})
s1	11	72	100	32.86
s2	11	72	100	32.86
s3	19	164	78.9	14.67
s4	11	73	100	32.4
s5	17	131	82.4	17.6
s6	11	67	100	35.31
s7	11	72	100	32.86
s8	13	93	92.3	20.41
s9	11	79	100	29.95
s10	11	66	100	35.85
Mean	12.6	88.9	95.9	28.47

FFT-based online test results of the SSVEP BCI in ten subjects

Results

- Tables show results of the SSVEP BCI using FFT and CCA.

Subject	Online CCA	Online FFT	Offline FFT	Putative ITR from offline FFT			
				Ch1	Ch2	Ch3	Ch4
s1	44.79	32.86	36.68	**36.68**	33.58	32.48	29.77
s2	46.25	32.86	26.49	**26.49**	10.51	5.91	9.29
s6	49.05	35.31	19.43	**19.43**	3.03	3.15	1.92
s10	43.18	35.85	15.24	2.2	8.46	**15.24**	4.21
Mean	45.82	34.22	24.46	21.2	13.9	14.2	11.3

CCA-based test results (ITR) of the SSVEP BCI in four subjects. In each row, the bold value highlights the maximum ITR of single channel FFT.

Discussions and conclusions

- This study designed, developed and evaluated a portable, cost effective and miniature cell-phone-based online BCI platform for communication in daily life.
- The practicality and implications of the proposed BCI platform were demonstrated through the high accuracy and ITR of an online SSVEP-based BCI.
- The decline in accuracy and ITR in offline FFT analysis could be attributed to a lack of sufficient data for FFT to obtain accurate results.
- In other words, FFT, in general, required more data than CCA to accurately estimate the dominant frequencies in SSVEPs.

Thank you!

Appendix(CCA)

- Canonical correlation analysis (CCA) is a multivariable used when there are two sets of data, which may have some underlying correlation.
- It finds a pair of linear combinations, for two sets, such that the correlation btw the two canonical variables is maximized.
- Consider two multidimensional random variables X, Y and their linear combinations $x = X^T W_x$ and $y = Y^T W_y$.

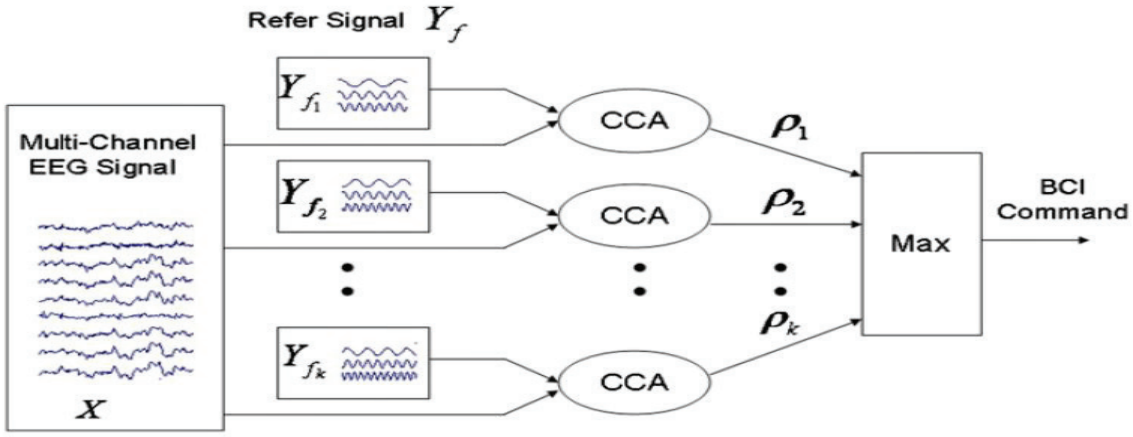

An illustration for usage of CCA in EEG signals analysis

Appendix(CCA)

- CCA finds the weight vectors, W_x and W_y, which maximize the correlation btw x and y, by solving the following problem:

$$\max_{W_x, W_y} \rho(x, y) = \frac{E[x^T y]}{\sqrt{E[x^T x]E[y^T y]}}$$
$$= \frac{E[W_x^T X Y^T W_y]}{\sqrt{E[W_x^T X X^T W_x]E[W_y^T Y Y^T W_y]}}$$

- The maximum of ρ with respect to W_x and W_y is the maximum canonical correlation. Projections onto W_x and W_y, i.e. x and y, are called canonical variants.

Supervised Machine Learning: A Review of Classification Techniques

Kotsiantis S.B.

Informatica (2007)

Presenter : Evgenii Kim

GIST, Dept. of Information and Communication

Gwangju Institute of Science and Technology

Outline

- Introduction
- General issues of supervised learning algorithms
- Logic based algorithms
- Perceptron-based techniques
- Instance-based learning
- Support Vector Machines
- Discussion
- Conclusion

Introduction

- Machine learning (ML) is about the construction and study of systems that can learn from data.
- There are three types:
  - Supervised
  - Unsupervised
  - Reinforcement (The training information provided to the learning system by the environment)
- Numerous ML can be set up as supervised

General issues of supervised ML

- There are several main steps:
  1. Collecting the dataset. In case of unknowing required feature we are measuring everything available in the hope that it is right. But in most of cases it contains noise and missing feature values, therefore the pre-processing is significant.
  2. Data pre-processiong. The goal is to maintain the mining quality while minimizing the sample size.
  3. Feature subset selection (feature extraction). It is a process of identifying and removing as many irrelevant and redundant features as possible. This reduces the dimensionality of the data
  4. Classification

Algorithm selection

- The choice of which specific learning algorithm we should use is a critical step. The classifier's evaluation is most often based on prediction accuracy.
- There are at least three techniques:
  - Split training set by two-thirds for training and the other third for estimate accuracy.
  - Cross-validation
  - Leave-one-out

Decision trees

- Decision trees are trees that classify instances by sorting them based on feature values.
- Each node in the tree represents a feature in an instance to be classified
- Each branch represents a value that the node can be assume
- The feature that best divides the training data would be the root node of the tree.
- This method is quite sensitive to overfitting
- The most straightforward way of tackling overfitting is to prune the decision tree.
- One of the famous algorithm to generate a decision tree is C4.5

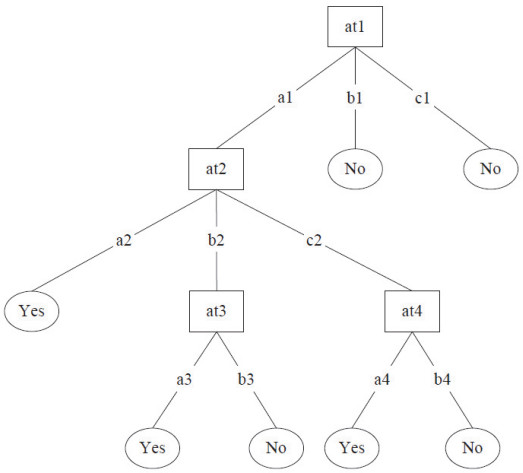

A decision tree

Single layered perceptrons

- Input feature values $x_1,...,x_n$
- Connection weights/predication vector (typically real numbers in the interval [-1,1]) $w_1,...,w_n$
- The single layered perceptron computes the sum of weighted inputs: $\sum x_i w_i$ and output goes through an adjustable threshold: if the sum is above threshold, output is 1; else it is 0.
- WINNOW (1994) is based on the perceptron idea and updates its weights.
- If prediction value $y' = 0$ and actual value is 1 , then the weights are too low; so, for each feature x_i, $w_i = w_i \cdot \alpha$, where $\alpha > 1$
- If $y' = 1$ and actual value is 0, then the weight is too high $w_i = w_i \cdot \beta$, where $0 < \beta < 1$

Multilayered perceptrons

- Perceptrons can not classify non-linear problem.
- To solve this problem the multilayered perceptron has been created.
- A multi-layer neural neural network consists of large number of units joined together in a pattern of connections
- Units are usually segregated into three classes: input units; output units; and units in between known as hidden units

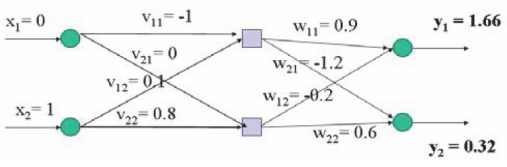

Feed-forward ANN

Multilayered perceptrons

- Generally, properly determining the size of the hidden layer is a problem, because to small number can be cause lower accuracy , while excessive nodes can result of overfitting.
- The second important step is to calculate weight
- The most well-known and widely used learning algorithm to estimate the values of the weights is the Back Propagation

Radial Basis Function (RBF) networks

- An RBF network is a three-layer feedback network, in which each hidden unit implements a radial activation function aand each output unit implements a weighted sum of hidden units outputs
- Training procedure:
  - Determining of hidden layer
  - Connections between hidden layer and output are determined by LMS

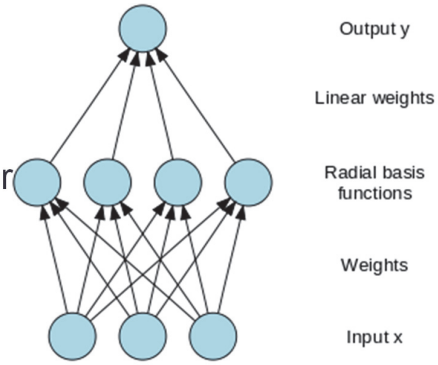

- The problem of selecting the appropriate number of basis functions remains a critical issue for RBF.

Instance-based learning

- Instance-based learning is lazy- learning algorithm, as they delay the induction or generalization process until classification is performed.
- It is required less time during training (compare with decision tree, neural, Bayes) but more time during making decision.
- One the instance-based algorithm is nearest neighbour
- The absolute position of the instances within this space is not as significant as the relative distance between instances.
- This distance is determined by using a distance metric

kNN

- The power kNN has been demonstrated in a number of real domains, but it also has some problem:
  - It is required large storage
  - It is sensitive to the choice of the similarity function that is used to compare instances
  - There is not principle way to choose k

Minkowsky: $D(x,y)=\left(\sum_{i=1}^{m}\lvert x_i-y_i\rvert^r\right)^{1/r}$
Manhattan: $D(x,y)=\sum_{i=1}^{m}\lvert x_i-y_i\rvert$
Chebychev: $D(x,y)=\max_{i=1}^{m}\lvert x_i-y_i\rvert$
Euclidean: $D(x,y)=\left(\sum_{i=1}^{m}\lvert x_i-y_i\rvert^2\right)^{1/2}$
Camberra: $D(x,y)=\sum_{i=1}^{m}\frac{\lvert x_i-y_i\rvert}{\lvert x_i+y_i\rvert}$
Kendall's Rank Correlation: $D(x,y)=1-\frac{2}{m(m-1)}\sum_{i=j}^{m}\sum_{j=1}^{i-1}sign(x_i-x_j)sign(y_i-y_j)$

Approaches to define the distance between instances (x and y)

Support Vector Machines

- SVMs revolve around the notation of a "margin"- either side of hyperplane that separates two data classes.
- Maximizing the margin and thereby creating the largest possible distance between the separating hyperplane and the instances on either side of it has been proven to reduce an upper bound on the expected generalization error.
- If the training data is linearly separable, then a pair (*w,b*) exists such that $\mathbf{w}^T\mathbf{x}_i + b \geq 1, \text{ for all } \mathbf{x}_i \in P$

  $\mathbf{w}^T\mathbf{x}_i + b \leq 1, \text{ for all } \mathbf{x}_i \in N$
- With the decision rule given by $f_{\mathbf{w},b}(\mathbf{x}) = \text{sgn}(\mathbf{w}^T\mathbf{x} + b)$
- Kernel trickes

Discussion

	Decision Trees	Neural Networks	Naïve Bayes	kNN	SVM	Rule-learners
Accuracy in general	**	***	*	**	****	**
Speed of learning with respect to number of attributes and the number of instances	***	*	****	****	*	**
Speed of classification	****	****	****	*	****	****
Tolerance to missing values	***	*	****	*	**	**
Tolerance to irrelevant attributes	***	*	**	**	****	**
Tolerance to redundant attributes	**	**	*	**	***	**
Tolerance to highly interdependent attributes (e.g. parity problems)	**	***	*	*	***	**
Dealing with discrete/binary/continuous attributes	****	***(not discrete)	***(not continuous)	***(not directly discrete)	**(not discrete)	***(not directly continuous)
Tolerance to noise	**	**	***	*	**	*
Dealing with danger of overfitting	**	*	***	***	**	**
Attempts for incremental learning	**	***	****	****	**	*
Explanation ability/transparency of knowledge/classifications	****	*	****	**	*	****
Model parameter handling	***	*	****	***	*	***

Comparing learning algorithms (**** stars represent the best and * star the worst performance)

Conclusion

- The SVM has been shown the best accuracy, but it also has weak point.
- By combination of different ML algorithms the efficiency can be improved.

Title: Digital holography for quantitative phase-contrast imaging

Etienne Cuche, Frederic Bevilacqua, and Christian Depeursinge
Institute of Applied Optics, Swiss Federal Institute of Technology, CH-1015 Lausanne, Switzerland

Presenter: Nitin Rawat

The holographic process is described mathematically as follows:

$$O(x,y) = o(x,y)\,\mathrm{e}^{i\varphi_o(x,y)} \quad \text{... (1.1)}$$

Is the complex amplitude of the object wave with real amplitude o and phase φ_o and

$$R(x,y) = r(x,y)\,\mathrm{e}^{i\varphi_R(x,y)} \quad \text{... (1.2)}$$

Is the complex amplitude of the reference wave with real amplitude r and phase φ_R

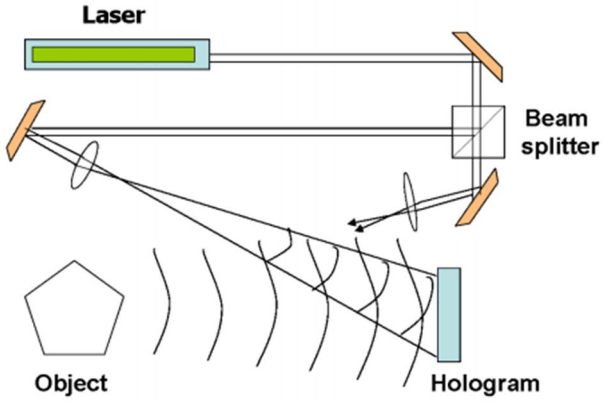

Fig. 1 Construction of a hologram

Both waves interfere at the surface of the recording medium. The intensity is calculated by

$$\begin{aligned} I_H(x,y) &= \left|O(x,y)+R(x,y)\right|^2 \\ &= (O(x,y)+R(x,y))(O(x,y)+R(x,y))^* \\ &= R(x,y)R^*(x,y)+O(x,y)O^*(x,y) \\ &+ O(x,y)R^*(x,y)+R(x,y)O^*(x,y) \end{aligned} \quad \text{... (1.3)}$$

Digital Recording

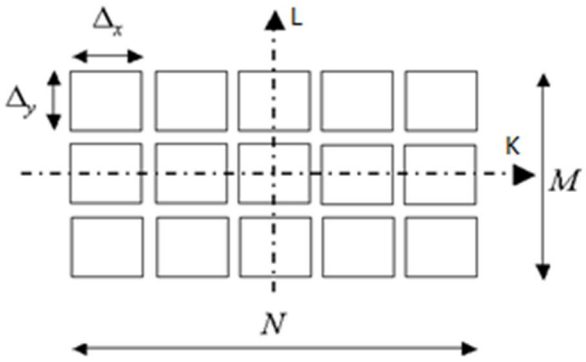

Fig. 2 Concept diagram of a surface-pixel sensor

The digital recording will (depending on the directions x and y on the recording plane) consist of M x N pixels. Each of these pixels is of a dimension $\Delta_x \times \Delta_y$. In CCD sensors, Matrices made up of photosensitive elements called pixels are generally square-shaped. In our case it is $12 \times 12 \mu m$

In their case, the hologram intensity was recorded by a standard black and white CCD camera (Hitachi Denshi KP-M2).

The two neutral-density filters allow the adjustment of the object and the reference intensities.

A square image of area LxL (Sensor size) = 4.83mm X 4.83mm containing N x N= 512 x 512 pixels is acquired in the center of the CCD sensor, and a digital hologram is transmitted to a computer via a frame grabber.

The digital hologram $I_H(k,l)$ results from two-dimensional spatial sampling of $I_H(x,y)$ by the CCD:

$$I_H(k,l) = I_H(x,y) rect\left(\frac{x}{L}, \frac{y}{L}\right) \times \sum_{k}^{N} \sum_{l}^{N} \delta(x - k\Delta x, y - l\Delta y) \quad \text{... (1.5)}$$

Where k and l are integers $(-N/2 \le k,l \le N/2)$ and Δx and Δy are the sampling intervals in the hologram plane i.e. pixel size: $\Delta x = \Delta y$ =L/N

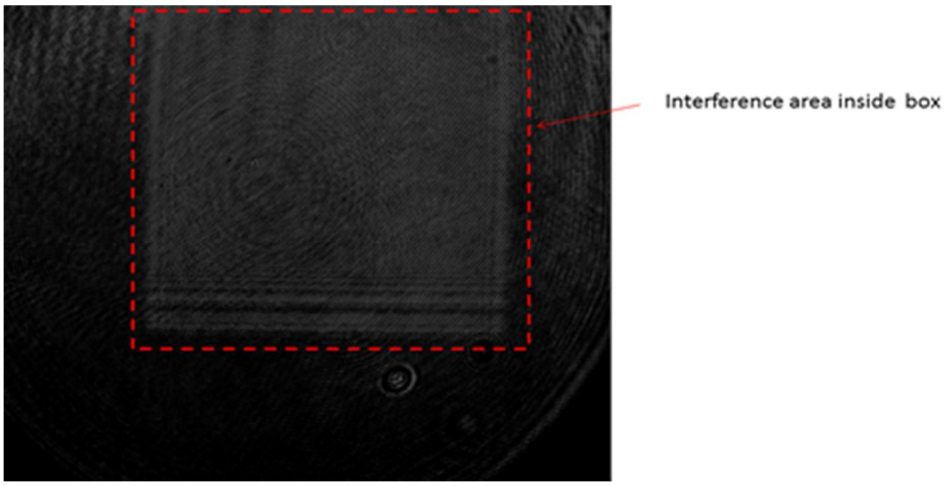

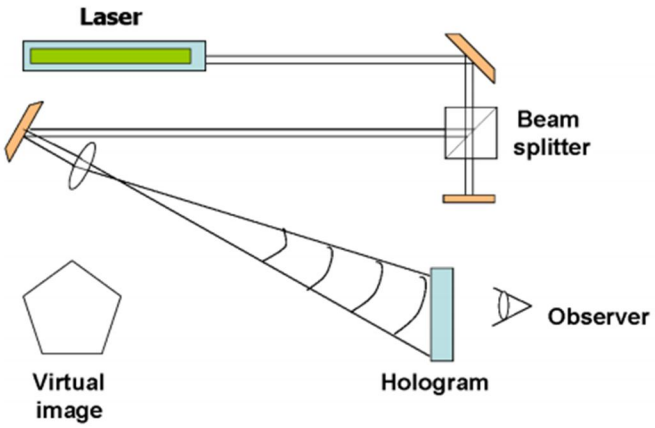

Fig.3 Reconstruction of a hologram

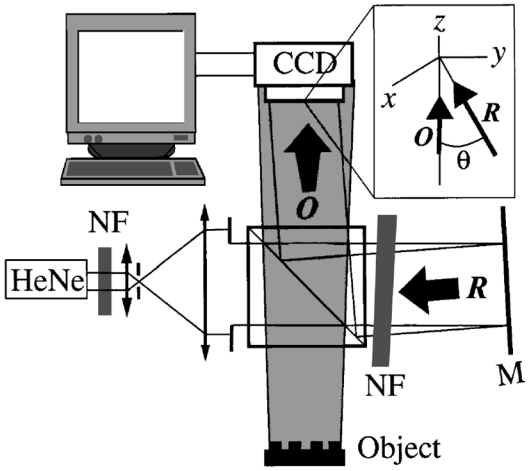

Fig.4 Experimental setup

A wave front $\psi_H(x,y) = R(x,y)I(x,y)$ is transmitted by a hologram and propagates toward an observation plane, where a three-dimensional image of the object can be observed.

For reconstructing a digital hologram, a digital transmitted wave front $\psi_H(k\Delta x, l\Delta y)$ is computed by multiplication of digital hologram $I_H(k,l)$ by a digital computed reference wave, $R_D(k,l)$,called the digital reference wave.

Taking into account the definition of hologram intensity [Eq. 1.3], we have

$$\psi\ (k\Delta x, \Delta y) = R_D(k,l)I_H(k,l) \qquad \text{... (1.7)}$$

$$= \underbrace{R_D\left|R\right|^2 + R_D\left|O\right|^2}_{Zero\ order\ of\ diffraction} + \underbrace{R_D R^* O}_{Twin\ image} + \underbrace{R_D R O^*}_{real\ image}$$

To avoid an overlap of these three components of ψ during reconstruction, they recorded the hologram in the so-called off-axis geometry. For this purpose the mirror in the reference arm, M is oriented such that the reference wave **R** reaches the CCD at an incidence angle θ .The value θ must be sufficiently large to ensure separation between the real and the twin images in the observation planes. However, θ must not exceed a given value so that the spatial frequency of the interferogram does not exceed the resolving power of the CCD.

$$\theta \le \theta_{\max} = arc\ \sin\left(\frac{\lambda}{2\Delta x}\right) \qquad \text{... (1.8)}$$

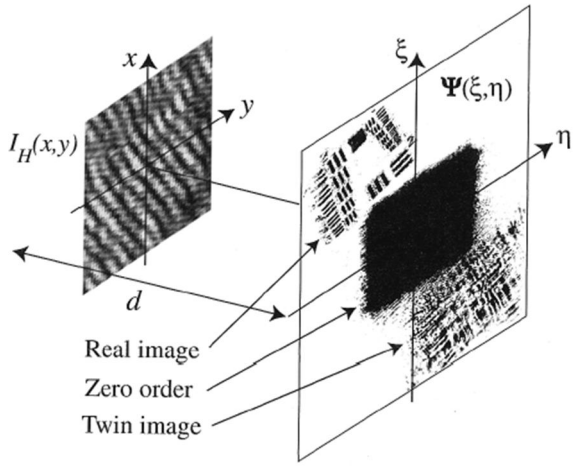

Geometry for hologram reconstruction. *0xy*, hologram plane; *0*ξη, observation plane; *d*, reconstruction distance; **Ψ**(ξ, η), reconstructed wave front.

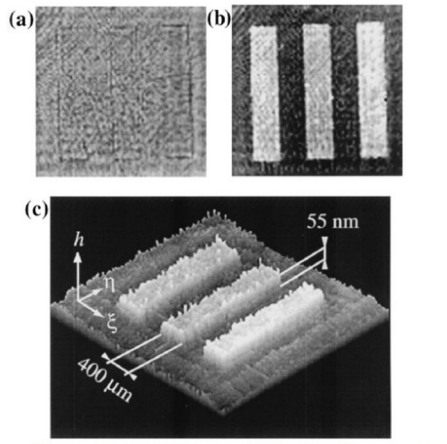

Reconstructed images obtained with a pure phase object: (a) amplitude contrast, (b) phase contrast, (c) three-dimensional perspective of the reconstructed height distribution (the vertical scale is not equal to the transverse scale).

The reconstructed wave front $\psi(m\Delta\xi, n\Delta\eta)$, at a distance d from the hologram plane, is computed by use of a discrete expression of the Fresnel integral:

$$\psi(m\Delta\xi, n\Delta\eta) = A\exp\left[\frac{i\pi}{\lambda d}(m^2\Delta\xi^2 + n^2\Delta\eta^2)\right] \times FFT\left\{R_D(k,l)I_H(k,l)\exp\left[\frac{i\pi}{\lambda d}(k^2\Delta x^2 + l^2\Delta y^2\right]\right\}_{m,n} \quad \text{... (1.9)}$$

Where m and n are integers $(-N/2 \le m, n \le N/2)$, FFT is the fast Fourier transform operator, and $A = \exp(i2\pi d/\lambda)/(i\lambda d)$

$\Delta\xi$ and $\Delta\eta$ are the sampling intervals in the observation plane and define the transverse resolution of the reconstructed image.

This transverse resolution is related to the size of the CCD (L) and to the distance d by,

$$\Delta\xi = \Delta\eta = \lambda d / L \quad \text{... (1.10)}$$

The reconstructed wave front is an array of complex numbers. The amplitude and the phase contrast images can be obtained by calculation of the square modulus.

A new (semantic) reflexive brain–computer interface: In search for a suitable classifier

A. Furdea et al. University of Tubingen, Germany

Journal of Neuroscience Methods (2012)

Presenter : Younghak Shin
GIST, Dept. of Information and Communication, INFONET Lab.

Gwangju Institute of Science and Technology

Objective

- The goal of this study is to find a suitable classifier for EEG data derived from a new learning paradigm which aims at communication in paralysis.
- A reflexive semantic classical (Pavlovian) conditioning paradigm is explored as an alternative to the operant learning paradigms, currently used in most BCIs.
- Four classification algorithms are compared for classifying off-line data collected from a group of 14 healthy participants
  - stepwise linear discriminant analysis (SWLDA)
  - shrinkage linear discriminant analysis (SLDA)
  - linear support vector machine (LIN-SVM)
  - radial basis function kernel support vector machine (RBF-SVM)

Introduction

- BCIs provide a non-muscular communication channel for individuals who are no longer able to communicate due to severe physical impairment.
- Over the last years it has been shown that patients with severe motor disability are able to control an EEG based BCI (e.g. sensori-motor rhythm (SMR) and P300)
- However, there are no documented cases of CLIS(completely locked-in state : all motor control is lost) patients communicating by means of BCI
- It has been suggested that a paradigm shift from instrumental-operant learning to classical conditioning is necessary to overcome the failure of CLIS patients to achieve BCI control
- The aim of this study is to find a suitable classifier and to assess the relative performance of four classification techniques on EEG data derived from a classical conditioning paradigm.

Introduction

- Classical conditioning (Pavlovian conditioning)

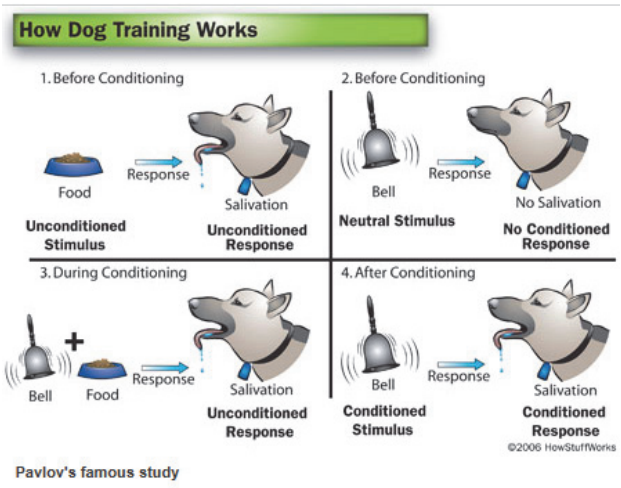

Pavlov's famous study

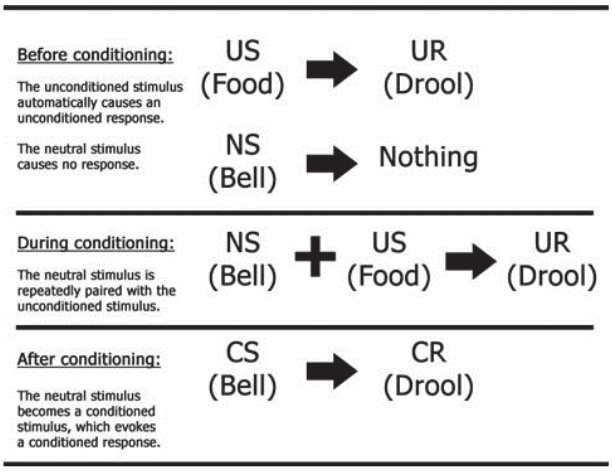

http://drlack.wikispaces.com/Principles+of+Learning

Data collection

- Participants
  - Fourteen healthy participants (8 women and 6 men, mean age 24.36, SD 5.4, range 21–42) took part in this study
- Task procedure and design
  - All participants took part in two experimental sessions
  - Each session was divided into three blocks, each block consisted of 50 true and 50 false sentences, i.e. trials.
  - In each block, the sentences were presented in random order through earphones.
  - The conditioned stimuli (CS) were either ‘yes’ or ‘no’ sentences, according to the type of the sentence (CS1 and CS2).

Data collection

- Task procedure and design

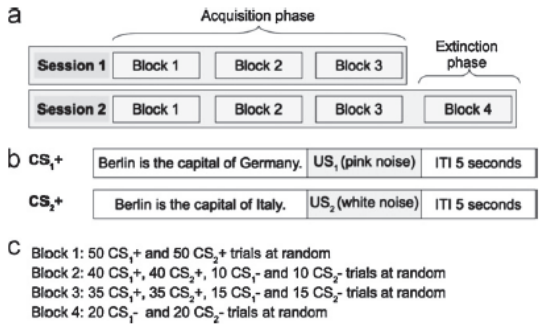

Fig. 2. The experimental design. (a) Session setup: blocks 1, 2 and 3 from sessions 1 and 2 are referred to as the *acquisition phase*; block 4 from session 2 is referred to as *extinction phase*. (b) An example of the conditioned stimuli CS_1+ and CS_2+. (c) Number of randomly presented trials per block.

  - To learn ‘yes-’ or ‘no-thinking’ two different unconditioned stimuli (US) were used:
    - a pink noise US1 immediately following a true sentence
    - a white noise US2 immediately following a negative sentence which produced the unconditioned brain response(UR)

Data collection

- Both US were set to have the same duration of 500 ms and were presented monaurally at different intensities.
- US1 was always presented to the right ear with an intensity of 75 dB and US2 was always presented to the left ear with an intensity of 105 dB.
- For each session, during the first block, every CS was paired with an US and denoted as CS1+ and CS2+.
- In the second block 10 CS, at random, were not paired with US1 and US2 and are referred to as CS1− and CS2−.
- In the third block 15 CS, at random, were not paired with US1 and US2.
- CS1- and CS2- are of a particular importance for on-line communication because in an on-line scenario only unpaired sentences can be used.
- At the end of the second session a fourth block of sentences was introduced, further referred to as the extinction phase.
- The purpose of this phase was to assess the lasting effects of conditioning.

Data acquisition and processing

Data collection

- stepwise Linear Discriminant Analysis

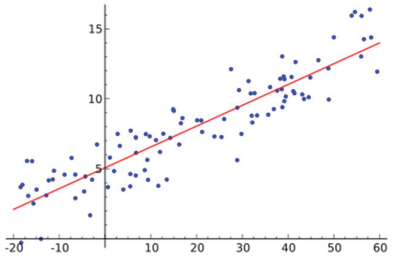

Example of simple linear regression

Methods

- Shrinkage LDA

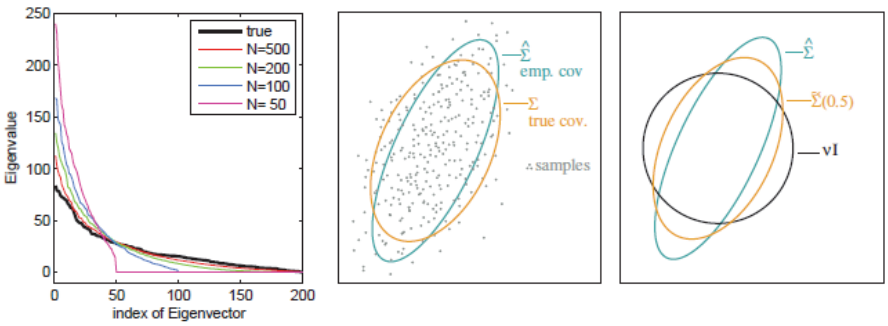

Figure 7: *Left:* Eigenvalue spectrum of a given covariance matrix (bold line) and eigenvalue spectra of covariance matrices estimated from a finite number of samples drawn (N= 50, 100, 200, 500) from a corresponding Gaussian distribution. *Middle:* Data points drawn from a Gaussian distribution (gray dots; d = 200 dimensions, two dimensions selected for visualization) with true covariance matrix indicated by an orange colored ellipsoid, and estimated covariance matrix in cyan. *Right:* An approximation of the true covariance matrix can be obtained as a linear interpolation between the empirical covariance matrix and a sphere of approriate size.

Thank you

Conditions for practicing compressive Fresnel holography

Speaker : Sangjun Park
Authors: Yair Rivenson* and Adrian Stern
{rivenson@ee.bgu.ac.il}

OPTICS LETTERS, 2011

INFONET Lab, Dept. of Information and Communication, GIST

Gwangju Institute of Science and Technology

Background- the coherence parameter μ

- The coherence parameter that measures the dissimilarity between the sensing matrix Φ and the sparsifying matrix Ψ is defined as

$$\mu(\Phi,\Psi) := \max_{k,j} \left| \langle \phi_k, \psi_j \rangle \right|.$$

- Then, CS theory asserts that the signal can be accurately reconstructed by taking m uniformly at random selected measurements, obeying

$$m \geq C\mu(\Phi,\Psi) s \log n$$

where C is a positive constant.

Backgrounds - the Fresnel approximation

- The Fresnel approximation is used for representing the complex values of a propagating wave measured in a planer perpendicular to the direction of propagation and separated by a distance **z**.

$$u_z(x) = u_{in} * \exp\left\{\frac{j\pi}{\lambda z}x^2\right\}$$

The one-dimensional Fresnel approximation

$$= \int u_{in}(\xi)\exp\left\{\frac{j\pi}{\lambda z}(x-\xi)^2\right\}d\xi$$

$$= \exp\left\{\frac{j\pi}{\lambda z}x^2\right\}\int u_{in}(\xi)\exp\left\{\frac{j\pi}{\lambda z}\xi^2\right\}\exp\left\{-\frac{2j\pi x\xi}{\lambda z}\right\}d\xi$$

The term is related to the Fourier transform

- Here, λ is the wavelength of the light wave and $u_{in}(\xi)$ is the input object.
- We refer the Fresnel approximation as the Fresnel transform.

Backgrounds - the form of the Fresnel transform depending on propagation distances.

- Let **z** be infinity.
- The Fresnel transform becomes the Fourier transform.

$$u(x) = \exp\left\{\frac{j\pi}{\lambda z}x^2\right\}\int u_{in}(\xi)\exp\left\{\frac{j\pi}{\lambda z}\xi^2\right\}\exp\left\{-\frac{2j\pi x\xi}{\lambda z}\right\}d\xi$$

$$\approx \exp\left\{\frac{j\pi}{\lambda z}x^2\right\}\int u_{in}(\xi)\exp\{0\}\exp\left\{-\frac{2j\pi x\xi}{\lambda z}\right\}d\xi$$

$$= \exp\left\{\frac{j\pi}{\lambda z}x^2\right\}\int u_{in}(\xi)\exp\left\{-2j\pi\xi\frac{x}{\lambda z}\right\}d\xi$$

$$= \exp\left\{\frac{j\pi}{\lambda z}x^2\right\}\mathcal{F}\left[u_{in}\left(\frac{x}{\lambda z}\right)\right]$$

- The complex values of the propagating wave are easily obtained by using the Fourier transform.

A problem statement

- Can we derive theoretical bounds on the performance of compressive imaging systems based on Fresnel wave propagation?

- The authors presented theoretical bounds in terms of imaging sensor's physical attributes, illumination wavelength, and working distance.

The definition of far-field and near-field regimes

- Let n be the number of object and CCD pixels.
- Let Δx_z be the object resolution element size, and Δx_z be the output field's pixel size.
- If the distance z obeys

$$z \geq n \Delta x_0^2 / \lambda$$

then we say that the distance z belongs to far-field regime.

- Otherwise, the distance z belongs to near-field regime.
- Also, there is the relation between the input and output pixel sizes should be

$$\Delta x_z = \lambda z / (n \Delta x_0)$$

The term can be considered as the length of an input object (Here, we only consider the one dimensional case.)

The Fresnel transform for the far field regime – 1

- For the far-field regime, the Fresnel transform is given as

$$u_z\left(r\Delta x_z\right)=\exp\left\{\frac{j\pi}{\lambda z}\left(r\Delta x_z\right)^2\right\}\times\mathcal{F}\left[u_{in}\left(q\Delta x_0\right)\exp\left\{\frac{j\pi}{\lambda z}\left(q\Delta x_0\right)^2\right\}\right]$$

- To comply with standard CS formulations, the Fresnel transform is represented in a vector-matrix form:

$$\mathbf{u}_z=\mathbf{Q}_{\Delta x_z}\mathbf{F}\mathbf{Q}_{\Delta x_0}\mathbf{u}_{in}=\mathbf{\Phi}^{FF}\mathbf{u}_{in}$$

$$\mathbf{Q}_{\Delta x_z}=diag\left[\exp\left(\frac{j\pi}{\lambda z}\left(\Delta x_z\right)^2\right)\quad\exp\left(\frac{j\pi}{\lambda z}\left(2\Delta x_z\right)^2\right)\quad\cdots\quad\exp\left(\frac{j\pi}{\lambda z}\left(n\Delta x_z\right)^2\right)\right]$$

$$\mathbf{Q}_{\Delta x_o}=diag\left[\exp\left(\frac{j\pi}{\lambda z}\left(\Delta x_o\right)^2\right)\quad\exp\left(\frac{j\pi}{\lambda z}\left(2\Delta x_o\right)^2\right)\quad\cdots\quad\exp\left(\frac{j\pi}{\lambda z}\left(n\Delta x_o\right)^2\right)\right]$$

$\mathbf{F}$ is the Fourier transform matrix

The Fresnel transform for the far field regime – 2

- Since the matrix Φ^{FF} is the Fourier transform matrix and remaining matrices are phase matrices, the mutual coherence for the far-field case is one.
- Thus, the number of measurements are represented by

$$m\geq Cs\log n$$

- This results means that the distance *has no effect* on the sparse signal reconstruction guaranties, and *it behaves exactly as compressive Fourier* sensing.

The Fresnel transform for the near field regime

- For the near field regime, the Fresnel transform is represented in a vector-matrix form:

$$\mathbf{u}_z = \mathbf{F}^{-1}\tilde{\mathbf{Q}}_{\Delta x_0}\mathbf{F}\mathbf{u}_{in} = \mathbf{\Phi}^{NF}\mathbf{u}_{in}$$

$$\tilde{\mathbf{Q}}_{\Delta x_0} = diag\left[\exp\left(\frac{j\pi\lambda z}{(n\Delta x_0)^2}\right) \quad \exp\left(\frac{j\pi\lambda z 2^2}{(n\Delta x_0)^2}\right) \quad \cdots \quad \exp\left(\frac{j\pi n^2}{\lambda z}\right)\right]$$

- For the one-dimensional case, the mutual coherence is

$$\mu_{1D} \approx n\frac{\Delta x_0^2}{\lambda z}.$$

- The mutual coherence for the two-dimensional case is

$$\mu_{2D} \approx n^2\left(\frac{\Delta x_0^2}{\lambda z}\right)^2 = N\left(\frac{\Delta x_0^2}{\lambda z}\right)^2$$

- Then, the number of measurements are represented by

$$m \geq Cn\left(\frac{\Delta x_0^2}{\lambda z}\right)s\log n \text{ or } m \geq CN\left(\frac{\Delta x_0^2}{\lambda z}\right)^2 s\log N$$

Conclusions

- For the far field case, the distance *has no effect* on the number of measurements.

$$m \geq Cs\log N$$

- For the near field case, the distance *has effect* on the number of measurements. Also, the object resolution element size *has effect* on the number of measurements.

$$m \geq Cn\left(\frac{\Delta x_0^2}{\lambda z}\right)s\log n \text{ or } m \geq CN\left(\frac{\Delta x_0^2}{\lambda z}\right)^2 s\log N$$

- But, we remind that the object resolution element size must satisfy the below relation

$$\Delta x_z = \lambda z/(n\Delta x_0)$$

Random-Frequency SAR Imaging Based on Compressed Sensing

J. Yang et al.

IEEE Trans. Geo. Remot. Sensing (2013. Feb.)

Presenter : Jin-Taek Seong

GIST, Dept. of Information and Communications, INFONET Lab.

Gwangju Institute of Science and Technology

Introduction

- The stepped-frequency waveform consists of sequences of single-frequency pulses
- The stepped-frequency waveform can be viewed as the frequency sampling of the total bandwidth
- The advantages of a single frequency
  - Simple hardware requirements
  - High resolution
- The drawback is
  - A long time period to transmit the signals, since the transmitter must scan over the radar bandwidth using a sequence of discrete frequencies
- Therefore, this leads to many limitations for the application of the stepped-frequency waveform in SAR.
- There has to be a tradeoff between the resolution and imaging range width.

Introduction

- If the targets are sparse or compressible, the required frequencies in the stepped-frequency SAR can be reduced significantly using a CS theory
- In this paper, a random-frequency SAR imaging scheme based on CS is proposed
  - Reconstruction the 2-D image of the sparse targets by transmitting a small number of random frequencies.
- A sparse transform structure is proposed for the reshaped 2-D reflectivity map.
- The main advantages of the proposed imaging scheme
  - 1) the available imaging range width can be enlarged significantly, while the range and azimuth resolutions are both maintained
  - 2) the required number of frequencies can be reduced
  - 3) random undersampling is very easy to implement for both range and azimuth

Stepped-Frequency Waveform (1/2)

- The stepped-frequency waveform uses a sequence of pulses to achieve an ultrawide bandwidth
- We denote the transmitted waveform as

$$s_t(n,t) = \text{rect}\left(\frac{t}{T_p}\right)\exp\left[j2\pi f_c(n)t\right] \qquad (1)$$

- For a point reflector at range *R*, the echo signal is

$$s_e(n,t) = g\cdot\text{rect}\left(\frac{t-2R/c}{T_p}\right)\exp\left[j2\pi f_c(n)(t-2R/c)\right] \qquad (2)$$

  - *g* is the reflectivity coefficient of the target
- The demodulation reference signal is

$$\begin{aligned} s(n,t) &= s_e(n,t)\cdot s_{\text{ref}}^*(n,t) \\ &= g\cdot\left(\frac{t-2R/c}{T_p}\right)\exp\left[j2\pi f_c(n)(t-2R/c)\right] \\ &\quad\cdot\exp\left[-j2\pi f_c(n)t\right] \\ &= g\cdot\text{rect}\left(\frac{t-2R/c}{T_p}\right)\exp\left[-j\frac{4\pi f_c(n)R}{c}\right] \end{aligned} \qquad (4)$$

Stepped-Frequency Waveform (2/2)

- We consider that the frequency interval is equal to Δ*f*, so that

$$f_c(n) = f_c + n\Delta f, \qquad n = 1, 2, \ldots N \qquad (5)$$

- The demodulated signal can be rewritten as

$$s(n,t) = g \cdot \text{rect}\left(\frac{t - 2R/c}{T_p}\right) \exp\left[-j\frac{4\pi(f_c + \Delta f n)R}{c}\right]. \qquad (6)$$

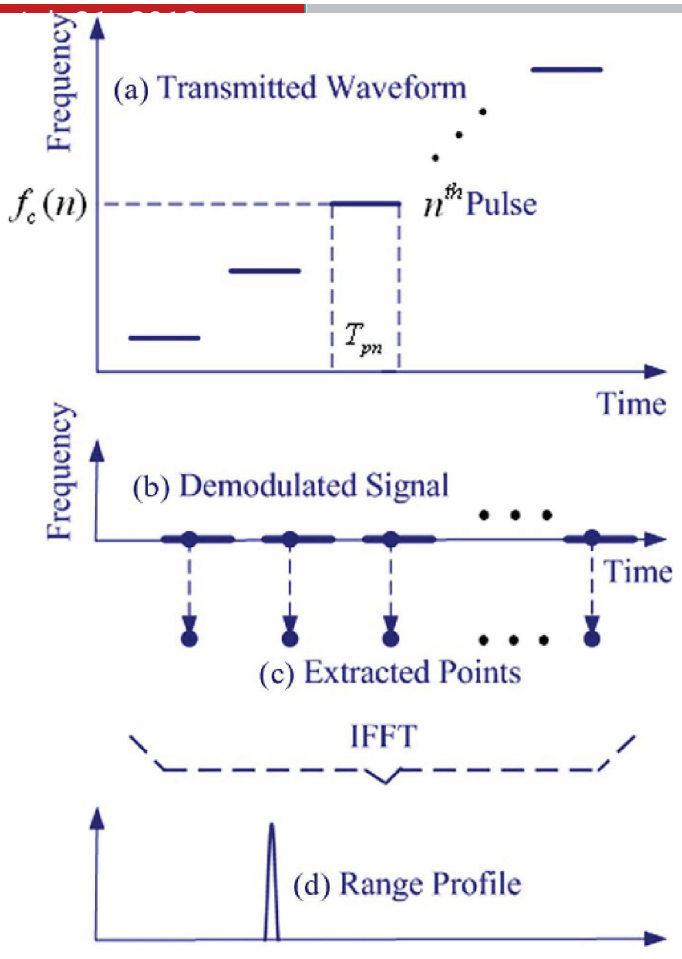

Fig. 1. Processing of stepped-frequency waveform. (a) Transmitted waveform. (b) Demodulated signal. (c) Extracted data points. (d) Range profile.

Limitations of Stepped-Frequency Waveform Applied to SAR (1/2)

- Sampling with Δ*f* results in periodic repetition in the time domain, and the repetition period is 1/Δf
- The corresponding repetition period for range is *c*/(*2Δf*), so the nonaliasing range width is limited to

$$R_w < \frac{c}{(2\Delta f)} \tag{8}$$

- For a fixed pulse time interval, to avoid overlapping of the echoes, the maximum range width is

$$D_1 = \frac{\Delta tc}{2} \tag{9}$$

- For a given frequency step, the maximum nonaliasing range width is

$$D_2 = \frac{c}{2\Delta f} = \frac{Nc}{2B} \tag{10}$$

- Therefore, the **maximum available range width** is

$$D = \min\{D_1, D_2\}. \tag{12}$$

Limitations of Stepped-Frequency Waveform Applied to SAR (2/2)

- The equivalent azimuth sampling interval is *NΔtV*, where *V* is the radar velocity.

$$r_a = N\Delta tV. \tag{13}$$

- The range resolution is

$$r_r = \frac{c}{2B}. \tag{14}$$

- The available imaging range width and the range resolution and azimuth resolution must be traded off against each other
- To let the available range width become wider, *Δt* and *N* should be bigger, *B* should be smaller, but all of these requirements will decrease the resolution in both the range and azimuth dimensions.

Random-Frequency SAR Imaging Based on CS-SAR Imaging Model (1/3)

- The radar data are the superposition of the echoes of all scatterers in the area illuminated by the radar's beam (i.e., the scene)
- The received signal of the *n*th pulse in the *m*th sequence can be expressed as

$$s(m,n) = \iint_G g(x,y) \cdot \exp\left[-j\frac{4\pi f_c(n) R(m,n,x,y)}{c}\right] dxdy$$

  - x and y are the coordinates of the target
  - *g*(x, y) is the reflectivity coefficient of the target at (x, y)
  - *R*(m, n, x, y) is the range of the target at (x, y)
  - *G* is the area illuminated by the beam

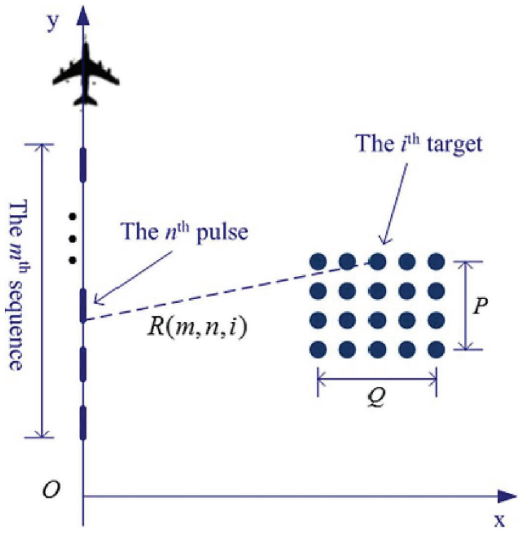

Fig. 2. Geometry model for SAR imaging.

Journal Club Meeting, Jul. 31, 2013

Random-Frequency SAR Imaging Based on CS-SAR Imaging Model (2/3)

- The scene consists of a set of point scatterers on a grid, and the interval of the grids should be smaller than the radar resolution
- The reflectivity coefficients of the scatterers can be denoted as a 2-D matrix

$$\mathbf{G} = \begin{bmatrix} g(1,1) & \cdots & g(1,Q) \\ \vdots & \ddots & \vdots \\ g(P,1) & \cdots & g(P,Q) \end{bmatrix}$$

- The 2-D reflectivity coefficient matrix should be reshaped to a column vector, i.e., *g* is a PQ×1 vector
- The discrete expression of the radar data of the *n*th pulse in the *m*th sequence is

$$s(m,n) = \sum_{i=1}^{PQ} g(i) \cdot \exp\left[-j\frac{4\pi f_c(n) R(m,n,i)}{c}\right]$$

Random-Frequency SAR Imaging Based on CS-SAR Imaging Model (3/3)

- The linear equation can be expressed in matrix form as

$$\mathbf{s} = \mathbf{A}\mathbf{g} + \mathbf{n}$$

  - where *s* is an *MN*×1 vector, *A* is an *MN*×*PQ* matrix, *g* is a *PQ*×1 vector, and *n* is the noise term. *M* is the total number of sequences; *N* is the number of frequencies in one sequence.

- The detailed form is

$$\mathbf{s}=\begin{bmatrix} s(1,1) \\ \vdots \\ s(1,N) \\ s(2,1) \\ \vdots \\ s(2,N) \\ \vdots \\ s(M,1) \\ \vdots \\ s(M,N) \end{bmatrix} = \mathbf{A}\mathbf{g}+\mathbf{n} = \begin{bmatrix} \mathbf{a}(1,1)^{\mathrm{T}} \\ \vdots \\ \mathbf{a}(1,N)^{\mathrm{T}} \\ \mathbf{a}(2,1)^{\mathrm{T}} \\ \vdots \\ \mathbf{a}(2,N)^{\mathrm{T}} \\ \vdots \\ \mathbf{a}(M,1)^{\mathrm{T}} \\ \vdots \\ \mathbf{a}(M,N)^{\mathrm{T}} \end{bmatrix} \begin{bmatrix} g(1) \\ g(2) \\ \vdots \\ g(PQ) \end{bmatrix} + \mathbf{n}.$$

Random-Frequency SAR Imaging Based on CS-CS Imaging Scheme

- In order to apply a CS scheme, a reduced set of elements in *s* is selected randomly, and a reduced set of rows in *A* is also selected accordingly. It means that a small number of frequencies are selected randomly.

- The CS measurement can be expressed as

$$\mathbf{s}' = \mathbf{A}'\mathbf{g} + \mathbf{n}'$$

- The targets can be reconstructed as

$$\min \|\mathbf{g}\|_1 \quad s.t. \quad \|\mathbf{A}'\mathbf{g} - \mathbf{s}'\|_2 \leq \varepsilon.$$

- Assume that *L* samples are selected from the total of *MN* samples; then, the uniform pulse time interval becomes (*MN*/*L*)*Δt*, so that the maximum available range width becomes

$$D' = \frac{MN}{L}\frac{\Delta tc}{2}.$$

Random-Frequency SAR Imaging Based on CS-Sparsity of Targets

- A Priori Sparse Targets: it means that the targets consist of a small number of dominant scatterers
- Sparsely Representable Targets: we can find a transform to make most of the coefficients in the transform domain
- The CS imaging scheme combined with the sparse transform (see the appendix) can be expressed as

$$\mathbf{s}' = \mathbf{A}'\mathbf{g} + \mathbf{n}' = \mathbf{A}'(\tilde{\mathbf{\Psi}}_r\tilde{\mathbf{\Psi}}_c)^{-1}\tilde{\mathbf{\Psi}}_r\tilde{\mathbf{\Psi}}_c\mathbf{g} + \mathbf{n}'.$$

- This equation can be rewritten as

$$\mathbf{s}' = \mathbf{A}'(\tilde{\mathbf{\Psi}}_r\tilde{\mathbf{\Psi}}_c)^{-1}\mathbf{x} + \mathbf{n}'.$$

- We can solve for the transform coefficients using

$$\hat{\mathbf{x}} = \min \|\mathbf{x}\|_1 \quad s.t. \quad \left\|\mathbf{A}'(\tilde{\mathbf{\Psi}}_r\tilde{\mathbf{\Psi}}_c)^{-1}\mathbf{x} - \mathbf{s}'\right\|_2 \le \varepsilon.$$

- Then, the reflectivity coefficients can be obtained by

$$\hat{\mathbf{g}} = (\tilde{\mathbf{\Psi}}_r\tilde{\mathbf{\Psi}}_c)^{-1}\hat{\mathbf{x}}.$$

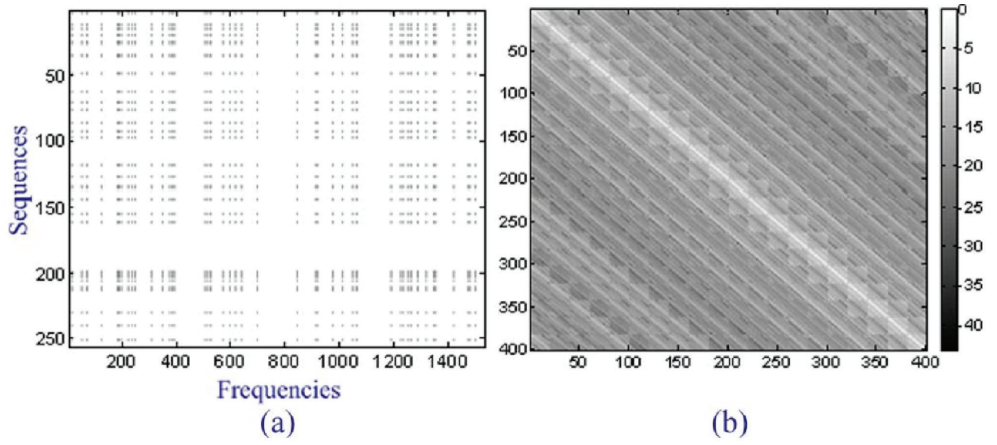

Fig. 3. Selected samples and mutual coherences for Option 1. (a) Selected samples. (b) Mutual coherences of the sensing matrix (scaled in decibels).

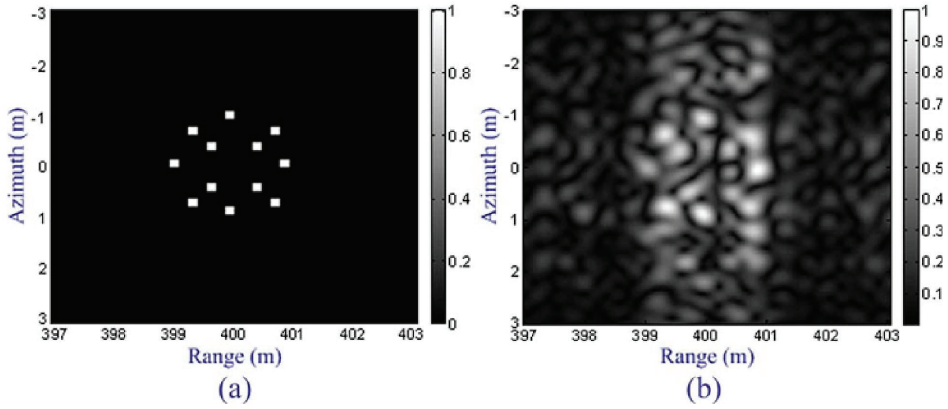

Fig. 6. Results of Option 1. (a) CS reconstruction result of the 1/192 data. (b) Imaging result of the 1/192 data using the Omega-K algorithm.

Experimental Results

- In order to show the validity, an experiment is carried out for stepped-frequency and random-frequency SAR imaging
- A stepped-frequency radar is mounted on a rail to acquire data
- The rail is controlled by a microcomputer, and the radar can move on the rail with a preset velocity

(a)

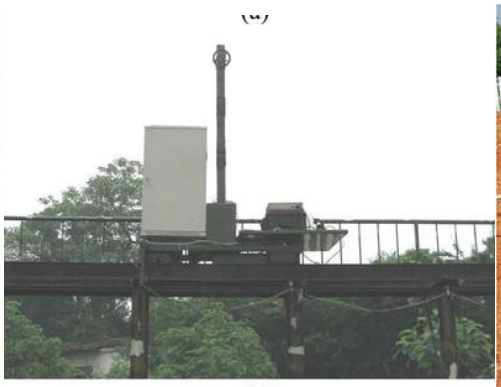

(b)

(c)

TABLE II
EXPERIMENT PARAMETERS

Bandwidth	512MHz
Pulse Time Interval	1e-3s
Radar Velocity	0.05m/s
Squint Angle	0°
Range Resolution	0.293m
Azimuth Resolution	0.05m
Number of Frequencies	512
Number of Sequences	480
Scene Azimuth Points	40
Scene Range Points	20
Selected Samples for CS	1024

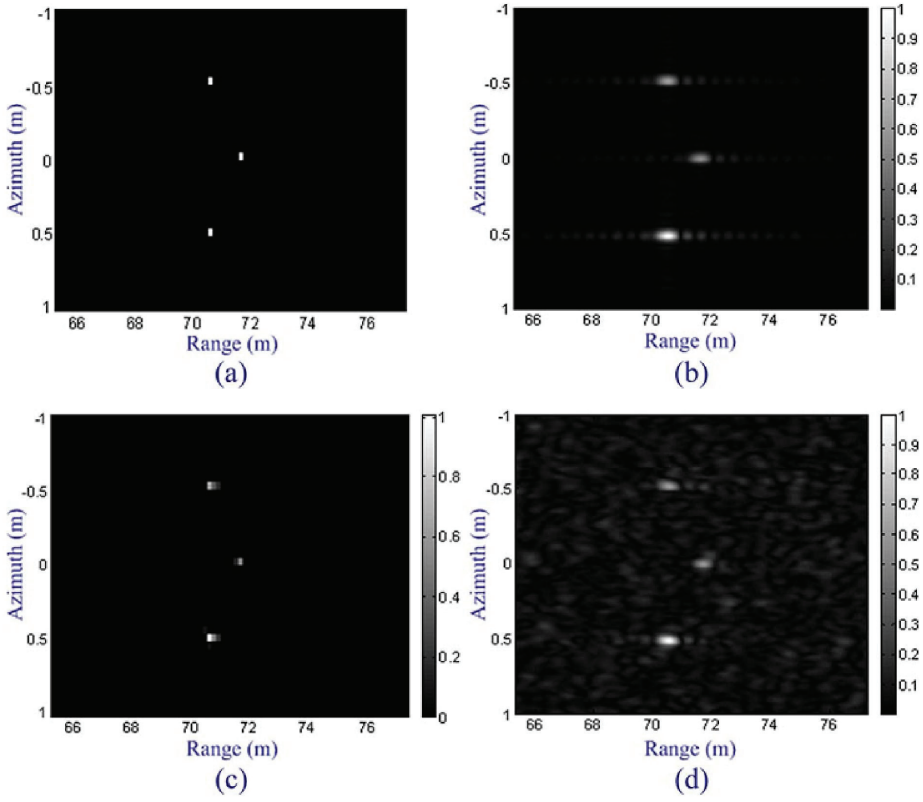

Fig. 12. Experimental results. (a) Position of the three corner reflectors. (b) Imaging result of the full data using the Omega-K algorithm. (c) CS reconstruction result of 1/240 data. (d) Imaging result of 1/240 data using the Omega-K algorithm.

Conclusions

- The theory of CS has been used to reduce the required frequencies in a stepped-frequency SAR system
- Based on the theory of CS, the traditional sampling requirements can be avoided, and the limitations of the stepped-frequency waveform applied in SAR are overcome
- The available imaging range width can be enlarged significantly, while the range and azimuth resolutions are maintained.
- The results of the CS imaging scheme are even better than the traditional results of the fully sampled data
- Future work will include fast reconstruction strategies and detailed investigations of the sparsity and compressibility of the targets
- Speckle noise will make the phase of the reflectivity map random, and it is difficult to find an effective sparse transform for a complex reflectivity map

Appendix – Transform of the 2D Matrix

- We begin with the sparse transform for the 2-D reflectivity matrix. The sparse transform can be applied to both the columns and rows of the 2-D matrix, and it can be expressed as.

$$\mathbf{X} = \mathbf{\Psi}_c \mathbf{G} \mathbf{\Psi}_r$$

  - where X contains the coefficients after the sparse transform, G is shown in (29), Ψ_c is the sparse transform matrix for the columns, the size of Ψ_c is $P \times P$, Ψ_r is the sparse transform matrix for the rows, and the size of Ψ_r is $Q \times Q$. Ψ_c and Ψr are full rank matrices.
- In the imaging scheme based on CS, the 2-D reflectivity matrix G is reshaped to a column vector g

$$\tilde{\mathbf{\Psi}}_c = \begin{bmatrix} \mathbf{\Psi}_c & & & \\ & \mathbf{\Psi}_c & & \\ & & \ddots & \\ & & & \mathbf{\Psi}_c \end{bmatrix} \qquad \tilde{\mathbf{\Psi}}_r = \begin{bmatrix} \mathbf{\Psi}_{r1} \\ \mathbf{\Psi}_{r2} \\ \vdots \\ \mathbf{\Psi}_{ri} \end{bmatrix}$$

- The sparse transform of the reshaped reflectivity vector can be expressed as

$$\mathbf{x} = \tilde{\mathbf{\Psi}}_r \tilde{\mathbf{\Psi}}_c \mathbf{g}$$

Optimizing the Channel Selection and Classification Accuracy in EEG-Based BCI.

Mahnaz Arvaneh et al. (Chai Quek*)

IEEE Transactions
on Biomedical Engineering (2011)

Presenter : SeungChan Lee

GIST, Dept. of Information and Communication, INFONET Lab.

Gwangju Institute of
Science and Technology

Background

- Channel selection problems in EEG-based BCI
  - A large number of EEG channels
    - It may include noisy and redundant signals. – degradation of performance
    - It needs a prolonged preparation time. – inconvenience in installation process
  - Selecting the least number of channels with required accuracy can balance both needs.
- Various channel selection methods
  - SVM based
    - Recursively eliminates the least-contributed channels based on classification accuracy.
  - Mutual information(MI) based
    - Rank the channels based on MI between channels and class labels
  - Common spatial filter(CSP) based
    - Directly select the channels according to their CSP coefficients
  - RCSP based
    - used sparse solutions of spatial filters

Background

- Research problems in EEG channel selection
  - How many channels are required for the best classification accuracy?
  - What is the minimum number of channels required to achieve the same accuracy as obtained by using all the channels?
- To address the research questions…
  - They proposed a sparse common spatial pattern(SCSP) algorithm.
  - The proposed algorithm minimizes the number of channels by sparsifying the common spatial filters within a constraint of classification accuracy.

CSP algorithm

- The CSP algorithm is effective in discriminating two classes of EEG data by maximizing the variance of one class while minimizing the variance of the other class.
- Summary of formula derivation
  - Let single trial EEG data $\mathbf{X} \in \mathbf{R}^{N \times S}$
    (N : the number of channels, S: the number of measurement samples)
  - The CSP algorithm projects **X** to spatially filtered **Z** as $\mathbf{Z} = \mathbf{W}\mathbf{X}$
    (the rows of $\mathbf{W}$: the spatial filters, the columns of $\mathbf{W}^{-1}$: CSP)
  - Normalized covariance matrix $\mathbf{C} = \frac{\mathbf{X}\mathbf{X}^T}{\mathrm{trace}(\mathbf{X}\mathbf{X}^T)}$
    trace(X) : sum of diagonal elements of **X**
  - $\mathbf{C}_C = \mathbf{C}_1 + \mathbf{C}_2 = \mathbf{F}_C \psi \mathbf{F}_C{}^T$
    $\mathbf{C}_1, \mathbf{C}_2$: Computed by averaging over multiple trials of EEG data
    $\mathbf{F}_C$: matrix of normalized eigenvectors
    ψ : diagonal matrix of eigenvalues
  - Whitening transformation matrix
  - Transformation of covariance matrices

CSP algorithm

- Summary of formula derivation
  - Whitening transformation matrix $\mathbf{P} = \sqrt{\Psi^{-1}}\mathbf{F}_C^T$
  - Transformation of covariance matrices

$$\mathbf{C}_1' = \mathbf{P}\mathbf{C}_1\mathbf{P}^T, \quad \mathbf{C}_2' = \mathbf{P}\mathbf{C}_2\mathbf{P}^T$$

$$= \mathbf{U}\Lambda_1\mathbf{U}^T \qquad = \mathbf{U}\Lambda_2\mathbf{U}^T \qquad \Lambda_1 + \Lambda_2 = \mathbf{I}$$

$\mathbf{C}_1', \mathbf{C}_2'$: share common eigenvectors,
$\mathbf{U}$: eigenvectors matrix
Λ : diagonal eigenvalues matrix

  - Apply CSP projection matrix $\mathbf{W} = \mathbf{U}^T\mathbf{P}$

$$\mathbf{C}_1' = \mathbf{U}^T\mathbf{P}\mathbf{C}_1\mathbf{P}^T\mathbf{U} = \Lambda_1, \quad \mathbf{C}_2' = \mathbf{U}^T\mathbf{P}\mathbf{C}_2\mathbf{P}^T\mathbf{U} = \Lambda_2 \qquad \Lambda_1 + \Lambda_2 = \mathbf{I}$$

  - Because $\Lambda_1 + \Lambda_2 = \mathbf{I}$, the maximum variance of one class lead to the minimum variance of the another class.→ Optimal discrimination
  - Projection matrix **W** can be formulated as an optimization problem

$$\min_{\mathbf{w}_i}\left(\sum_{i=1}^{i=m}\mathbf{w}_i\mathbf{C}_2\mathbf{w}_i + \sum_{i=m+1}^{i=2m}\mathbf{w}_i\mathbf{C}_1\mathbf{w}_i\right)$$

$$\text{Subject to : } \mathbf{w}_i(\mathbf{C}_1 + \mathbf{C}_2)\mathbf{w}_j^T$$

$\mathbf{C}_i$: covariance matrix of class i

$\mathbf{w} \in {}^{1\times N}, i = \{1, \quad, 2m\}$ indicate

$\mathbf{w}$ $\mathbf{C} + \mathbf{C}$ $)\mathbf{w}^T$

(

CSP algorithm

$= 1,$

$= 1,$

$i =$ $_i$

$\{1,$ first and last m rows
$2,$ of CSP projection
i, j matrix
$= \{1,$
$2,$ $, 2m\}$ $i \neq j$

SCSP algorithm

- Motivation
  - Sparsify the CSP spatial filters to emphasize on a limited number of channels with high variances between the classes
  - Discard the rest of the channels with low or irregular variances that may be due to noise or artifacts.
- Sparsity measurement
  - $l_1 / l_2 = \frac{\|\mathbf{x}\|_1}{\|\mathbf{x}\|_2}$
  - The sparsest possible vector(only a single element is nonzero) has a sparseness of one.
  - Non-sparsity measurement : l_1 / l_2 norm increases when the sparsity decreases.
- Modification of CSP algorithm

SCSP algorithm

- Modification of CSP algorithm
  - Include regularization parameter in optimization problem

$$\min_{\mathbf{w}_i} (1-r)\left(\sum_{i=1}^{i=m} \mathbf{w}_i \mathbf{C}_1 \mathbf{w}_i^T + \sum_{i=m+1}^{i=2m} \mathbf{w}_i \mathbf{C}_2 \mathbf{w}_i^T\right) + r \sum_{i=1}^{i=2m} \frac{\|\mathbf{w}_i\|_1}{\|\mathbf{w}_i\|_2}$$

$$\text{Subject to : } \mathbf{w}_i(\mathbf{C}_1 + \mathbf{C}_2)\mathbf{w}_i^T = 1,\ i = \{1, 2, \ldots, 2m\}$$

$$\mathbf{w}_i(\mathbf{C}_1 + \mathbf{C}_2)\mathbf{w}_j^T = 1,\ i, j = \{1, 2, \ldots, 2m\}\ i \neq j$$

  - Parameter $r(0 \le r \le 1)$ controls the number of removed channels and classification accuracy.
  - Non-linear optimization problem → solved using sequential quadratic programming(SQP) and augmented Lagrangian methods

SCSP algorithm

- Channel selection
  - From training set of two class motor imagery data, first two sparse spatial filters corresponding each class are obtained by solving the optimization problem.
  - Zero element channel → discard
    Non-zero element channel → select the channels
  - Importance order : apply ranking method(used maximum of the absolute values of the corresponding sparse spatial filter.

Datasets and processing

- Datasets
  - With a moderate number of channels (22 channels)
    - Dataset 2a from BCI competition 4
    - 9 subjects
    - Used only right and left hand motor imagery tasks
    - 72 trials training set + 72 trials testing set on each subjects
  - With a large number of channels (118 channels)
    - Dataset 4a from BCI competition 3
    - 5 subjects
    - Right hand and foot motor imagery tasks
    - 140 trials training set + 140 trials testing set on each subjects
- Data processing
  - Extract 0.5 ~ 2.5 seconds data samples after the visual cue
  - Apply 8 ~ 35Hz band-pass filter
  - (Training set) select optimal channels using first and last sparse spatial filter
  - (Test set) CSP retraining over selected channels and dataset spatially filtered using the first and last 3 spatial filters.
  - Variance of spatially filtered signal applied SVM classifier

Results and Discussion

- Performance comparison of l_1 and l_1 / l_2 Regularization term
  - Varying r value(different number of channels)
  - l_1 / l_2 norm based SCSP algorithm leads better classification accuracies when two different regularization based SCSP algorithm select same number of channels.

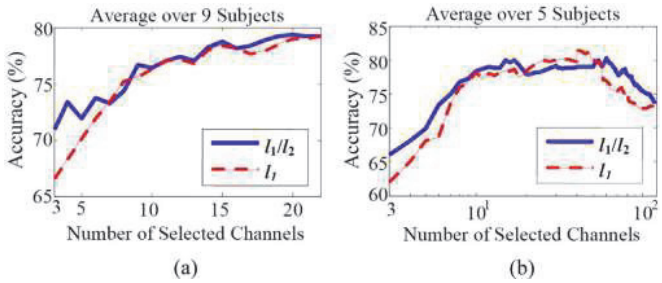

Results and Discussion

- Channel selection with different criteria
  - Two channel selection criteria
    - First criterion : maximizes the accuracy by removing noisy and irrelevant channels.(SCSP1)
    - Second criterion : minimizes the number of selected channels while maintaining the classification accuracy.(SCSP2)
  - Procedure
    - r was chosen from 0.01 to 0.99.
    - For each r, a set of selected channels was determined.
    - Using 10x10 fold cross validation on training set, compute classification accuracy with each set of the selected channels.
    - Optimal r was selected based on the accuracy.

Results and Discussion

- Channel selection with different criteria

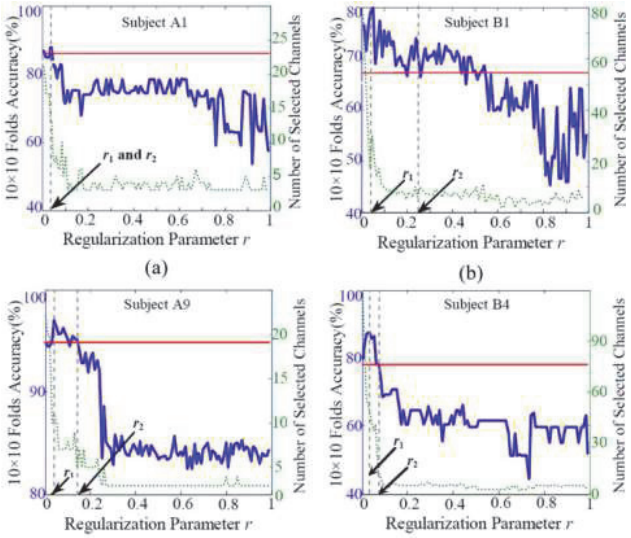

  - Summary
    - the use of small values of r improved the accuracy by removing some noisy and redundant EEG channels, while increased values of r reduced the number of channels but also decreased the classification accuracy.
    - further increase of the r value did not yield further reduction in the number of selected channels.

Results and Discussion

- Classification accuracy vs. number of selected channels.
- About bellow table (overall 22 channel subjects)
  - Decreasing the number of channels is very effective without accuracy degradation.(SCSP1: reduced 40% of the channels, SCSP2: reduced 61.2% of the channels)
  - the proposed SCSP algorithm using both criteria yielded significantly better classification accuracies (average 9.45% more) compared to the use of three typical channels.

Dataset IIa, BCI Competition IV						
			SCSP1		SCSP2	
Subject	All Ch Acc(%)	(C3,C4,Cz) Acc(%)	Acc (%)	♯ Selected Ch	Acc (%)	♯ Selected Ch
A1	90.97	75.69	91.66	13	91.66	13
A2	56.25	53.47	67.36	9	60.41	4
A3	96.52	93.05	97.91	14	97.14	12
A4	72.91	68.05	72.22	14	70.83	11
A5	63.88	53.47	65.27	11	63.19	9
A6	63.88	61.11	66.67	14	61.11	10
A7	79.86	57.63	84.72	19	78.47	15
A8	97.22	86.80	97.22	15	95.13	5
A9	91.66	88.88	91.66	10	93.75	5
Mean	79.23	70.90	81.63	13.22	79.07	8.55
Std	15.63	15.72	13.7	2.99	15.61	3.90
p-value	0.006	–	0.003	–	0.004	–

P-value denotes the paired T-test between results of (C3,C4,CZ) and other results.
(CH: Channels, ACC: Accuracy, ♯ : Number).

Results and Discussion

- Classification accuracy vs. number of selected channels.
- About bellow table (overall 118 channel subjects)
  - Decreasing the number of channels is very effective without accuracy degradation.(SCSP1: reduced 81% of the channels, SCSP2: reduced 93% of the channels)
  - The results also show an average improvement of 11.5% in the classification accuracy compared to the use of three typical channels.

Dataset IVa, BCI Competition III						
			SCSP1		SCSP2	
Subject	All Ch Acc(%)	(C3,C4,Cz) Acc(%)	Acc (%)	♯ Selected Ch	Acc (%)	♯ Selected Ch
B1	74.28	54.28	80.71	17	71.42	7
B2	94.28	80	97.14	12	95.71	10
B3	49.28	55	57.14	33	57.14	3
B4	77.14	70	85	36	77.85	10
B5	72.85	87.14	91.42	15	94.28	10
Mean	73.56	69.28	82.28	22.6	79.28	7.6
Std	16.06	14.69	15.38	11.05	16.19	3.08
p-value	0.535	–	0.043	–	0.023	–

P-value denotes the paired T-test between results of (C3,C4,CZ) and other results.
(CH: Channels, ACC: Accuracy, ♯ : Number).

Results and Discussion

- Spatial filter coefficient distribution
  - CSP filters have large weights in several unexpected locations.→ degradation of classification accuracies.
  - the SCSP filters have strong weights over the motor cortex areas and smooth weights over the other areas. → the proposed SCSP yielded filters that are neurophysiologically more relevant and interpretable.

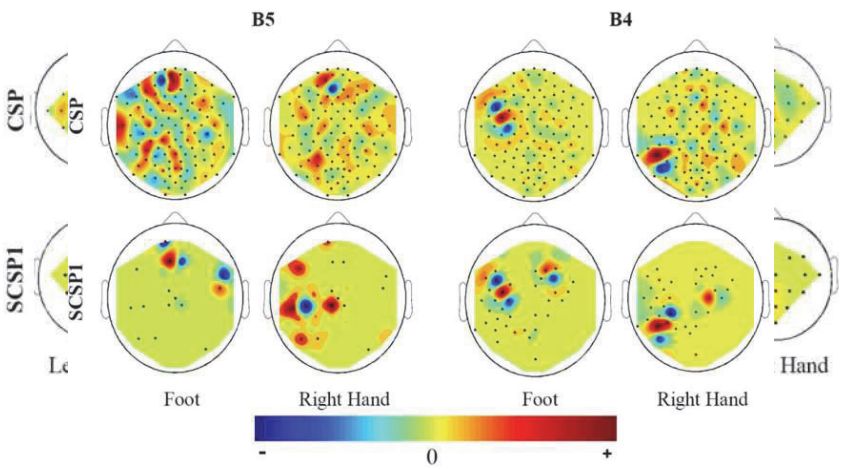

Conclusion

- They investigated the reduction of channels whereby the classification accuracy is constrained to an acceptable range.
- Two criterions
  - Using the first criterion yielded the best classification.
  - Using the second criterion retained the least number of channels.
- The proposed SCSP algorithm yielded an average improvement of 10% in classification accuracy compared to the use of typical three channels
- A visualization of the obtained sparse spatial filters
  - The proposed algorithm improved the results by emphasizing on a limited number of channels with high variances between the classes.

INFONET Seminar Application Group 2013/08/13

Compressed sensing in photoacoustic tomography

Lihong V. Wang.

Journal of Biomedical Optics 2010

Presenter Pavel Ni

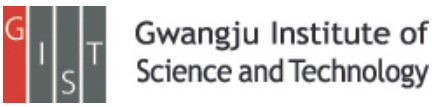

Contents

- Introduction
- Compressive sensing
- Results
- Conclusion

Introduction

- Photoacoustic formation sound waves, following light absorption in a material sample.
- For Photoacoustic effect the light intensity must vary periodically or as a single flash.
- The Photoacoustic effect is quantified by measuring the formed sound.
- By processing acquired signal map of absorbed light can be reconstructed.

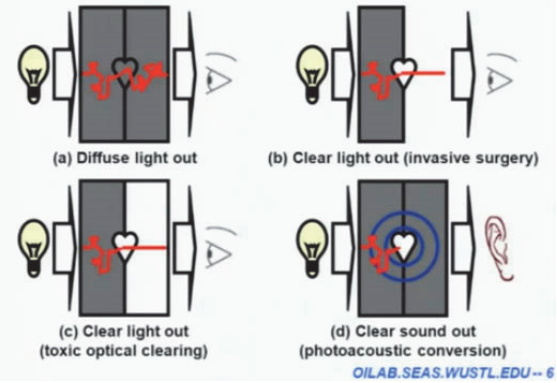

Pic. 1. Optical modalities compared to photoacoustic

- Tissues are irradiated by a pulsed laser
- Absorbed energy converted into heat
- Which further converted to thermoelastic expansion
- Initial pressure raise then propagates as ultrasonic waves

- Laser could be replaced by microwave or RF sources

Introduction

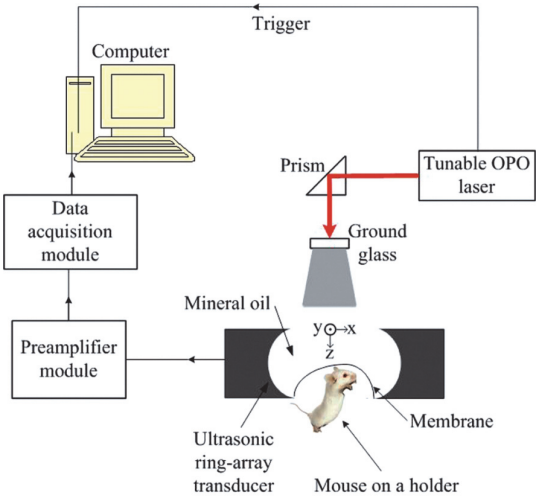

Pic. 2. Photoacoustic setup

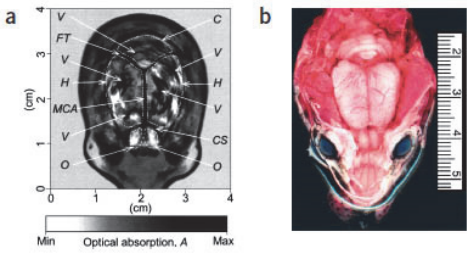

Pic. 3. a) Noninvasive PAT image of the superficial layer of a rat brain acquired with the skin and skull intact
b) Open-skull photograph of the rat brain surface after PAT

- Unfocused ultrasonic transducer with 512 elements is placed outside of object
- 64-channel data acquisition module (DAQ) is used

Compressive sensing

Pressure measurement at detecting aperture $p(\vec{r},t)$

Initial pressure raises distribution $p_0(\vec{r})$

$$p(\vec{r},t)=\frac{d}{dx}\left[\frac{1}{4\pi c^3 t}\int d\vec{r}\,' p_0(\vec{r})\partial\left(t-\frac{|\vec{r}-\vec{r}\,'|}{c}\right)\right] \quad (1)$$

Forward problem which predicts $p(\vec{r},t)$ by $p_0(\vec{r})$
Where c-is a speed of sound, $\vec{r}$ is a position of ultrasonic sensor
Velocity potential $\varphi(\vec{r},t)$

$$p_0(\vec{r})=\int_{S_0}\left[2p(\vec{r}_0,\bar{t})-\frac{2\bar{t}\,\partial p(\vec{r}_0,\bar{t})}{\partial\bar{t}}\right]_{t=|r-r_0|} d\Omega_0/\Omega_0 \quad (2)$$

Inverse problem which reconstruct $p_0(\vec{r})$ with $p(\vec{r},t)$
Where $\bar{t}=ct$, S_0 is the detecting aperture, $d\Omega_0/\Omega_0$ solid-angle weighting factor

Compressive sensing

x to represent $p_0(\vec{r})$ where each element of x is the average value of initial pressure per unit volume
Size of x depends on the field of view (N_x*N_y*N_z)

Vector y is velocity potential measured by all sensors as a function of time
Size of y is the number of detecting positions (L) times the number of temporal position (M)

Forward problem can be described as $y=\Phi x$
Where Φ is projection matrix

Inverse problem can be written as $\bar{x}=\Phi^{-1}y$
Where $\bar{x}$ is reconstructed image

Φ containing N_x*N_y*N_z*L*M
Even for 256x256 image with measurement fro 512 positions, each position has 1024 time points contain 3.4×10^{10} points (~256 GB)

Results

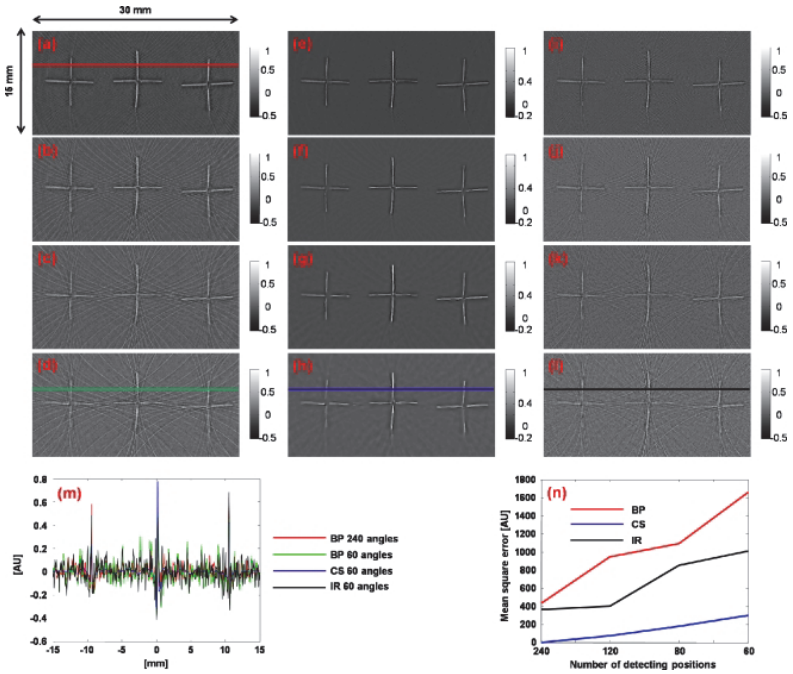

Pic. 4. (a) to (d) Images reconstructed using the BP method with 240, 120, 80, and 60 tomographic angles. (e) to (h) Images reconstructed using the CS method with 240, 120, 80, and 60 tomographic angles. (i) to (l) Images reconstructed using the traditional iterative reconstruction method with 240, 120, 80, and 60 tomographic angles. (m) Lines extracted from (a), (d), (h), and (l). (n) Comparison of the mean square errors of the three reconstruction methods.

Conclusion

They demonstrated the CS method using tissue-mimicking phantom with 3 human hair crosses with interval 10 mm. Laser pulses 10 Hz. 20 measurements at 240 different angles. Acquisition time was 8 min. Experiment shows that CS method can efficiently reduce the undersampling artifacts.

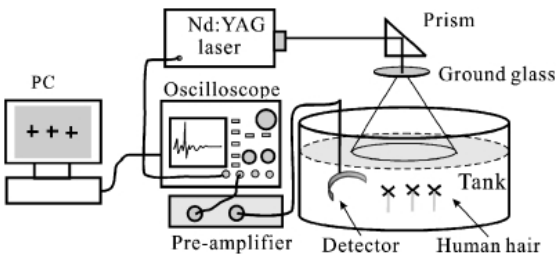

Pic. 5. used PA setup

Thank you

Toward Brain-Actuated Humanoid Robots: Asynchronous Direct Control Using an EEG-Based BCI

Yongwook Chae, Jaeseung Jeong, Sungho Jo

IEEE Transactions on Robotics.(2012.10)

Presenter : Soogil Woo

GIST, Dept. of Information and Communication, INFONET Lab.

Gwangju Institute of Science and Technology

Introduction

- In the past, there have been numerous attempts to design and build full-bodied humanoid robots.
- The realization of a robotic system that understands human intentions and produces complex behaviors is needed, for disabled or elderly persons.
- The EEG-based BCI system for robots has been suggested in robotics and neural engineering fields because some elderly or disabled people can control robots naturally and intuitively by thinking while using this system.
- The active BCI can control an application using consciously intended brain signals without external events.
- BCI methods using sensorimotor rhythms belong to the active BCI.
- These methods classify specific motor images in a general sense through the power over the frequency ranges [e.g., mu (8–12 Hz) or beta (18–22 Hz)].

Introduction

- In a synchronous BCI system, sequential cues are provided at a fixed rate.
- Because a user cannot control the timing of motion commands, it tends to lower the information transfer rate (ITR).
- One main goal of EEG-based BCIs for human robot interaction is being able to command a robot directly by thinking.
- This paper describes a new brain-actuated humanoid robot navigation system that allows for asynchronous direct control of humanoid motions using the active BCI system.
- Their system provides five low-level motion commands (e.g., “stop,” “turn the head to the left,” “turn the head to the right,” “turn the body,” or “walk forward”) by combining the classification of three motor imagery (MI) states (e.g., “left hand,” “right hand,” or “foot”) with a posture-dependent control paradigm.
- To evaluate the proposed system, a humanoid robot navigation experiment in a maze was conducted with human subjects.

Methods

- Their proposed system has four key features.
- First, low-level commands make the humanoid turn at any angle and walk to any position.
- Second, five complex humanoid motions are controlled by three intentional mental states.
- Third, the subject can command the humanoid using asynchronous protocol.
- Fourth, their system does not employ a reactive but rather an active system.

Methods(System Description)

- The system consists of three main subsystems: the BCI system, the interface system, and the humanoid control systems.
- The BCI system classifies four user mental states.
- The non-control state is referred to as "rest" and the three MI states are referred to as "left hand", "right hand", and "foot".

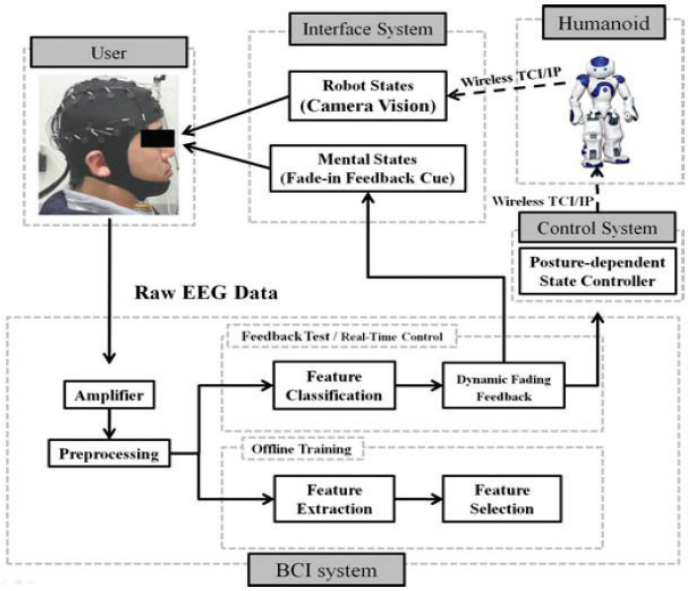

Methods(Experimental Protocol)

- 1) Offline training session
- 2) Selection of informative feature components and training of two classifiers
- 3) Online testing sessions
- 4) Checking the accuracy of the online session
- 5) Real-time humanoid navigation control experiment

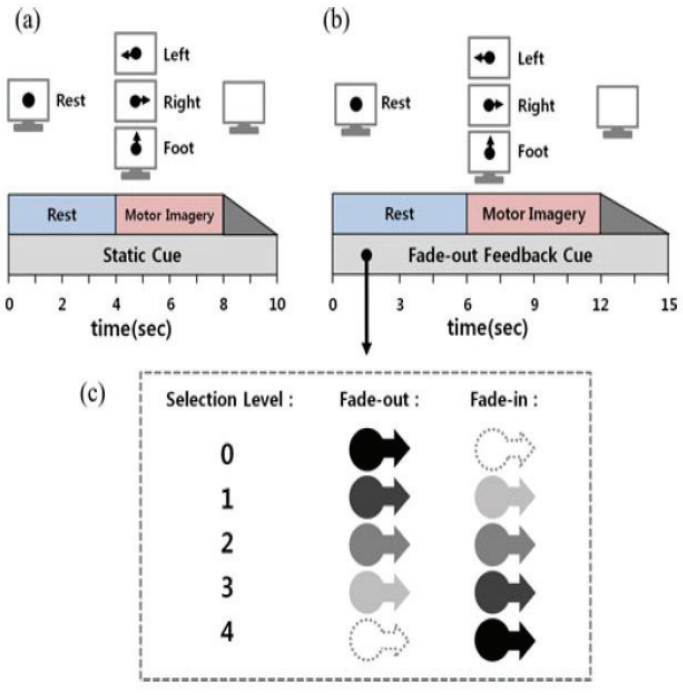

Fig. 2. (a) Offline training protocol: After the rest sessions, the subject is asked to imagine a motor imagery indicated by a static cue. (b) Online feedback testing protocol: 6 s are allowed to test the performance of the classification with dynamic fade-out feedback. (c) Dynamic fading feedback is used to secure a robust classification of a mental state from the ongoing EEG (see Section II-H).

Methods(Experimental Protocol)

- To verify the navigation performance of system, an indoor maze was designed.
- It was aimed to reduce the bias through an order of experiments (manual control or BCI control).
- If they missed any waypoints, they could skip them.
- Each subject conducted the experiment 3 times using the BCI system and one time through keyboard control for comparison.

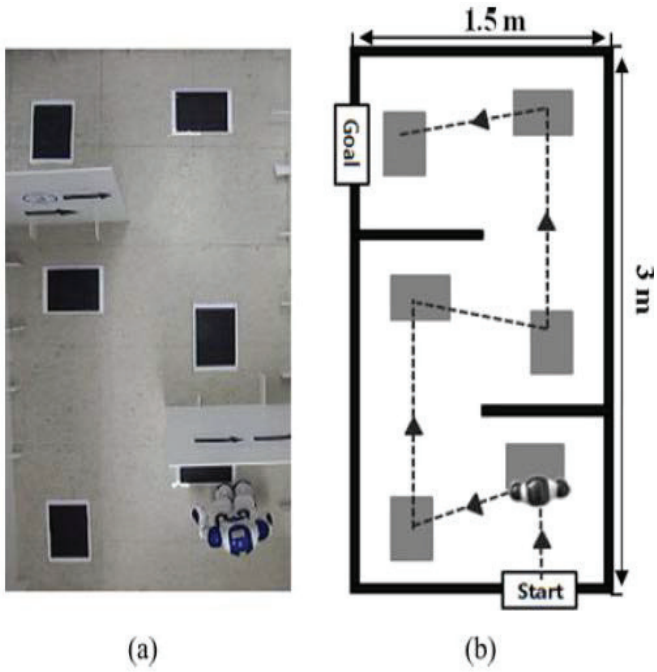

(a) (b)

Methods(Data acquisition & Feature Extraction)

- In this paper, they applied this signal processing protocol to filter and detect the sensorimotor rhythm.
- An electrode at the vertex of the head was used as a reference, and extra electrode was used as a ground.
- The impedances of all of the electrodes were lower than 5 kΩ.
- For the real-time process, a total of 21 electrodes around the sensorimotor cortex were used to apply the large Laplacian filter over the nine frontocentroparietal locations based on the international 10-20 system as show in fig.

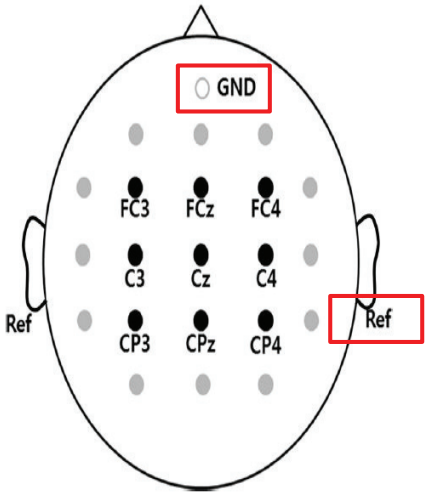

Fig. 4. EEG electrode positions with respect to the international 10–20 system. Electrode positions marked with gray circles were only used to compute the spatial filter. The nine black circles indicate the electrode positions used as the main feature channels. All electrodes are referenced to the left and right mastoids.

Methods(Data acquisition & Feature Extraction)

- To extract amplitude features, every 250ms observation segment recorded for 2 s (500 samples) from nine channels was analyzed by the autoregressive algorithm, and the square root of power in 1Hz wide frequency bands within 4-36 Hz was calculated.
- In the offline training session, 32 feature vectors with 288 dimensions (9 channels * 32 frequency components) were collected within the MI and rest periods (4 s for each) for one trial.
- These feature vectors were used to select informative feature components and train the classifiers.
- During the online testing and real-time control session, the feature vectors were sampled from the selected informative feature components and these were used to produce real-time feedback and classification for the motion commands.

Methods(Feature Selection)

- In this study, the Fisher ratio was used to select informative feature components of each subject that can be interpreted as suitable channel–frequency bands.
- For the amplitude feature vector from the “rest” and MI states, let μ_{rest} and σ_{rest} denote the mean and variance, respectively, of the amplitude feature set from the “rest” state, and let μ_{MI} and σ_{MI} denote the mean and variance, respectively, of the amplitude feature set from the MI state.
- The Fisher ratio is defined as the ratio of the between-class variance to the within-class variance as follows:

$$fr = \frac{\sigma^2_{between}}{\sigma^2_{within}} = \frac{\left(\mu_{rest} - \mu_{MI}\right)^2}{\sigma^2_{rest} + \sigma^2_{MI}}$$

- The Fisher ratio is a measure of the (linear) discrimination of two variables, and it can also be considered as a signal-to-noise ratio.

Methods(Feature Selection)

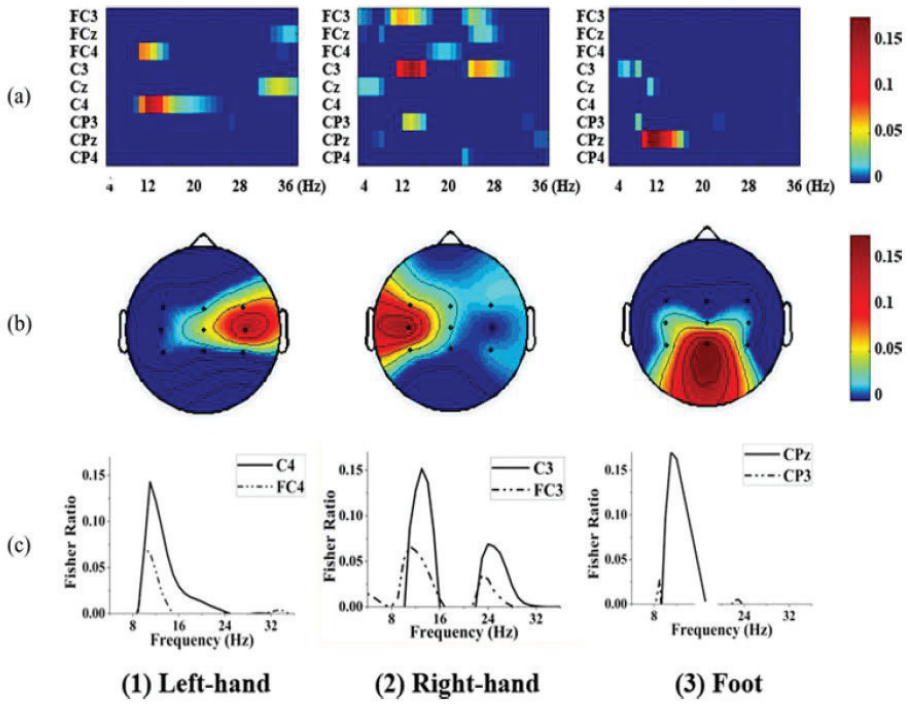

Fig. 5. Channel–frequency selection using the Fisher ratios from three sets of "rest" versus MI tasks. (a) Channel–frequency distribution of the Fisher ratios of subject A. (b) Topographical distribution of the Fisher ratios of subject A at the highest frequency bands (12, 14, and 10 Hz, respectively). The first two top-scoring channels for the "left-hand" imagery tasks were channels C4 and FC4, while channels C3 and FC3 were selected for the "right-hand" imagery tasks, and channels CPz and Cz were selected for the "foot" imagery tasks. (c) Spectral distribution of the Fisher ratios for subject A. For the "left-hand" imagery tasks, the maximum Fisher ratio of C4 was 0.15 at 12 Hz, and a 5-Hz window centered at 12 Hz was selected as the optimal frequency region.

Methods(Classification)

- To translate the intended EEG data into appropriate movement commands for the humanoid robot, the intentional activity classifier (IAC) and movement direction classifier (MDC) were employed.
- If the signals are interpreted as the MI state by the IAC, then the MDC classifies the specific MI state as either a "left hand", "right hand", or "foot" states.
- For the initial training, the features from the training trials between 0 and 4 s (e.g., rest period) were assigned to the "rest" class, and the signal segments between 4 and 8 s (e.g., MI period) were assigned to the MI class.
- For the training, the negative output values of the IAC denote the "rest" classes, while the positive output values of the IAC denote the MI classes.

Methods(Classification)

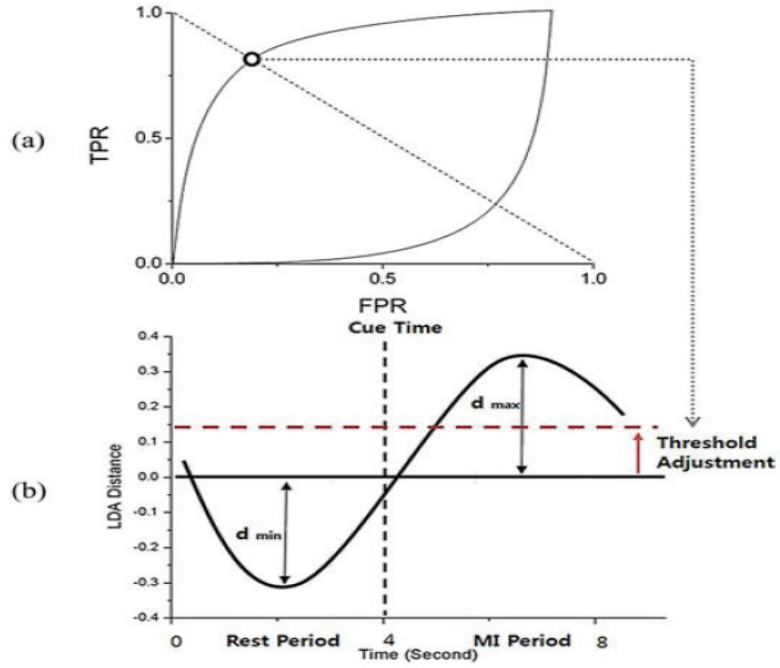

Fig. 6. Time period selection using the LDA distance metric and determination of a classifier threshold. (a) ROC curve determines an appropriate threshold value and (b) a typical intention level curve of a subject to discriminate the rest and MI time periods. As the informative time period, a 1-s interval centered at the maximum and minimum LDA distance points was selected.

Methods(Dynamic Fading Feedback rule)

- Because the classification results of the sensorimotor rhythm based active BCI could generate the misclassification results, some normalization methods would be used to enable a smooth transition between class-specific feedbacks.
- In this study, the dynamic fading feedback rule was designed to avoid abrupt false classifications, as shown in fig.

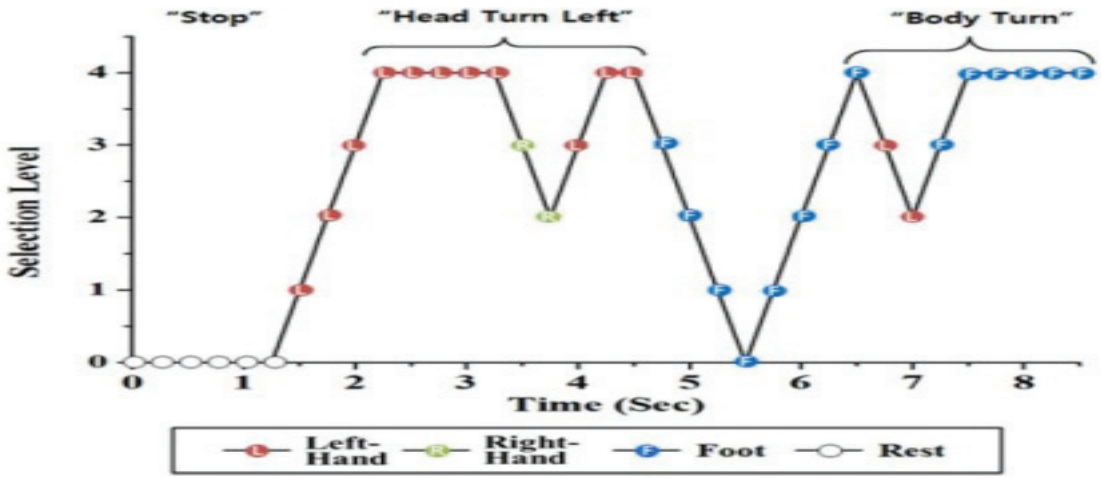

Fig. 8. Dynamic fading feedback rule. Variation of selection levels and classifications of a real-time BCI experiment over 8.5 s.

Methods(Dynamic Fading Feedback rule)

- 1) the candidate decision produced during the online feedback testing session and the real-time control session
- 2) the selection level associated with the confidence measurement of selected classifications.

➢ Rule 1: When the selection level is zero, the next first classification is newly set to be the candidate's decision.

➢ Rule 2: Whenever the classification result is identical to the candidate decision, the selection level is increased by 1; otherwise, the selection level is decreased by 1.

➢ Rule 3: When the selection level reaches 4, the control system confirms its decision and generates a motion command accordingly (i.e., "left," "right," or "forward").

➢ Rule 4: The fading feedback cues and the arrow and text shown on the display are transparentized according to the candidate's decision and its selection level.

Methods(Dynamic Fading Feedback rule)

- Fig. 8 illustrates an example of the command selection procedure.
- For the first 1 s, the consecutive "rest" commands appear.
- At 1.25 s, the four consecutive "left-hand" classifications increase the selection level up to 4, and then, the system generates a "left" command. The robot executes its motion accordingly through the control paradigm, as described in Fig. 7 (i.e., "head turn left").
- Next, consecutive "left-hand" classifications cause the robot to keep turning its head to the left up to 15◦ (3◦ per command).

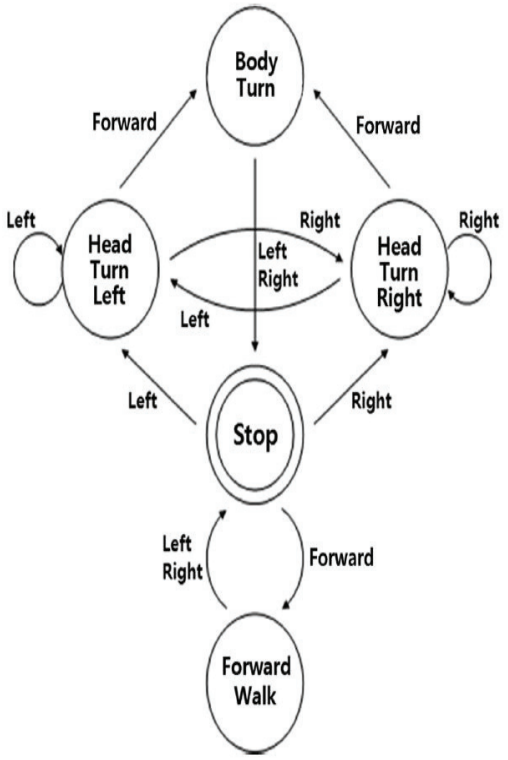

Fig. 7. Diagram of humanoid navigation control. (Left) Left-hand imagery. (Right) Right-hand imagery. (Forward) Foot imagery.

Methods(Evaluation)

- 1) Performance of the Brain–Computer Interface System: (ITR)

$$I_d = \log_2 N + p\log_2 p + (1-p)\log_2\{(1-p)/(N-1)\}, \quad \text{ITR}=f_d \times I_d$$

- I_d is the bit rate (bits/trial) for the three mental state choices (N=3), p is the accuracy, and f_d is the decision rate (trial/min).
- 2) Navigation Performance

✓ Total Time: total time taken to accomplish the task (in seconds);

✓ Traveled Distance: distance traveled to accomplish the task (in centimeters);

✓ Forward Steps: number of walking steps during forward movement;

✓ Turning Steps: number of walking steps to turn the robot body;

✓ Explored Angle: total turning angle of the robot head to explore the surrounding environment (in degrees);

✓ # Trans: number of transitions between the walking mode and the exploration mode;

✓ Waypoint: number of waypoints on which the robot

Results(Feature Selection)

- The Fisher ratios for the channel and frequency components and averaged discriminant values for the offline training period for each motor imagery and subject are illustrated.
- Table I describes the selected feature components of the five subjects.

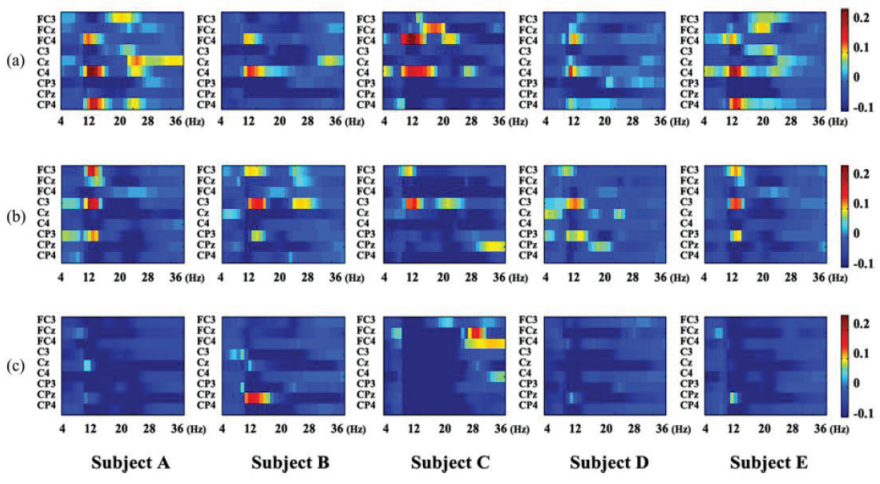

Fig. 10. Channel–frequency distributions of Fisher ratios for all subjects for "left-hand," "right-hand," and "foot" imagery tasks. (a) Left. (b) Right. (c) Foot.

TABLE I
FEATURE SELECTION RESULTS

Subject	Left-hand		Right-hand		Foot	
	Ch	Freq	Ch	Freq	Ch	Freq
A	C4	9-13	FC3	10-14	Cz	8-12
	CP4	10-14	C3	9-13	CPz	7-11
B	C4	11-15	C3	12-16	CPz	10-14
	FC4	9-13	FC3	8-12	CP3	21-25
C	FC4	9-13	C3	9-13	FCz	26-30
	C4	10-14	FC3	7-11	FC4	28-32
D	C4	9-13	C3	10-13	CPz	8-12
	FC4	10-14	CP3	11-15	FC4	6-10
E	C4	9-13	C3	11-15	CPz	9-13
	CP4	10-14	FC3	11-15	FCz	6-10

Results(Navigation Performance)

- Tables II and III provide details about the performance of the two hierarchical classifiers (IAC and MDC) for the five subjects.
- Table II shows the number of offline training trials per mental task, the TPR and FPR of the IAC, and the accuracy of the MDC for each task.
- Table III shows the online testing performance achieved using the fading feedback rule for the given mental tasks.

TABLE II
OFFLINE TRAINING RESULTS

		A	B	C	D	E
Trials		140	160	120	200	200
Accuracy (%)	Left-hand	79.0	88.8	96.6	86.0	78.5
	Right-hand	85.9	89.4	82.0	62.3	74.0
	Foot	59.3	75.3	83.2	63.8	75.0
	Average	74.7	84.5	87.3	70.7	75.8
ITR (bit/min)		7.7	12.1	13.6	6.4	8.2

TABLE III
ONLINE FEEDBACK TESTING RESULTS

		A	B	C	D	E
Response Time (sec)	T1	2.2	1.6	1.4	1.9	2.1
	T2	3.4	3.1	2.6	3.5	3.3
Accuracy (%)	Left-hand	86.7	80.0	100.0	93.3	86.7
	Right-hand	80.0	86.7	93.3	66.7	66.7
	Foot	66.7	73.3	86.7	66.7	73.3
	Average	77.8	80.0	93.3	77.8	75.6
ITR (bit/min)		10.6	12.8	26.5	10.4	9.8

Results(Navigation Performance)

- The results of the real-time navigation experiments of the humanoid robot.
- During the manual control experiments, all of the subjects controlled the robot to pass through all five waypoints without any collisions during navigation.
- During the BCI control experiments, the robot stepped on 3.2 waypoints with an average of 0.3 collisions, while the robot always successfully reached the final position.

Subject	Session	Total time (sec)	Distance travelled (cm)	Forward steps (times)	Turning steps (times)	Explored angle (°)	# Trans. (times)	Waypoint (times)	Collisions (times)
A	BCI	634.1	335.5	102.7	64.3	1161.3	39.7	2.3	0.7
	Manual	479.7	415.8	126.0	64.0	543.0	27.0	5.0	0.0
B	BCI	642.4	429.0	129.3	78.3	1485.9	40	4	0.7
	Manual	432.7	403.7	129.0	58.0	501	21	5	0
C	BCI	632.3	430.1	130.3	69.7	974.0	49.7	4.7	0.0
	Manual	452.9	389.4	118.0	64.0	605.0	34.0	5.0	0.0
D	BCI	448.8	307.0	86.7	46.0	704.9	31.3	2.0	0.0
	Manual	410.5	481.0	134.0	61.0	494.1	21.0	5.0	0.0
E	BCI	448.8	410.0	115.0	51.7	585.1	27.0	2.7	0.3
	Manual	424.4	508.9	143.0	58.0	509.0	24.0	5.0	0.0
BCI	Mean (± Std)	561.3 (± 102.8)	382.3 (± 57.2)	112.8 (± 18.5)	62.0 (± 13.2)	982.2 (± 360.7)	37.5 (± 8.8)	3.1 (± 1.2)	0.3 (± 0.4)
Manual	Mean (± Std)	440.0 (± 27.0)	439.8 (± 52.2)	130.0 (± 9.3)	61.0 (± 3.0)	530.4 (± 45.7)	25.4 (± 5.4)	5.0 (± 0.0)	0.0 (± 0.0)

Results(Navigation Performance)

- Fig. shows the sequential snapshots taken during an experiment.

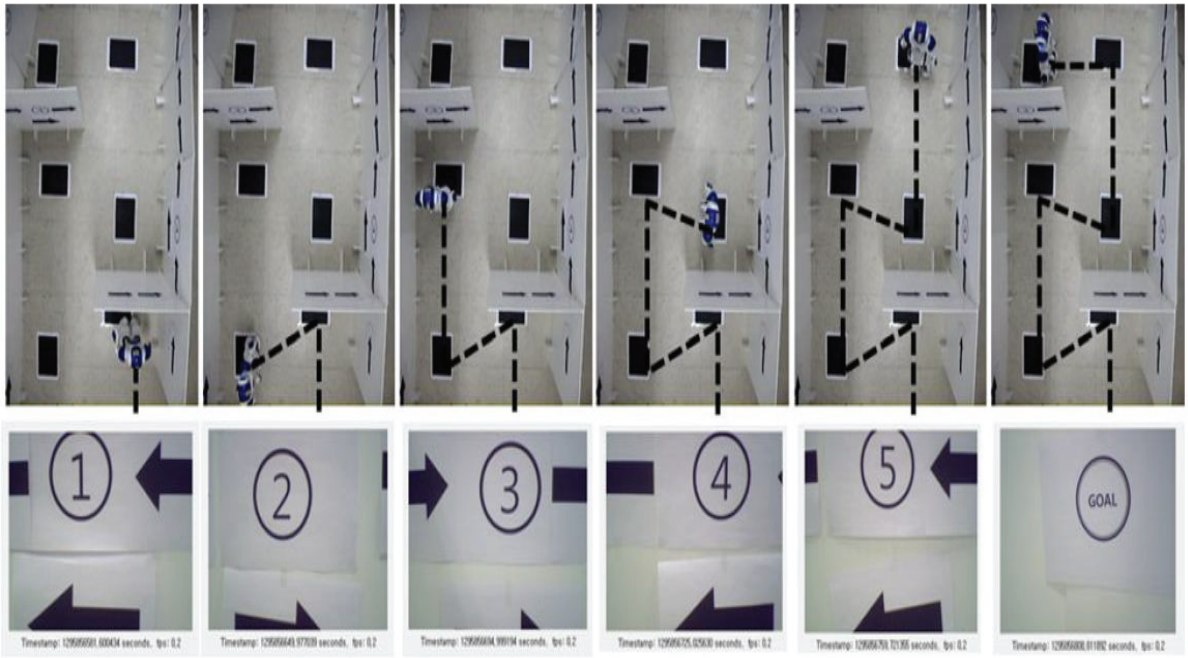

Fig. 12. Navigation task is to make the robot move from a starting position to destination regions, while passing through the five waypoints at the corners of the maze. The first row shows snapshots taken during a trial, and the second row shows images acquired from the robot camera at each position.

Discussions

- This paper has described a new humanoid navigation system that is directly controlled through an asynchronous sensorimotor rhythm-based BCI system.
- Their approach allows for flexible robotic motion control in unknown environments using a camera vision.
- Brain-actuated humanoid control by this active BCI could be further improved in speed and accuracy.
- Recently, researchers have introduced hybrid BCIs that exploit the advantages of different reactive approaches (e.g., P300 or steady-state visually evoked potentials) and active approaches to improve the overall performance of BCI system.
- Another extension of this study is to realize human–robot interaction that can recognize high-level human cognitions, such as affective states.

Thank you!

Digital image information encryption based on compressive sensing and double random-phase encoding technique

Etienne Cuche, Frederic Bevilacqua, and Christian Depeursinge
Institute of Applied Optics, Swiss Federal Institute of Technology, CH-1015 Lausanne, Switzerland

Presenter: Nitin Rawat

Considering the threat of accessing and tempering data by an unauthorized person, a secure transmission of multimedia information like image data using cryptography technique has received attention in recent years. The encryption methods enable security of data by converting it into more complex form. Besides security, the database and communication problems are critical problems due to large data size and complexity. It has become important to reduce the size of the data by preserving the complexity.

Image Encryption using FFT with Single random matrix

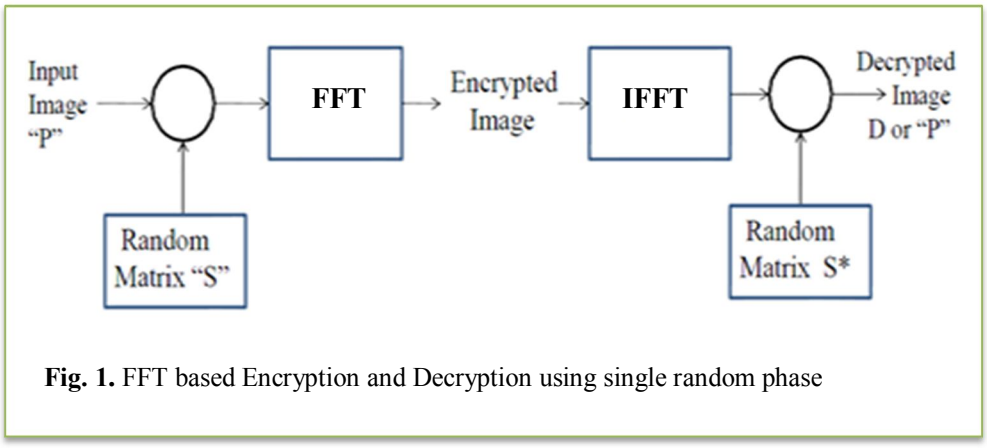

Fig. 1. FFT based Encryption and Decryption using single random phase

Fig. 1 shows the Encryption approach using single random phase method. Let an image multiplied by a single random matrix $\exp[i\phi_1(x,y)]$ and further taking Fourier transform of the result to get an encrypted image.

Decryption process is reversed by taking the complex conjugate of the random phase and further its inverse Fourier transform. Here the key is formed by the combination of the transform and the random matrix.

Approach

Double random phase encoding technique involves the use of two 2-D random phase masks. Let $h(x,y)$ indicates the image to be hidden and $g(x,y)$ denotes the encrypted image. $\exp[i\phi_{1,2}(x,y)]$ stands for the random phase masks 1 & 2 represented as the key values. The encryption process can be expressed as:

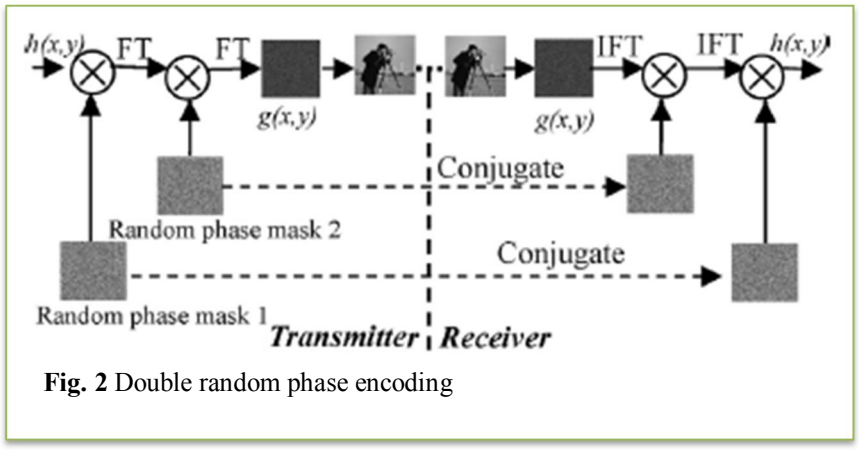

Fig. 2 Double random phase encoding

$$g(x,y) = FT\left\{FT\left[h(x,y)\exp[i\phi_1(x,y)]\right]\exp[i\phi_2(x,y)]\right\} \tag{1}$$

Then the encrypted image is dispersed and embedded into a host image to form a combined image. The corresponding decryption process is:

$$h(x,y) = FT^{-1}\left\{FT^{-1}\left[g(x,y)\exp[-i\phi_2(x,y)]\right]\exp[-i\phi_2(x,y)]\right\} \tag{2}$$

Compressive Sensing

CS is based on the recent understanding that a small collection of measurements of a compressible signal contain enough information for reconstruction and processing.

$$y = \Phi f = \Phi\Psi\tilde{x} \tag{3}$$

Where the sensing matrix Φ is a $M \times N$ matrix, where $M \ll N$. So, y becomes a $M \times 1$, while f is $N \times 1$.

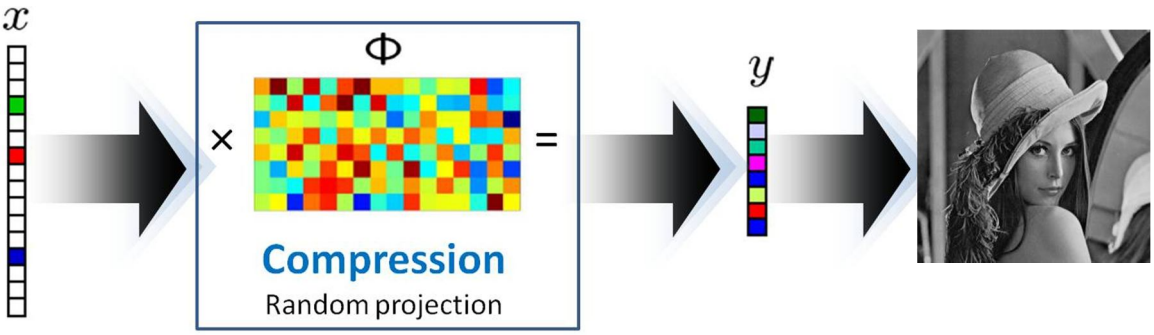

Fig. 3 Compressive sensing model shows the dimension reduction and the compression after sampling process

Digital image information encryption scheme using CS Scheme

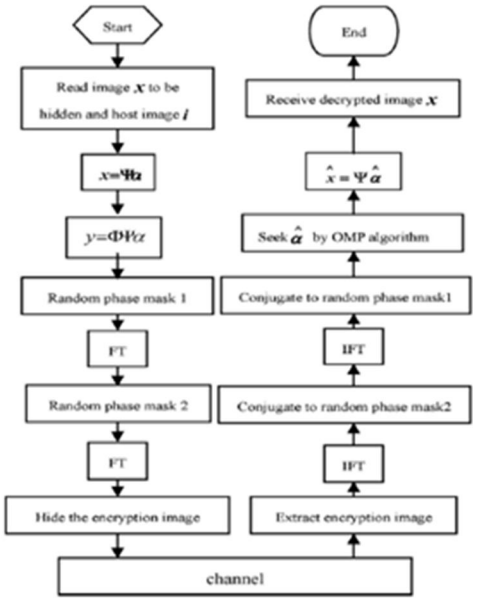

Fig. 4 Flow diagram of image information encryption and decryption

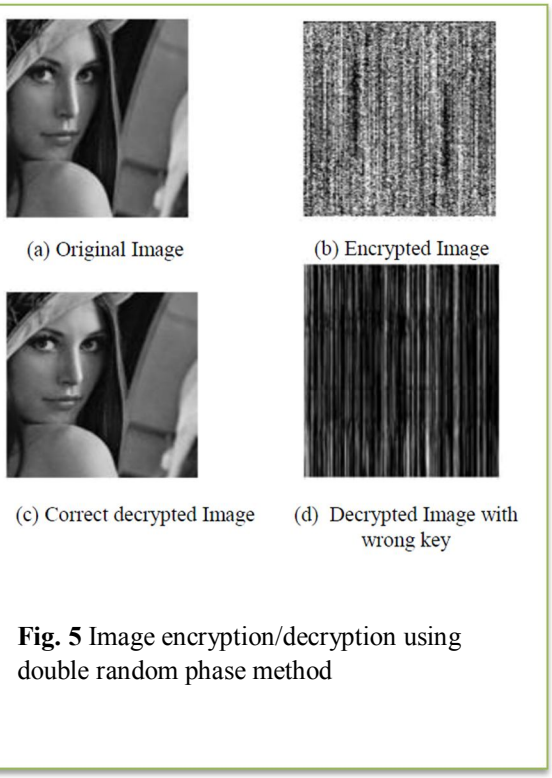

Fig. 5 Image encryption/decryption using double random phase method

In this method, the image information to be hidden is encrypted by CS firstly and the size of sampled information is reduced compared with original image.

Then, it is re-encrypted by DRPE technique where the scales of random-phase masks are also reduced correspondingly. The double-encrypted information is dispersed and embedded into the host image then transmitted through a channel. At the received terminal, original image information is reconstructed approximately via OMP algorithm after the decryption of double random-phase encoding. For CS, in order to recover the signal, the matrix A^{CS} should be available to the receiver otherwise, the gathered samples appear useless to anyone eavesdropping on the channel. This encryption comes naturally and requires no additional cost.

Simulation result

Considering natural images tend to be compressible in the transform domain, here Ψ is designed a $N \times N(N = 256)$, 2-D wavelet transform matrix which have the same size with image x to be hidden, Φ is a $M \times N$ random measurement matrix and the measuring length $M = 192$ is less than N (the value of M changes with the signal sparsity of hiding image).

Peak-to-peak Signal-to-Noise Ratio (PSNR) is used for measuring the quality of decrypted digital image as described in following equation

$$\text{PSNR}= 10\log\frac{255^2}{(1/NN)\sum_{i=1}^{N}\sum_{j=1}^{M}[R(i,j)-I(i,j)]^2} \tag{4}$$

where $R(i,j)$ is the reconstructed image and $I(i,j)$ is the initial image. The experimental result shows that the quality of decrypted digital image is very well and the PSNR is 30.8874 dB.

Wrong Key

Fig. 6 shows that when the keys of random-phase mask cannot be deciphered correctly, people who intercept information illegally cannot reconstruct original image, the security of information is ensured. It shows the decrypted image obtained after using the right key and random phase matrix. For hacker, it would be extremely difficult to acquire the correct key because one needs to know the random phase mask and the key.

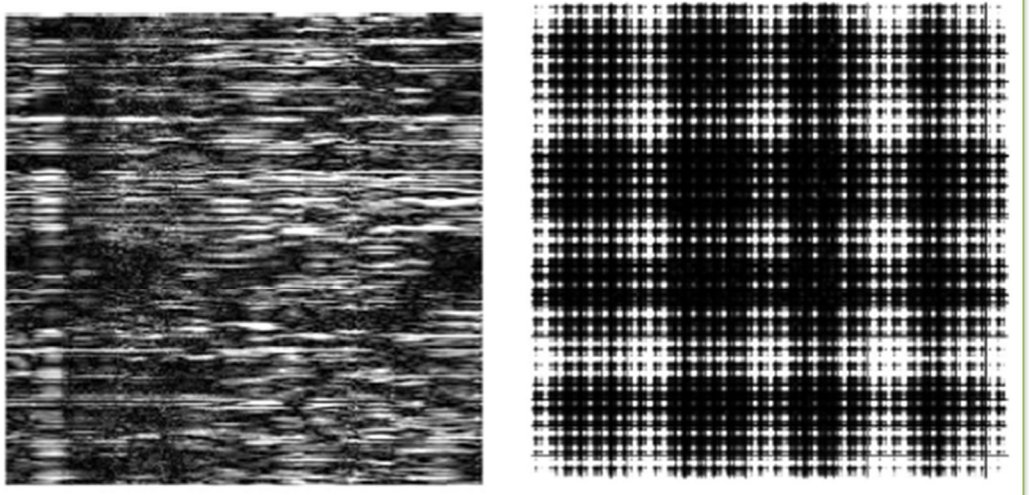

Fig.6. (a & b) Reconstructed image with a condition of wrong measurement

Conclusion

In this paper, they utilized the characteristics of CS, signal sparsity , dimensional reduction and random projection, to sample or encrypt a digital image. Then, the transformed image information can be re-encrypted by DRPE technique. In order to improve information security effectively, the image information is encrypted twice with low data volume transmission.

Sparsity driven ultrasound imaging

A. Tuysuzoglu et al.

J. Acoustical Society of America (Feb. 2012.)

Presenter : Jin-Taek Seong

GIST, Dept. of Information and Communications, INFONET Lab.

Gwangju Institute of Science and Technology

Overview of Scenarios

- A broadband single-element unfocused transducer performs a raster scan in a plane parallel to the cross section of the object.
- At each scan position, the transducer sends an acoustic pulse and then detects the echo.
- For all experiments, the initial distance between the object and transducer was set to be 75 mm.

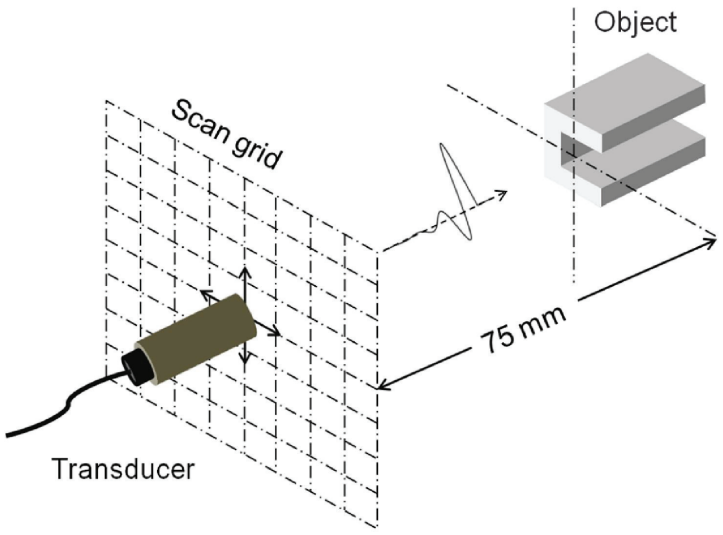

Introduction

- A new model-based framework for ultrasound imaging that estimates a complex-valued reflectivity field is presented.
- The benefits are:
  - Providing improved resolution and reduced diffraction artifacts.
  - Overcoming challenging observation scenarios involving sparse and reduced apertures.
- The framework is based on a regularized reconstruction of the underlying reflectivity field using a wave-based linear model of the ultrasound observation process.
- The physical model is coupled with nonquadratic regularization functions, exploiting prior knowledge that the underlying field should be sparse.
- These nonquadratic functions enable the preservation of strong physical features, i.e., strong scatterers or boundaries.

Observation model for ultrasound scattering

- The free space Green's function is used to model the scattered field in space in response to a point source of excitation,

$$G(|\mathbf{r}' - \mathbf{r}|) = \frac{\exp(jk(|\mathbf{r}' - \mathbf{r}|))}{4\pi|\mathbf{r}' - \mathbf{r}|},$$

- This can linearize the Lippmann–Schwinger equation using Born approximation to obtain the following observation model:

$$y(\mathbf{r}') = c \int G^2(|\mathbf{r}' - \mathbf{r}|) f(\mathbf{r})\, dr$$

  - where **y**(·) denotes the observed data, **f**(·) denotes the unknown complex-valued reflectivity fields
  - Note that squaring the Green's function captures the two-way travel from the transducer to the target and back

Observation model for ultrasound scattering

- The model is discretized and the presence of measurement noise is taken to be additive to obtain the following discrete observation model:

$$\mathbf{y} = \mathbf{T}\mathbf{f} + \mathbf{n}$$

  - where **y** and **n** denote the measured data and the noise, respectively, at all transducer positions; **f** denotes the sampled unknown reflectivity field; and **T** is a matrix representing the discretized version of the observation kernel.

- Given the noisy observation model, the imaging problem is to find an estimate of **f** based on the measured data **y.**

Sparsity-driven ultrasound imaging-Imaging problem formulation

- The conventional ultrasound imaging method of synthetic aperture focusing technique (SAFT) essentially corresponds to using $\mathbf{T}^H$ to reconstruct the underlying field **f**,

$$\hat{\mathbf{f}}_{\mathrm{SAFT}} = \mathbf{T}^H\mathbf{y}$$

- The proposed method produces an image as the solution of the following optimization problem, which will be called sparsity-driven ultrasound imaging (SDUI):

$$\hat{\mathbf{f}}_{\mathrm{SDUI}} = \underset{f}{\operatorname{argmin}}\, J(\mathbf{f})$$

  - where the objective function has the following form:

$$J(\mathbf{f}) = ||\mathbf{y} - \mathbf{T}\mathbf{f}||_2^2 + \lambda_1 ||\mathbf{f}||_p^p + \lambda_2 ||\mathbf{D}|\mathbf{f}||_p^p$$

  - **D** is a discrete approximation to the derivative operator or gradient, λ_1, λ_2 are scalar parameters

Sparsity-driven ultrasound imaging-Solution of the optimization problem (1/2)

- The following smooth approximation is used as

$$||\mathbf{z}||_p^p \approx \sum_{i=1}^{K} \left(|(\mathbf{z})_i|^2 + \epsilon \right)^{p/2}$$

- Using the approximation, we obtain a modified cost function,

$$J_m(\mathbf{f}) = ||\mathbf{y} - \mathbf{T}\mathbf{f}||_2^2 + \lambda_1 \sum_{i=1}^{N} \left(|(\mathbf{f})_i|^2 + \epsilon \right)^{p/2} + \lambda_2 \sum_{i=1}^{M} \left(|(\mathbf{D}|\mathbf{f}|)_i|^2 + \epsilon \right)^{p/2}.$$

- The quasi-Newton method is employed.
- The gradient of the cost function is expressed as

$$\nabla J_m(\mathbf{f}) = \tilde{\mathbf{H}}(\mathbf{f})\mathbf{f} - 2\mathbf{T}^H\mathbf{y}$$

Sparsity-driven ultrasound imaging-Solution of the optimization problem (2/2)

- The Hessian is

$$\tilde{\mathbf{H}}(\mathbf{f}) \triangleq 2\mathbf{T}^H\mathbf{T} + p\lambda_1\Lambda_1(\mathbf{f}) + p\lambda_2\Phi^H(\mathbf{f})\mathbf{D}^T\Lambda_2(\mathbf{f})\mathbf{D}\Phi(\mathbf{f})$$

- They use $\tilde{\mathbf{H}}(\mathbf{f})$ as an approximation to the Hessian in the following quasi-Newton iteration:

$$\hat{\mathbf{f}}^{(n+1)} = \hat{\mathbf{f}}^{(n)} - \left[\tilde{\mathbf{H}}\left(\hat{\mathbf{f}}^{(n)} \right) \right]^{-1} \nabla J_m\left(\hat{\mathbf{f}}^{(n)} \right)$$

- The following fixed point iterative algorithm can be obtained:

$$\tilde{\mathbf{H}}\left(\hat{\mathbf{f}}^{(n)} \right) \hat{\mathbf{f}}^{(n+1)} = 2\mathbf{T}^H\mathbf{y}$$

- The iteration runs until $\| \hat{\mathbf{f}}^{(n+1)} - \hat{\mathbf{f}}^{(n)} \|_2^2 / \| \hat{\mathbf{f}}^{(n)} \|_2^2 < \delta$

Experiments and Results

- Ultrasound experiments were carried out in a tank of water (2 X 1 X 1 m).
- Data acquisition scenarios are considered: (a) full aperture case, (b) sparse aperture case, and (c) reduced aperture case.
- A full scan forms a 64 X 64 grid with a total of 4096 scan locations.

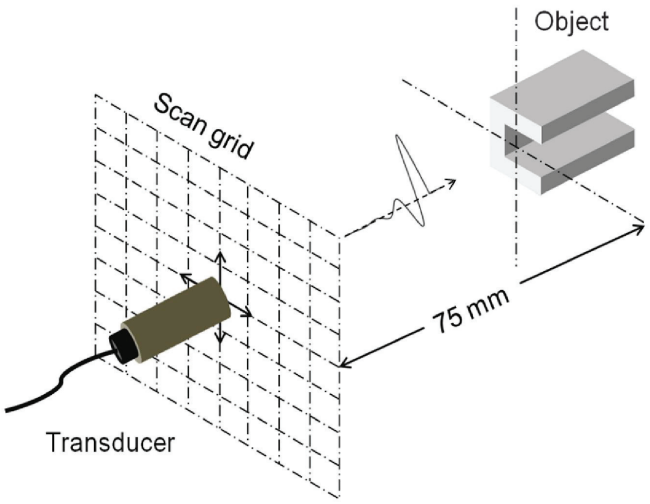

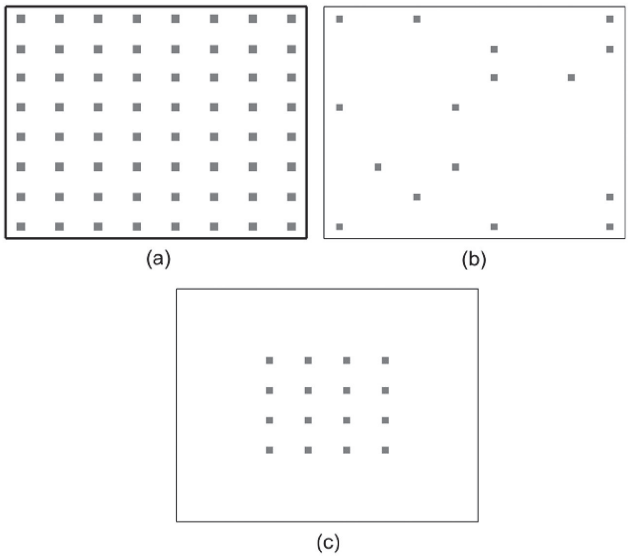

- Images of the 3.2 mm steel rod using full, sparse, and reduced aperture data
  - Reconstructions by SAFT using (a) full data, (c) 6.25% sparse data, and (e) 6.25% reduced data
  - Reconstructions by the SDUI method using (b) full data with λ_1=500, λ_2=100, (d) 6.25% sparse data with λ_1=25, λ_2=5, and (e) 6.25% reduced data λ_1=170, λ_2=5

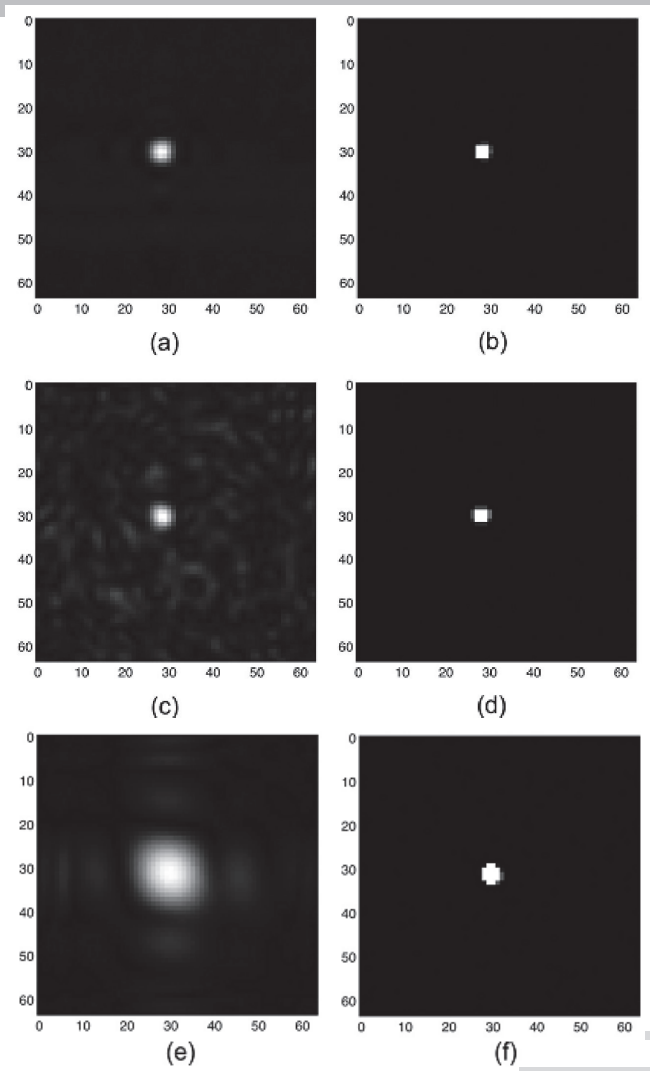

- Effect of the gradient-based regularization
  - Images of the channel using sparse aperture data. Reconstructions by SAFT using (a) 14.06% and (d) 6.25% sparse data
  - Reconstructions by the SDUI method with $\lambda_2=0$ using (b) 14.06% sparse data with $\lambda_1=20$, (e) 6.25% sparse data with $\lambda_1=5$
  - Reconstructions by the SDUI method using with (c) $\lambda_1=600$, $\lambda_2=20$ and (f) $\lambda_1=250$, $\lambda_2=10$

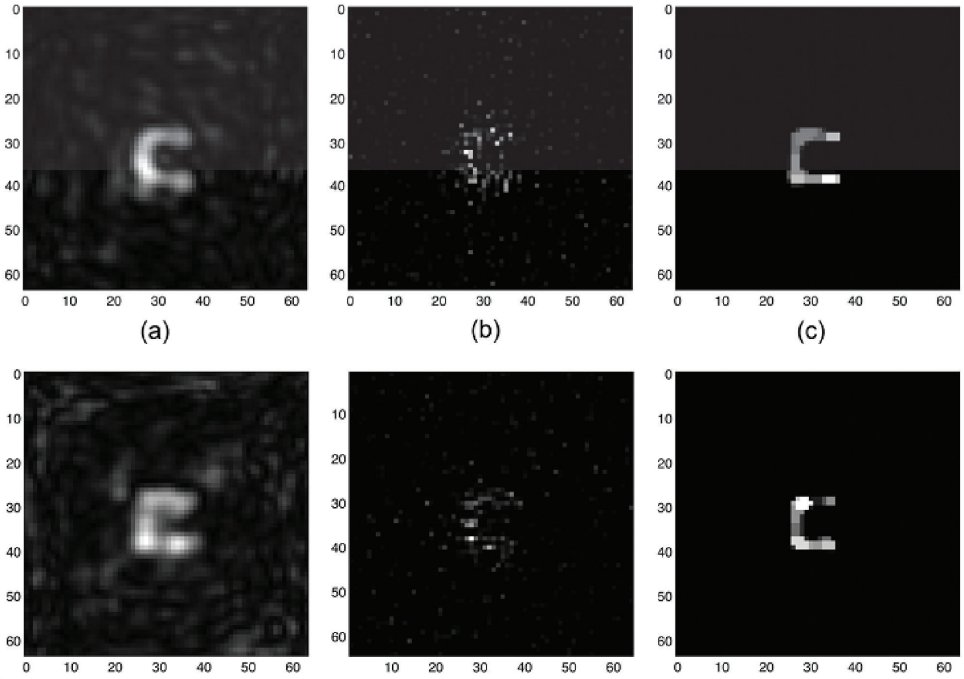

Selection of regularization parameters

- Recall that λ_1 scales the term that emphasizes preservation of strong scatterers, whereas λ_2 scales the gradient of the image and emphasizes smoothness and sharp transitions.
  - If the object features of interest are below the size of a nominal resolution cell, that is they should appear as “points,” then they can be emphasized by choosing $\lambda_1 \gg \lambda_2$. This case leads to sparse reconstructions and can produce super-resolution.
  - If instead the object features of interest span multiple pixels, and thus form regions, these homogeneous regions can be recovered with sharp boundaries by choosing $\lambda_1 \ll \lambda_2$

- SDUI reconstructions of the 3.2 mm steel and the 3.2 mm aluminum rod separated by 10 mm reconstructed from 6.25% reduced aperture data for various choices of the regularization parameters.

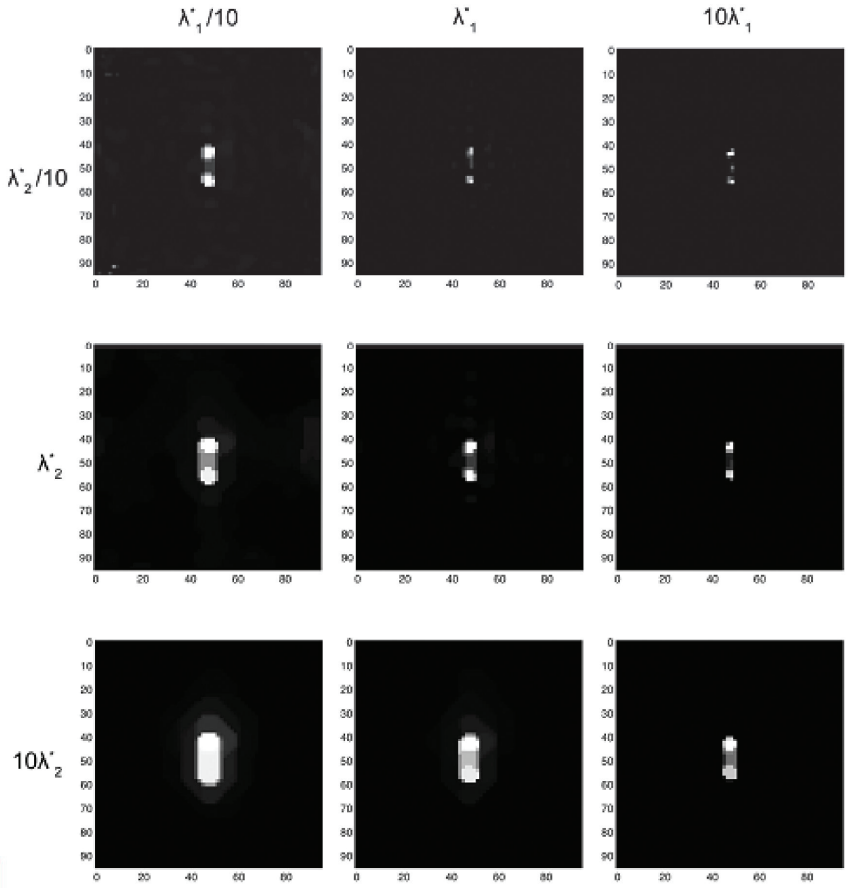

Conclusions

- A new method for ultrasound image formation has been described that offers improved resolvability of fine features, suppression of artifacts, and robustness to challenging reduced data scenarios.
- The resulting nonlinear optimization problem was solved through efficient numerical algorithms exploiting the structure of the SDUI formulation.
- Results obtained from sparse aperture data scenarios suggest that SDUI can alleviate the motion artifact problem.
- The performance of the SDUI could be likely enhanced using multi-frequency data where the choice of number of frequency components and the appropriate weightings will be key factors to consider.

An auditory brain–computer interface evoked by natural speech

M A Lopez-Gordo, E Fernandez, S Romero, F Pelayo and Alberto Prieto

Journal of Neural Engineering (2012)

Presenter : Younghak Shin

GIST, Dept. of Information and Communication, INFONET Lab.

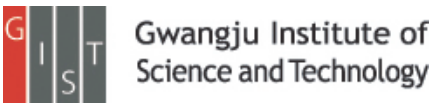

Introduction

- The vast majority of BCIs use visual interaction with the subjects, either as stimulation, biofeedback or as visual support for the paradigm.
- Examples are the BCIs based on steady-state visual evoked potentials or the P300.
- However, some patients (in an advanced stage of ALS with visual impairment or patients under the condition of unresponsive wakefulness syndrome, who still preserve the necessary level of consciousness to process auditory stimuli and follow verbal instructions) can not use the above BCIs.
- In this regard, an auditory BCI seems to be a more appropriate solution.
- There have not been many attempts to use the auditory modality instead of the visual one.

Introduction

- The auditory BCIs present some inconveniences that have not been suitably addressed so far.
- For instance, the number of channels used (e.g. 67 and 16 channels in [10, 27] respectively), because it can be a limitation in the usability and increases the time for the initial setup.
- This BCI requires considerable cognitive effort in terms of training (up to several weeks [33]), length of the trials or number of stimuli
- The use of synthetic sounds instead of natural ones (e.g. tone beeps [10]) or complex auditory paradigms [27, 34] - since they can affect the level of interest and cognitive effort of the participants.
- In this paper, they postulate that an auditory BCI based on natural sound (e.g. human voice), a simple and low-demanding task (e.g. selective attention), a small number of electrodes and a simple paradigm (e.g. binary class) with little or no training.

Objective

- The main goal of this study is to determine the viability of a BCI based on a dichotic listening task with natural speech
  - **Dichotic listening** is a psychological test commonly used to investigate selective attention within the auditory system
  - pay attention to the stream of stimuli delivered to one ear and to ignore the stream delivered to the other one

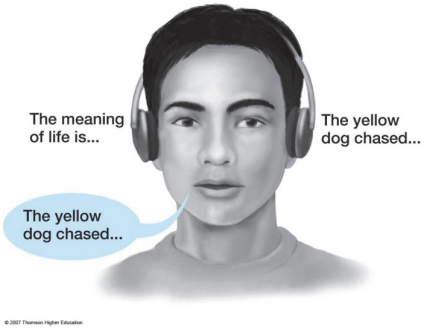

- The usability is expected to be improved due to a careful design based on:
  - first, a minimum number of EEG channels, namely, just one, which makes this BCI suitable for subjects attached to electronic devices in a hospital or lying on a bed;
  - second, minimum cognitive effort by means of short trials;
  - third, no need of formal training, which was substituted for a calibration run and the use of the native-to-human selective attention in a dichotic listening paradigm.

Methods

- The experiment is based on the dichotic listening paradigm
- The essence of dichotic listening is to pay attention to the stream of stimuli delivered to one ear and to ignore the stream delivered to the other one.
- A dichotic listening paradigm was established by means of two streams of stimuli, one per ear, which were presented simultaneously to the subject through earphones
- Five stimuli are given per second (ISI = 200 ms) and an interleaving interval (ILI) is 100 ms between streams.
- The beginning and the end of each trial was signaled by means of a high beep and a low beep, respectively.

Methods

- The figure shows the typical structure of a evaluation trial
- After the beep, the trial starts with two streams of 30 stimuli per ear.
- Each stimulus corresponds to a letter from words with five and six letters (left and right respectively) that are repeated six and five times respectively.
- In this example the words ‘rezos’ and ‘sabana’ were used for both streams.
- The lower graph shows the typical steady response obtained after the average of the calibration trials for one of the streams.

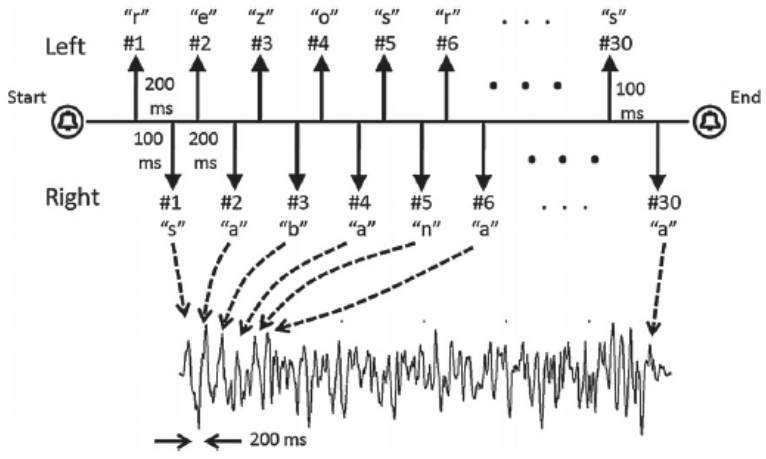

Methods

- It is established that early components of the human auditory evoked potentials, namely N1 and P2 are larger when the stimulus is attended compared to when it is ignored [38, 39].
- This effect can be observed in the dichotic listening paradigm.
- Because the ISI and ILI of each stimulation were fixed to a value (respectively, 200 and100 ms)
- for the two streams of stimuli, to two counter-phased responses of the same frequency (5 Hz =ISI−1) whose amplitudes can be cognitively modulated.
- The net effect is a sinusoidal-shaped response with most of the energy located around the frequency of 5 Hz

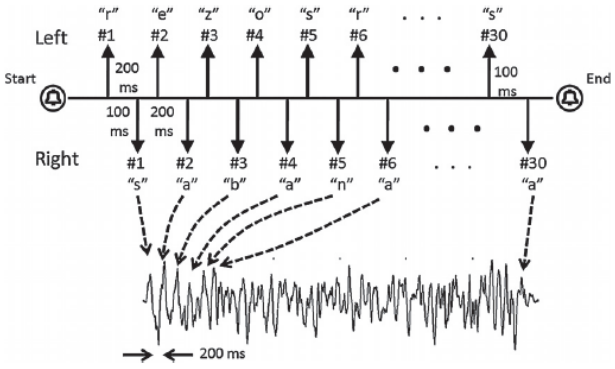

Subjects and recording

- A total of 12 healthy subjects (7 men, 5 women; aged 31.1 ± 6.0 years) participated in the experiment.
- No type of auditory or cognitive disease was reported by the subjects
- The experiment was conducted in a quiet room isolated from external disturbances throughout.
- As visual stimulation was not needed, the subjects were recommended to close their eyes during the whole experiment.
- They configured a single channel with an active electrode placed on the vertex (Cz) and referenced to the mean value of the mastoids.
- The ground electrode was placed between the Fpz and the Fz.
- The recordings were acquired on Neuroscan, were band-pass filtered between 1 and 30 Hz and were sampled at a rate of 1 kHz.

Stimulation

- Two conditions were established:
  - first, a dichotic listening condition wherein two distinct streams of letters were read out simultaneously (condition 1)
  - second, the same as condition 1 except that complete sentences were used rather than letters (condition 2).
- Letters in condition 1 that were randomly picked from a dictionary with more than 13 000 entries.
- The letters were previously sampled (16 bits per sample at 44100 Hz and 200 ms length) from a male voice that read the Spanish alphabet.
- a total number of 30 stimuli (6 × 5 or 5 × 6) were delivered to each ear
- The total duration of the stimulation was 6.1 s.
- For condition 2, two different speeches were delivered simultaneously, one per ear
- The sentences were previously recorded with the same characteristics as depicted for condition 1.
- The subjective perception of the stimuli of condition 2 is similar to a low-quality cellular phone call

Experimental design

- Because the experiment was purely auditory without any visual stimulation, an assistant was needed to give verbal statements to the participants.
- The experiment consisted of two sessions, namely the spelling session (condition 1) and the speech session (condition 2).
- Each session consisted of five runs that, in turn, consisted of ten trials.
- The first run of each session was used for calibration and the other four were used for evaluation.
- Because selective attention is a native skill for humans, no training was needed to perform the dichotic listening task
- only the first ten trials (first run) of each session dedicated to calibrate the system (calibration for classifier).
- During the calibration, only one stream was delivered at a time to one of the ears.
- The result was that a very stable and reliable pattern was extracted in just one run.

Experimental design

- During the evaluation, and previous to the stimulation onset, an auditory sentence was read by an assistant to the participant
- After beep, the participant had to take a binary decision, either 'yes/true' or 'no/false', for that sentence.
- The sentence was randomly picked from a list and sentences were composed in such a way that the number of positive and negative answers was the same.
- e.g., 'I am Spanish', 'I am not Spanish' or 'two plus three equals five', 'two plus three equals six'
- If the correct answer was 'yes/true', the participant had to pay attention to the stimulus delivered to the left ear and vice versa if the decision was 'no/false'.

Experimental design

- In general, the communication was intended as a conversation initiated by the assistant in which he asks binary response questions to which the participant answers
- e.g., 'Do you need pain relief?', or 'Would you prefer a warmer room?'.
- The correct word was given to the participants as feedback at the end of each trial
- The feedback was solely intended to help them to find a more efficient strategy to focus their attention.

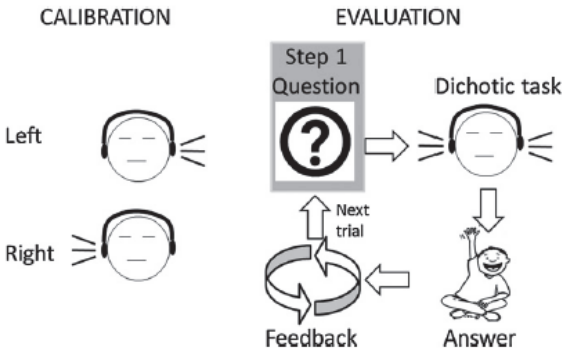

Figure 2. Synoptic representation of the procedure followed in the experiment.

Feature extraction and Classification

- The data collected during the calibration trials were separated into the left ear and right ear data; these two types of data were averaged separately.
- The DFT was computed on each and the DFT coefficients at the frequency of repetition (5 Hz) were extracted and used as patterns for classification.
- These coefficients are complex numbers that convey information about the amplitude and phase of the event-related responses.
- As both streams were presented at the same frequency but with an ILI of half period (100 ms), the DFT coefficients differed only in the phase (180◦).
- The typical representation of the DFT coefficients in polar coordinates

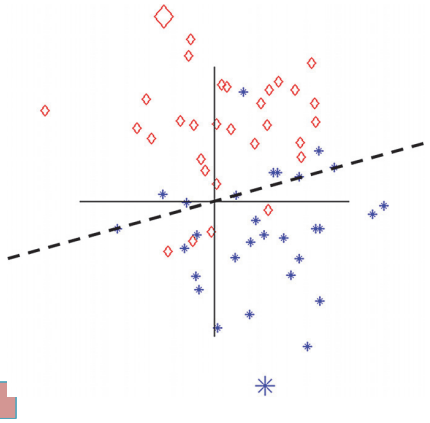

(stars and diamonds represent the left and right, respectively; the big star and diamond for the patterns).

Feature extraction and Classification

- Given that during the evaluation both sequences were delivered simultaneously, the amplitudes of the features extracted are smaller than the patterns.
- Because the responses to both sequences are counter-phased (180◦ phase shift), they partially cancel each other, thus giving rise to lower levels of signal.
- During the evaluation, the extracted features of each trial were compared to the pattern and were classified under the criterion of the minimum Euclidean distance: $S_t = \min_i |\psi_t - \psi_i|$,
- where S_t is the classification decision for trial *t*, ψ_i are the DFT coefficients of the two patterns extracted, ψ_t is the DFT coefficient extracted from trial *t*

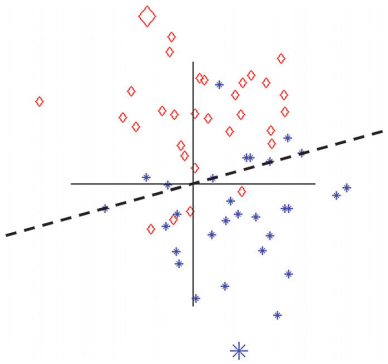

Results

	Spelling session				
Subject	acc (%)	ITR (bits m^{-1})	# of stimuli	acc (%)	ITR (bits m^{-1})
S01	73	1.55	26	68	1.13
S02	83	3.31	13	78	5.33
S03	80	2.78	9	73	5.05
S04	68	0.90	28	68	0.97
S05	75	1.89	18	75	3.15
S06	65	0.66	17	60	0.51
S07	75	1.89	5	73	9.09
S08	75	1.89	15	70	2.37
S09	50	0.00	30	50	0.00
S10	80	2.78	14	75	4.04
S11	50	0.00	30	50	0.00
S12	60	0.29	30	60	0.29
GAV1	69	1.49	20	67	2.66
GAV2	73	1.79	18	70	3.19

	Speech session				
Subject	acc (%)	ITR (bits m^{-1})	# of stimuli	acc (%)	ITR (bits m^{-1})
S01	63	0.23	46	70	0.77
S02	93	3.08	20	73	2.27
S03	78	1.15	9	70	3.96
S04	85	1.95	27	65	0.73
S05	85	1.95	31	70	1.15
S06	65	0.33	60	65	0.33
S07	75	0.94	30	65	0.66
S08	73	0.76	48	70	0.74
S09	53	0.01	60	48	0.00
S10	80	1.39	18	83	5.52
S11	45	0.00	60	53	0.02
S12	83	1.65	20	65	0.99
GAV1	73	1.12	36	66	1.43
GAV2	78	1.34	31	70	1.71

- The experiment did not work for two of the twelve participants (S09, S11).
- Columns two and three denote the full-length trials and last three columns denote the optimum number of stimuli.
- Two grand averages across the subjects are presented, one across all of the participants (GAV1) and the other excluding S09 and S11 (GAV2).

Results

	Spelling session				
Subject	acc (%)	ITR (bits m^{-1})	# of stimuli	acc (%)	ITR (bits m^{-1})
S01	73	1.55	26	68	1.13
S02	83	3.31	13	78	5.33
S03	80	2.78	9	73	5.05
S04	68	0.90	28	68	0.97
S05	75	1.89	18	75	3.15
S06	65	0.66	17	60	0.51
S07	75	1.89	5	73	9.09
S08	75	1.89	15	70	2.37
S09	50	0.00	30	50	0.00
S10	80	2.78	14	75	4.04
S11	50	0.00	30	50	0.00
S12	60	0.29	30	60	0.29
GAV1	69	1.49	20	67	2.66
GAV2	73	1.79	18	70	3.19

	Speech session				
Subject	acc (%)	ITR (bits m^{-1})	# of stimuli	acc (%)	ITR (bits m^{-1})
S01	63	0.23	46	70	0.77
S02	93	3.08	20	73	2.27
S03	78	1.15	9	70	3.96
S04	85	1.95	27	65	0.73
S05	85	1.95	31	70	1.15
S06	65	0.33	60	65	0.33
S07	75	0.94	30	65	0.66
S08	73	0.76	48	70	0.74
S09	53	0.01	60	48	0.00
S10	80	1.39	18	83	5.52
S11	45	0.00	60	53	0.02
S12	83	1.65	20	65	0.99
GAV1	73	1.12	36	66	1.43
GAV2	78	1.34	31	70	1.71

- S09 and S11 were not able to transmit any amount of information (ITR = 0.0, accuracy = 50%).
- However, when both are excluded to compute GAV2, accuracies exceed 70%,with an ITR of 3.19 (70%- 1.71 for speech session) for the optimal number of stimuli.

Results

- For the optimal number of stimuli, incremental fractions of trials in steps of 200 ms (each including unitary incremental of responses)were extracted and classified.
- The optimal length of trials was defined, for each subject, as the mean of two numbers.
- The first number is calculated as the number of stimuli for which fewer stimuli always cause an accuracy equal to or below 70%.
- The second number is the number of stimuli for which a higher number of stimuli always yield an accuracy equal to or above 70%.
- According to [45], 70% corresponds to the minimum accuracy that guarantees meaningful communication.

Results

- Figure 4 (left) shows the averaged performance across subjects versus the number of stimuli used for the classification of the spelling session.
- Both the ITR and the accuracies smoothly converge to 1.49 bits min−1 and 69%, respectively, as the number of stimuli increases. (see table1, GAV1)
- The ITR is 6.3 bits min−1, obtained for just two stimuli, corresponding to an accuracy of 57%, far below 70%.

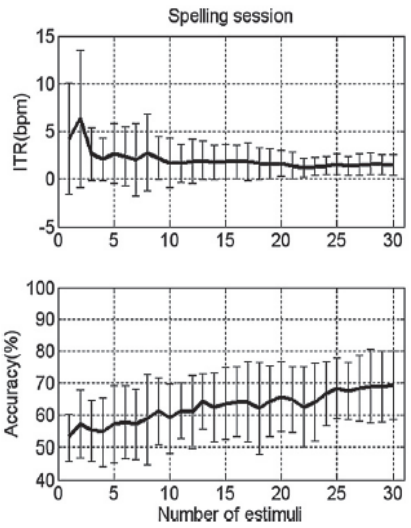

Figure 4(left). Mean performance (thick lines) and standard deviation (vertical bars) across subjects versus incremental number of stimuli for the spelling and speech sessions (left and right respectively).

Results

- Figure 4 (right) shows the averaged performance across subjects achieved during the speech session.
- The ITR–accuracies converge to 1.12–73%(see table 2, GAV1)
- The maximum ITR obtained corresponds to 2.7, which was achieved with an accuracy of 52% and just one stimulus
- However, this accuracy is considerably under 70% and chance level.

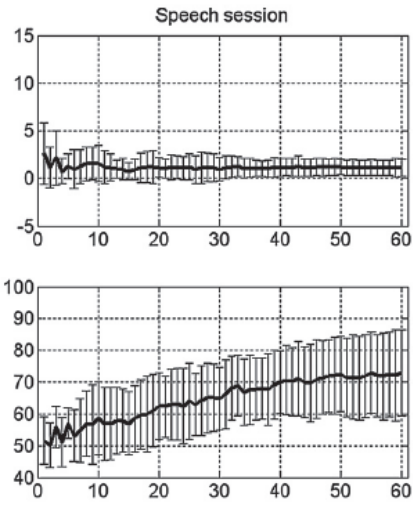

Figure 4(right). Mean performance (thick lines) and standard deviation (vertical bars) across subjects versus incremental number of stimuli for the spelling and speech sessions (left and right respectively).

Conclusions

- This intuitive and easy to use auditory BCI founds a novel approach in the field of BCIs
- This system may provide a clinically useful communication device to those that are in a locked-in state.(can not use visual stimuli)
- From the results, they can state that the use of the dichotic listening paradigm is a feasible approach for auditory BCIs.
- Beyond the performance, the results show that an auditory BCI based on natural speech is a reasonable approach indicated for users unable to use a visual BCI.
- The use of selective attention enhances the usability of the system, with a minimum of training (one run for calibration) and a minimum number of EEG channels (just one).
- In the future, simultaneous feedback will be allowed; thus, they expect an improvement in the performance.

Thank you

Temporal classification of multichannel near-infrared spectroscopy signals of motor imagery for developing a brain-computer interface

Sitaram et al.

NeuroImage (2007)

Presenter : Evgenii Kim

GIST, Dept. of Information and Communication

Gwangju Institute of Science and Technology

Outline

- Introduction
- Experimental procedure
- Signal acquisition
- Preliminary signal analysis
- Pattern classification
- Support Vector Machine
- Hidden Markov Model
- Result
- Conclusion

Introduction

- NIRS is non-invasive optical method that allows us to detect brain activity.
- It possesses a number of advantages:
  - Portability
  - Good spatial resolution
  - Metabolic specificity
  - Low-cost

Disadvantages:
The signal is affected by hair;
Motion artifacts.

- The main goal of the study is to ascertain the feasibility of using NIR for developing a BCI.
- Motor imagery of left/right hand has been used as a paradigm for this work.
- In addition, two pattern recognition technique, SVM and Hidden Markov Model (HMM) were applied to the classification problem.

Experimental procedure

- Five healthy subjects (3 males and 2 females, mean age =30) participated in the study.
- NIRS signals were collected from both overt motor execution (finger tapping) and covert motor imagery

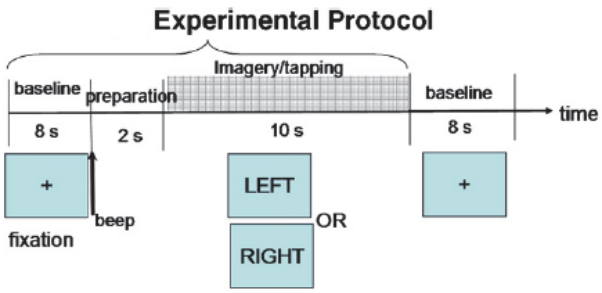

Data for finger tapping and imagery were collected in two separate session. Each tasks was carried out for 80 trials.

Signal acquisition

- The NIRS instrument (OMM-1000 from Shimadzu Co, Japan) was used in this study. The system operated at three different wavelength of 780, 805,and 830 nm, emitting an average power of 3 mW/mm^2
- The data were acquired at a sampling rate of 14 Hz and digitized by the 16-bit analog to digital converter

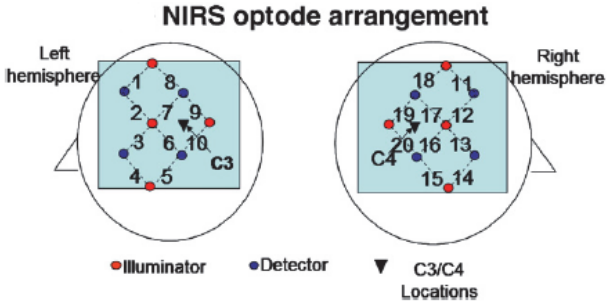

Preliminary signal analysis

- The reason of preliminary analysis was to observe the responses of HbO2 and Hb at different channels on both hemispheres due to left/right-hand imagery tasks.
- A custom Matlab NIRS data analysis program (HomER) was used
- Preprocessing
  - The raw intensity data from all channels being normalized

$$\text{Norm Intensity}(t) = \text{Intensity}(t)/\text{Mean Intensity}.$$

  - Chebyshev type II filter with cut-off frequency of 0.7 Hz and pass-band attenuation 0.5dB
  - The changed of optical density was calculated for each wavelenght

$$\Delta\text{OD} = -\log(\text{Norm Intensity}(t)).$$

  - PCA filters to remove head movement and to project out systemic physiology
  - Calculate HbO2 and Hb concentration changes from modified Beer-Lamber law.

$$\Delta\text{Hb}X = (e^T e)^{-1} e^T [\Delta\text{OD}].$$

Where e is the molar absorption coefficient for Hb and HbO2

$$\begin{pmatrix} Hb \\ HbO2 \end{pmatrix} = \frac{1}{L} \overline{\begin{pmatrix} \varepsilon_{Hb}^{\lambda 1} & \varepsilon_{HbO2}^{\lambda 1} \\ \varepsilon_{Hb}^{\lambda 2} & \varepsilon_{HbO2}^{\lambda 2} \\ \vdots & \vdots \\ \varepsilon_{Hb}^{\lambda n} & \varepsilon_{HbO2}^{\lambda n} \end{pmatrix}^{-1}} \begin{pmatrix} A^{\lambda 1} \\ A^{\lambda 2} \\ \vdots \\ A^{\lambda n} \end{pmatrix}$$

- Image of brain activity was reconstructed

Pattern classification

- the raw signals obtained from the signal acquisition process were used for the pattern classification.
- Only Chebyshev type II filter was utilized to remove artifacts from heart beat and high frequency noise
- Time series of amplitude changes of HbO2 and Hb in period 2-10 s after stimulation for the motor task were extracted and fed to the pattern classification system

SVM

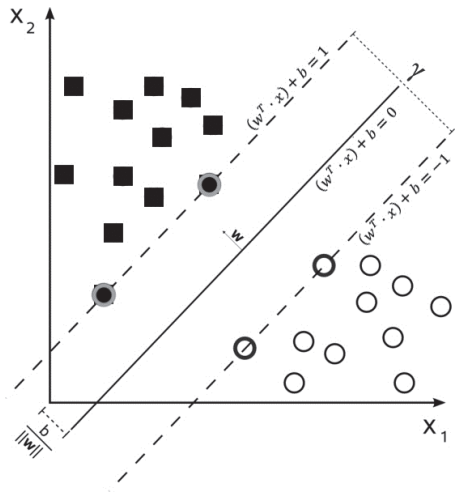

y_t represents the type of task (left/right hand)
$\mathbf{X}_t$ represents the concentration values HbO2 and Hb from all the number of channels

HMM

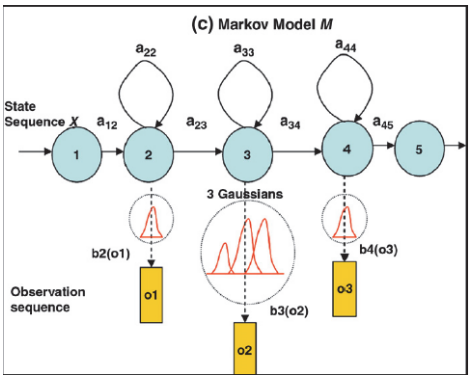

At each time t that a state j is entered, an observation vector O is generated from the probability density $b_j(\mathbf{O}_j)$. Transition from state i to state j is also probabilistic and is governed by the discrete probability a_{ij}. The joint probability O generated by model moving through the state sequence X.

$$P(O,X|M) = \sum_x a_{x(o)x(1)} \prod_{t=1}^{T} b_{x(t)}(o_t) a_{x(t)x(t+1)}$$

X is unknown

$\{a_{ij}\}$ and $\{b_j(O_t)\}$ are determined by an estimation procedure. To determine Baum-Welch re-estimation procedure was used.

Result

Accuracy of Support Vector Machine (SVM) and Hidden Markov Model (HMM) classification of finger tapping and motor imagery tasks for 5 healthy volunteers

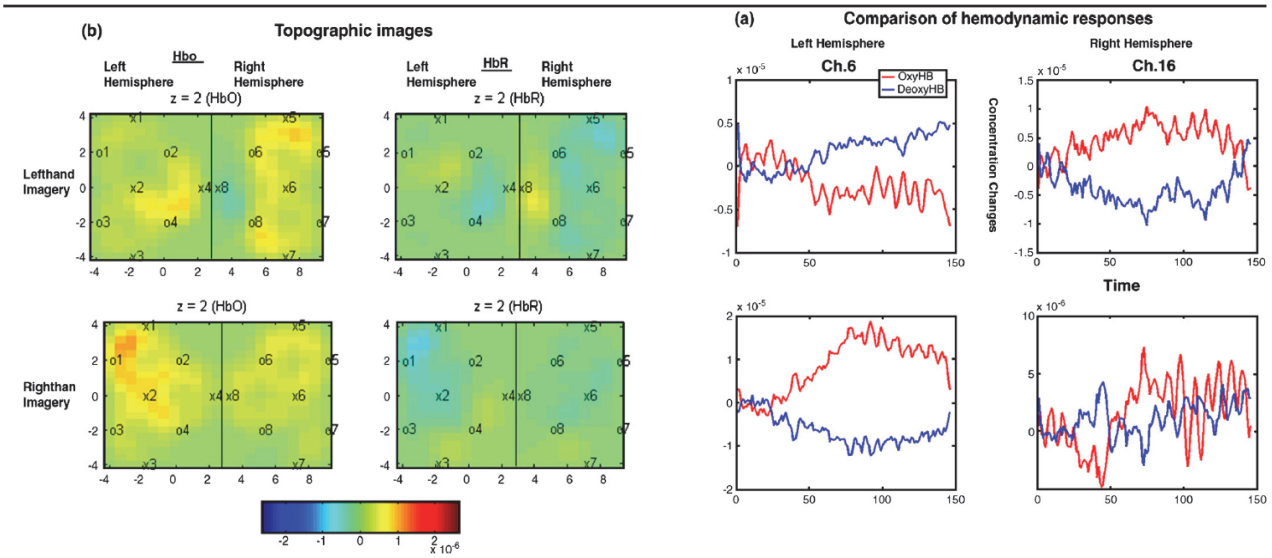

Conclusion

- The NIRS has been demonstrated as reliable technique for BCI application.

Thank you

INFONET Seminar Application Group 2013/10/22

A measurement-domain adaptive beamforming approach for ultrasound instrument based on distributed compressive sensing: Initial development

Quiong Zhang.
Ultrasounics, Elsevier
June 2012
Presenter Pavel Ni

Gwangju Institute of Science and Technology

Contents

Introduction

- Sensor arrays are used in ultrasound imaging, broad band wave transmitted and backscat tered signal is acquired
- The received signal is amplified LNA (Low Noise Amplifier) and VGA (Variable Gain Amplifier) filtered by AAF (Anti Alias Filter) and sampled by ADC (Analog Digital Con verter).
- Conventional Ultraosund systems use DAS beamformer (Delay And Sum) to process high-speed sampled data Fig. 1
- Conventional Beamformer delays received signals by array elements appropriate to their distances from the main target of imaging, weights them with predetermined coefficients and then sums the weighted signal to reconstruct the echo signal originating from main target.
- In conventional beamformer weights are independent of the array data therefore reducing the overall quality of the image
- In Adaptive Beamformer(ABF) delayed sensor signals are fed to the adaptive processor, which continuously updates the appodization weights for the specific sensor signal that provides significant increase in lateral resolution compared with DAS

Introduction

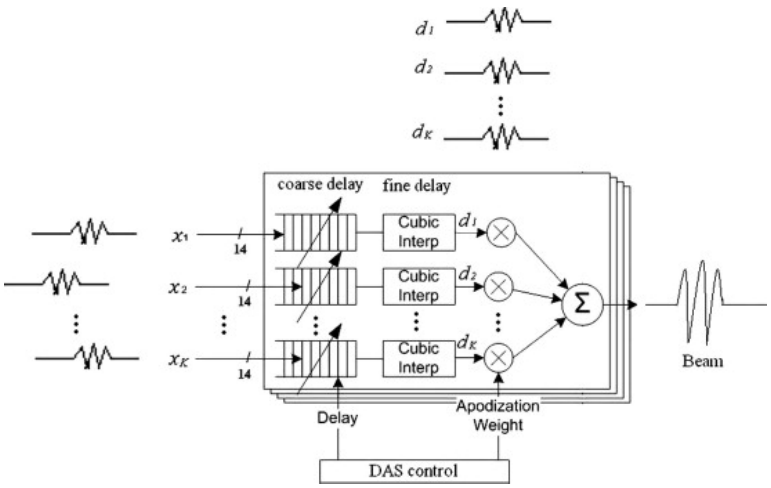

Fig. 1. The process diagram of traditional delay-and-sum (DAS) beamformer used in ultrasound imaging instrument.

- Author proposed framework for ultrasound sensor array data acquirement based on DCS and sample data with sub-Nyquist-rate
- High resolution MABF approach to reconstruct ultrasound images adaptively without recovering signal

Basis theory of distributed compressed sensing

Distributed compressed sensing (DCS) enables new distributing codding algorithms for multi-Signal ensembles that exploit both intra- and inter-signal correlation structures.

- In DCS scenario, a number of sensors measure signals that are each individually sparse in some basis and also correlated from sensor to sensor. Think about it as a multiple sensors acquire the same signal but with phase shift and attenuation caused by signal propagation (Joint Sparsity Model-2)
- Then each sensor independently encodes its received signal by projection it onto another, incoherent basis and then transmits just few essential coefficients.
- Under the right conditions decoder at the collecting point can jointly reconstruct all of the signals precisely.

Basis theory of distributed compressed sensing

In JSM-2 system all K sensor-array signals share a common support set but with different coefficients. Then signal on sensor i is:

$x_i = \Psi\theta_i$

Measurement vector y_i is computed as

$y_i = \Phi_i x_i.$

Where $\Phi_i \in \Re^{MixN}$ with $M_i << N$ and $y_i \in \Re^{M_i}$.

M_i is the number of measurements in the i-th sensor.

All the sensor array signals and measurements can be represented respectively as:

$$x = \begin{bmatrix} x_1 \\ x_2 \\ \vdots \\ x_K \end{bmatrix} = \begin{bmatrix} \Psi & 0 & \cdots & 0 \\ 0 & \Psi & \cdots & 0 \\ \vdots & \vdots & \ddots & \vdots \\ 0 & 0 & \cdots & \Psi \end{bmatrix} \begin{bmatrix} \theta_1 \\ \theta_2 \\ \\ \theta_K \end{bmatrix} = G\theta. \qquad y = \begin{bmatrix} y_1 \\ y_2 \\ \vdots \\ y_K \end{bmatrix} = \Phi x = \Phi G\theta = \Omega\theta \qquad (1)$$

The recovering of x can be achieved by solving a L1 minimization problem:

$\theta = \arg\min(\|\theta\|_1)$ s.t. $y = \Omega\theta$

In ultrasound, each sensor acquires a replica of the same frequency-sparse signal but with phase shift and attenuation caused by signal propagation

The measurement-domain adaptive beamforming (MABF) based on DCS

- The amount of acquired data is decreased by implementing DCS at the front-end.
- High-resolution ultrasound images can be obtained from few measurements of DCS using MABF directly without recovering raw sensor signals with complex convex optimization algorithm.

The author used a single unfocused transmission wave. K elements of transducer are exited by the identical wave at the same time, and entire region of interest is covered in a single transmission. The same transducer array is used to receive corresponding backpropagated acoustic echo signals.

The time signal received by the ith element is denoted by $s_i(t,\vec{\rho})$, assuming that there is only single scatterer $\vec{\rho}$.

$$y_i = \Phi_i x_i = \Phi_i \cdot \int_{ROI} s_i(t,\vec{\rho}) \cdot f(\vec{\rho})\vec{\rho} \qquad (2)$$

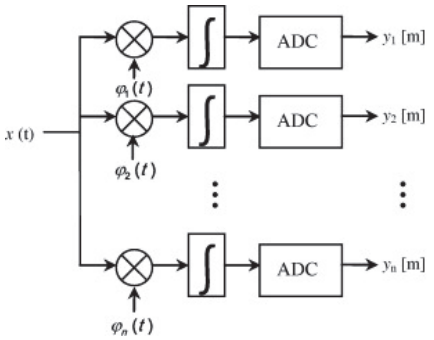

Fig. 2. The possible distribute compressive sensing implementation of one sensor signal at the ultrasound imaging instrument receiver. $\Phi=[\varphi_1,\varphi_2,\ldots,\varphi_n]$.

The measurement-domain adaptive beamforming (MABF) based on DCS

If Φ_i does not map two distinct S-sparse signals to the same measurement vector then it is possible to reconstruct image directly from measurements without signal reconstruction. Restricted Isometry Property (RIP) should hold for all S-sparse vectors x_i

To solve (2) the ROI must be discretized as shown in Fig. 3. The ROI lies in the product space $[x_s, x_e] \times [y_s, y_e]$, where (x_s, y_s) and (x_e, y_e) denote initial and final positions of the ROI to be imaged

The received measurements in the ith element can be expressed

The measurement-domain adaptive beamforming (MABF) based on DCS

$$y_i = \Phi_i \cdot \sum_{j=1}^{LxP}\left[s_i(t,\vec{\rho}_j) f(\vec{\rho}_j)\right] = \sum_{j=1}^{LxP} d_{ji} \cdot f(\vec{\rho}_j) = D_i f \quad (3)$$

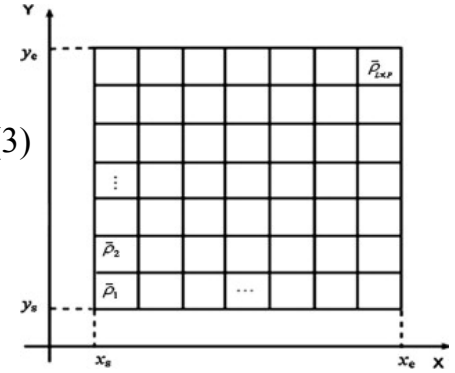

Fig. 3. RIO discretization. The ROI lies in the product space $[x_s, x_e] \times [y_s, y_e]$ and is discretized into in L by P scatterers $\vec{\rho}_1, \vec{\rho}_2, \ldots \vec{\rho}_{LxP}$

Consider all the elements, the measurements of actual backscattering signals can be represented as

$$y = \begin{bmatrix} y_1 \\ y_2 \\ \vdots \\ y_K \end{bmatrix} = \begin{bmatrix} D_1 f \\ D_2 f \\ \vdots \\ D_K f \end{bmatrix} = V_{DCS} f \quad (4)$$

Where V_{DCS} is a dictionary matrix of dimensions MKxLP, $Di = [d_{1i}, d_{2i}, \ldots d_{(LxP)i}]$ and f is a target vector.

The measurement-domain adaptive beamforming (MABF) based on DCS

The maximum likelihood estimate of f is given by

$$\hat{f} = \max_f p(y, f) \text{ s.t. } y = V_{DCS} \cdot f \quad (5)$$

Where is the pdf. Then (5) becomes MAP optimization problem

$$\hat{f} = \max_f p(f \mid y) = \max_f [p(y \mid f) p(f)] \quad (6)$$

To find the MAP estimate of target vector f, we must maximize the priori PDF $p(f)$.

Results

To show efficiency of reduce numb er of samples and image reconstruc tion

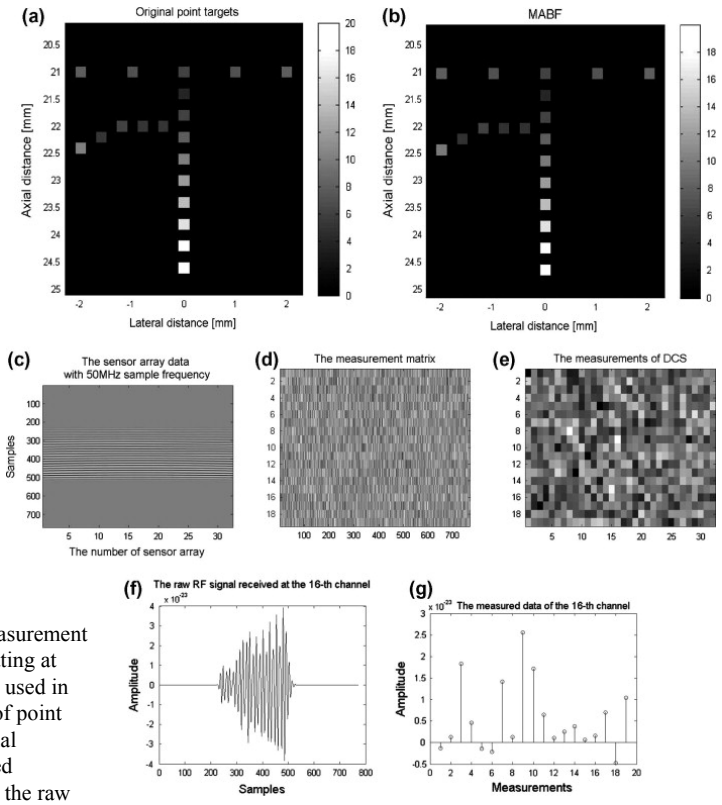

Fig. 4. The example of sensor array data acquirement, measurement and image reconstruction. A 32 element linear array operating at 5 MHz with 80% bandwidth in plane wave emission were used in simulation. (a) the positions and backscattering intensity of point targets, (b) the result of the proposed method, (c) the spatial response, (d) the linear measurement matrix, (e) distributed compressive measurements of the sensor array signals, (f) the raw RF signal received at the 16th channel, (g) the measured data corresponding to the 16th channel.

Results

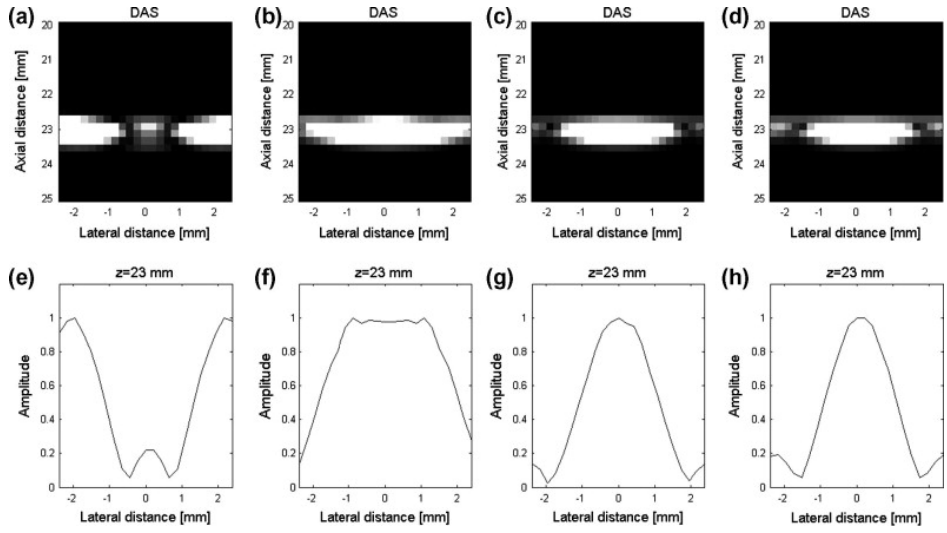

Fig. 5. Simulated lateral resolution of DAS for a 32 element linear array operating at 5 MHz with 80% bandwidth in plane wave emission. (a) shows the case, where the point targets are separated by 5 mm at depth of 23 mm; (b)–(d) correspond to point targets separations of 2, 1 and 0.2 mm, respectively. (e)–(h) show the normalized lateral variation of (a)–(d) at depth of 23 mm.

Results

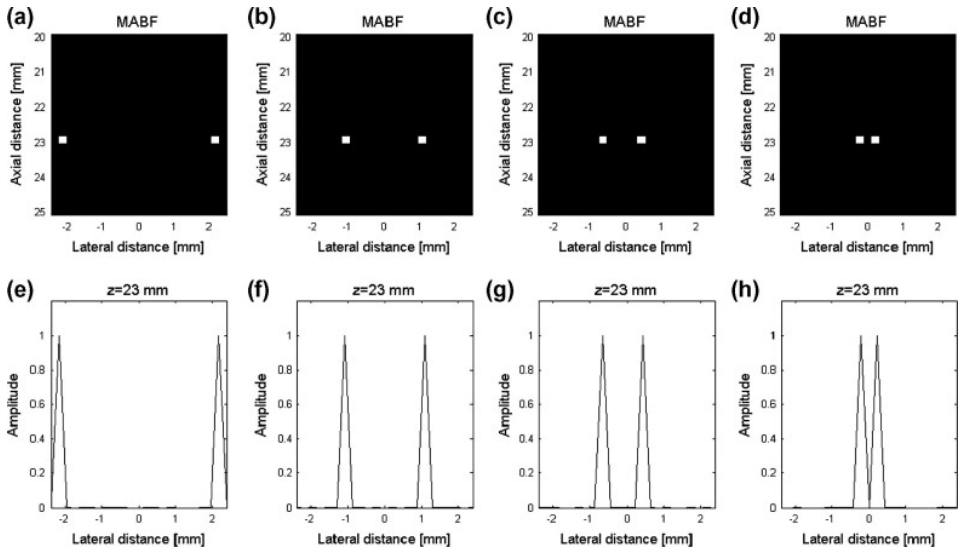

Fig. 6. Simulated lateral resolution of MABF for a 32 element linear array operating at 5 MHz with 80% bandwidth in plane wave emission. The hypothetical targets separated 0.2 mm in range and 0.2 mm in azimuth. (a) shows the case, where the point targets are separated by 4.5 mm at depth of 23 mm; (b)–(d) correspond to point targets separations of 2, 1 and 0.2 mm, respectively. (e)–(h) show the normalized lateral variation of (a)–(d) at depth of 23 mm.

Results

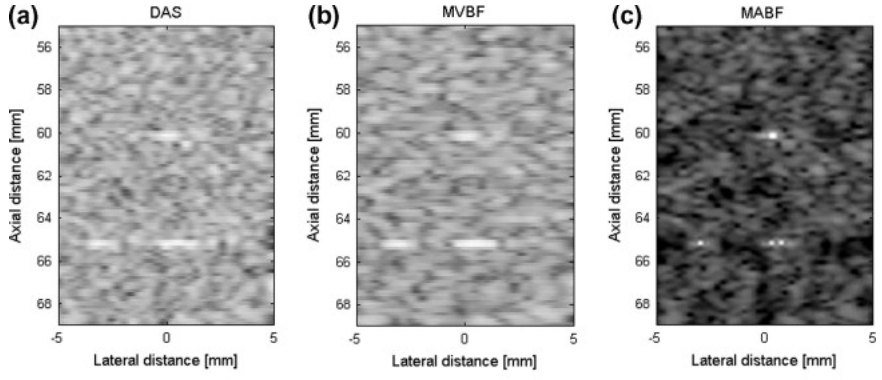

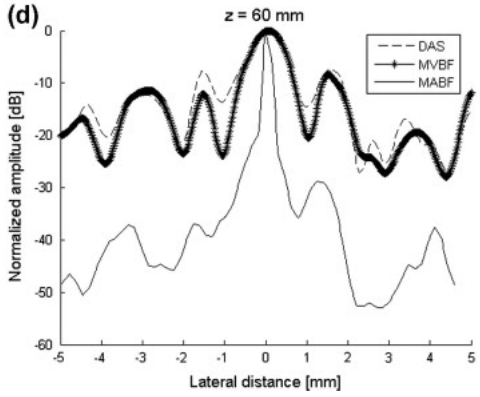

Fig. 7. Beamformed responses of four point targets in a speckle pattern with a 5-MHz, 80% bandwidth, 32-element, half-wavelength spacing linear array in the PW emission. The four point targets are located at $(x, z) = \{(0, 60), (-3.4, 65), (0, 65), (0.5, 65)\}$ mm. Both DAS and MVBF are implemented on the raw data, while the proposed MABF is implemented on the measurements. (a) DAS, (b) MVBF and (c) MABF. (d) shows the normalized lateral variation of (a)–(c) at depth of 60 mm. All images are shown with a dynamic range of 60 dB.

Conclusion

Using DCS few measurements are acquired by projecting the sensor array signals onto the s elected basis.
High resolution image is reconstructed by using MABF approach to the few measurements directly without recover the raw signals.

Further work
Computational time is not suitable for real-time applications

Q&A

A novel BCI based on ERP components sensitive to configural processing of human faces.

Yu Zhang et al. (Andrzej Cichocki*)

Journal of Neural Engineering (2012)

Presenter : SeungChan Lee

GIST, Dept. of Information and Communication, INFONET Lab.

Gwangju Institute of Science and Technology

Background

- Face-sensitive event related potentials(ERPs)
  - Related ERPs
    - N170 : a large negative component peaking at the lateral occipito-temporal sites between 140 ~ 200ms
    - VPP(Vertex Positive Potential) : a large positive component at the fronto-central sites with a similar latency to the N170
    - P1, N250
  - Previous study
    - Oddball paradigm-based BCI with stimuli of natural faces
    - Online accuracy reaches over 90% with two trials (better performance using facial images instead of using intensified icon stimuli)
    - The prominent features derived from the facial images at visual cortex, which may be associated with the cognitive components reflecting face perception.

Introduction

- Motivation
  - Face perception rely more on configural information rather than other visual object perception.
  - The inversion of a face can disrupt the configural face information, thereby making the face processing slower and more difficult.
  - The two components N170 and VPP are believed to reflect the configural processing of the face, their amplitudes and latencies can be modulated by the inversion of the face.
  - Could the signal modulation caused by the loss of configural face information be applied to the BCI using stimuli of facial images and improve the system performance?

Methods

- Subjects
  - 7 healthy right-handed volunteers (aged from 24 to 49, all males)
- Stimuli
  - 9 types of stimuli on ERP components(N170, VPP, and P300)

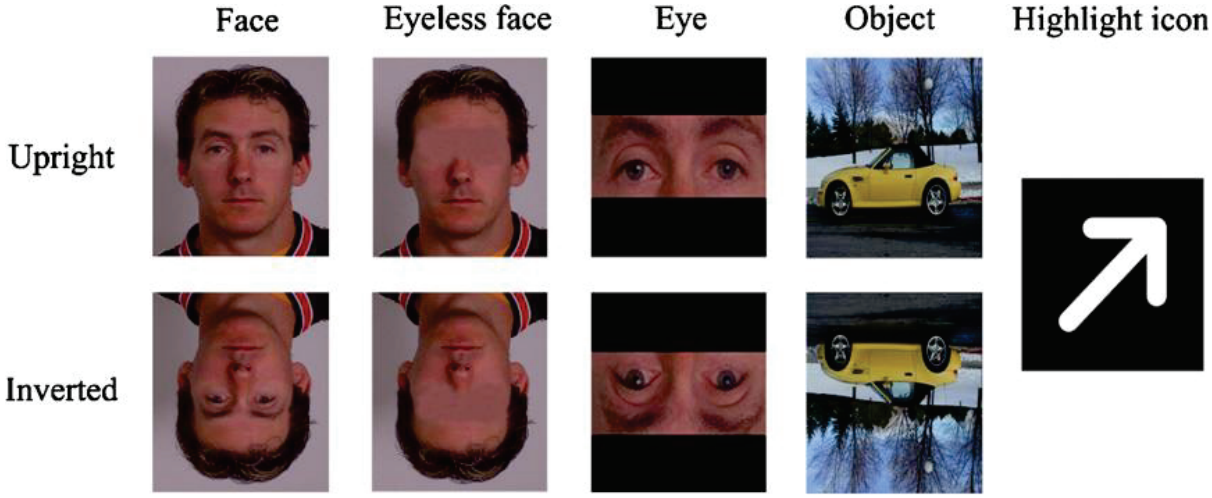

  - 4 natural human faces(2 females) : face-related stimuli
  - 4 objects(car, ship, bicycle and house) : object stimuli

Methods

- Paradigm
  - Each subject completed two experimental sessions on two separate days. (interval : less than three days)
  - Each part being tested with same stimulus type.

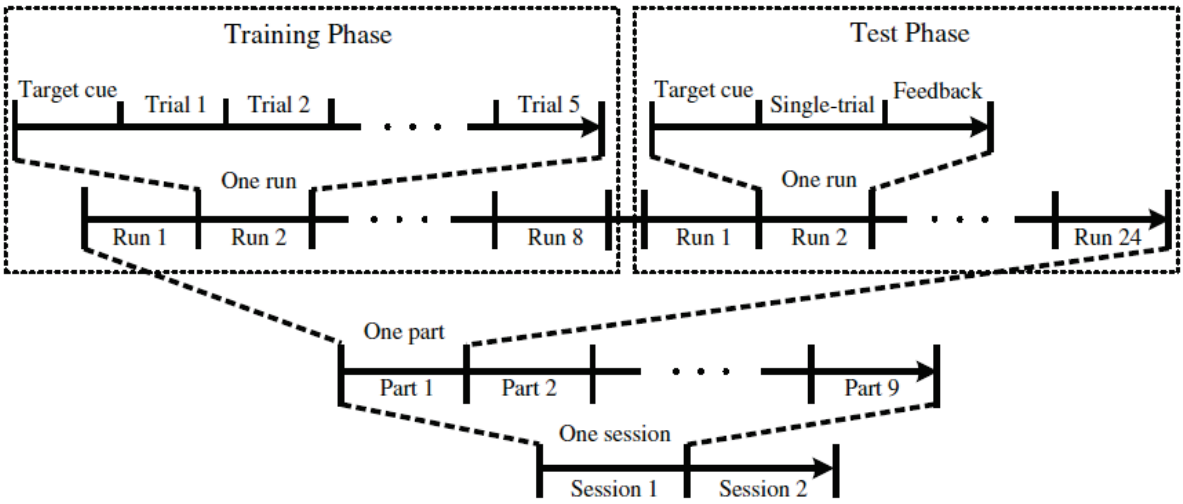

  - Total 48 direction commands were implemented for each subject in the online test phases of the two sessions

Methods

- Paradigm
  - The timing of one run

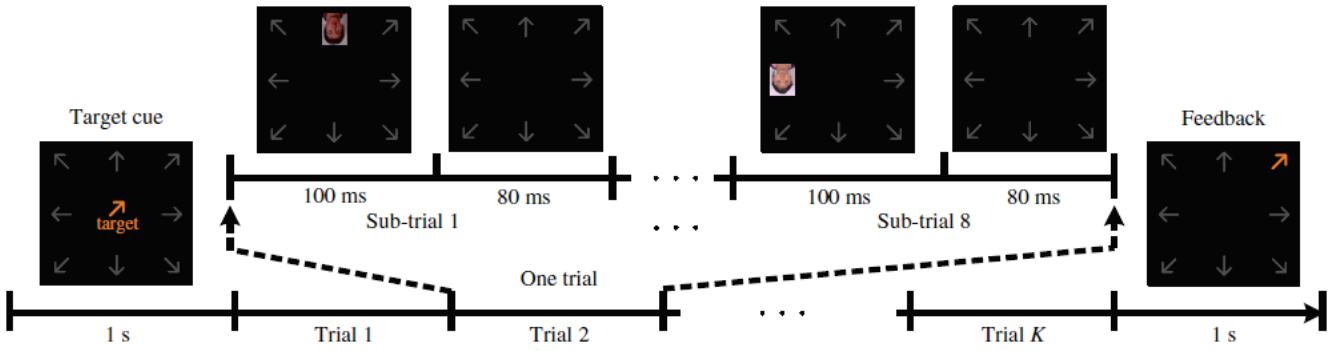

  - Training phase : K=5, each run consisted of 40 flash sub-trials (5 targets and 35 non-targets) with no feedback
  - Online test phase : k=1(single trial), feedback was provided.

Methods

- EEG acquisition
  - 256 Hz sampling rate with the g.USBamp amplifier (high-pass and low-pass filters 0.1Hz and 30 Hz; a notch filter 50 Hz)
  - 16 electrodes were used (F3, Fz, F4, T7, C3, Cz, C4, T8, P7, P3, Pz, P4, P8, PO7, PO8, Oz, two ear references, and one ground on the Fpz)

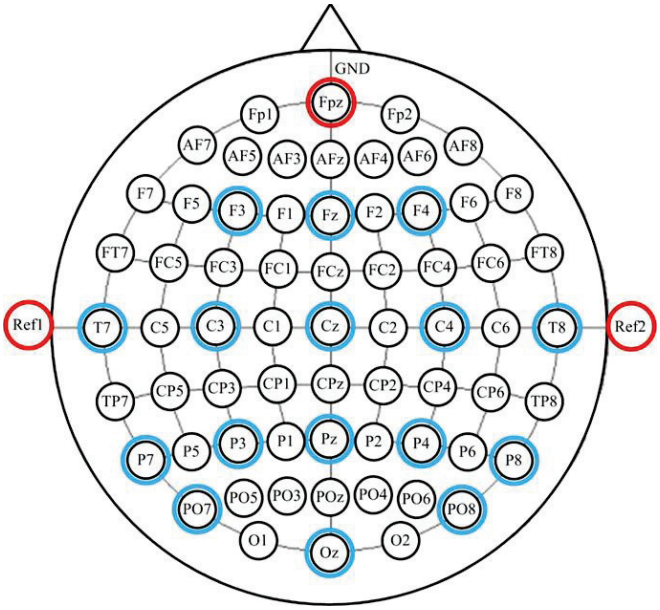

Methods

- Feature extraction
  - 700 ms data segment after baseline corrected (100 ms pre-stimulus interval was extracted)
  - Total 320 such data segments consisting of 40 targets and 280 non-targets were derived from each part during the training phase.
  - Each data segment was downsampled to 21 Hz after 12-point moving average.
  - A spatiotemporal feature vector with dimension of 240 (i.e. 16 channels × 15 sampling points)
  - 320 feature vectors were collected for each type of stimulus.
- Classification
  - Linear discriminant analysis(LDA) was used.
  - Procedure
    - Eight spatiotemporal feature vectors were extracted during the single trial.
    - Calculate their posterior probabilities belonging to the target class.
    - stimulus direction with the maximal posterior probability was detected and presented to the subject as feedback.
  - Classification accuracy was averaged over the two sessions.

Methods

- Evaluation
  - Information transfer rate(ITR)

$$ITR = M\left\{\log_2 N + P\log_2 P + (1-P)\log_2\left(\frac{1-P}{N-1}\right)\right\} bits/\min$$

    - N possible choices in which each choice is equally probable to be selected by the user.
    - The probability (P) that the desired choice will indeed be selected remains invariant.
    - Each error choice has the same probability of selection.
    - M denotes the number of commands per minute.
  - One-way analysis of variance(ANOVA)
    - ANOVA is a collection of statistical models used to analyze the differences between group means and their associated procedures (such as "variation" among and between groups)
    - ANOVAs are useful in comparing (testing) three or more means (groups or variables) for statistical significance.

Results

- Online accuracy and ITR

Stimulus	Performance	Subject S1	S2	S3	S4	S5	S6	S7	Average
Upright face	Acc	83.3	81.3	75.0	81.3	50.0	83.3	85.4	77.1 ± 12.4
	ITR	32.8	31.0	25.9	31.0	10.4	32.8	34.7	28.4 ± 8.39
Inverted face	Acc	**93.8**	**87.5**	**85.4**	**89.6**	**70.8**	**95.8**	**97.9**	**88.7** ± 9.08
	ITR	**43.4**	**36.7**	**34.7**	**38.8**	**22.8**	**45.9**	**48.7**	**38.7** ± 8.63
Upright eyeless face	Acc	85.4	79.2	81.3	79.2	58.3	87.5	93.8	80.7 ± 11.2
	ITR	34.7	29.3	31.0	29.3	14.8	36.7	43.4	31.3 ± 8.83
Inverted eyeless face	Acc	89.6	77.1	**85.4**	79.2	54.2	**95.8**	95.8	82.4 ± 14.5
	ITR	38.8	27.6	**34.7**	29.3	12.5	**45.9**	45.9	33.5 ± 11.8
Upright eye	Acc	91.7	70.8	75.0	72.9	45.8	87.5	79.2	74.7 ± 14.9
	ITR	41.1	22.8	25.9	24.4	8.43	36.7	29.3	26.9 ± 10.6
Inverted eye	Acc	89.6	68.8	77.1	70.8	41.7	81.3	87.5	73.8 ± 16.2
	ITR	38.8	21.4	27.6	22.8	6.69	31.0	36.7	26.4 ± 10.9
Upright object	Acc	70.8	75.0	64.6	66.7	37.5	77.1	81.3	67.6 ± 14.5
	ITR	22.8	25.9	18.6	20.0	5.08	27.6	31.0	21.6 ± 8.45
Inverted object	Acc	77.1	66.7	75.0	58.3	39.6	70.8	83.3	67.3 ± 14.6
	ITR	27.6	20.0	25.9	14.8	5.86	22.8	32.8	21.4 ± 8.92
Highlight icon	Acc	48.3	68.8	41.7	43.8	33.3	47.9	45.8	47.1 ± 10.8
	ITR	9.58	21.4	6.69	7.56	3.65	9.39	8.43	9.53 ± 5.61

  - The best performance with accuracy of 88.7% and ITR of 38.7 bits min−1 was yielded by the inverted face.

Results

- Online accuracy and ITR
  - Accuracies
    - Compared with the highlight icon (accuracy of 47.1%), other stimuli achieved significantly higher accuracies.
    - While the accuracy had no significant difference between upright and inverted for all face-related stimuli and objects, the difference was marginally significant for the inverted face in contrast to the upright face.
    - Comparing the face-related stimuli with the object, only the inverted face generated significantly higher accuracy than that of the object.
  - ITRs
    - Both the face-related stimuli and the object achieved significantly higher ITRs than the ITR 9.53 bits min−1 of the highlight icon.
    - The inverted face yielded significantly higher ITR than that of the upright face while there was no significant difference between upright and inverted for the eyeless face, eye and object.
    - The inverted face also significantly improved the ITR in comparison to the object.

Results

- Offline analysis
  - Why performance improved for the inverted face?
  - Methods
    - For each type of stimulus, 8 runs were randomly selected from the 16 runs (5 targets and 35 non-targets in each run) of the two experimental sessions for the classifier training.
    - The remaining 8 runs were used as test data.
    - Such procedure was repeated 100 times and the average classification accuracy and ITR were then calculated.

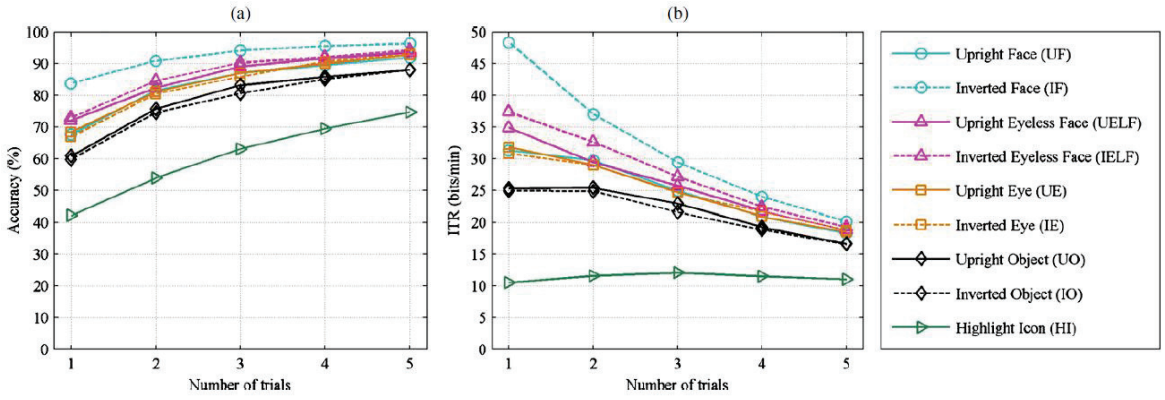

Results

- Offline analysis
  - Comments
    - The inverted face yielded higher accuracy and ITR than those of the other stimuli across various trials.
    - The face-related stimuli obtained a performance exceeding that of the object, while both of them performed better than the highlight icon.
    - There was no big difference between upright and inverted for the eyeless face, eye and object, whereas the inverted face was noticeably better than the upright face.

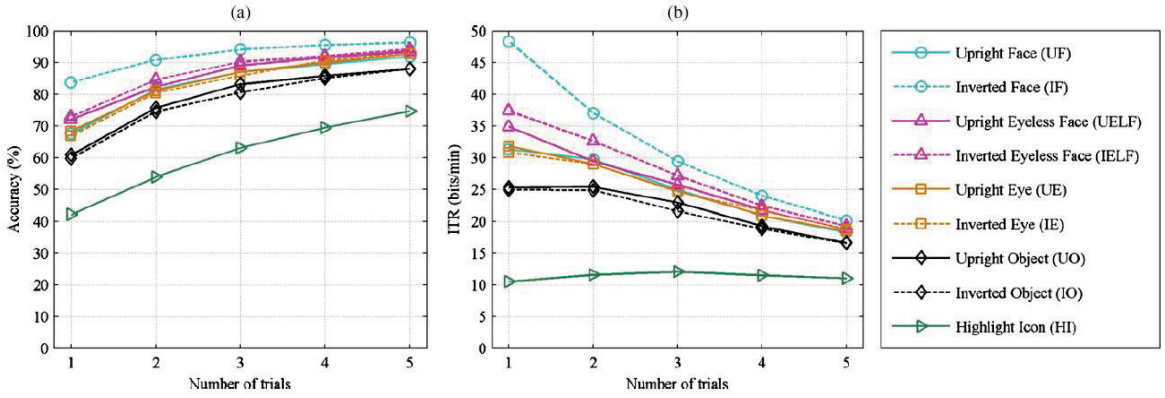

Results

- ERP analysis

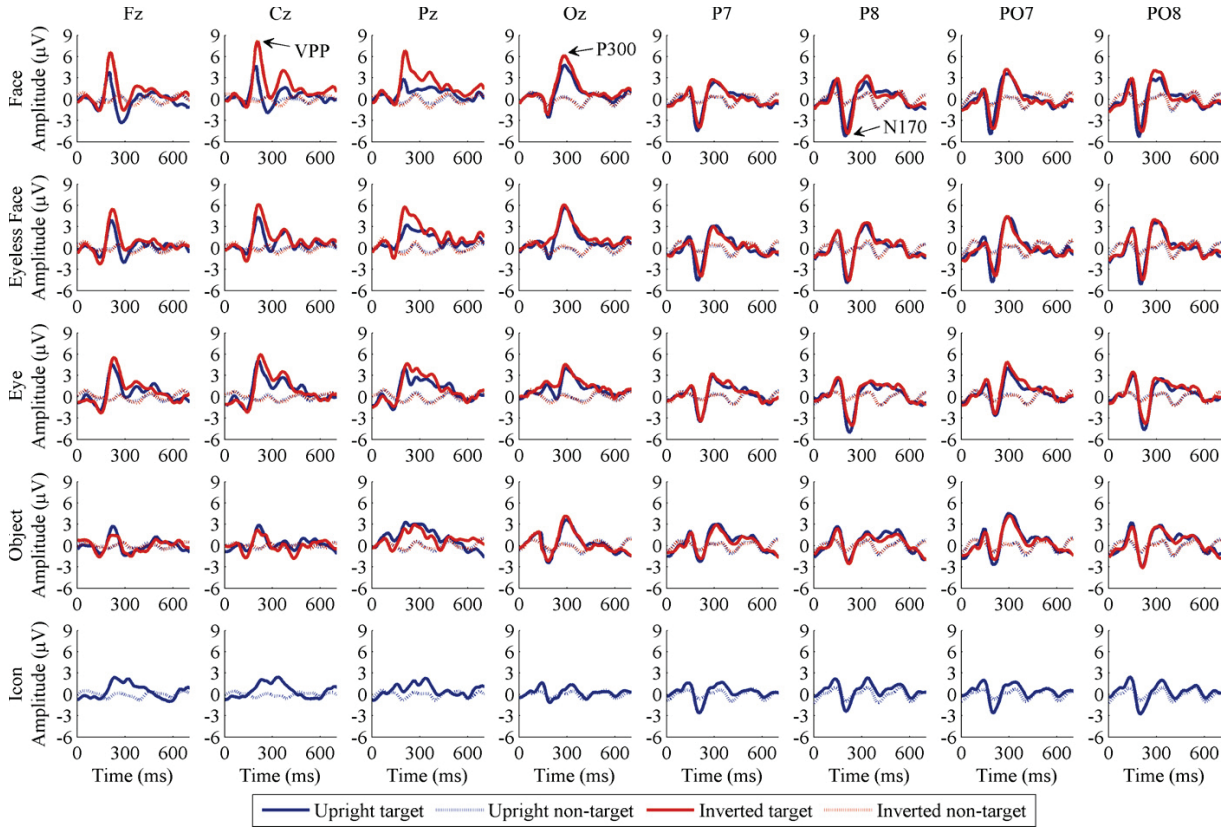

Results

- ERP analysis

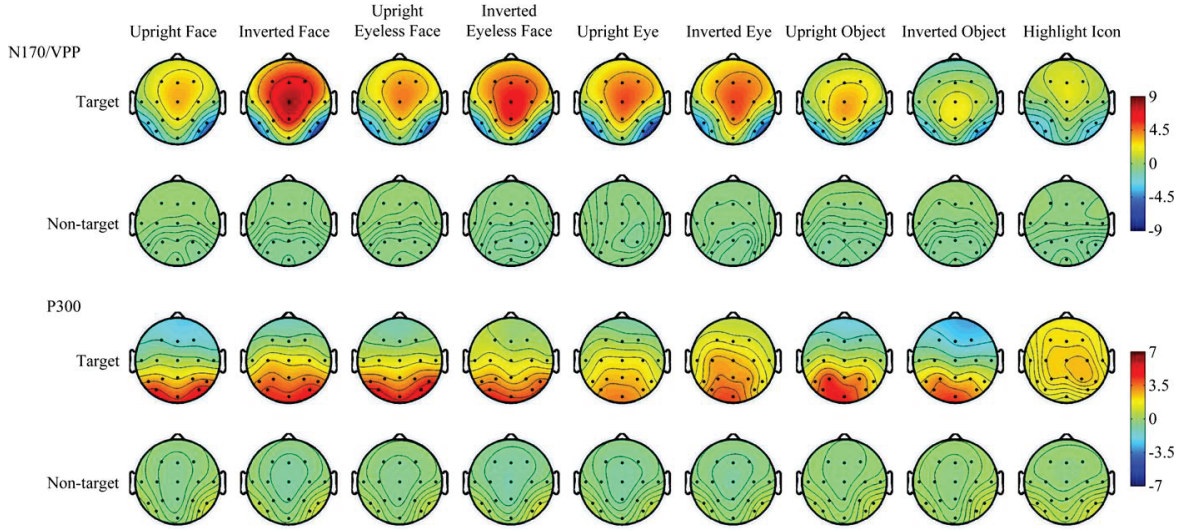

	N170		VPP		P300	
Paradigm	Amplitude	Latency	Amplitude	Latency	Amplitude	Latency
Upright face	−6.36 ± 2.64	200.9 ± 16.4	5.17 ± 1.10	199.2 ± 13.2	5.40 ± 1.15	274.1 ± 59.8
Inverted face	−6.18 ± 2.34	217.1 ± 11.7	8.37 ± 1.71	214.9 ± 7.81	6.68 ± 1.17	279.6 ± 44.6
Upright eyeless face	−6.19 ± 2.39	204.8 ± 12.9	5.36 ± 1.06	206.3 ± 12.7	6.44 ± 1.02	284.1 ± 30.1
Inverted eyeless face	−5.83 ± 2.13	218.8 ± 7.80	7.12 ± 1.94	218.3 ± 8.80	6.58 ± 1.24	281.6 ± 37.2
Upright eye	−5.60 ± 1.87	207.6 ± 9.30	6.22 ± 2.11	208.7 ± 9.10	5.15 ± 1.36	282.3 ± 45.8
Inverted eye	−5.22 ± 1.18	217.1 ± 10.7	7.06 ± 2.40	219.3 ± 8.10	5.20 ± 1.31	276.3 ± 25.2
Upright object	−3.44 ± 1.61	208.7 ± 11.0	3.43 ± 1.47	201.5 ± 26.1	5.19 ± 1.13	290.7 ± 35.9
Inverted object	−3.54 ± 1.24	209.8 ± 10.7	3.15 ± 1.79	199.2 ± 31.0	5.16 ± 1.03	294.0 ± 24.4
Highlight icon	−3.25 ± 1.79	199.8 ± 11.8	2.79 ± 1.86	205.4 ± 32.3	3.57 ± 1.44	301.5 ± 37.4

Results

- ERP analysis
  - N170
    - Larger N170 amplitudes evoked by the face-related stimuli than by the highlight icon.
    - No significant difference was found among the face-related stimuli and between the object (both upright and inverted) and highlight icon.
    - A longer N170 latency was observed for the inverted than the upright.
  - VPP
    - A larger VPP amplitudes evoked by the face-related stimuli than by the highlight icon and by the object.
    - The inverted face elicited significantly larger VPP than the upright face.
    - A longer VPP latency was observed for the inverted than the upright.
  - P300
    - A larger P300 amplitudes evoked by the face-related stimuli and the object than by the highlight icon, especially at the parietal-occipital and occipital sites.
    - The inverted face yielded higher P300 amplitude than that of the upright face.
    - the P300 amplitude evoked by the eyeless face (both upright and inverted) was higher than by the upright face.
    - the P300 amplitudes derived from the inverted face and eyeless face were significantly higher than that of the object.

Results

- Discriminative feature analysis
  - r^2-value(squared pointwise biserial correlation coefficients)
    - Pointwise biserial correlation coefficient
      - Definition

$$r(x) = \frac{\sqrt{N_1 N_2}}{N_1 + N_2} \frac{\text{mean}\{x_i | y_i = 1\} - \text{mean}\{x_i | y_i = 2\}}{\text{std}\{x_i | y_i = 1, 2\}}$$

Where N1 and N2 are the numbers of variables belonging to class 1 (target) and class 2 (non-target), xi and yi are the value and class label of the ith variable.

    - The r2-value is equal to the squared of r(x).
    - Larger r2-value indicates higher separability of distributions.

Results

- Discriminative feature analysis
  - Temporal and spatial distributions of the most discriminative information for the nine stimuli

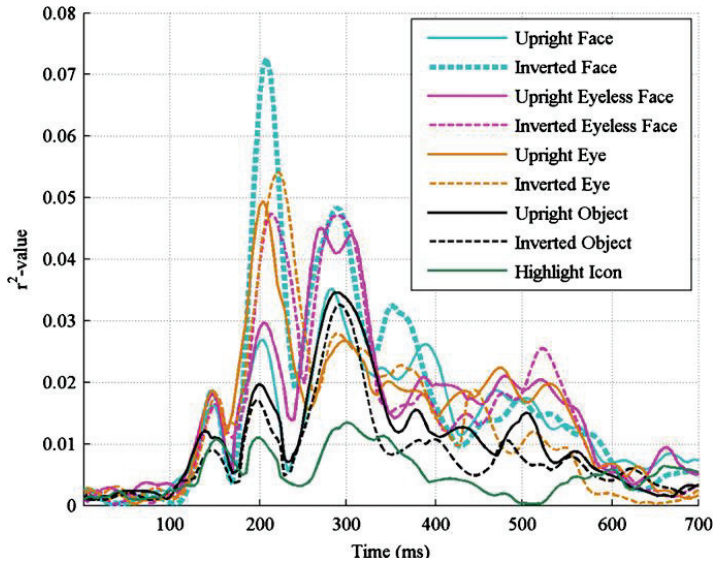

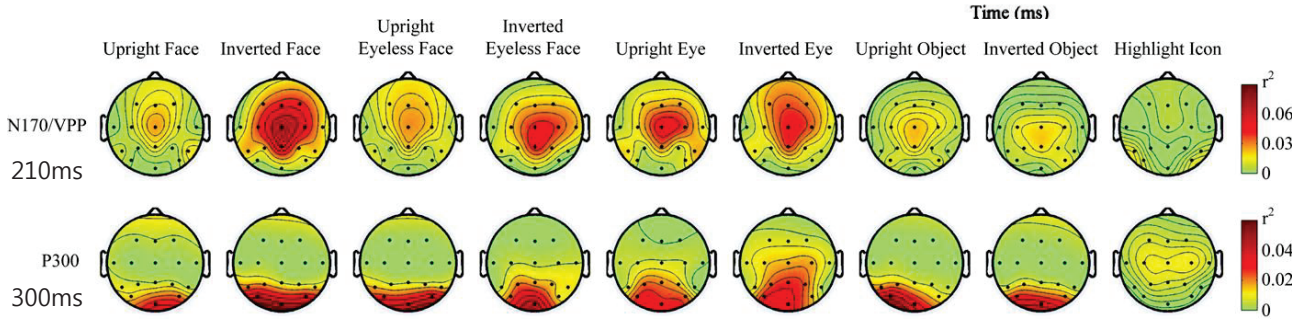

Results

- Discriminative feature analysis
  - Comments
    - Almost all of the face-related stimuli and the object yielded more discriminative features than the highlight icon from 200 to 500 ms after stimulus onset.
    - The most outstanding components in the features were found around 200 and 300ms, which just correspond to N170/VPP and P300.
    - The discriminative features around 200 ms for the face-related stimuli and the object were mainly located at the fronto-central sites(Cz)
    - the P300 distributions for the face-related stimuli and the object were mainly located at the parietal-occipital sites, compared with the centro-parietal distribution of P300s elicited by the highlight icon

Discussion

- Advantages of facial images based BCI
  - A high luminance contrast is usually required to elicit a prominent visual evoked potential for the visual stimuli, and this may cause visual fatigue and discomfort for the user.
  - The facial images are more vivid than icons, letters or symbols, they may resist fatigue and discomfort to improve the visual attention for subjects.
  - Loss of configural information makes face perception more difficult and associated with higher cognitive functions. This encourages subjects to focus attention on the target more actively.
- Performance
  - Both the face related stimuli and the object yielded significantly higher accuracies and ITRs than that of the highlight icon.
    - This implies that stimuli with higher cognitive task requirement, such as face and object perception, are more effective than the intensified stimuli of dull icons for the P300-based BCI system.
  - The ITR derived from the inverted face was significantly higher than that of the upright face.
    - This suggests that the loss of configural face information assists in improving the performance of the BCI system.

Conclusion

- They proposed a novel BCI system using multi-component ERPs sensitive to configural processing of human face with an oddball paradigm.
- The performance of the proposed BCI is significantly improved in comparison to the conventional P300-based BCI with stimuli of intensification pattern.
  - The online performance of classification accuracy 88.7% and ITR of 38.7 bits min−1 obtained by the LDA classification using only single trial without any optimization of algorithm for feature extraction.

Securing information by use of digital holography

Bahram Javidi
Department of Electrical and systems Engineering, University of Connecticut
Takanori Nomura
Department of Opto-Mechatronics, Wakayam Univeristy, Japan

Presenter: Nitin Rawat

Considering the threat of accessing and tempering data by an unauthorized person, a secure transmission of multimedia information like image data using cryptography technique has received attention in recent years. The encryption methods enable security of data by converting it into more complex form. Besides security, the database and communication problems are critical problems due to large data size and complexity. It has become important to reduce the size of the data by preserving the complexity.

Image Encryption using FFT with Single random matrix

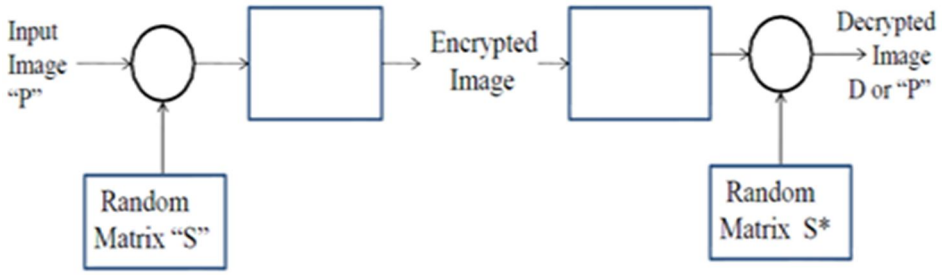

Fig. 1. FFT based Encryption and Decryption using single random phase matrix

Fig. 1 shows the Encryption approach using single random phase method. Let an image multiplied by a single random matrix $\exp[i\phi_1(x,y)]$ and further taking Fourier transform of the result to get an encrypted image.

Decryption process is reversed by taking the complex conjugate of the random phase and further its inverse Fourier transform. Here the key is formed by the combination of the transform and the random matrix.

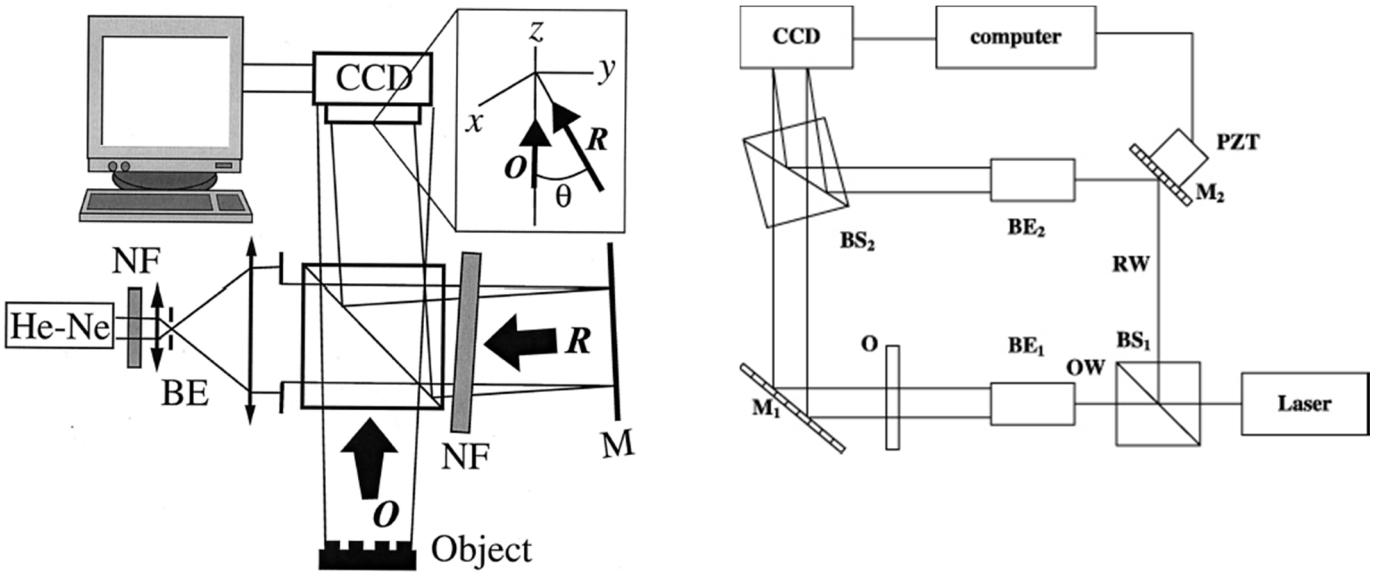

Fig. 2. Experimental setup of digital holography

Let the object wave $O(x,y)$ and reference wave $R(x,y)$ interferes. The intensity is calculated by

$$I(x,y) = \left|O(x,y) + R(x,y)\right|^2$$

$$= \left(O(x,y) + R(x,y)\right)\left(O(x,y) + R(x,y)\right)^*$$

$$= R(x,y)R^*(x,y) + O(x,y)O^*(x,y) + O(x,y)R^*(x,y) + R(x,y)O^*(x,y) \quad \text{..... (1)}$$

Zero order term

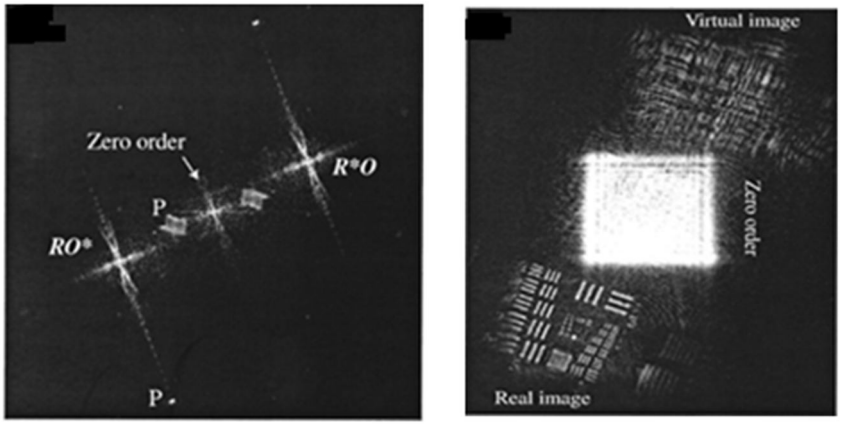

Fig. 3. Elimination of zero-order term of diffraction. () Two-dimensional Fourier spectrum of the original hologram, (b) amplitude-contrast image obtained by numerical reconstruction of the original hologram.

Let $f(x,y)$, $\alpha(x,y)$, and $H(\xi,\eta)$ denote the image to be encrypted, the input random phase mask, and the Fourier random phase mask, respectively.

$f(x,y)$ Image

$\alpha(x,y)$ RPM

$H(\xi,\eta)$ FRPM

The input random phase mask $\alpha(x,y)$, is bonded with the image $f(x,y)$. The resultant product of the two images is Fourier transformed and is multiplied by the Fourier phase mask $H(\xi,\eta)$.

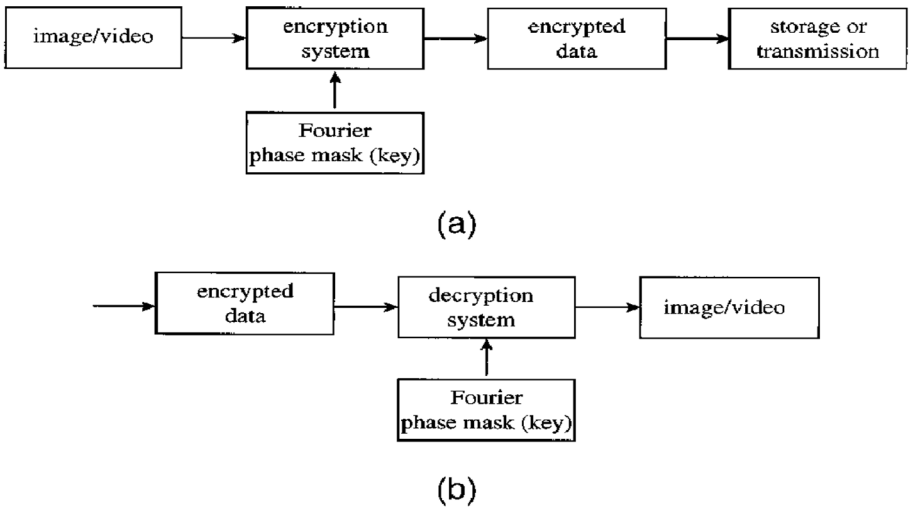

Fig. 4. Secure image/video-data-storage/transmission system that uses a combination of double-random phase encryption and a digital holographic technique: (a) transmitter-encoder, (b) receiver-decoder.

A second Fourier transform produces the encrypted data. The encrypted data as a Fourier hologram, using an interference with the reference wave $R(\xi,\eta)$ is recorded. The hologram $I_E(\xi,\eta)$ can be written as

$$I_E(\xi,\eta) = \left|\left[F(\xi,\eta)\otimes A(\xi,\eta)\right]H(\xi,\eta)\right|^2 + \left|R(\xi,\eta)\right|^2$$ Zero order term

$$+\left\{\left[F(\xi,\eta)\otimes A(\xi,\eta)\right]H(\xi,\eta)\right\}R(\xi,\eta)^*$$ Real Image

$$+\left\{\left[F(\xi,\eta)\otimes A(\xi,\eta)\right]H(\xi,\eta)\right\}^* R(\xi,\eta)$$ Virtual Image ..... (2)

where $F(\xi,\eta)$ and $A(\xi,\eta)$ denote Fourier transforms of $f(x,y)$ and $\alpha(x,y)$, respectively, and

⊗ denotes a convolution operation.

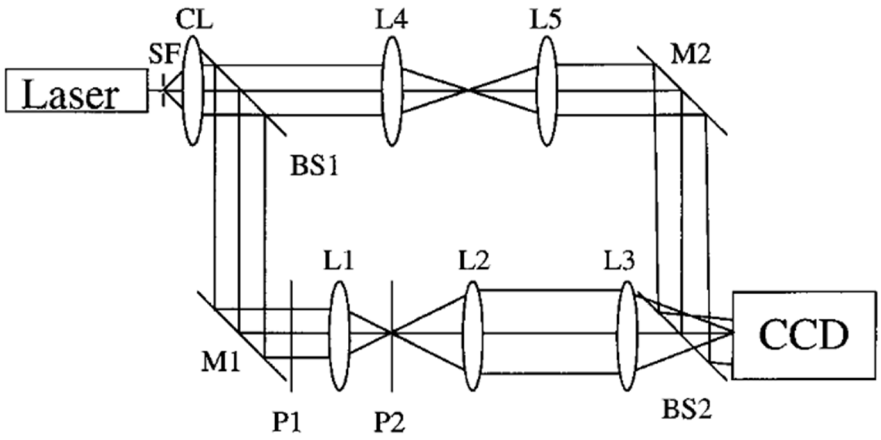

Fig. 5. Optical experiment setup: SF, spatial filter; CL, collimating lens; M, mirrors; L's, lenses; BS's, beam splitters; P1, input plane; P2, Fourier plane.

The first and second terms on the right-hand side of Eq. (2) by obtaining the power spectrum of the encrypted data and reference beam, we can get the following holographic data, $I_{E'}(\xi,\eta)$:

$$I_{E'}(\xi,\eta)=\left\{\left[F(\xi,\eta)\otimes A(\xi,\eta)\right]H(\xi,\eta)\right\}R(\xi,\eta)^{*} \quad \text{Real Image}$$

$$+\left\{\left[F(\xi,\eta)\otimes A(\xi,\eta)\right]H(\xi,\eta)^{*}\right\}R(\xi,\eta) \quad \text{Virtual Image} \qquad \ldots\ldots (3)$$

Similarly, we can also obtain the holographic data of the Fourier phase mask, $I_{M'}(\xi,\eta)$ given by

$$I_{M'}(\xi,\eta)=H(\xi,\eta)R(\xi,\eta)^{*}+H(\xi,\eta)^{*}R(\xi,\eta) \qquad \ldots\ldots (4)$$

Real Image Virtual Image

When the reference beam is a slightly inclined planar, we can extract the first term on the right-hand side of Eq. (3) and the second term on the right-hand side of Eq. (4) by Fourier transforming the holographic data to obtain the encrypted data and the Fourier phase mask, respectively. By multiplying the extracted encrypted data and the Fourier phase mask followed by inverse Fourier transformation, we can obtain the decrypted data $d(x,y)$ as:

$$d(x,y)=\mathrm{FT}^{-1}\left[\left(\left\{F(\xi,\eta)\otimes A(\xi,\eta)H(\xi,\eta)\right\}R(\xi,\eta)^{*}\right)\right]$$

$$\times \left[H(\xi,\eta)^{*} R(\xi,\eta) \right]$$

$$= \mathrm{FT}^{-1}\left[F(\xi,\eta) \otimes A(\xi,\eta) \right]$$

$$= f(x,y)\alpha(x,y) \qquad \text{..... (5)}$$

where $\mathrm{FT}^{-1}[]$ denotes the inverse Fourier transform operation and $\left|H(\xi,\eta)\right|^2$ is equal a constant because the phase masks only phase value. The intensity of Eq. (5) produces the original image because $f(x,y)$ is a positive real-valued function and $\alpha(x,y)$ is phase only.

The experimental system is shown in Fig. 5 consists of Mach-Zehnder interferometer.

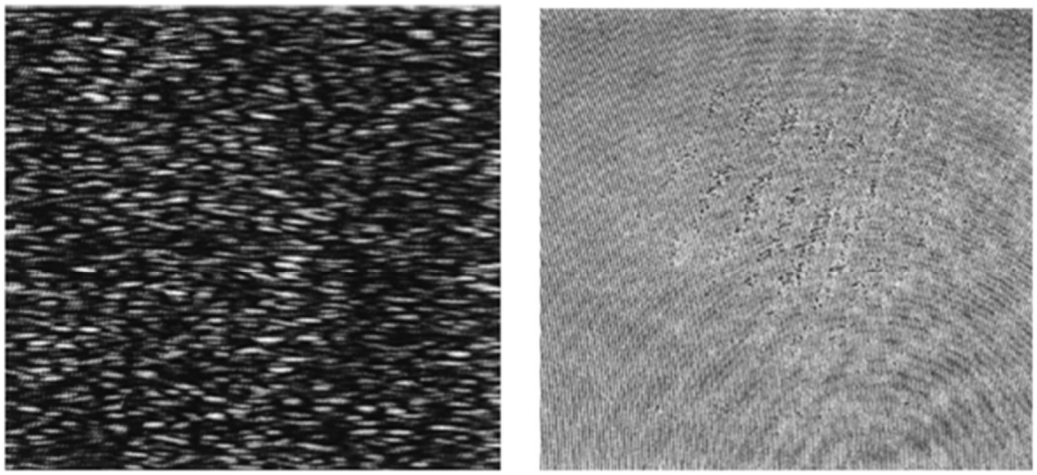

(a) (b)

Fig. 6. Digital holograms of (a) the encrypted data and (b) the Fourier phase mask.

The lower arm of the interferometer is the optical path of the image encryption. The upper arm is the reference wave. The input image to be encrypted is bonded with the input phase mask at plane P1. This product is Fourier transformed by lens L1 and is multiplied by the Fourier phase mask at plane P2 and imaged onto the CCD camera by the 4-f optical system of lenses L2 and L3.

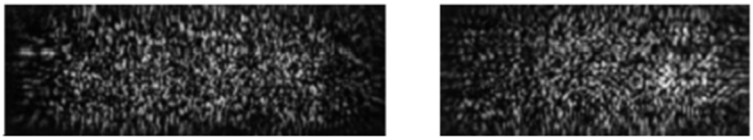

Fig. 7. Images that have been digitally reconstructed by inverse Fourier transformation of the digital hologram of the encrypted data.

Fig. 8. Images that have been digitally reconstructed with the digital hologram of both the encrypted data and the Fourier phase mask.

Digital holograms of the encrypted data and the Fourier phase mask are shown in Fig. 6. The digitally reconstructed encrypted images are shown in Fig. 7. These images were obtained by inverse Fourier transforming of the digital hologram of the encrypted data. The original images cannot be recognized. The digitally reconstructed images that have been decrypted with the hologram of the Fourier phase mask are shown in Fig. 8

Conclusion

This paper has presented an image security method that uses digital holography. The method allows the encrypted data to be stored, transmitted, and decrypted digitally.

A Head-Up Display-Based P300 Brain–Computer Interface for Destination Selection

Luzheng Bi, Xin-An Fan, Nini Luo, Ke Jie, Yun Li, and Yili Liu

IEEE Transactions on Intelligent transportation systems (2013.12)

Presenter : Soogil Woo
GIST, Dept. of Information and Communication, INFONET Lab.

Gwangju Institute of Science and Technology

Introduction

- Brain–computer interfaces (BCIs) can translate user brain activity patterns into corresponding commands to communicate with or control the external world without using conventional communication channels.
- The brain signals widely used to develop EEG-based BCIs include:

➢ 1) P300 potentials, which are a positive potential deflection on the ongoing brain activity signal at latency of roughly 300 ms after the random occurrence of a desired target stimulus from nontarget stimuli

➢ 2) steady-state visual evoked potentials (SSVEPs), which are visually evoked by a stimulus modulated at a fixed frequency and occur as an increase in EEG activities at the stimulus frequency; and

➢ 3) the event-related desynchronizations (ERDs) and event-related synchronization (ERS), which are induced by performing mental tasks such as motor imagery, mental arithmetic, or mental rotation.

Introduction

- Since P300-based BCI systems are more suitable to output more commands compared with SSVEP-based and ERD/ERS-based BCI systems and have a relatively high level of accuracy, P300-based BCIs are currently used for destination selections.
- The preliminary experimental results provide an indication of the feasibility of using EEG to drive a vehicle.
- However, they did not describe the specific speed of the controlled simulated car and the specific accuracy.

Introduction

- Their long-term goal is to develop a brain-controlled vehicle by using BCI systems to select a destination and issue a control command.
- In this paper, they proposed a new P300 BCI with visual stimuli presented on a windshield via a head-up display (HUD) and develop a destination selection system for a simulated vehicle using the proposed BCI.
- Furthermore, to improve the usability of this destination selection system, they analyze the effects of the number of rounds of EEG on the performance of the proposed system.
- This paper lays a foundation for developing a brain-controlled vehicle that uses a BCI to select a desired destination from a list of predefined destinations and then uses an autonomous navigation system to reach the desired destination.

Head-up Display

- A HUD is any transparent display that presents data without requiring users to look away from their usual viewpoints.
- HUDs were initially developed for military aviation, they are now used in commercial aircraft, automobiles, and other applications.

Hud-Based P300 BCI for destination selection

A. Visual Stimuli

- The P300 visual stimuli used in this paper are a 3*3 matrix of characters, which are displayed on a real windshield (whose top, bottom, left, and right edges are 102, 138, 59, and 59 cm) of vehicles via a HUD system constructed by ourselves.

- Each character represents a predefined destination.

  "B" -> "Bank", "H" -> "Hospital."

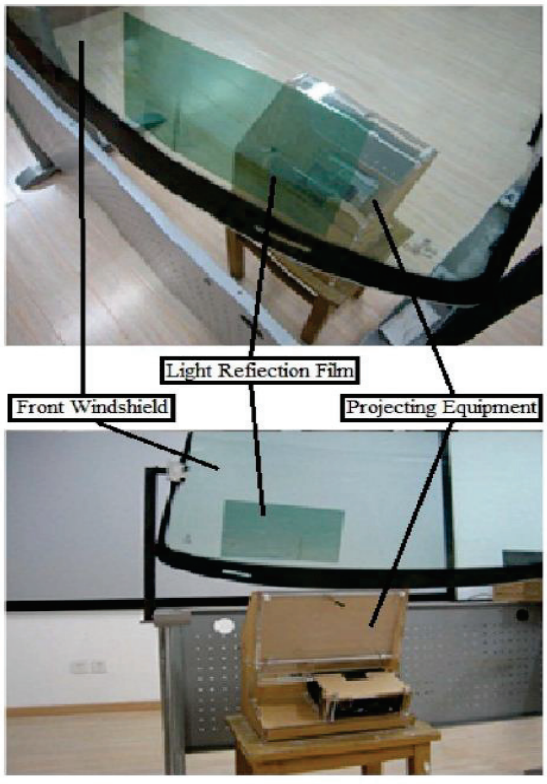

Fig. 1. HUD system.

Hud-Based P300 BCI for destination selection

A. Visual Stimuli

- The HUD system consists of a projecting device and some light reflection films (17.5 cm * 13 cm in size) pasted on the bottom-left area of the windshield.
- All of the nine characters flash on the windshield in sequence and in random order in each round.
- Each flash lasts 125 ms with an interstimulus interval of 15 ms, and thus, each round takes 1260 ms ((125 + 15) * 9).
- When the user wants to reach a destination, he focuses attention on the character associated with the destination, and the BCI interprets the EEG to infer the character to which the user is attending.

Hud-Based P300 BCI for destination selection

B. Data Collection

- They used a 16-channel amplifier to acquire the EEG signals at eight standard locations (i.e., Fz, Cz, Pz, Oz, P3, P4, P7, and P8), as shown in Fig. 2.
- The reference potential was the average of the potentials of the left and right earlobes.
- The EEG signals were amplified and digitalized with a sampling rate of 1000 Hz and a power-line notch filter to remove the line noise.

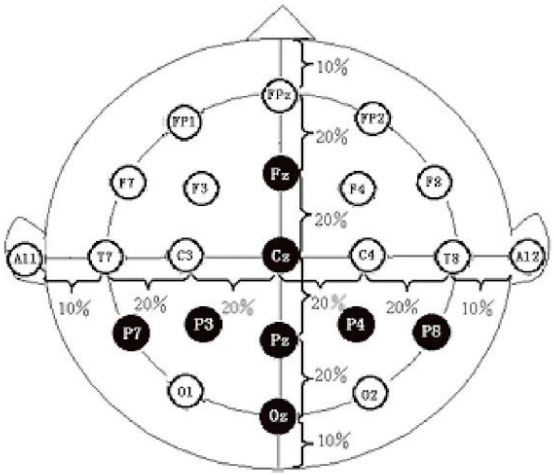

Fig. 2. Placements of eight channels used to collect EEG data are marked in black.

Hud-Based P300 BCI for destination selection

C. Signal Processing and Classification

- The collected EEG data are first decimated by a factor of 2 and filtered with a bandpass filter between 0.53 and 15 Hz.
- To improve the signal-to-noise ratio, *M* rounds of EEG data are summed. (M is number)
- To reduce the feature dimensionality in order to lower the redundancy of the features, the principal component analysis (PCA) is used, which transforms the feature space into an orthogonal space consisting of uncorrelated variables called principal components, and selects components with the highest eigenvalues as new features.

Hud-Based P300 BCI for destination selection

C. Signal Processing and Classification

- The input to the classifier of P300 is a vector of *N* dimensions, as follows:

$$x = [x(1), x(2), \ldots, x(N)]$$

➢ where *x*(*N*) is the *N*th new feature of each sample selected from the original features by using PCA.

- Linear discriminant analysis (LDA) was first used to develop the classifier, which can be represented in the following form

$$y = w^T x$$

➢ where *w* is the projection direction determined by maximizing the following cost function.

$$J_F(w) = \frac{w^T S_b w}{w^T S_w w}$$

➢ where S_b is the between-class scatter matrix, and S_w is the within-class scatter matrix.

Experiment

A. Experimental Platform

- A simulated vehicle has been designed and constructed. It includes three main parts, as shown in Fig. 3.
- 1) the HUD-based P300 BCI system for destination selection.
- 2) the 3-D driving scene and simulated vehicle based on the virtual reality technology.
- 3) the communication system between the computer supporting the 3-D driving scene and virtual vehicle.

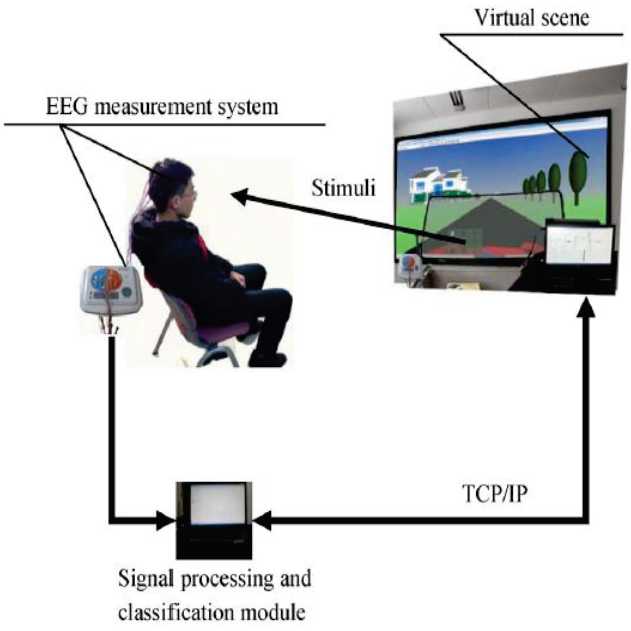

Fig. 3. Block diagram of the brain-controlled virtual vehicle.

Experiment

B. Experimental Procedures

- The experimental procedure includes two phases.
- The first is for training the HUD-based P300 BCI model for destination selection, and the second one is for evaluating and testing the destination selection system.
- In the phase of training the destination selection model, each participant completed four sessions of the P300 experiment in order to collect the data and train the model offline.
- In the second phase, they investigated the effects of the number of EEG rounds on the performance of the proposed system and demonstrated the simulated vehicles based on the destination selection system using a static and a dynamic experiment.

Result

- They used the 108 training samples collected in the experimental procedure to determine the parameters of the model of each subject, and 50 features selected by PCA are used for each model.
- In practice, first, it is desirable for the destination selection system to have high accuracy and short selection time.
- They investigated the destination selection accuracy as a function of the number of rounds when this system is used online.
- Second, given the required accuracy and selection time, it is desirable to reduce the time needed to build the corresponding model.
- They analyzed the selection accuracy as a function of the number of rounds used in building the model of each subject given the required selection time.

Result

A. Destination Selection Accuracy

- Fig. 4 shows the accuracy of the HUD-based BCI system used to select a destination as a function of the number of rounds of EEG used online by the model of the selection system.
- In this figure, the *x*-axis represents the number of rounds whereas the *y*-axis represents the accuracy gained if the BCI system selects a destination using only as many rounds as the *x*-axis.

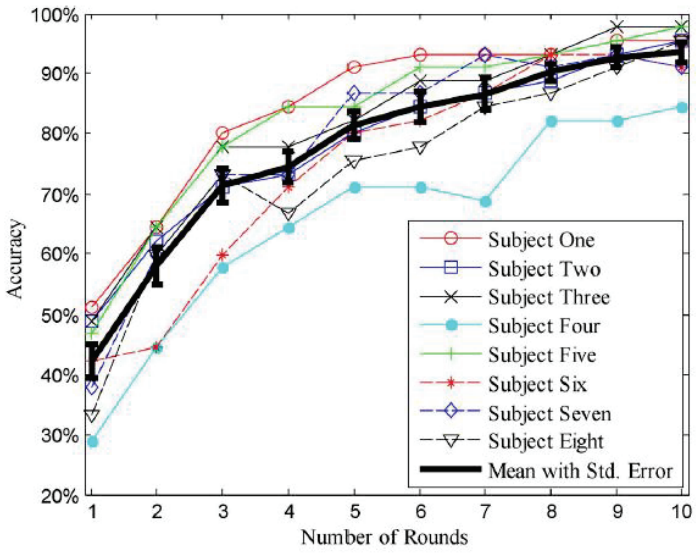

Fig. 4. Accuracy of the models as a function of the number of rounds of EEG data in testing.

Result

B. Reducing the Time Needed to Build a Model

- Given the desired accuracy and selection time to explore whether they can reduce the time needed to build the models, they analyzed the accuracy as a function of the number of rounds used in building the model of each subject.
- Fig. 5 shows the accuracy of the models as a function of the number of rounds used to build models by using ten rounds of EEG data to test each model.

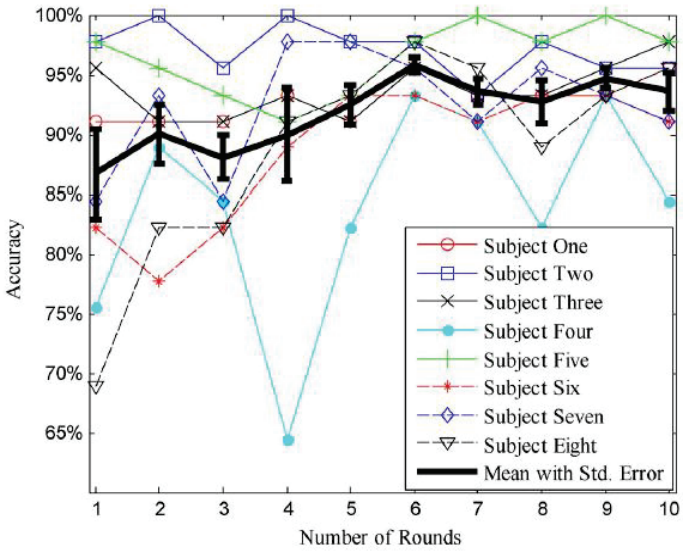

Fig. 5. Model accuracy as a function of the number of rounds of EEG data used in training the models.

Discussion and Conclusion

- First, although the accuracy is 93.6%, this accuracy may not be high enough for some applications.
- Second, the number of predefined destinations of the current system is small.
- Third, the users lose their control of the vehicle after the BCI-based destination selection system sends a destination to the autonomous vehicle.
- Fourth, they conducted the experiment in a laboratory, where the environmental factors were constant. However, in practice, vehicles are used outdoors.
- Their future work focuses on addressing the issues listed above and developing brain-controlled vehicles by combining the HUD-based BCI with other BCIs for issuing motion commands.
- The current and future research in this area will help further improve the mobility, independence, and quality of life for people with disabilities, as well as the general public.

Thank you!

Linear discriminant analysis (LDA)

- The LDA (also known as Fisher's LDA) approach aims to find the optimal direction, $\mathbf{w}_1$, to project data upon and maximize the Fisher ratio:

$$J(\mathbf{w}_1) = \frac{\mathbf{w}_1^T \mathbf{S}_\mathbf{B} \mathbf{w}_1}{\mathbf{w}_1^T \mathbf{S}_\mathbf{w} \mathbf{w}_1} \qquad \text{where, } \mathbf{S}_\mathbf{B} = (\mathbf{m}_1 - \mathbf{m}_2)(\mathbf{m}_1 - \mathbf{m}_2)^T$$
$$\mathbf{S}_\mathbf{w} = \sum_i (\mathbf{x} - \mathbf{m}_i)(\mathbf{x} - \mathbf{m}_i)^T$$

- The maximization of mean distances and minimization of class scatters.

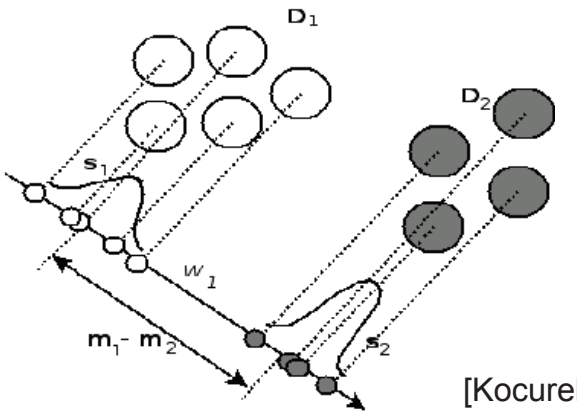

[Kocurek 2007]

Principal Component Analysis

- Eigen Vectors show the direction of axes of a fitted ellipsoid.
- Eigen Values show the significance of the corresponding axis.
- The larger the Eigen value, the more separation between mapped data.
- For high dimensional data, only few of Eigen values are significant.

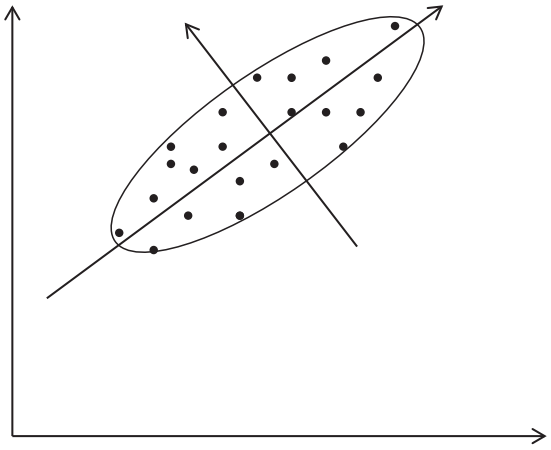

Title: Some fundamental properties of speckle.

Authors: J. W. Goodman.

Published in: J. Opt. Soc. Am., Vol. 66, No. 11, November 1976.

Presenter: Hwanchol Jang.

Abstract: A probabilistic modeling for speckle pattern is introduced. Ways to suppress the speckle pattern is also presented.

I. Introduction

Speckle

The vast majority of surfaces, synthetic or natural, are extremely rough on the scale of an optical wavelength. Under illumination by coherent light, the wave reflected from such a surface consists of contributions from many independent scattering areas. Interference of these de-phased but coherent wavelets results in the granular pattern we know as speckle.

Note that if the observation point is moved, the **path length**s traveled by the scattered components change, and a **new and independent valued of intensity** may results from the interference process.

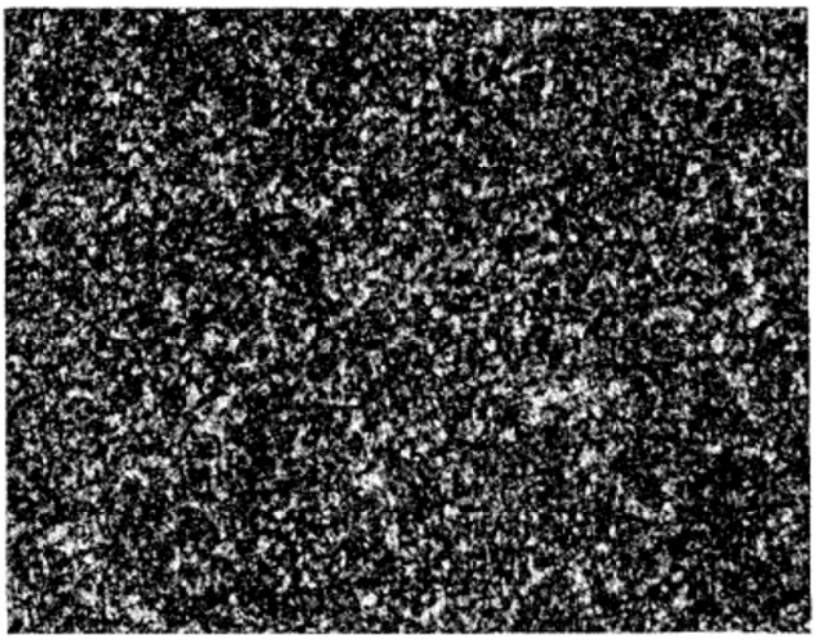

FIG. 1. Typical speckle pattern.

II. Speckle as a random-walk phenomenon

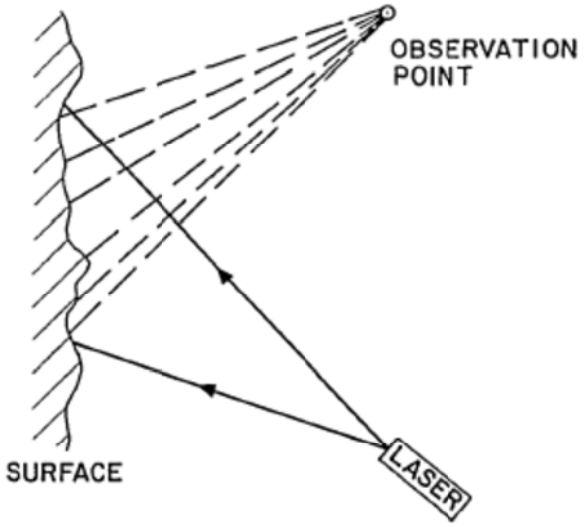

FIG. 2. Speckle formation in the free-space geometry.

The signal:

$$u(x, y, z; t) = A(x, y, z)\exp(i2\pi\nu t)$$

where ν is the optical frequency and $A(x, y, z)$ is a complex phasor amplitude

$$A(x, y, z) = A(x, y, z)\exp(i\theta(x, y, z)) .$$

The irradiance:

The directly observable quantity is the irradiance at (*x*,*y*,*z*), which is given by

$$I(x, y, z) = \lim_{T\to\infty}\int_{-T/2}^{T/2}\left|u(x, y, z; t)\right|^2 dt = \left|A(x, y, z)\right|^2 .$$

The complex amplitude of the field at (*x*,*y*,*z*) may be regarded as resulting from the sum of contributions from many elementary scattering areas on the rough surface. Thus the phasor amplitude of the field can be represented by

$$A(x,y,z)=\sum_{k=1}^{N}a_k=\sum_{k=1}^{N}|a_k|\exp(i\phi_k)$$

where $|a_k|$ and ϕ_k represent the amplitude and phase of the contribution form the *k*th scattering area and *N* is the total number of such contributions.

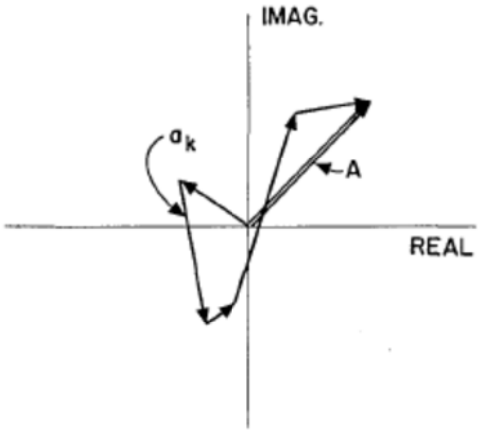

FIG. 4. Random walk in the complex plane.

Two important assumptions

(i) The amplitude and the phase of the *k*th elementary phasor are statistically independent of each other and of the amplitudes and phases of all other elementary phasors.

(ii) The phases of the elementary contributions are equally likely to like anywhere in the primary interval $(-\pi,\pi)$.

With these two assumptions, the similarity of our problem to the classical random walk in a plane becomes complete.

Provided the number *N* of elementary contributions is large, we find (a) the real and imaginary parts of the complex filed at (*x*,*y*,*z*) are independent, zero mean, identically distributed Gaussian random variables, and (b) the irradiance *I* obeys negative exponential statistics, i.e., its pdf is of the form

$$p(I)=\begin{cases}(1/\bar{I})\exp(-I/\bar{I}), & I\geq 0\\ 0, & \text{otherwise}\end{cases}$$

where $\bar{I}$ is the mean irradiance.

A fundamental important characteristic of the negative exponential distribution is that its standard deviation precisely equals its mean. Thus, the contrast of a polarized speckle pattern, as defined by

$$C = \sigma_I / \bar{I}$$

is always unity. Herein lies the reason for the subjective impression that the variations of irradiance in a typical speckle pattern are indeed a significant fraction of the mean.

III. Suppression of speckle

The sum of *M* identically distributed, real-valued, uncorrelated random variables has a mean value which is *M* times the mean of any one component, and a standard deviation which is $\sqrt{M}$ times the standard deviation of one component. Thus, if we add *M* uncorrelated speckle patterns on an irradiance basis, the contrast of the resultant speckle pattern is reduced in accord with the law

$$C = \sigma_I / \bar{I} = 1/\sqrt{M} \ .$$

Uncorrelated speckle patterns can be obtained from a given object by means of time, space, frequency, or polarization diversity.

Pure spatial diversity occurs, for example, when a reflecting surface is illuminated by several different lasers from different angles. If the **angles of illumination** are sufficiently separated, the path length delays experienced by each of the reflected beams will be different enough to generate uncorrelated speckle patterns.

A second way of changing optical paths (in wave lengths) traveled by a reflected wave is to change the optical **frequency of the illuminations**. If the separation of these frequency components is sufficiently great, *M* uncorrelated speckle patterns will result, with addition on an irradiance basis.

Ex) In a reflection geometry, with angles of incidence and reflection near normal to the surface, the separation required to produce uncorrelated speckle is approximately

$$\Delta \nu \cong c / 2\sigma_z$$

where c is the light velocity and σ_z is the standard deviation of the surface height fluctuations.

Time diversity: If a transparency object is illuminated through a diffuser, then motion of that diffuser results in a continuous changing of the speckle pattern in the image. A **time exposure** in the image plane then results in the addition, on an intensity basis, of a number of uncorrelated speckle patterns, thus suppressing the contrast of the detected speckle pattern.

IV. Discussion

The speckle phenomenon happens in turbid lens imaging (TLI) systems []. On the one hand, it is used as useful information. On the other hand, it is regarded as a noise that we try to suppress.

TLI is one new technique that increases the resolution of an imaging system beyond the physical limitation given by lenses. In TLI, a turbid medium is inserted between a sample and an objective lens. The turbid medium has many small particles in it, and the wavelets in the sample beam experience multiple scattering inside the medium. This scattering is good in a sense that higher angle mode waves, which usually go out of the detector, experience the scattering and may be redirected into the detector. This makes it possible to collect higher mode wave information which tells us the details of the sample. Also, the scattering is bad in a sense that it scrambles the sample image in the detector. But if we know i) the way how the medium scrambles images and ii) the way how to recover it using “i)”, it is no longer a problem. Here we can obtain “i)” because the input and output relationship of the turbid medium can be measured. “ii)” is also known as it is just an inverse problem given linear system model and the system response.

The sample beam is a weighted sum of waves with many spatial frequencies, written as follows,

$$x(t) = \sum_l x_l \exp(i2\pi f_l t)$$

where f_l is a spatial frequency and t is a spatial index.

We measure response of the optical system for a wave $\exp(i2\pi f_l t)$

$$T_l(t) = T\left(\exp(i2\pi f_l t)\right).$$

Assuming TLI system is linear time-invariant (LTI), the response to the input x can be written

$$y(t) = T(x(t)) = T\left(\sum_l x_l \exp(i2\pi f_l t) \right) = x_l \sum_l T_l \ .$$

Here, the index *t* and *l* actually have dimension two. Then, the response can be represented by a linear system model as follows

$$\mathbf{y} = \mathbf{T}\mathbf{x} \, .$$

Here, we can estimate **x** with given **y** and **T**, where **y** and **T** are measured in the experiments. Here, note that a column of **T** is a speckle pattern and the columns in **T** are uncorrelated to each other for their path lengths differ enough; if the spatial frequency gap is more than a certain value, it is true. So, we can see that the matrix **T** is well conditioned for recovery.

We also note that the **y** is in fact is a noisy measurement where speckle pattern is included in the noise. For the suppression of the noise, we can use multiple uncorrelated measurement as it is presented in the talk.